

Lehrstuhl für Raumfahrttechnik
Technische Universität München

Data Handling and Evaluation for Autonomous Experiments in Interplanetary Missions

Robert Senger

Vollständiger Abdruck der von der Fakultät für Maschinenwesen der Technischen Universität
München zur Erlangung des akademischen Grades eines

Doktor Ingenieurs

genehmigten Dissertation.

Vorsitzender: Univ.-Prof. Dr. rer. nat. Ulrich Walter
Prüfer der Dissertation: 1. Univ.-Prof. Dr.-Ing. Eduard Igenbergs, i. R.
2. Univ.-Prof. Dr.-Ing. Horst Baier
3. apl. Prof. Dr. rer. nat. Eberhard Grün,
Ruprecht-Karls-Universität Heidelberg

Die Dissertation wurde am 16.10.2006 bei der Technischen Universität München eingereicht
und durch die Fakultät für Maschinenwesen am 26.06.2007 angenommen.

Data Handling and Evaluation for Autonomous Experiments in Interplanetary Missions

Robert Senger

Für meinen Vater Heinz
† 30.12.2004

Vorwort

An dieser Stelle möchte ich allen danken die mich während der Anfertigung dieser Arbeit über all die Jahre begleitet haben. An erster Stelle meinem Doktorvater Prof. Eduard Igenbergs für seine immerwährende Unterstützung und Geduld. Seinem Nachfolger als Leiter des Lehrstuhls, Prof. Ulrich Walter, für die Freiheiten die ich am Lehrstuhl genießen durfte. Allen Kollegen, deren namentliche Nennung den Rahmen dieser wenigen Zeilen sprengen würde, für die stets gute Atmosphäre am Lehrstuhl.

Mein ganz besonderer Dank gilt meiner Mutter Ursula und meiner Lebensgefährtin Dagmar. Ohne ihr unerschütterliches Vertrauen und ihre fortwährende bedingungslose Unterstützung auch in schwierigsten Zeiten wäre die Fertigstellung dieser Arbeit nicht möglich gewesen.

München, den 2.11.2006

Table of Contents

1	Introduction	1
2	Exploration of cosmic dust.....	3
2.1	Dust in the solar system	4
2.1.1	Physical properties and orbital dynamics.....	5
2.1.2	Interplanetary and interstellar dust in the heliosphere	7
2.1.3	Circumplanetary dust	10
2.1.4	Space debris.....	12
2.1.5	Exemplary instruments and missions.....	13
2.2	The MDC mission HITEN, (formerly MUSES-A).....	17
2.2.1	Spacecraft properties	17
2.2.2	Mission.....	18
2.2.3	Results of the MDC-HITEN dust measurements.....	20
2.3	The MDC mission NOZOMI, (formerly PLANET-B).....	21
2.3.1	Spacecraft properties and operations.....	21
2.3.2	Mission.....	22
2.3.3	The scientific mission of the MDC	26
3	The Mars Dust Counter	27
3.1	The MDC measuring principle.....	28
3.1.1	Physical background of the impact ionization process	28
3.1.2	Material, geometrical and other artifacts.....	29
3.2	Technical properties	31
3.2.1	Experiment design.....	31
3.2.2	Onboard data processing	32
3.2.3	MDC structural integration and effective solid angle	36
3.2.4	Instrument detection capabilities.....	50
3.3	Data processing on ground	52
3.3.1	Calibration.....	52
3.3.2	Data analysis	54
4	Signal screening	57
4.1	Basics and motivation	57
4.2	Improvement of the onboard qualification.....	57
4.2.1	The qualification routine	58
4.2.2	Genetic algorithms	59
4.2.3	Optimization of the qualification parameter set.....	60
4.3	Signal screening by neural networks.....	65
4.3.1	History and basics	65
4.3.2	Components and functionality of neural networks	66
4.3.3	Implementation.....	69
4.3.4	Reduction of the input parameters	70
4.3.5	Determination of the optimal topology	72
4.3.6	Further potential applications.....	75
4.4	Summary and discussion.....	76
5	Data compression onboard the MDC	79
5.1	Basics and motivation	80
5.2	Data compression	81
5.2.1	Lossy compression	81
5.2.2	Discrete Wavelet Transformation (DWT).....	82

5.2.3	Compression of MDC signals	86
5.3	Implementation and integration of the MDC onboard software upgrade	89
5.3.1	Hardware and software restrictions.....	89
5.3.2	Integration of the upgrade into the existing software.....	90
5.4	Verification of the new analysis process.....	92
5.4.1	Analysis of MDC-NOZOMI data after compression/decompression.....	94
5.4.2	Analysis of MDC-HITEN data after compression/decompression.....	94
5.5	Summary and discussion.....	96
6	Mission results.....	103
6.1	Overview	103
6.2	Noise signals and flight data interpretation.....	104
6.2.1	Noise signals and instrument dead time.....	105
6.2.2	MDC view-axis determination from NOZOMI attitude	123
6.2.3	NOZOMI flight data and sensor pointing directions	131
6.2.4	MDC operating data	145
6.3	Particles detected in the vicinity of Earth and Moon	149
6.3.1	Overview	149
6.3.2	Dust flux determination.....	156
6.3.3	Characteristics of the detected particles	158
6.4	Particles detected in the interplanetary space.....	160
6.4.1	Overview	160
6.4.2	Determination of interplanetary dust flux	166
6.4.3	Characteristics of the detected particles	167
6.5	Summary	186
7	MDC online application and file database.....	189
7.1	Basics and motivation	189
7.2	Description	189
7.2.1	Online application	190
7.2.2	File database.....	192
7.3	Summary and future prospects.....	194
8	Summary and discussion.....	197
	Appendix A: Bibliography.....	199
	Appendix B: Picture credits	213
	Appendix C: Tables.....	215
	Appendix D: XML files Document Type Descriptions	241
	Appendix E: MDC-NOZOMI Publications	245
	Appendix F: Curriculum vitae.....	247
	Appendix G: Legal information	249

Figures

Figure 2-1: The zodiacal light	3
Figure 2-2: A micrometer sized dust particle	4
Figure 2-3: Dust flux at 1 AU as derived by Grün et al.	9
Figure 2-4: Theoretically predicted dust rings	11
Figure 2-5: The GALILEO spacecraft	14
Figure 2-6: The ULYSSES spacecraft	14
Figure 2-7: The CASSINI spacecraft	15
Figure 2-8: The STARDUST spacecraft	15
Figure 2-9: The CASSINI Cosmic Dust Analyzer	16
Figure 2-10: The HITEN spacecraft	17
Figure 2-11: HITEN orbit	19
Figure 2-12: HITEN distance from earth	20
Figure 2-13: The NOZOMI spacecraft	21
Figure 2-14: NOZOMI orbit in the Earth-Moon system	23
Figure 2-15: NOZOMI orbit in the interplanetary space	24
Figure 2-16: NOZOMI end of mission	25
Figure 3-1: The MDC	27
Figure 3-2: The MDC measuring principle	32
Figure 3-3: MDC data processing	35
Figure 3-4: MDC integration, details	36
Figure 3-5: MDC integration, overview	37
Figure 3-6: Latitude β and longitude λ of an impacting particle	38
Figure 3-7: Position of the MDC on NOZOMI's side panel #8	39
Figure 3-8: Illustration of the MDC entrance grid geometry	40
Figure 3-9: Penetrability of the MDC entrance grid over particle size	41
Figure 3-10: Illustration of the geometry for the calculation of Ω	43
Figure 3-11: Visualization of the MDC view area	45
Figure 3-12: Effective solid angle $\Omega_{nm}(D)$ for a particle size of $D = 5 \mu\text{m}$	46
Figure 3-13: Particle size dependence of the effective solid angle $\Omega_{\text{MDC}}(D)$	47
Figure 3-14: Geometry of the calculation of the spin-averaged sensitivity	48
Figure 3-15: Spin-averaged sensitivity of the MDC on NOZOMI	49
Figure 3-16: Integrated spin-averaged sensitivity	50
Figure 3-17: MDC measuring range	51
Figure 3-18: The MDC inside the calibration setup	52
Figure 3-19: Calibration impacts	53
Figure 3-20: Impact positions inside the sensor box	54
Figure 3-21: Typical calibration signal with characteristic points	55
Figure 4-1: Evolution of the performance r_{imp} of the parameter sets	62
Figure 4-2: Separation capabilities of the original parameter set	63
Figure 4-3: Separation capabilities of the best resulting parameter set	64
Figure 4-4: Biological and artificial neurons and related networks	66
Figure 4-5: Input, attributes and output of neurons	67
Figure 4-6: Illustration of the basic learning strategy	68
Figure 4-7: Training process of the neural network	70
Figure 4-8: Significance of the input parameters	71
Figure 4-9: Correlations of the specific values	72

Figure 4-10: Final topology of the neural network with one hidden layer	75
Figure 5-1: Some families of Wavelets.....	83
Figure 5-2: Decomposition tree of an MDC neutral channel signal	85
Figure 5-3: Compression of an MDC signal	87
Figure 5-4: Performance of the data compression	88
Figure 5-5: Flow chart of data processing of the new memory management.....	91
Figure 5-6: A typical MDC signal before and after compression.....	93
Figure 5-7: Impact speed ratio new/original analysis, MDC-HITEN.....	96
Figure 5-8: Particle mass ratio new/original analysis, MDC-HITEN.....	97
Figure 5-9: Impact speed ratio new/original analysis, MDC-NOZOMI.....	97
Figure 5-10: Particle mass ratio new/original analysis, MDC-NOZOMI.....	98
Figure 6-1: Angle of the NOZOMI spin-axis to the Sun over mission time.....	105
Figure 6-2: A series of noise signals with period \approx NOZOMI spin-period	107
Figure 6-3: Distribution of noise signals over spin-phase, half years.....	109
Figure 6-4: Distribution of noise signals over spin-phase, spin-dependency	110
Figure 6-5: 2-Dimensional illustration of the principles of cluster analysis.....	111
Figure 6-6: 2-Dimensional illustration of linkage methods	112
Figure 6-7: Results of the evaluation of metric and linkage method	114
Figure 6-8: Cluster analysis result of MDC eval. noise data and control data.....	116
Figure 6-9: Hierarchy tree of MDC evaluation noise data and control data	117
Figure 6-10: Cluster analysis result of the full MDC data	118
Figure 6-11: Signals assigned to cluster no. 2, signal shape.....	121
Figure 6-12: Illustration of NOZOMI attitude (λ , β) and spin-axis vector s_{ecc}	123
Figure 6-13: The Earth-ecliptic and the Earth-equatorial reference system	124
Figure 6-14: Illustration of correction angle α and spin-phase φ and $\tilde{\varphi}$	127
Figure 6-15: Illustration of the shift of the y_{ecc} axis and the spin-phase φ	128
Figure 6-16: Spin-phase correction angle α .for longitudes $\lambda = -180^\circ \dots 180^\circ$	130
Figure 6-17: NOZOMI spin-axis latitude β over mission time,1998-2002	131
Figure 6-18: NOZOMI spin-axis longitude λ over mission time, 1998-2002	132
Figure 6-19: Overall heliospheric coverage of the MDC sensor view.....	133
Figure 6-20: Heliospheric coverage, illustration.....	134
Figure 6-21: NOZOMI spin rate over mission time.....	135
Figure 6-22: Angle of NOZOMI spin-axis to NOZOMI radius vector.....	136
Figure 6-23: Angle of the NOZOMI spin-axis to the velocity vector.....	136
Figure 6-24: NOZOMI distance from the Earth 1998.....	138
Figure 6-25: NOZOMI distance from the Earth, duration of stay	138
Figure 6-26: NOZOMI distance from the Sun	139
Figure 6-27: NOZOMI distance from the Sun, duration of stay	139
Figure 6-28: MDC sensitivity for apex-particles	140
Figure 6-29: MDC sensitivity for ISD grains.....	141
Figure 6-30: MDC sensitivity for β -meteoroids	142
Figure 6-31: Simulation of inclination of a model particle population.....	143
Figure 6-32: Simulation of eccentricity of a model particle population	144
Figure 6-33: Power supply voltages and high-voltages	146
Figure 6-34: Temperatures of the MDC electronics- and sensor-box.....	147
Figure 6-35: Spatial distribution of the particles in the Earth-Moon system.....	149
Figure 6-36: Mass vs. imp. speed of the particles in the Earth-Moon system	150
Figure 6-37: Mass vs. abs. speed of the particles in the Earth-Moon system	152
Figure 6-38: Mass vs. abs. speed of the particles in the ecc system	152
Figure 6-39: Orbital radius vs. abs. speed of the particles in the eeq system	153

Figure 6-40: Orbital radius vs. abs. speed of the HITEN particles	153
Figure 6-41: Number of particles per radius interval	155
Figure 6-42: Number of particles per radius interval, HITEN	155
Figure 6-43: Flight direction of 1998 particles	158
Figure 6-44: Spatial distribution of the particles in the interplanetary space.....	161
Figure 6-45: Mass vs. impact speed of the particles in the int. space	162
Figure 6-46: Mass vs. absolute speed of the detected particles	168
Figure 6-47: Orbital radius vs. abs. speed of the particles	169
Figure 6-48: Number of particles per radius interval, corrected	169
Figure 6-49: Number of particles vs. absolute speed	171
Figure 6-50: Number of particles vs. mass	171
Figure 6-51: Number of particles vs. inclination	172
Figure 6-52: Number of particles vs. eccentricity	172
Figure 6-53: Number of particles over mission time	173
Figure 6-54: Eccentricity over mass, identified populations.....	176
Figure 6-55: Inclination over mass, identified populations.....	176
Figure 6-56: Latitude vs. longitude of population E1 particles.....	177
Figure 6-57: Mass distribution of population E1 particles.....	178
Figure 6-58: Impact direction distribution population E1 particles	178
Figure 6-59: Eccentricity distribution population E1 particles	179
Figure 6-60: Inclination distribution population E1 particles	179
Figure 6-61: Latitude vs. longitude of population E2 particles.....	180
Figure 6-62: Mass distribution of population E2 particles.....	181
Figure 6-63: Impact direction distribution population E2 particles	181
Figure 6-64: Eccentricity distribution population E2 particles	182
Figure 6-65: Inclination distribution population E2 particles	182
Figure 6-66: Latitude vs. longitude of population E3 and E4 particles	183
Figure 6-67: Latitude vs. longitude of population H1 particles	184
Figure 6-68: Latitude vs. longitude of population H2 particles	185
Figure 7-1: Table structure of the MDC online database.....	191

Tables

Table 2-1: Interplanetary missions carrying in situ dust experiments	13
Table 3-1: Effective solid angle $\Omega_{\text{MDC}}(D)$, final values	47
Table 4-1: Results of the optimization of the quality routine parameter set	64
Table 4-2: Performance of neural networks with 1 HL	73
Table 4-3: Performance of neural networks with 2 HL, best 15 topologies	74
Table 5-1: Validation of the compression on the MDC-HITEN data	99
Table 5-2: Validation of the compression on the MDC-NOZOMI data	99
Table 6-1: Detector dead time	106
Table 6-2: Results of the evaluation of metric and linkage method	114
Table 6-3: Clustering results, real impact signals	119
Table 6-4: Signals assigned to cluster no. 2, excerpt	120
Table 6-5: MDC command log, first day of mission	148
Table 6-6: Detected particles in the vicinity of Earth and Moon	151
Table 6-7: Dust flux measurements by MDC-HITEN and MDC-NOZOMI	157
Table 6-8: Particles detected around Nov. 18, 1998	159
Table 6-9: Detected particles in the interplanetary space, Part 1	163
Table 6-10: Detected particles in the interplanetary space, Part 2	164
Table 6-11: Detected particles in the interplanetary space, Part 3	165
Table 6-12: Comparison of the MDC results and the Grün model	166
Table 6-13: Dust populations according to Grün et al.	174
Table 6-14: Properties of the 31 population E1 particles	177
Table 6-15: Properties of the 24 population E2 particles	180
Table 6-16: Properties of the 6 population E3 particles	183
Table 6-17: Properties of the 3 population E4 particles	183
Table 6-18: Properties of the 7 population H1 particles	184
Table 6-19: Properties of the 5 population H2 particles	185

Acronyms and Symbols

A/D	analog to digital
AOCS	Attitude and Orbit Control System
CI-PSU	Common Interface Power Supply Unit
CSS	cascaded style sheet
EC	electron channel
EC	event count
eec	Earth-ecliptic reference system
eeq	Earth-equatorial reference system
FIFO	first in first out
GEO	geostationary Earth orbit
HGA	high gain antenna
HGA	high gain antenna
IC	ion channel
IC	impact count
IDP	Interplanetary Dust Particles
IMF	Interplanetary Magnetic Field
ISAS	Institute of Space and Astronautical Science
ISD	Interstellar Dust
ISM	Interstellar Medium
J-KSC	Kagoshima Space Center
JPL	Johnson Propulsion Laboratory
JSP	java server pages
LDEF	Long Duration Exposure Facility
LEO	low Earth orbit
LGA	low gain antenna
LIC	Local Interstellar Cloud
LRT	Lehrstuhl für Raumfahrttechnik
LRZ	Leibniz Rechenzentrum der Bayerischen Akademie der Wissenschaften
MDC	Mars Dust Counter on NOZOMI
MDC-BremSat	Munich Dust Counter on BremSat
MDC-HITEN	Munich Dust Counter on HITEN
MDC-NOZOMI	Mars Dust Counter on NOZOMI
MLI	Multi Layer Insulation
MMR	Mean Motion Resonance
MUSES-A	Former name of the HITEN spacecraft
NASA	National Aeronautics and Space Administration
NC	neutral channel
NC	Noise count
noz	NOZOMI fixed reference system
noz φ	NOZOMI fixed reference system, rotated by the angle φ
PLANET-B	Former name of the NOZOMI spacecraft
PVDF	polyvinylidene fluorid
RAM	random access memory
ROM	read only memory
SSAS	Spin-type Sun Aspect Sensor
SSOC	Sagamihara Spacecraft Operation Center
TUM	Technische Universität München

UDSC	Usuda Deep Space Center
VBA	<i>Visual Basic</i> [®] for Applications
XML	eXtensible Markup Language

A	Ampere
mA	milliampere
AU	Astronomical Unit
bit	binary digit
bps	bits per second
kbps	kilobits per second
Byte	Byte
kByte, kB	kilobyte
C	Coulomb
deg	degree
g	gram
kg	kilogram
h	hour
Hz	Hertz
kHz	kilohertz
m	meter
mm	millimeter
km	kilometer
m, min	minute
rad	radian
rpm	revolutions per minute
s, sec	second
ms	millisecond
μs	microsecond
sr	sterradian
V	Volt
W	Watt

1 Introduction

The main subject of this work is the operation and data analysis of the space science experiment “Mars Dust Counter”, abbreviated as MDC (or in some cases, MDC-NOZOMI to avoid confusion of names, since the predecessors are named “Munich Dust Counter”, MDC) in the following. The MDC was designed and developed by the Lehrstuhl für Raumfahrttechnik (LRT) at the Technische Universität München (TUM) from 1995 to 1998. Its deep space mission began on July 4, 1998, when it was launched by a Japanese M-V launcher from Kagoshima/Japan onboard Japan’s first interplanetary mission NOZOMI (formerly PLANET-B), and was completed by the turn of the year 2003/2004 when the NOZOMI space probe was lost due to technical failure. An overview about the whole mission is given in paragraph 2.3.

The MDC’s primary scientific mission was the detection of interplanetary, interstellar and circumplanetary cosmic dust particles. A brief overview on origin and properties of cosmic dust particles is given in paragraph 2.1. Although the MDC could not fulfill its main mission goal, which was the detection of theoretically predicted dust rings around Mars, the experiment was able to collect valuable scientific data about cosmic dust in the Earth-Moon system and in the interplanetary space between the orbits of Earth and Mars. These scientific results are described in chapter 6.

Despite its name, which can be translated as “hope”, the satellite NOZOMI was a quite unlucky guy. Several technical problems that occurred one after the other since mission launch in 1998 not only challenged the operators at the Japanese Institute of Space and Astronautical Science (ISAS), but also the operators of the MDC who had to think about workarounds that were supposed to secure the MDC operation and data transmission despite the aggravated environmental conditions. These considerations and solutions are described in chapters 4 and 5.

The technical properties of the MDC, its onboard computing and data processing capabilities and the final data analysis process, all which set the boundaries to the upgrades and workarounds mentioned above, are described in chapter 3. The actual data analysis software and the MDC data formats are based on proprietary single user software solutions and local data storage, which can cause problematic redundancies in data storage, software version conflicts and even incompatibilities in a worldwide-distributed scientific community. A solution of this problem that is also a proposal for future projects, based on a database system with worldwide access via standard software and XML-based data formats, is presented in chapter 7.

Finally, the results of this work are summarized and discussed in chapter 8.

The Mars Dust Counter Project was supported by the Bundesministerium für Bildung und Forschung (BMBF) and the Deutsches Zentrum für Luft- und Raumfahrt (DLR) under the grants 50QM9501 (1995 to 1998) and 50QM9801 (1998 to 2004). The author of this work was in charge of the MDC operations and data analysis from July 2001 until December 2004.

2 Exploration of cosmic dust

The existence of cosmic dust particles was known long before the scientific exploration could take place, due to phenomena that can be viewed without technical utilities like meteors and the zodiacal light, a phenomenon that is caused by the scattering of sunlight on small particles in space. It was first described and correctly interpreted in 1683 by Giovanni Domenico Cassini [Cas1699] (Cassini also proposed that the zodiacal light may have been the biblical phenomenon known as the “Star of Bethlehem”). The scientific exploration of cosmic dust began in the early 1950s with the beginning of human space exploration, when the first acoustic dust detection devices were flown onboard A-4 launchers. Main intention of these first dust detection devices and later devices in the low Earth orbit was to determine the danger that future spacecrafts are exposed to due to the existence of micrometeoroids. Today, spacecrafts in the low Earth orbit (LEO) and also in geostationary Earth orbit (GEO) are exposed to another, man-made hazard caused by waste products of the exploration of space itself, the so-called space debris. The properties of cosmic dust and space debris are discussed in paragraph 2.1.



Figure 2-1: The zodiacal light

Photograph of the zodiacal light, taken facing east just before the beginning of the morning twilight.

The MDC-NOZOMI and its predecessors were flown on three missions until now. While the BremSat mission was only a short term mission in the low Earth orbit and suffered from a troublesome data analysis due to massive interferences, the two missions on the satellites HITEN and NOZOMI were a great success for the MDC and the Lehrstuhl für Raumfahrttechnik. The first mission HITEN was launched in 1990 and was cruising in the vicinity of Earth and Moon for about three years. The actual mission NOZOMI was launched in 1998 and was cruising between Earth orbit and Mars orbit for nearly 4 years. In both missions, the MDC was working properly and yielded valuable data from the beginning to the end of the missions. The missions HITEN and NOZOMI are described in paragraph 2.2 and 2.3, respectively.

2.1 Dust in the solar system

Within the scope of this work, only a brief introduction on the actual knowledge about cosmic dust can be given. Cosmic dust research covers a wide field of topics related to each other, including e.g. solar and planetary formation and evolution, formation of comets and asteroids, interstellar dust clouds, and exobiology. In the following, the known properties of cosmic dust derived from observations and theoretical considerations in the solar system as it is today are discussed. The term interplanetary dust (or interplanetary dust particles, IDPs) is used for dust grains that are orbiting on heliocentric trajectories and are either gravitationally bound to the heliosphere or originate directly from solar system objects. In paragraph 2.1.1, a short and only qualitative introduction into the physical properties and the complex orbital dynamics of dust particles in the heliosphere is given. Interplanetary dust (also named zodiacal dust) and interstellar dust are discussed in paragraph 2.1.2. The term interstellar dust (ISD) is used for particles that do not originate from the solar system, but are part of the interstellar medium (ISM) or, more precisely, of the local interstellar cloud (LIC) that surrounds the sun. As the properties of the ISM are not discussed in this work, the term interstellar dust is limited to interstellar dust particles that penetrate into the solar system due to the relative motion of the sun through the LIC. Dust surrounding the planets (circumplanetary dust), with a special respect to the proposed dust rings around Mars, is discussed in paragraph 2.1.3. For the sake of completeness, a special, man-made population of particles from macroscopic to microscopic sizes orbiting the Earth and known as space debris is discussed in paragraph 2.1.4. In paragraph 2.1.5, a short description of recent missions of dust experiments is given.

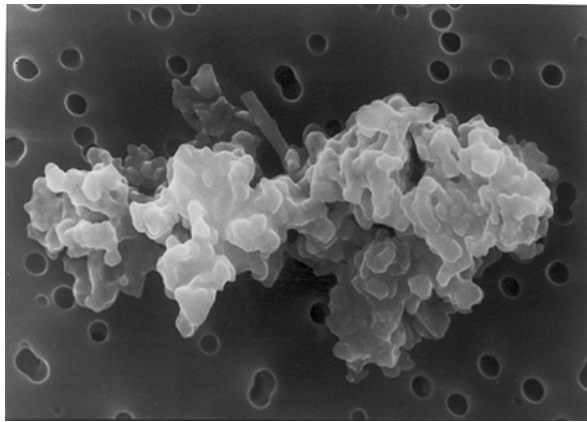


Figure 2-2: A micrometer sized dust particle

Photograph of a micrometer sized dust particle like it can be detected by the MDC experiment. The shown particle is 0.01 mm in size, and has a mass of 10^{-9} g.

2.1.1 Physical properties and orbital dynamics

Most information about structure, chemical composition and optical properties of cosmic dust particles is gained from collected samples. Sample collection is not limited to in-situ collection with sample return space experiments like LDEF or on the STARDUST mission, but was carried out even before space flight became possible by collection of micrograins in suitable environments on Earth, e.g. from the antarctic peninsula (see e.g. Schmidt [Sch1964]) or the ground sediments of the oceans (see e.g. Grjebine [Grj1964]). Microparticles were also collected from the stratosphere by experiments on high altitude aeroplanes, see Melton [Mel1964]. Typically, dust particles have chondritic elemental composition, dark surface and are porous or fluffy. Densities vary between 1 and 3 g/cm³ for most investigated particles, with a mean value of 2.0 g/cm³, see Love et al. [Lov1994].

Unlike the largest celestial bodies, the planets, the orbital dynamics of small bodies and dust are not only subject to the gravitational force, but are also affected or even dominated by a variety of minor forces that originate from solar radiation, solar wind, and interplanetary and planetary magnetic fields. In the following, the various forces acting on cosmic dust particles and their basic influences on the orbital evolution of the particles are discussed.

Gravitation itself exploits different perturbations on a dust particle's orbit. Particles orbiting the sun on a typical low inclination orbit may encounter one of the inner planets and experience significant changes of the orbital elements inclination i , eccentricity e and longitude of the ascending node Ω , as Gustafson & Misconi [Gus1986] have demonstrated by model calculations of the trajectories of sample particles between 10 μm and 100 μm in size encountering Earth and Venus during a ≈ 6000 year journey from 1.1 AU down to 0.3 AU. Particles may even be trapped in mean-motion-resonances (MMRs) of the Sun-Planet system (which means, that the particle's evolution in orbital elements is then primarily controlled by the trapping planet, while it is still in heliocentric orbit), and (with consideration of further disturbances caused by radiation pressure and the planets magnetosphere) finally form a circumsolar dust ring, see Liou et al. [Lio1995a], [Lio1997]. In a similar study on trapping of dust in the Earth's 1/1 resonance, Marzari & Vanzani [Mar1994] found long-lasting, up to 10⁵ years trapping of particles in Trojan-type orbits. Retrograde dust particles originating from retrograde sources nearly always get trapped in MMRs mainly with Jupiter, and even can evolve to prograde orbits when trapped in long-lasting resonances until they are ejected from the resonance, as Liou et al. [Lio1999] showed by theoretical modeling. Circumplanetary dust particles orbiting planets are even exposed to further gravitational disturbances caused by the oblateness of the specific planet, or a possibly irregular shape of the planet's moons, see Davis et al. [Dav1981] for a discussion of the gravitational environment in the Mars-Phobos-Deimos system.

The radiation of the Sun has strong effect on the orbital evolution of smaller bodies in the solar system. Macroscopic bodies in a size range of meters to some 100 meters like asteroids are affected by the Yarkovski drag that was discovered by I.O. Yarkovski in 1900, a force that results as a consequence of the time a rotating bodies surface needs to warm up when exposed to sunlight and cool down subsequently. The radiation pressure resulting from the thermal emission of the heated surface that has rotated away from direct sunlight produces a drag that leads to an increase or decrease of the semi-major axis a of a prograde or retrograde rotating body, respectively. The Yarkovski effect can be observed directly by radar observation of

asteroids, see Chesley et al. [Che2003]. In contrary, microscopic bodies are always in thermal equilibrium, and the therefore isotropic thermal emission does not produce a net radiation force. For particles lighter than 10^{-10} g, the radial pressure originating from the Sun's radiation becomes evident. The resulting force is strongly dependent on the particle's albedo and density and is usually described by the ratio β of the radiation force to the gravitational force, which is independent from the heliocentric distance and defined as $\beta = F_{rad}/F_{grav}$, see Burns et al. [Bur1979]. Typical values of β were obtained by Gustafson [Gus1994] by Mie-theory for homogenous spheres with optical constants of the astronomical silicate model by Draine & Lee [Dra1984], and show that radiation pressure is negligible ($\beta = 0$) for particles with mass greater than 10^{-10} g, has a maximum for particles with mass 10^{-13} g ($\beta = 1.5$) and decreases for smaller particles when particle size falls below the wavelengths of the solar radiation. Wilck & Mann [Wil1996] also calculated β -values from Mie-theory but used models of "typical" dust grains (asteroidal, young cometary, old cometary and interstellar) instead of solid spheres that represent the known albedo and density values of the grains. For all dust particle models, except the fluffy young cometary particles, the calculated β -values had a maximum of around 0.9 at $m = 10^{-13}$ g. Particles with $\beta > 1$ will spiral outwards from the Sun due to the Sun's radiation pressure. Particles that show this behavior are called β -meteoroids. Another weak, but highly important effect of radiation on a particle's orbit was first described (and misinterpreted) by Poynting [Poy1903] and discussed later by Robertson [Rob1937], named the Poynting-Robertson effect after its discoverers. The Poynting-Robertson drag causes a loss in orbital angular momentum of particles orbiting the Sun, therefore the particles spiral inwards into the Sun in $400 r^2/\beta$ years (r given in astronomical units) with decreasing eccentricity. A descriptive explanation of the effect is that the radial traveling photons of the Sun's radiation hit a particle on a circular orbit in an angle lower than 90° to its motion vector as seen from the particle's own inertia system, and thus produce a small braking force. An exact physical interpretation of the Poynting-Robertson effect requires covariant calculations and is given by Srikanth [Sri1999]. Although the Poynting-Robertson drag force is very low, it has significant effect on dust particles' orbital evolution. Further, non-radial drag forces caused by solar radiation that may originate from irregular particle shape are discussed but not well established. Ion impact drag force and the plasma Poynting-Robertson effect caused by solar wind particles are very low (around 10^4 times weaker than the radiation pressure), but due to the non-isotropic nature of the mass flow (decrease by about 50% from the ecliptic plane to the poles) the plasma PR drag effects orbital elements and increases orbital lifetime of particles on high inclined orbits by 5-10% (Banaszkiewicz et al. [Ban1994]). Unlike this, planetary perturbations on a particle's eccentricity can reduce the orbital lifetime by a few percent up to 50% due to altered PR drag on high eccentric orbits, see Gustafson et al. [Gus1987a].

Particles inside the heliosphere are exposed to ultraviolet radiation and a flow of electrons and ions known as solar wind. In laboratory simulation experiments, Cermák et al. [Cer1995] demonstrated that the equilibrium electrostatic potential of dust particles bombarded by ion and electron streams is around +5 V. Several theoretical studies about charging of dust grains inside plasmas of planetary magnetospheres (reviewed by Horányi [Hor1996b]) showed that the effective equilibrium potential of dust grains depends strongly on the individual characteristics of the plasma and varies between -30 V and +10 V. Due to this usually non-zero electrostatic potential of dust grains, they couple to the interplanetary magnetic field (IMF) or planetary magnetic fields. In the heliosphere, the electrostatic potential of dust grains is around a few volts positive due to the dominating effect of photo-ionization by UV radiation. The IMF is mainly dominated by the solar magnetic field that is carried outside from the Sun by the solar wind plasma. Theoretical considerations by Consolmagno

[Con1980] showed that the altering polarity of the field can have a random scattering effect on the orbital elements of small dust grains ($< 3 \mu\text{m}$) in the order of the Poynting-Robertson effect. Hamilton [Ham1994] showed by theoretical modeling that Lorentz forces acting on a particle within a planet's magnetosphere can induce orbital resonances similar to those of the gravitational force.

2.1.2 Interplanetary and interstellar dust in the heliosphere

Dust in the solar system is mainly produced by mutual collisions of larger objects. Most important sources of interplanetary dust particles are asteroids and comets (see e.g. Mann et al. [Man1996a], Liou & Zook [Lio1996b], Liou et al. [Lio1995b]). Also, Kuiper-belt objects contribute to the zodiacal cloud in the inner solar system, as it was shown by Liou et al. [Lio1996a] and Landgraf et al. [Lan2002], although most of the dust produced in the Kuiper-belt is ejected from the solar system by the giant planets.

For the determination of the overall flux of interplanetary dust, several sources of information are available and were used for developing models. Besides specialized in-situ dust detection experiments that are discussed in paragraph 2.1.5, lunar microcraters were an important source of information about spatial density and mass distribution of cosmic dust particles, see Hartung [Har1976]. Also, the surfaces of returned spacecraft, e.g. periscopic lenses of the early Mercury missions (see Hemenway et al. [Hem1964]) or the replaced and returned Hubble Space Telescope solar arrays (see Moussi et al. [Mou2005]) give information about flux and mass distribution of micrometeoroids.

The dust population in the solar system is not static, but undergoes a permanent dynamical evolution that is discussed by Grün et al. [Grü1985]. For particle masses $> 10^{-3}$ g, many more particles are destroyed by collisions than are generated, while for particle masses $< 10^{-6}$ g more new particles are generated than lost. Average lifetime until destruction by collision for particles with mass between 10^{-4} g to 1 g is about 10^4 years at 1 AU, which is short in comparison to the age of the solar system. It was estimated that about 9 tons/sec of particles with masses $> 10^{-5}$ g are lost inside 1 AU due to collisions. For particle mass between 10^{-5} g and 10^{-10} g, production rate is 16 times larger than the net loss by Poynting-Robertson drag, which is estimated to 0.26 tons/sec. The main loss mechanism of cosmic dust in the solar system is caused by solar radiation pressure, as discussed above. Particles with mass $< 10^{-10}$ g are affected by this force due to their small size, are largely injected into hyperbolic orbits and leave the solar system as so called β -meteoroides.

Most information about the three-dimensional shape of the interplanetary dust cloud is obtained by remote observation of the intensity of the zodiacal light. Polarization of the scattered sunlight also gives information about the surface structure of the scattering particles. Observation of the thermal emission of the dust particles can also be used to determine the three-dimensional structure of the dust cloud, see e.g. Levasseur-Regourd & Dumont [Lev1990]. At 1 AU, temperatures of 130 to 190 K and 380 to 390 K for particle sizes of 10^{-4} and 10^{-6} m in size were obtained by Staubach et al. [Sta1993]. Observations by the IRAS spacecraft ("Infrared Astronomical Satellite", see Neugebauer et al. [Neu1984]) revealed even local dust bands that were soon assigned to cometary dust trails, see Sykes & Walker [Syk1992] for a survey.

To gather information about the orbital dynamics of interplanetary dust particles, in-situ measurements of the particles' trajectory are required. Impact-ionization dust detectors provide the most efficient facilities for the measurement of dust particles' orbital speed and flight direction. Most in-situ detectors were on low inclined orbits. The observed isotropic distribution of the solar F-corona gives evidence to a small population of dust on isotropic inclined orbits. Although it is possible to determine the dust distribution outside the ecliptic plane from in-ecliptic measurements, since all possible orbits cross the ecliptic plane (Mann & Kneißel [Man1991]), this is limited due to the low detection rates of high inclined particles, which is caused by the short ecliptic encounter of these particles. The dust detector on the ULYSSES spacecraft is the first experiment on a high inclined orbit.

Several models of the distribution of cosmic dust in the solar system were developed from experimental data obtained by optical observations and in-situ measurements. One of the most popular is that of Divine [Div1993]. Five populations of dust particles were described, namely asteroidal, core, halo, inclined and eccentric that are distinguished by their distribution in size and orbital characteristics. Based on the model of Divine, a new model of the interplanetary dust flux which includes new in-situ measurements by the dust detectors on ULYSSES and GALILEO at orbital distances from 0.7 to 5.4 AU, and also incorporates radiation pressure forces acting on small dust particles as described in paragraph 2.1.1., was developed (Staubach & Grün [Sta1995], Grün et. al. [Grü1997]). While the asteroidal and core populations of Divine's model are left unaltered since the mass ranges of the particles in these populations are not covered by the ULYSSES and GALILEO dust experiments, the populations of the lighter particles ($m < 10^{-9}$ g) were altered to fit the new dust data, and to include the new population of interstellar dust grains detected by ULYSSES and GALILEO. Three new populations A, B and C of dust grains on bound orbits were defined with different dominant, but overlapping mass range of 10^{-10} g to 10^{-12} g, 10^{-11} g to 10^{-14} g, and 10^{-12} g to 10^{-15} g, respectively. Each of the three new populations shows individual characteristics in the distribution of orbital elements eccentricity e and inclination i of its appropriate particles. While population A mainly consists of low inclination, low eccentricity particles, populations B and C show a wider distribution of eccentricity and inclination with higher mean values in inclination. All three populations have a peak at low eccentricities, but also a significant component at high eccentricities. In chapter 6, this model is used to validate the MDC dust data.

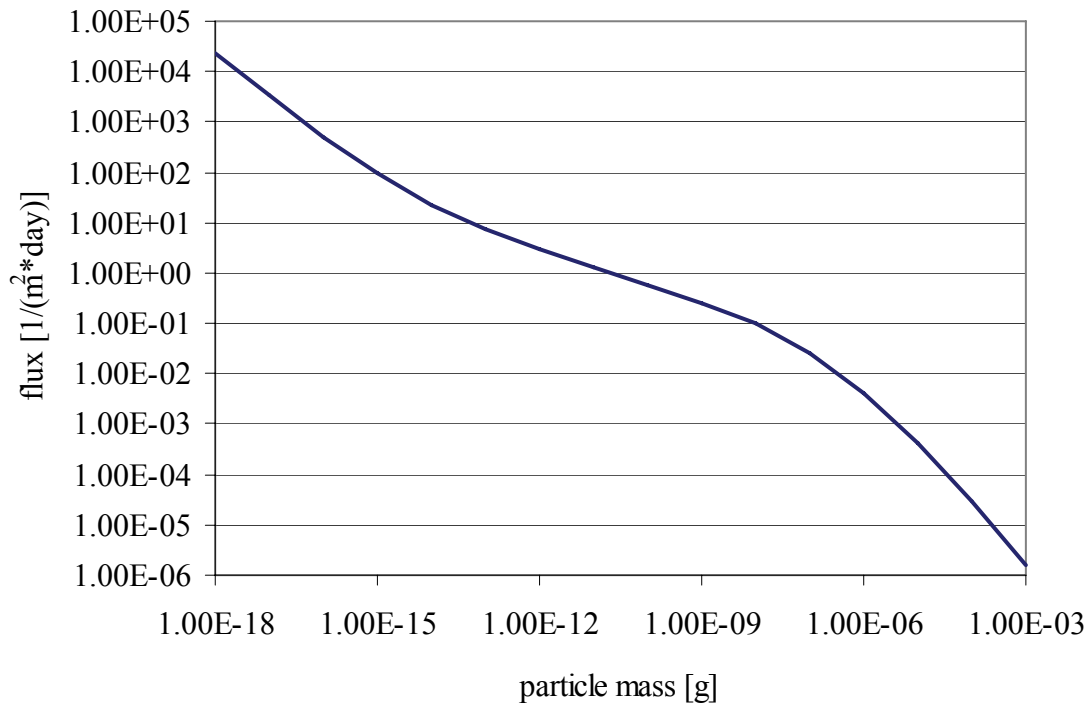


Figure 2-3: Dust flux at 1 AU as derived by Grün et al.

Cumulative flux of cosmic dust particles at 1 AU far away from the Earth as derived by Grün et al. [Grü1985].

Main points of criticism at the models described above are that they do not include any theoretical models of particle dynamics, and that there is no known fundament based on particle dynamics or dust source distribution (e.g. comets) for the empirical definition of the different particle populations. The development of models that include even newer data derived from in-situ measurements (e.g. again GALILEO, ULYSSES, CASSINI) and optical observations (e.g. the DIRBE instrument on COBE), and involve theoretical models of the long-term particle dynamics, are discussed by Dikarev et al. [Dik2002], [Dik2005].

While moving through the interstellar medium, the solar system encounters the interstellar gas and dust cloud, whose existence is known from optical and ultraviolet observations. Currently, the solar system is surrounded by a substructure called the Local Interstellar Cloud (LIC), relative speed of the solar system to the LIC was determined to 26 km/sec. Dust particles that belong to the interstellar medium penetrate into the inner solar system and contribute to the interplanetary dust flux, although small particles are deflected by the hot plasma in the heliopause, see Linde et al. [Lin2000]. ISD particles that penetrate into the heliosphere interact with the interplanetary magnetic field and are deflected away from the Sun, see Grün et al. [Grü2001]. Interstellar dust particles were detected by the dust detectors on the GALILEO, CASSINI and HELIOS missions in the inner solar system at orbital radii ≤ 1 AU, see Altobelli et al. [Alt2005], [Alt2003], [Alt2006], and by the GALILEO and ULYSSES missions outside 1 AU, see Baguhl et al. [Bag1995], [Bag1996]. ISD grains were separated from the interplanetary dust flux by their speed and flight direction. ULYSSES measurements showed that the flight direction of the interstellar dust flux is well aligned with the direction of the interstellar gas flow, which arrives from longitude 252° and latitude 2° , and never deviates more than 30° from this direction, see Grün et al. [Grü1997]. ISD grains show a

constant flux that is independent from orbital radius and ecliptic latitude. Mean mass of the ISD grains detected by ULYSSES at an orbital radius of 5 AU was 10^{-13} g. See also Grün et al. [Grü1994] for a discussion. The in-situ measurements also showed a dependence of the flux of ISD grains from the solar activity due to the filtering effects caused by the interplanetary magnetic field. As Grün et al. [Grü1997] showed, ISD particles with β -values > 1.5 will never reach 1 AU. It was shown by theoretical considerations that ISD grains may be captured by the sun by electromagnetic forces (see Kocifaj & Klačka [Koc2003]), by the Lorentz force (see Kocifaj & Klačka [Koc2004]) and by Poynting-Robertson drag (see Jackson [Jac2001]). ISD grains are supposed to consist of old matter that originated directly from supernovae explosions, but it is suggested that they undergo significant changes when entering the heliosphere due to solar radiation, see Strazulla [Str1986].

2.1.3 Circumplanetary dust

Dust rings around Mars were predicted first by Soter [Sot1971] based on MARINER 6 and MARINER 7 photographs of the Mars surface. They are supposed to reside around the orbits of the two Martian moons Phobos and Deimos. The theoretical considerations are based on the assumption that the two satellites are exposed to the same flux of meteoroides as the crater-covered Mars itself; impacts of these particles should eject material from the surfaces into circum-Martian orbit at velocities of 5 to 15 km/sec. Since the inner moon Phobos resides inside the Roche limit, particle ejection becomes even easier (see Dobrovolskis et al. [Dob1980]). This material is supposed to form dynamic tori that are probably self-sustained by collisions between 20-50 μm ring particles and the moons Phobos and Deimos.

Unlike the Saturnian ring system, which consists of large bodies and shows a high grade of symmetry (except of the faint E-ring that consists of small dust particles and is currently investigated with the CASSINI dust experiment), the Martian dust rings are subject to a wide range of perturbations and show complex dynamics that lead to spatial and temporal asymmetries. Most significant disturbances of the dust particles besides the strong gravitational forces by the Sun and the moons themselves originate from the solar radiation pressure, electromagnetic forces and the oblate shape of Mars. All these forces show local variations and thus the faint rings show a wide variety of structure over time and space.

Many studies were carried out on the formation and modeling of dust rings around Mars and their supplement by dust grains that originate from impacts on the two moons' surfaces, see Ishimoto & Mukai [Ish1994], Ishimoto [Ish1996], Banaszekiewicz & Ip [Ban1991], Kholshchevnikov et al. [Kho1993], Krivov & Hamilton [Kri1997], Krivov & Jurewicz [Kri1999], Nazzario & Hyde [Naz1997], and their interaction with the Martian magnetic field and the solar wind, see Dubinin et al. [Dub1991] and Krymskii et al. [Kry1992]. A detailed analysis and numerical simulation of the dynamics and structure of the rings was performed by Hamilton [Ham1996]. The principle spatial distribution calculated by this model is summarized in Figure 2-4 as seen perpendicular to the Mars system. Although this picture gives only a simplified view, it shows one of the most interesting results; the dust ring around the orbit of the inner moon Phobos is shifted towards the Sun, while the ring around the orbit of the outer moon Deimos is shifted away from the Sun. Not visible in this picture is that the inner ring is even tilted out of the equatorial plane when viewed from the Martian vernal

equinox (the intersection of the Martian equatorial and orbital planes). A seasonal dependence of the dust rings' spatial distribution is obvious.

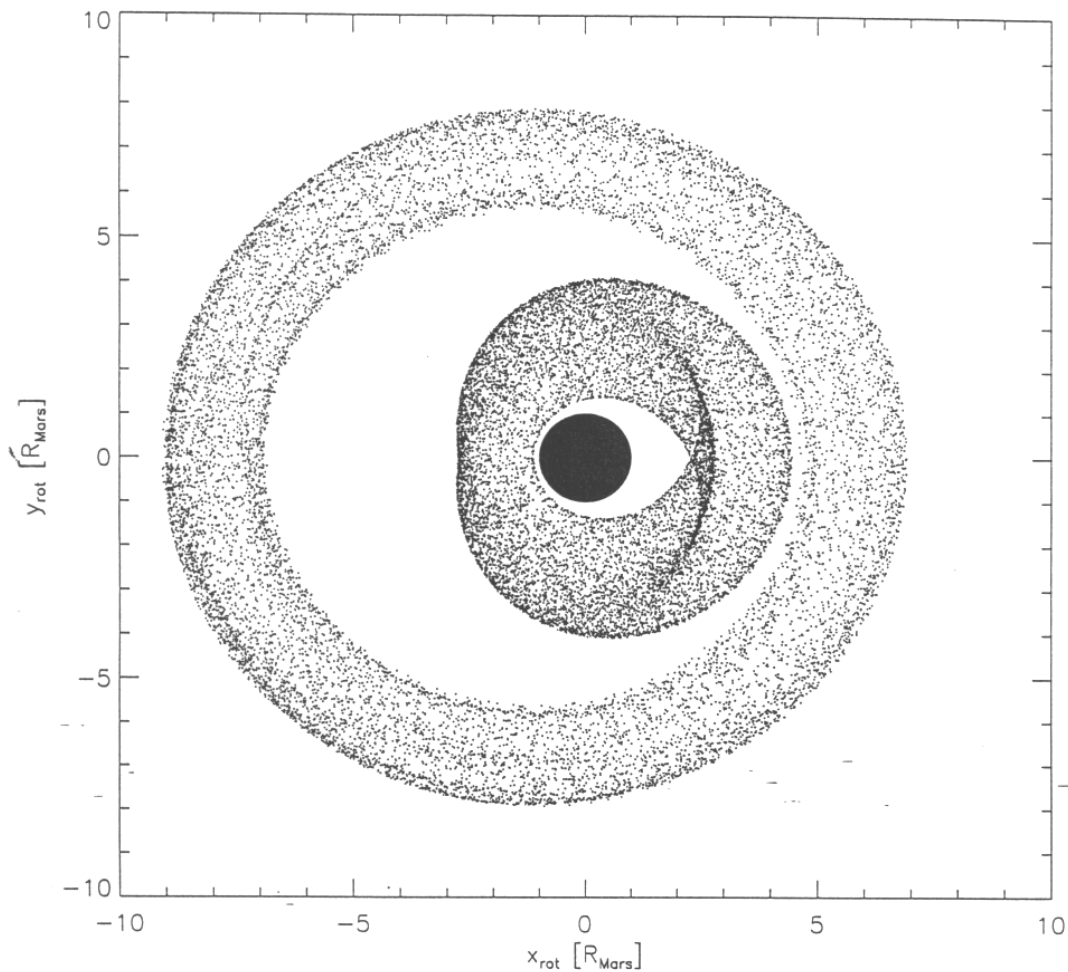


Figure 2-4: Theoretically predicted dust rings

The dust rings around the Martian moons Phobos (inner moon) and Deimos (outer moon) show a complex structure that was determined by Hamilton. The positive x-axis is pointing towards the sun.

Very little experimental data is available to validate the theoretical predictions and models. An analysis of images taken by the Viking spacecraft gave that the optical depth of the rings must be supposed to be lower than $3 \cdot 10^{-5}$. Solar wind disturbances in plasma and magnetic field observations observed by the Phobos-2 mission's instruments in the orbit of Phobos may correspond to a ring of dust or gas and give a first experimental but indirect evidence of the existence of the predicted dust rings, see Baumgärtel et al. [Bau1996]. The Mars Dust Counter would have been the first dust science experiment in Mars orbit. Although it was determined by Ishimoto et al. [Ish1997a] from the present models that during the two year stay in Mars orbit only a few ten dust ring particles would be detected by the MDC, a direct prove of the existence would have been possible. Observation from Earth comes out to be very difficult due to the very low optical depth of the rings, however, the brightness of the rings varies with the viewing geometry and thus some constellations are conceivable where they may be visible with terrestrial telescopes in future.

2.1.4 Space debris

Since the beginning of human space exploration, a large and still increasing part of particles of all sizes that populate the vicinity of Earth are not of natural origin, but man-made so called “space debris”. One can say that a large number of meteors that can be observed in clear nights are of artificial origin. Apart from ≈ 0.1 mm particles, space debris today dominates in all particle sizes in low Earth orbits, see ESA [ESA1999]. These artificial objects are classified into two groups, so called “primary objects” that were brought directly into orbit like burnt out rocket stages, disused satellites etc., and “secondary objects” that originate from the primary objects by collisions and explosions, or are generated by high velocity impacts of small particles on heavier objects as so called ejecta.

Sample return experiments like LDEF have shown further sources of sub-millimeter particles, like residues of solid rocket boosters that mainly consist of Al_2O_3 particles on high elliptic orbits, see Schobert [Sch1996], small particles that erode from the surfaces of spacecrafts by radiation effects or contact with atomic oxygen, see Stark et al. [Sta1997], and fluid metal beads that leaked from Russian RORSAT satellites, see Grinberg et al. [Gri1997]. Solid rocket boosters may even contribute to the debris population in the centimeter range, see Jackson et al. [Jac1997].

Most of the secondary objects are generated on high elliptic or even hyperbolic orbits and either re-enter the Earth’s atmosphere or leave Earth orbit. Atmospheric friction and thus caused re-entering of the atmosphere is also a natural drain for particles on stable orbits.

The known population of particles in less than 2000 km height and in stable orbits or orbits having not negligible half-life periods is composed in the ESA-MASTER-Model, see Klinkrad et al. [Kli1997]. Main purpose of the compilation of space debris catalogs and models is to get reliable information about the exposure of future spacecrafts. Micrometeoroids and sub-millimeter particles, that are the main objects of interest in dust science, do not bring out serious hazards for spacecrafts and are therefore accounted only secondarily. Nevertheless, especially the dynamics of aluminum-oxide particles generated by solid rocket boosters on their way to GEO is of interest, since the achieved results not only can be used for the validation of space debris models, but also the generation of high mass particles in the range of centimeters was noticed by radar observations and engine test bench experiments.

The long-term application of dust detectors like those of the MDC type series in LEO is therefore an interesting research field, and is a precondition to provide future spacecrafts and space stations with some kind of “space weather forecast”. The mission of the MDC-BremSat showed that a sophisticated screening of signals will be necessary for future MDC missions in LEO due to presumably massive atmospheric interferences that occurred in the MDC-BremSat data stream.

2.1.5 Exemplary instruments and missions

Several past and recent interplanetary missions carried dust experiments, which were designed to detect cosmic dust of different magnitudes. A short list of these missions is shown in Table 2-1 (content taken from [Grü1992a] and supplemented by CASSINI and STARDUST), the list also includes Earth orbiting missions outside LEO.

Table 2-1: Interplanetary missions carrying in situ dust experiments

Spacecraft	Heliocen. dist. [AU]	Detector type	Spin- or 3-Ax. stab.
Pioneer 8	0.97-1.09	impact ionization	in-ecl. spinning
Pioneer 9	0.75-0.99	impact ionization	in-ecl. spinning
HEOS 2	1	impact ionization	3-axis
Pioneer 10	1-18	penetration	out-of-ecl. spinning
Pioneer 11	1-10	penetration	out-of-ecl. spinning
Helios 1, 2	0.3-1	impact ionization	in-ecl. spinning
VEGA 1, 2	0.73-1.1	PVDF	3-axis
Galileo	0.7-5.2	impact ionization	out-of-ecl. spinning
Ulysses	1-5.4	impact ionization	out-of-ecl. Spinning
Cassini	0.7-9.5	impact ionization	3-axis
Stardust	1-2.6	various	3-axis

In the following, the four missions GALILEO, ULYSSES, CASSINI and STARDUST are described briefly. These are not only the actual missions, but also the dust experiments onboard the GALILEO and ULYSSES spacecrafts (see Grün et al. [Grü1992a], [Grü1992b], [Grü1995a]) are in some aspects similar to the MDC, while the CASSINI dust experiment (see Srama et al. [Sra2004], Auer et al. [Aue2002]) is an advanced version of these experiments. The LRT is project partner for the CASSINI dust experiment. In contrary to GALILEO, ULYSSES and CASSINI, that also carry a number of scientific instruments of other purpose, the STARDUST spacecraft is specially designed for dust measurements, see McDonnell et al. [McD2000] for a description of the STARDUST flux monitor, Brownlee et al. [Bro1996] for a description of the STARDUST mission.

Results of the dust experiments on the missions GALILEO and ULYSSES were published regularly. See Grün et al. [Grü1995b], Krüger et al. [Krü1999b] and Krüger et al. [Krü2001a] for GALILEO results, Grün et al. [Grü1995c], Krüger et al. [Krü1999c] and Krüger et al. [Krü2001b] for ULYSSES results. The results of these four missions are discussed regularly at the annual GUCS (GALILEO, ULYSSES, CASSINI, STARDUST) meetings, also status and results of the MDC-HITEN and MDC-NOZOMI missions were presented there.

GALILEO 1989-2003

NASA mission to Jupiter

Galileo Dust Detector



Figure 2-5: The GALILEO spacecraft

The GALILEO mission was launched on October 18, 1989. After a six-year journey, it arrived at Jupiter in September 1995. On September 21, 2003 it crashed onto Jupiter's surface. Besides a number of other experiments, it carried the Galileo Dust Detector, a descendant from the HEOS detector that was nearly identical to the ULYSSES dust experiment.

ULYSSES 1990-

NASA/ESA mission to polar
solar orbit

Ulysses Dust Experiment



Figure 2-6: The ULYSSES spacecraft

Launched on October 6, 1990, the ULYSSES spacecraft encountered Jupiter on February 8, 1992. After a swing-by at Jupiter, it travels on a high inclined orbit around the Sun. Like GALILEO, its dust detector is a descendant from the HEOS dust detector. See Wenzel et al. [Wen1989] for a description of the ULYSSES mission.

CASSINI 1997-
NASA mission to Saturn
Cosmic Dust Analyzer



Figure 2-7: The CASSINI spacecraft

Launched on October 15, 1997, CASSINI reached Saturn orbit on July 1, 2004 after fly-bys at Venus, Earth and Jupiter. It carries the CASSINI Cosmic Dust Analyzer, a descendant from the ULYSSES and GALILEO dust detectors with enhanced measuring capabilities.

STARDUST 1999-2006
NASA mission to comet Wild-2
Several dust experiments



Figure 2-8: The STARDUST spacecraft

Unlike most other missions, the STARDUST spacecraft was designed especially for dust science and carries a number of dust related experiments including a sample return experiment. It was launched on February 7, 1999, and flew by the comet Wild-2 to collect cometary dust particles. On January 15, 2006, a capsule containing these cometary dust particles was delivered back to the Earth.



Figure 2-9: The CASSINI Cosmic Dust Analyzer

The instrument consists of two independent experiments, the Dust Analyzer DA (cylindrical box on the left) and the High Rate Detection system HRD attached to the cylinder, which itself consists of two polyvinylidene fluoride (PVDF) sensors. The HRD is designed for measurements during Saturnian ring plane crossings.

Figure 2-9 shows the CASSINI Cosmic Dust Analyzer CDA, which was designed and developed by the Max Planck Institut für Kernphysik, Heidelberg (MPI-K), see Srama et al. [Sra1997], [Sra2004]. It is a descendant from the GALILEO and ULYSSES dust experiments, but with extended measuring capabilities. Like its predecessors, the CDA is primarily an impact ionization detector with a cylindrical shaped sensor box. Additionally, the CDA carries a time-of-flight mass spectrometer inside the sensor box that enables determination of the chemical composition of the impacting particles. A similar experiment setup based on the much smaller, lighter and cheaper MDC experiment is intended by the LRT, this is discussed in chapter 8. Calibration of the CDA was carried out in the dust accelerator facility at the MPI-K using various projectile materials; see Göller [Göl1988], Göller & Grün [Göl1989] and Goldsworthy et al. [Gol2002].

2.2 The MDC mission HITEN, (formerly MUSES-A)

HITEN, formerly named MUSES-A, was Japan's first mission outside the low Earth orbit. It was designed and developed by ISAS from 1985 to 1990. Main objective of the mission was the demonstration and testing of Japan's ability to navigate a spacecraft in the Earth-Moon system on complex trajectories, including orbit control, insertion of a sub satellite into lunar orbit, optical navigation experiments and cis-lunar aero brake demonstrations. Several maneuvers were conducted, including Moon swing-by and maneuvering of the spacecraft into the Lagrange points L4 and L5. HITEN carried a small piggyback Moon orbiter named HAGAROMO that was separated from the spacecraft during the mission. The MDC-HITEN was the only scientific experiment onboard. A description of the HITEN mission is given by Uesugi et al. [Ues1991].

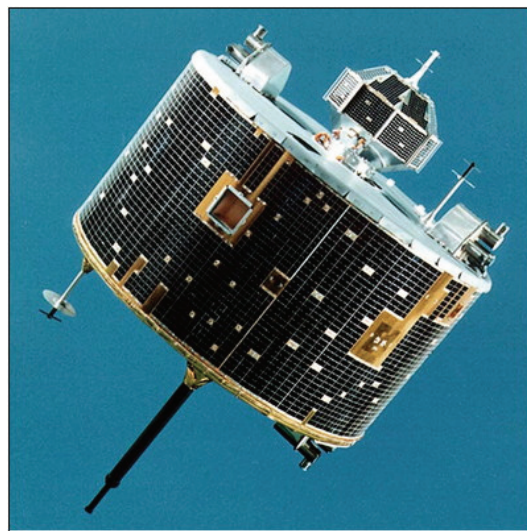


Figure 2-10: The HITEN spacecraft

Photograph of the fully integrated HITEN spacecraft. Mounted on top of the cylindrical body, the small octagonal Moon orbiter HAGAROMO can be seen. The MDC is mounted into the wall of the cylindrical body, the rectangular MDC sensor box and its gold plated inner walls can be seen here.

2.2.1 Spacecraft properties

The spacecraft HITEN was spin stabilized with a rotation period of 20 rpm. Its shape was cylindrical with a diameter of 1.4 m and a height of 0.8 m. The top of the spacecraft was coated with a special thermal blanket to cope with the heat that was generated during aero brake maneuvers when HITEN passes the upper limits of the Earth's atmosphere at a speed of about 11 km/sec. Also on top of the spacecraft, the polyhedral shaped small lunar orbiter HAGAROMO was fixed. Around the cylindrical body, solar cells were mounted that produced a power of about 110 W. HITEN's communication system consisted of two low-gain antenna (LGA) at the top and the bottom of the cylinder, respectively, and one medium-gain antenna (MGA) at the bottom. Both X-band and S-band downlink were available; up-

link was carried out on S-band. The propulsion system employs eight 23 N and four 3 N thrusters that are used for orbital control. Total weight of the spacecraft was 197 kg, where 12 kg account for the lunar orbiter HAGAROMO and 42 kg on hydrazine fuel. The MDC-HITEN was mounted into the side panels of the satellite, 25 mm counter-sunk. No other instruments did obscure the field of view of the MDC-HITEN; the aperture angle was 145 degrees.

2.2.2 Mission

On January 24, 1990, the spacecraft HITEN was launched by a Japanese Mu-3SII-5 rocket from Kagoshima Space Center, Japan, and was injected directly into a high eccentric trans-lunar orbit. After four orbits around Earth, the first lunar swing-by was conducted on March 18, 1990, when the orbiter HAGAROMO was released and injected into a lunar orbit. The following orbits no. 5 to 7 had a much higher apogee and the orbit describes a precession around Earth until the apogee was on night side. Several Moon swing-by's were conducted during the orbits no. 9 to 14 to keep the spacecrafts apogee on the Earth's night side, which was an essential requirement for the planned ISAS mission GEOTAIL and was demonstrated successfully by the HITEN mission. Aero brake experiments were conducted during the perigee of orbits no. 16 to 19 and were completed successfully. After the 10th lunar swing-by on October 2, 1992, the spacecraft was injected into a trajectory that brought it to two of the Lagrange points of the Earth-Moon system, L4 in October 1992 and L5 in January 1993. The MDC-HITEN was the first dust experiment that could conduct measurements of dust particles that may reside in the vicinity of these stable points. On February 15, 1993, the spacecraft was injected into a polar lunar orbit where it stayed for about one month. On March 10, 1993, it finally crashed onto the lunar surface. The overall results of the HITEN mission are summarized by Uesugi [Ues1996].

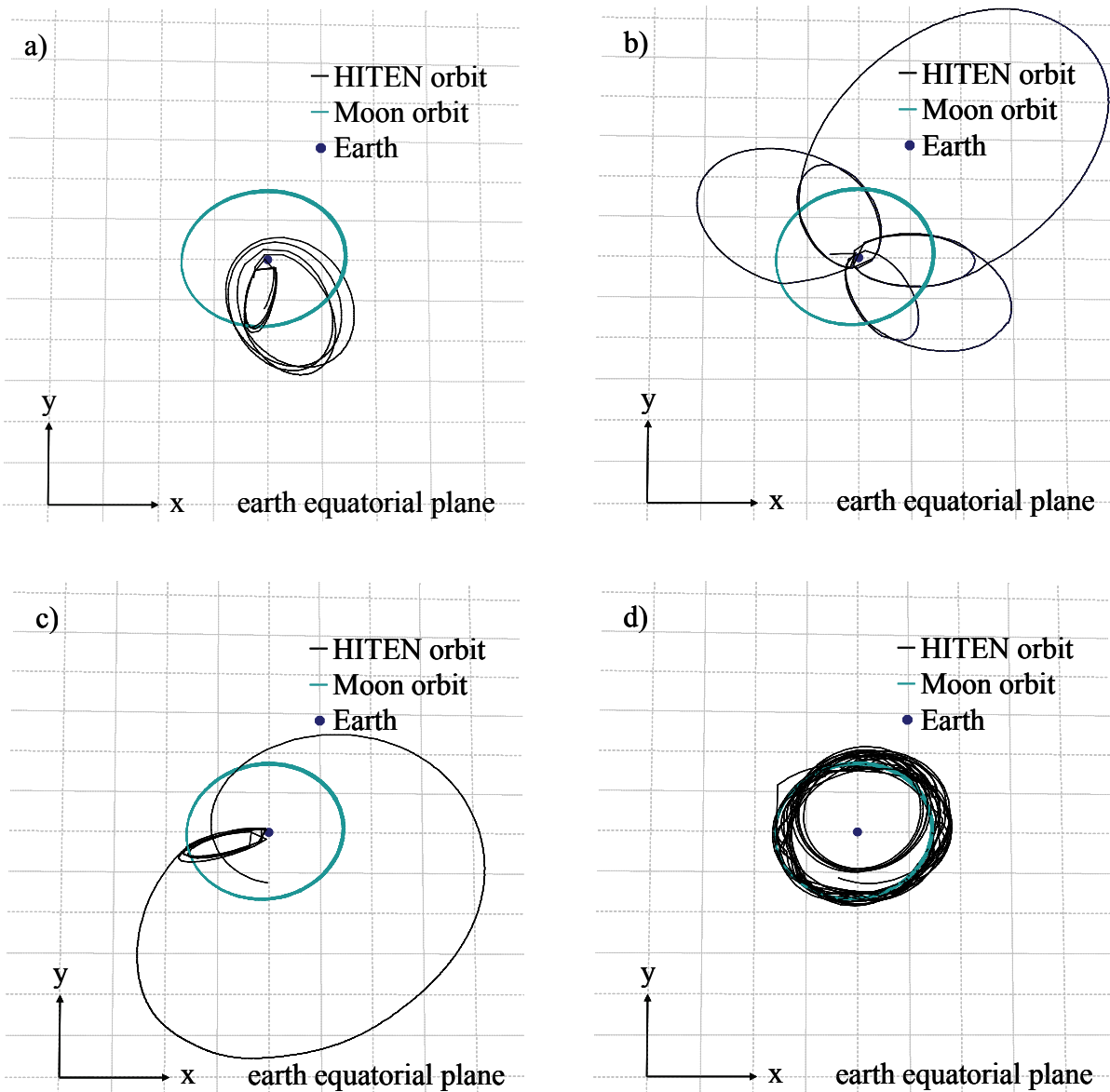


Figure 2-11: HITEN orbit

The complex trajectory of the HITEN spacecraft originated from the main purpose of the mission, which was to demonstrate the ability of the Japanese space organization ISAS to maneuver an interplanetary spacecraft. During the mission, HITEN performed several maneuvers including aero braking, several Moon swing-by's and orbits around the Lagrange points L4 and L5. a) Orbits 1-4 (initial), 5 to 8 (apogee to night side), b) Orbits 9 to 14 (keep apogee at night side), c) Orbits No. 15 to 19 (aero-brake experiments and transfer orbit), d) Orbits 20 to 24 (transfer), Lagrange points, Moon orbit. Note: Kinks in the HITEN orbit shown in this figure are caused by incomplete orbital data or small resolution (one data per day).

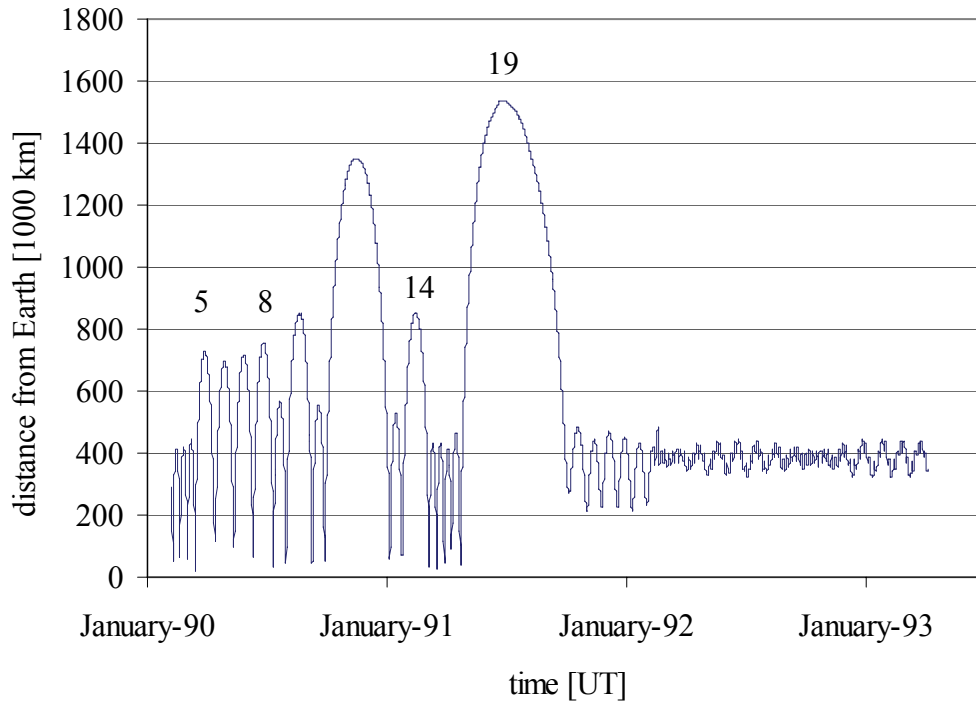


Figure 2-12: HITEN distance from earth

A more intuitive view on the complex HITEN trajectory. Orbit numbers are given for selected orbits, see text for details.

2.2.3 Results of the MDC-HITEN dust measurements

Calibration measurements for the MDC-HITEN were carried out at the Max-Planck Institut für Kernphysik in Heidelberg, Germany. Around 1000 particles were shot on locations inside the sensor box, and around 700 on locations outside the sensor box. The MDC-HITEN calibration is described by Münzenmayer et al. [Mün1997].

The MDC-HITEN operation started 38 days after launch. During the first two years of operation, the MDC-HITEN detected an average of slightly more than 0.5 particles per day, which corresponds to a dust flux of 2.2 to $5.5 \cdot 10^{-4}$ particles/($m^2 \cdot s$). Mass range of the detected particles was 10^{-16} to 10^{-7} g. The particles detected by the MDC-HITEN can be separated into two populations, apex-particles with low speed around 30 km/sec, and β -meteoroides with high speed > 45 km/sec and radial flight direction, see Iglseider et al. [Igl1993a]. A later look at the MDC-HITEN data gave evidence that interstellar dust particles were detected by the instrument, see Grün et al. [Grü2001b].

During the following 14 months in Moon orbit, the MDC-HITEN detected around 150 particles with a mass range of 10^{-16} to 10^{-7} g, which corresponds to a dust flux of 1.3 to $4.1 \cdot 10^{-4}$ particles/($m^2 \cdot s$). The particles observed in lunar orbit have the same properties in flight direction as during the first two years of the mission, see Iglseider et al. [Igl1996].

2.3 The MDC mission NOZOMI, (formerly PLANET-B)

NOZOMI, formerly named PLANET-B, was Japan's first interplanetary mission. It was designed and developed from 1992 to 1998 by the Institute of Space and Astronautic Science (ISAS), a department of the University of Tokyo. The objectives of the project are twofold, in addition to the scientific objective, that is the study of the structure and dynamics of the upper Martian atmosphere and its interaction with the solar wind, the engineering objective is to develop basic key technologies for future ISAS missions. The scientific objectives of the NOZOMI mission are described by Nakatani et al. [Nak1995], the engineering objectives by Tsuruda et al. [Tsu1996]. Since the launch capabilities of the designated launcher, the new M-V vehicle also developed by ISAS, are moderate, special emphasis was put on extremely lightweight construction of the satellite. NOZOMI was the second mission launched with the M-V.

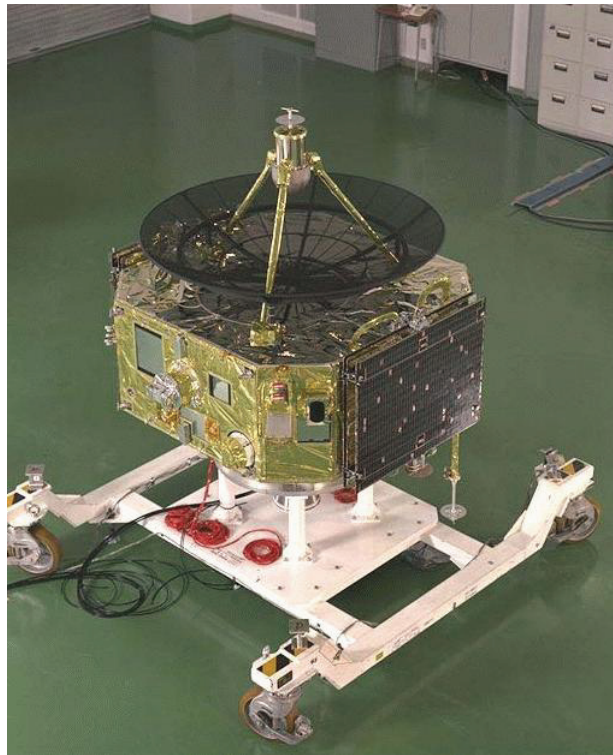


Figure 2-13: The NOZOMI spacecraft

Photograph of the fully integrated NOZOMI spacecraft. The MDC is mounted into the small side panel left of the folded solar panel. Its light grey outer wall and a small part of the gold plated inner wall can be seen here.

2.3.1 Spacecraft properties and operations

The NOZOMI spacecraft properties are described in the NOZOMI Prelaunch Report by ISAS [ISA1998]. The dry mass of the satellite without propulsion system is only 186 kg, whereof 35 kg account for the 14 scientific instruments; the complete wet mass was 580 kg. NOZOMI

was equipped with two high efficiency solar panels that produce more than 200 W of power through the mission period. The satellite is spin stabilized with a rotation period of ≈ 6 to 10 rpm. The telemetry system consists of a 1.6 m parabolic mesh X-band high gain antenna that requires pointing of the antennas bore sight direction and thus the satellites spin axis to Earth, and two omni directional S-band low gain antennas. Both the solar panels and the HGA are fixed to the body, neither Earth-pointing gimbals for the HGA nor a Sun-tracking mechanism for the solar panels were necessary because the angle between Earth and Sun seen from NOZOMI's orbit is within $\pm 45^\circ$, which secures power generation by the solar panels. The X-band downlink has bit rates from 2048 bps to 32768 bps, the S-band downlink from 64 bps to 1024 bps. Uplink is established via S-band at bit rates of 125 bps or 15625 bps. The design lifetime of the satellite was two years (one Martian year), and mainly limited by the amount of fuel that is needed to maneuver the spacecrafts attitude to direct the HGA dish to Earth for data transmission. Fuel became a critical factor after a problem during the first Earth fly-by occurred.

All data that are created by the scientific instruments can be stored by the data handling system in the onboard data recorder during periods when no telemetry via X-band downlink is possible or the instruments data stream exceeds the telemetry capacity. Main tracking of the spacecraft is carried out at Usuda Deep Space Center (UDSC) and Kagoshima Space Center (J-KSC), primary data processing, orbit and attitude determination and control is carried out at the Sagami Spacecraft Operation Center (SSOC). At the SSOC, the data acquired from NOZOMI is archived and distributed to the experimenters of the different scientific instruments. All MDC data was uploaded to the LRT via internet right after download from NOZOMI and extraction from the raw telemetry data stream.

2.3.2 Mission

Mission launch was scheduled to early July 1998. On July 4, 1998, the mission PLANET-B was launched at Kagoshima Space Center and renamed to NOZOMI following a Japanese tradition. The design of the NOZOMI orbit is described by Kawaguchi et al. [Kaw1995]. Five minutes after launch the spacecraft was inserted into a nearly circular orbit, another 13 minutes later it was kicked to a highly elliptic orbit with periapsis beyond the Moon orbit. Soon after launch, the MDC was set into operation and provided its first data. As the available energy was not sufficient for a direct injection into a Mars transfer orbit, some gravitational maneuvers were necessary. After $6 \frac{1}{2}$ elliptic orbits, the first Moon swing-by took place on September 24, 1998, and brought NOZOMI to a maximum distance of 1.7 million km from Earth. It returned on a retrograde orbit, and after a second Moon swing-by, a powered Earth swing-by should bring the spacecraft to the final Mars transfer trajectory.

During this powered swing by which took place in 1000 km height above the South Pacific Ocean, no orbital control was possible. Unfortunately, one of the oxidator vents of the propulsion system was not fully opened and the spacecraft's speed after the swing-by was 100 m/sec too low, the missing Δv increased to 350 m/sec until connection could be established again. Although it would have been possible to correct the trajectory by orbital maneuvers, this would consume too much fuel, endanger the later injection into Mars orbit and prohibit the maneuvers necessary during the mission time in Mars orbit. Hence, the operators at ISAS designed a new orbit strategy that enabled the spacecraft to reach Mars and

save the fuel needed for orbital operations around Mars, see Kawaguchi et al. [Kaw2003]. Initially the spacecraft remained on the orbit it reached after the Earth swing-by, an elliptic orbit around the Sun that crosses both Mars and Earth orbit. After three orbits around the Sun, NOZOMI reached the Earth again and a swing by maneuver was conducted on December 20, 2002, that brought NOZOMI to a high inclination Earth synchronic orbit. On June 19, 2003, NOZOMI approached Earth again and after a second Earth swing-by, it was brought on the final transfer trajectory to Mars. The Mars orbit insertion was scheduled to December 31, 2003, and required a Δv of 840 m/sec instead of 1257 m/sec with the original transfer strategy, which secures that enough fuel is left for future orbital maneuvers.

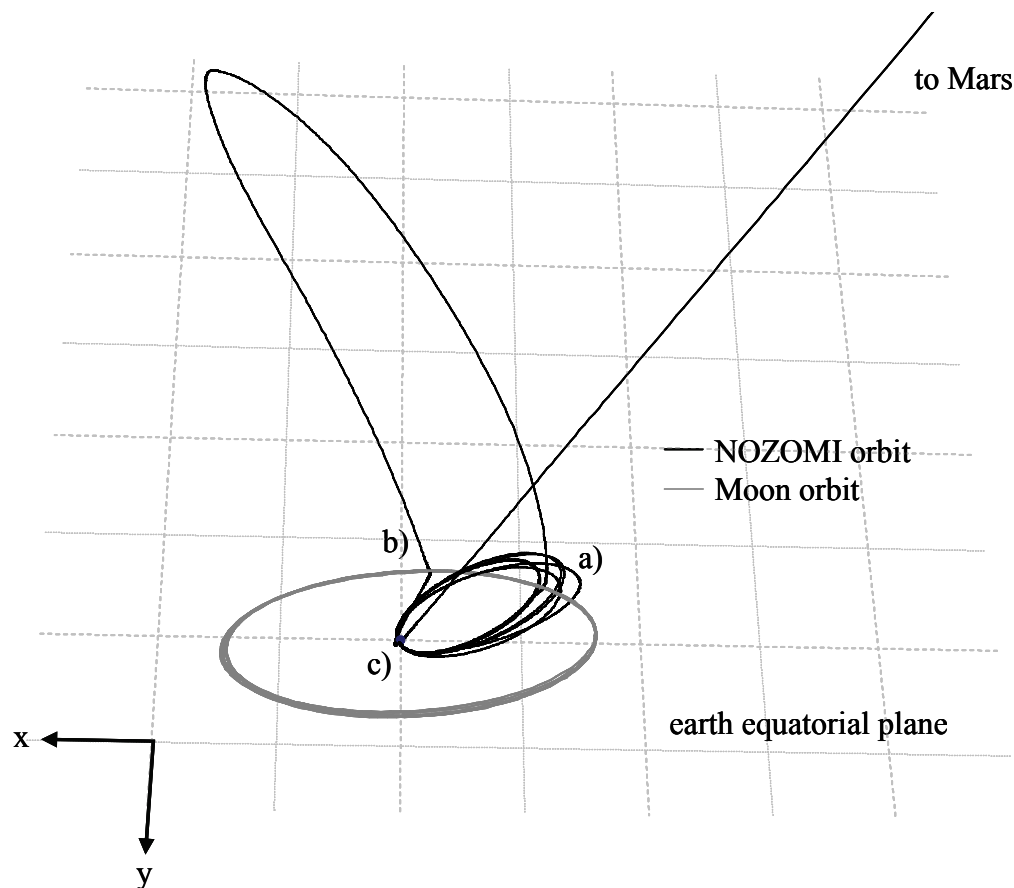


Figure 2-14: NOZOMI orbit in the Earth-Moon system

a) First Moon swing-by, September 24, 1998 b) Second Moon swing-by, December 18, 1998 c) Earth swing-by, December 20, 1998.

The prolonged transfer to Mars gave the MDC the possibility to measure dust in the interplanetary space for long period and thus need not to be seen as a drawback for the MDC project. Since the MDC-HITEN proved to work stable and reliable on a long-term mission, it was expected that the MDC-NOZOMI would do a good job as well. Data acquisition and data transfer during the interplanetary cruising phase were possible and were conducted regularly.

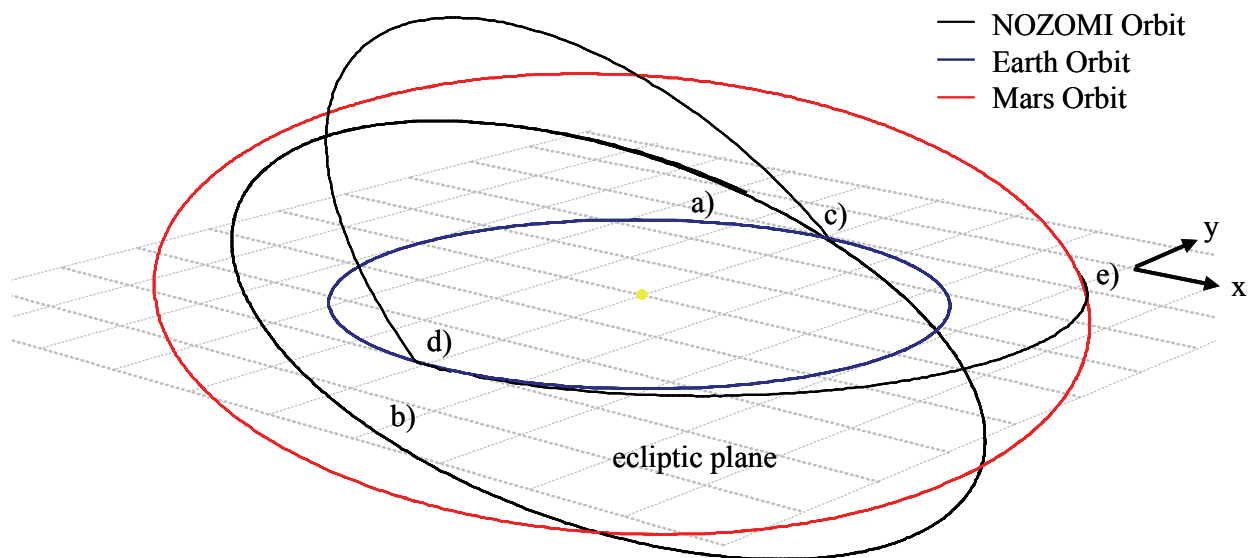


Figure 2-15: NOZOMI orbit in the interplanetary space

a) Insertion into Sun centered orbit January 1998 b) System failure, April 26, 2002 c) First Earth swing-by, December 21, 2002 d) Second Earth swing-by, June 19, 2003 e) Mars fly-by, December 14, 2003.

Insertion into Mars orbit was scheduled in December 2003. The planned orbit was highly elliptic with periapsis at 150 km and apoapsis at 15 Mars radii, inclination was 170° , which defines a retrograde orbit. The orbit crosses the orbits of the Martian satellites Phobos and Deimos, which both are subject of scientific interest as well. The MDC was expected to detect dust rings around Mars in the orbits of the two moons as they were predicted by theoretical considerations earlier (see paragraph 2.1.3).

On April 24, 2002, a system failure onboard NOZOMI happened that was probably caused by a solar eruption which occurred a few days earlier. The damage onboard NOZOMI was soon identified as a failure of the CI-PSU (Common Interface Power Supply Unit), a power supply unit that was responsible for a couple of satellite subcomponents including the data recorder, thermal control and a control unit that handles the telemetry modes. This failure severely endangered the continuation of the mission. E.g., the satellites telemetry system remained in ranging mode after the failure occurred which made it impossible to transfer MDC data or other data back to Earth. However, the most severe problem was the failure of the thermal control system, since without the heaters the fuel for the main propulsion system gets frozen at larger distances from the Sun. As a first workaround, all satellite systems including the scientific instruments were powered on to produce as much heat as possible, but this could not provide enough energy to heat the fuel. Without the main propulsion system, Mars orbit insertion was not possible.

Detailed analyses of the problem at ISAS lead to the assumption that a short circuit prevents the CI-PSU from working properly. As a solution strategy, a series of “CI-PSU power on” commands sent to the spacecraft was thought to eliminate the short circuit. During the first try in September 2002, the link to NOZOMI was completely lost and could be re-established a couple of weeks later. Because of this incident, further tries to solve the problem and re-

establish NOZOMI's full functionality were postponed for safety reasons until the last Earth swing by has happened.

These last tries to correct the problem were carried out from September 2003. A series of 10000 "CI-PSU power on" commands were sent to the spacecraft in a high frequency, telemetry was lost again like during the first try, but the failure of the CI-PSU could not be corrected. After re-establishing the telemetry link, a series of small orbital corrections were conducted using the small maneuvering thrusters to conduct NOZOMI on a secure trajectory that minimized the chance that NOZOMI crashes onto Mars' surface. Unlike landing devices, NOZOMI as an orbiter was not biologically clean and could possibly pollute the Mars surface with biological materials from Earth.

On December 12, 2003, NOZOMI passed Mars on the shadow side in a presumed height of 850 km. After the fly-by, ISAS tried to re-establish the telemetry link to NOZOMI. As the exact position and speed of NOZOMI after the fly-by were unknown, it was necessary to scan the potential space segment where it should reside as well as the frequency band due to the Doppler shift. After a couple of days, these tries were given up without any result and on January 10, 2004, the mission was finally declared as lost.

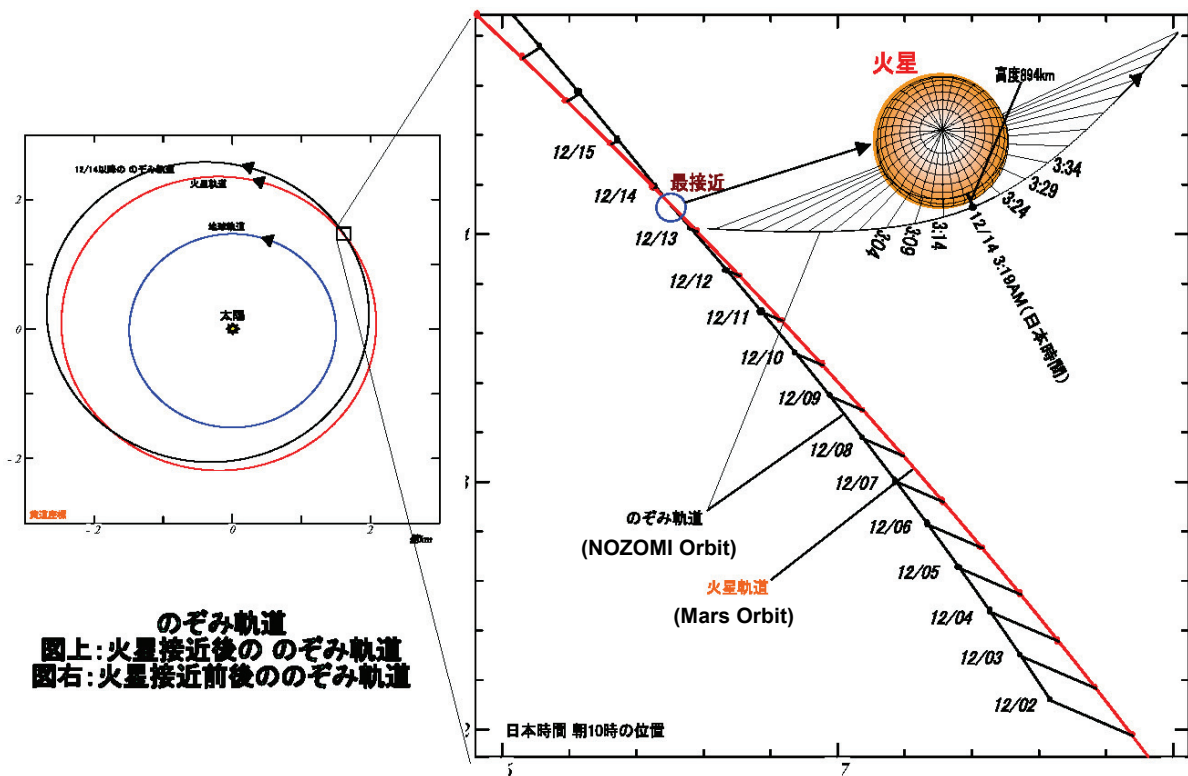


Figure 2-16: NOZOMI end of mission

On December 14, 2003, NOZOMI passed Mars in 894 km height above the surface. After the fly-by, the telemetry link to NOZOMI could not be re-established. (Image: ISAS, no English version available)

2.3.3 The scientific mission of the MDC

While the scientific missions of most other experiments onboard NOZOMI are limited to the Mars orbiting phase, the mission of the MDC can be separated into three mission phases with different scientific intentions. These MDC mission phases correspond to the different cruising phases of the spacecraft NOZOMI as follows:

1. The Earth-Moon phase: In this phase, dust particles in the Earth-Moon system were detected.
2. The interplanetary cruising phase: During this transfer phase to Mars, interplanetary and interstellar dust particles were detected. The results of these measurements are compared to the actual models of the interplanetary dust distribution.
3. The mission phase in Mars orbit: The main mission goal of the MDC was the detection of dust rings around Mars. These dust rings were predicted earlier as dust tori that should reside in the orbits of the two Martian moons Phobos and Deimos.

While the regions 1. and 2. were already explored by other experiments, the MDC would have been the first dust experiment in Mars orbit. The dust rings that first were theoretically predicted by Soter [Sot1971] are considered to consist of ejecta that are thrown from the surface of the moons after impacts of heavier particles. The basic assumption is that the two moons are exposed to the same stream of heavier asteroids as the Mars itself, whose surface is covered with impact craters. Those of these ejecta whose throw-out speed is sufficient to leave the gravitational field of the moon but not sufficient to leave Mars orbit are supposed to build a spatial distribution that at best can be described by a torus in the orbit of the particular moon. While the particle density of these dust rings is too low to be viewed from Earth with the available instruments, some disturbances of the Martian magnetic field recorded by the Phobos-2 spacecraft while passing the Phobos orbit (see Baumgärtel et al. [Bau1996]) give evidence of the existence of the predicted dust rings. The measurements of the MDC in Mars orbit would have been of great scientific interest, see Ishimoto et al. [Ish1997a], Sasaki [Sas1999] and Krivov & Hamilton [Kri1999]. The moons Phobos and Deimos themselves were also subjects of the NOZOMI scientific objectives, see Inada et al. [Ina1999] for a description of the planned observations by the Mars Imaging Camera (MIC).

3 The Mars Dust Counter

The Mars Dust Counter (MDC or MDC-NOZOMI) is the third in a series of dust experiments designed and developed by the Lehrstuhl für Raumfahrttechnik (LRT) at the Technische Universität München (TUM). In this chapter, the properties of the MDC-NOZOMI are described (see Igenbergs et al. [Ige1998] and ISAS [ISA1998]) since its predecessors, the Munich Dust Counters MDC-HITEN and MDC-BremSat are designed nearly identical and the basic properties and the functionality of the three experiments differ only in some details like size of the sensor box and the number of channels that are recorded by the electronics box.

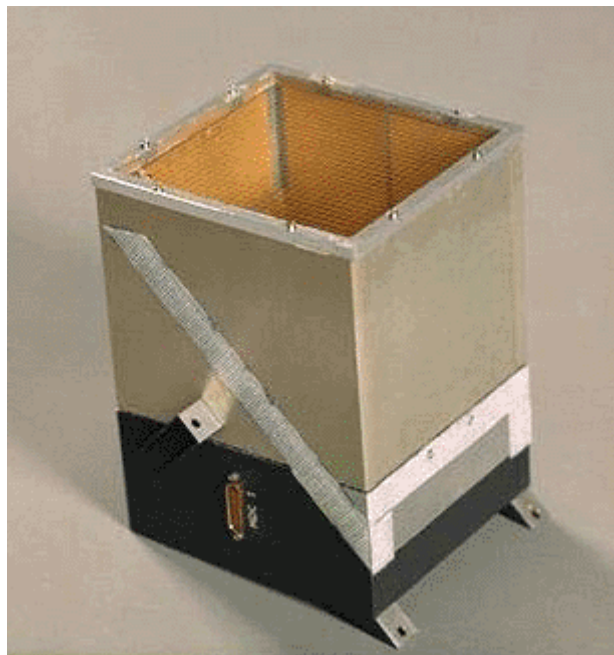


Figure 3-1: The MDC

Photograph of the MDC experiment. Below the sensor box with its gold-plated inner walls, the black electronics box is attached.

Paragraph 3.1 gives an overview of the physical principles that are used by the MDC for the detection of cosmic dust particles; paragraph 3.2 describes the technical properties of the MDC. Finally, paragraph 3.3 describes the calibration process of the MDC experiment.

3.1 The MDC measuring principle

The MDC measuring principle is based on the physical effects that are caused by impacts of dust particles on the solid target inside the sensor box. Impacts of particles at velocities greater than 1 km/sec cause rather complex phenomena. In principle, the kinetic energy of the impacting particle is transformed into heat that is high enough not only to break the molecular and atomic bindings but also to ionize the melted constituents of the particle and the target. Parts of this ionized matter are thrown out from the impact site at high velocity as so-called ejecta. The characteristics of the hypervelocity impacts, the ejecta and the charge generation process are described in the following paragraphs.

3.1.1 Physical background of the impact ionization process

The comprehensive stress that occurs during the first moments of a hypervelocity impact exceeds the rigidity of the solid materials of both the impacting particle and the target material by far, and the matter behaves like a compressible, in-viscid fluid. The shockwaves that run through the projectile and the target compress the material locally to more than 10 Mbar, and lead to a fast expanding crater in the surface of the target. Due to complex processes of interference of the shockwaves with their reflections from surfaces, the temperature rises up to 10^5 K in the immediate vicinity of the contact zone of projectile and target, while pressure falls. Either gaseous, fluid, or even solid material is then ejected from the impact site. The solid constituencies of these ejecta can reach as high velocities that are sufficient to cause subsequent hypervelocity impacts when these ejecta hit the target again.

The most important effect for the investigation of cosmic dust particles that occurs during this process is that the ejecta are ionized at least partially due to the high temperatures. This was first proven experimentally by Friichtenicht and Slattery [Fri1963]. Different theoretical models of the process of charge generation, depending on the particle's impact speed, were developed. As a basic assumption, the degree of ionization of the material is dependent on the specific intrinsic energy of the material, which can be described as (see Drapatz & Michel [Dra1974])

$$\Delta E = \frac{1}{2} \left(\frac{v}{\sqrt{\rho_p / \rho_T + 1}} \right)^2, \quad (3-1)$$

whereas v is the impact speed of the projectile, ρ_p the particle's density and ρ_T the target's density. According to this equation, a maximum specific intrinsic energy and therefore charge gain can be achieved by the use of high-density target materials, for this reason, the MDC target area was gold plated. Experimental measurements of the temperature of the plasma gave that the temperature is strongly affected by a wide range of environmental and local material conditions rather than showing a causal and reproducible relation to the total kinetic impact energy.

Although many studies on ion formation and plasma production during the hypervelocity impact process were made (see e.g. Hornung & Drapatz [Hor1981], Hornung et al.

[Hor1996a], Kissel & Krüger [Kis1987], Ratcliff et al. [Rat1996], [Rat1997], Dalmann et al. [Dal1977], Drapatz & Michel [Dra1974]), the complex process and all its different aspects cannot be explained satisfactory by one single model, not to mention a quantitative determination of the charge gain. For this reason, high effort must be put on experimental calibration of each individual sensor device with respect to its characteristics and operational area in order to allow reliable measurements of mass and impact speed of dust particles. For reliable measurements of particle mass and impact speed, the materials used in the laboratory as substitutes for natural cosmic dust particles must reproduce the properties of the natural particles as good as possible. New materials are developed and tested until today, see e.g. Burchell et al. [Bur2002] and Stübiger et al. [Stü2001]. MDC-NOZOMI calibration is described in paragraph 3.3.1.

The determination of impact speed and particle mass from the produced plasma by impact ionization detectors like the MDC is based on two empiric equations that are already described by Friichtenicht & Slattery [Fri1963],

$$\begin{aligned} t &= C_t m^\varepsilon v^\eta \\ Q &= C_\rho m^\alpha v^\beta, \end{aligned} \quad (3-2)$$

whereas t is the rise time of the charge signal, Q the charge amplitude, m the particle mass and v the impact speed. The parameters C_t , C_ρ , η and β must be determined by calibration experiments. The values of the mass exponents ε and α are set to 1 and 0, respectively, in the MDC-HITEN and MDC-NOZOMI calibration. Now, particle mass and impact speed can be determined from rise time and amplitude of a detector's charge signal.

Other studies on hypervelocity impacts showed, that the maximum intensity and total energy of the light flash emitted by a hypervelocity impact is a unique function of mass and impact speed of the impacting particle. Such measurements can also be used for particle properties determination, see e.g. Eichhorn [Eic1975], [Eic1976].

3.1.2 Material, geometrical and other artifacts

Experimental examination of hypervelocity impacts with different projectile and target materials gave that the charge gain is highly dependent on both the melting point and the density of the used materials. Using glass and carbon projectiles, the glass projectiles lead to a fourfold higher charge gain than the carbon projectiles despite their nearly same density (glass 2.5 g/cm³, carbon 2.2 g/cm³), this was explained by the lower melting point of glass that is responsible for the higher production of ejecta.

The effects of impacts with incident angles lower than 90° were thoroughly examined by Hoffmann [Hof1971], Dietzel et al. [Die1972] and Svedhem & Pedersen [Sve1992]. In summary, the rise time of the charge signals shows little to no dependence on the incident angle, while the charge gain varies by factors up to 6.

Also, the influence of the electric field strength inside impact ionization detectors was examined by Dalmann [Dal1977] in an experimental setup, and by Knabe [Kna1980] on the

GALILEO dust detector. In summary, the charge gain rises rapidly with the electric field, but the rise stops at an electric field strength of 1 V/mm (GALILEO Dust Detector) to 20 V/mm depending on the detector geometry. Inside the MDC, an electric field of about 4 V/mm or higher is given.

Willis et al. [Wil2004] carried out a study about the influence of a number of artifacts (e.g. natural particle charge, incident angles) on the derived mass and speed distribution of cosmic dust particles detected by typical impact ionization detectors. It was shown that the examined artifacts could cause shifts in mass distribution by an order of magnitude, and by a factor of two or three in velocity distribution.

3.2 Technical properties

The technical properties described here are valid for the MDC-NOZOMI. The design of the other members of the dust counter family developed at the LRT is nearly identical, most significant differences are the number of recorded channels (MDC-HITEN & MDC-BremSat: two, MDC-NOZOMI: three), and the size of the sensor box, which is marginally larger for the MDC-NOZOMI.

The MDC series of experiments are designed as impact ionization detectors. Particles that enter the box through the grid at high velocity will hit the target (the inner walls of the box build the target), vaporize together with a small amount of target material and build plasma. The negative and positive charges of this plasma are then separated by an electrical field inside the sensor box and move to the particular electrode where the charges are transformed into a voltage signal by one charge amplifier for each channel. This signal is digitized by a transient recorder and recorded by the MDC electronics if the amplitude exceeds a certain trigger level.

3.2.1 Experiment design

The MDC consists of a sensor box and an electronics box that are fixed by four small screws to each other. The overall dimensions of the experiment are 13.6·12.7·18.1 cm, its total weight is 730 g. The extremely lightweight outer structure is build from a *Nomex*[®] honeycomb structure that is plated with 0.1 mm aluminum. The inner walls of the sensor box are plated with gold to maximize the charge gain of hypervelocity impacts (see paragraph 3.1). Two electrodes are located at the top half of two opposite sides and are set to a potential of +220 V and -220 V, respectively. All other walls of the sensor box have a potential of 0 V. The open side of the sensor box is covered with a thin grid that is also set to a potential of 0 V, to shield the sensor box from outer electromagnetic fields. Due to the rectangular shape of the sensor box, the electrical field inside the box is highly inhomogeneous.

The electrodes and the remaining inner walls are connected to a particular charge amplifier each, this configuration builds the three channels that are recorded and finally build a full MDC-NOZOMI impact signal. The channels are named electron channel EC, ion channel IC and neutral channel NC, respectively (the MDC-HITEN and MDC-BremSat devices only possess two channels, EC and IC). While the EC mainly records negative charge and the IC positive, the NC records all the charge (positive and negative) that is not accelerated to the particular electrode. The characteristic of the charge amplifiers is logarithmic and the maximum charge that can be processed without overload is 10^{-10} C, which limits the measuring range of the MDC (see paragraph 6.2.1 for further discussion). The three signals are continuously digitized by two A/D converters, where the IC and NC share one of the A/D converters in multiplexing mode (in single mode, the NC is not recorded and the full sampling rate is available for the IC). The continuous digital data stream is initially recorded by a transient recorder that consists of a 1 kByte FIFO buffer. Further digital data processing is described in the following paragraph.

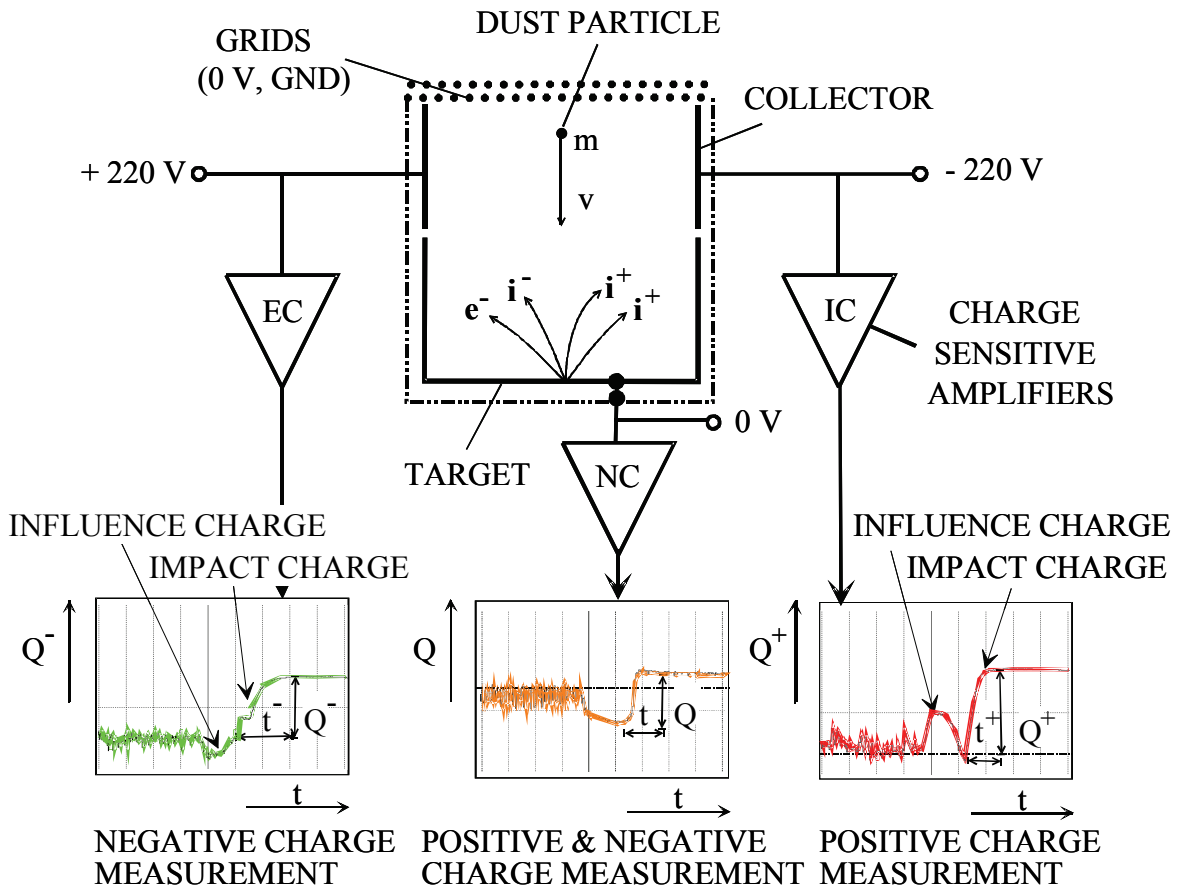


Figure 3-2: The MDC measuring principle

Impacting dust particles vaporize when hitting the target and produce plasma around the impact position. The charges of this plasma (negative free electrons and positive ions) are separated by the electric field inside the sensor box. Three charge sensitive amplifiers continuously convert the charge that hits the specific sensor areas into a voltage signal that is digitized and processed further as described in paragraph 3.2.2.

3.2.2 Onboard data processing

The MDC onboard software was developed by the Laboratory for Process Control and Real-Time Systems at the Technische Universität München, and is described by Fischer [Fis1998]. The MDC onboard computer consists of a single 8 bit *Intel*[®] 80C85 processor running at 1.5 MHz clock rate as central processing unit, 4 kByte read only memory (ROM) and 56 kByte of random access memory (RAM) that is used both for calculations and for data storage.

The 56 kByte random access memory is split into 56 single 1 kByte segments, 51 of these are used for impact data storage. One segment is required for actual HSK values and parameters needed for the calculation routines, another one contains a test pulse that is triggered and

recorded right after a new event is triggered to document the state of the charge amplifiers. The remaining four segments are needed by the qualification routine for calculations.

Each memory segment contains an eight-bit quality key that indicates the status of the segment. The intrinsic quality keys are calculated by a qualification routine and indicate the quality of the signal stored in the memory segment as a numerical value with a range from 2 to 245 (a detailed description of the qualification routine is given in paragraph 4.2.1). A quality key of zero indicates an empty or already read out segment, a quality key of 1 indicates a segment that contains a new recorded signal that is not qualified yet. Quality keys greater than 245 are reserved for special memory segments required for calculations.

A complete flow chart of the onboard data handling process is shown in Figure 3-3. Digital signal data is read from the 1 kByte FIFO buffer if one of the channels exceeds a certain trigger level. This trigger level and the trigger mode that determines which channels are triggered at all can be adjusted by telemetry commands to the desired value. If a signal is triggered, the content of the FIFO buffer is copied to the MDC memory with a temporal adjustment that the final signal contains 80 μ s pre trigger and 120 μ s post trigger data. A rough analysis of the new signal is carried out to check if the signal passes a set of criteria that have to be met by any signal that potentially represents a real impact signal at all, the so-called KO-criteria. If the signal passes these criteria, it is copied to a memory segment that is designated to hold the new-recorded signal. This memory segment can be an empty segment with quality key zero, or, if no empty segments are available, the segment that contains the signal with the lowest quality key which will be overwritten. During this process, some counters are set depending on the results of the KO-criteria check and the memory usage. Every signal that is discarded by the KO-criteria is documented by incrementing the so-called noise count NC. The NC therefore is an indicator of how noisy the MDC environment is at a given period of time. If the signal passes the KO-criteria and is stored in memory, either the so called impact count IC is incremented if an empty memory segment was available, or the so called event count EC is incremented if a previously recorded and qualified signal had to be overwritten. The EC therefore is an indicator of how much recorded and qualified signals were overwritten over time.

During this data handling process, the MDC electronics is busy and therefore cannot process eventually triggered further signals, which therefore get lost. The total dead time for processing events that are discarded by the KO-criteria check is 35 ms, the dead time for processing events that pass the KO-criteria is 65 ms. The total instrument dead time over longer periods can be appreciated by analyzing the progression of the noise count NC and the event count EC over time. A detailed analysis of instrument dead time during noisy mission phases was carried out and is described in paragraph 6.2.1

Every new signal that is stored in the MDC memory gets an initial quality key of 1. The qualification of new signals is carried out by the qualification routine that is running as a background task that can be interrupted if new signals are triggered and have to be processed. This is necessary because the qualification routine requires about 3 seconds processing time and would cause a much too high instrument dead time otherwise. Every signal that could not be qualified right after recording is being qualified later.

A memory segment of 1024 bytes contains 926 bytes of signal data, 463 bytes account for the electron channel EC, 232 bytes for the ion channel IC and 231 bytes for the neutral channel NC. The actual state of the MDC (voltages, temperatures) is stored in 7 bytes. 64 bytes each

contain the shape of a test pulse that is triggered right after the signal was recorded to give evidence about the state of the charge amplifiers. The remainder is used for quality key, impact time, phase count (the satellite's rotation angle) and some more information needed for later impact analysis.

Memory readout is performed at one go by transmission of the whole 56 kBytes of memory to the NOZOMI onboard computer, beginning with the lowest address.

The onboard software that handles all the data processing described above was developed prior to mission launch and is stored in the already mentioned 4 kByte read-only-memory. During the initialization process of the MDC onboard computer, the branch table that contains the memory addresses of the single routines of the software is copied to the random access memory, and this copy is used by the software to determine the address of each routine. This architecture allows the substitution of existing routines or the insertion of additional routines by uploading the new code into a certain memory segment and changing the branch address in the branch table to the memory address of the new routine. This feature was used in the year 2001 when a software upgrade was uploaded that should dynamically adjust the trigger level depending on the gradient of the noise counter, see Fischer [Fis1999]. The parameters of this upgrade were not adjusted properly to the environmental conditions in space, finally it was discarded a couple of months later. The software upgrade that should provide powerful data compression and was developed in 2003 also makes use of this feature, see chapter 5.

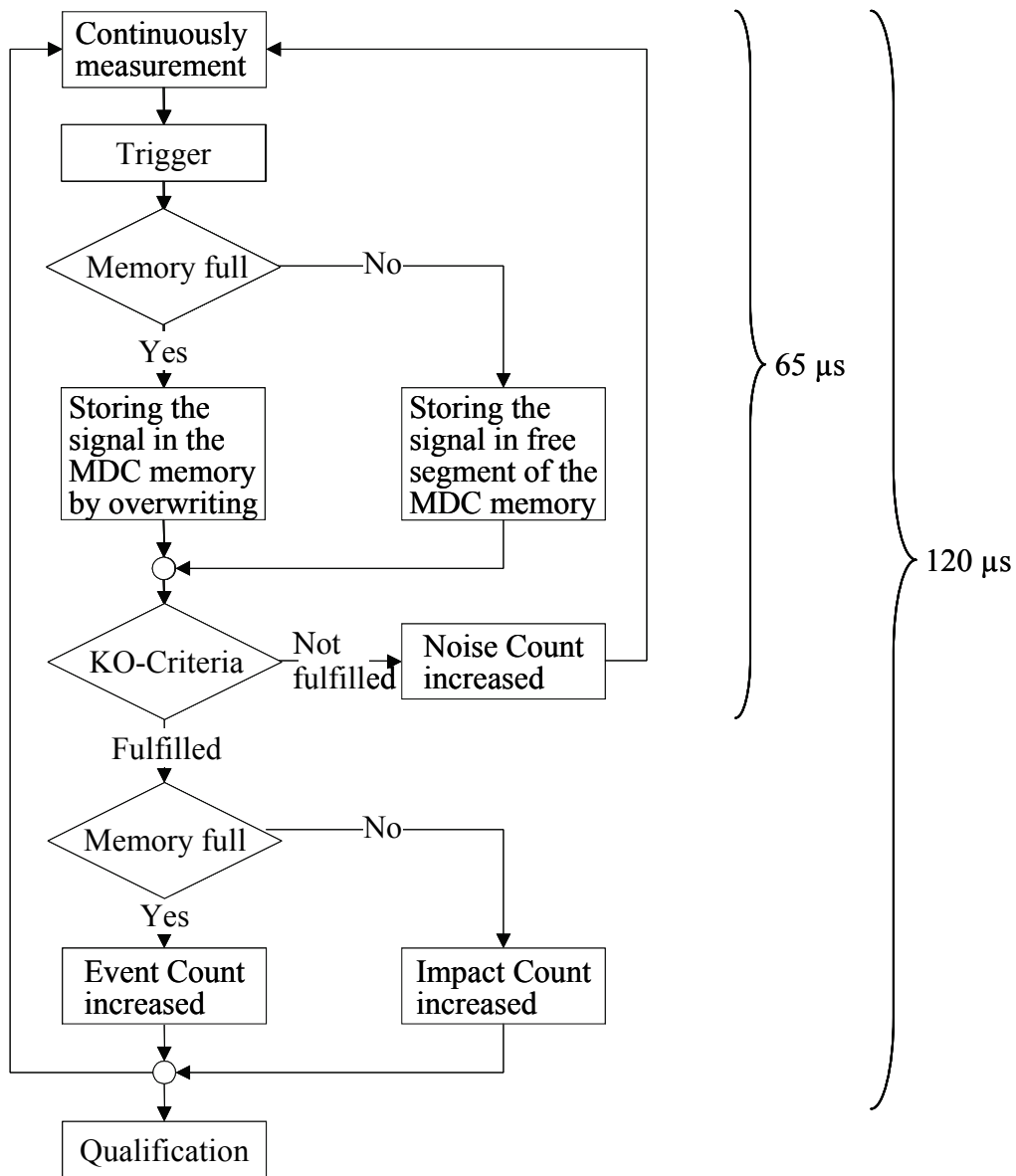


Figure 3-3: MDC data processing

Flow-chart of the data processing routine onboard the MDC. The time values indicate the instrument dead time that occurs during processing of newly triggered signals.

3.2.3 MDC structural integration and effective solid angle

For an exact determination of dust flux (particles per time and area) measured by the MDC, a detailed examination of the geometric conditions of the MDC and NOZOMI is required. The number of particles detected by a dust experiment like the MDC must be referred to a standardized field-of-view and sensor area to give comparable quantitative results. In this paragraph, the geometries of the MDC and of parts of the NOZOMI body that interfere the MDC's field-of-view are examined, and the final individual MDC/NOZOMI system parameter Ω_{MDC} (effective solid angle) required for dust flux analysis (see chapter 6) is determined. The structural integration of the MDC into the NOZOMI body is shown in Figure 3-4 and Figure 3-5 . All dimensions of parts of the NOZOMI body and information about the location of the MDC were derived from these technical drawings and from ISAS [ISA1998].

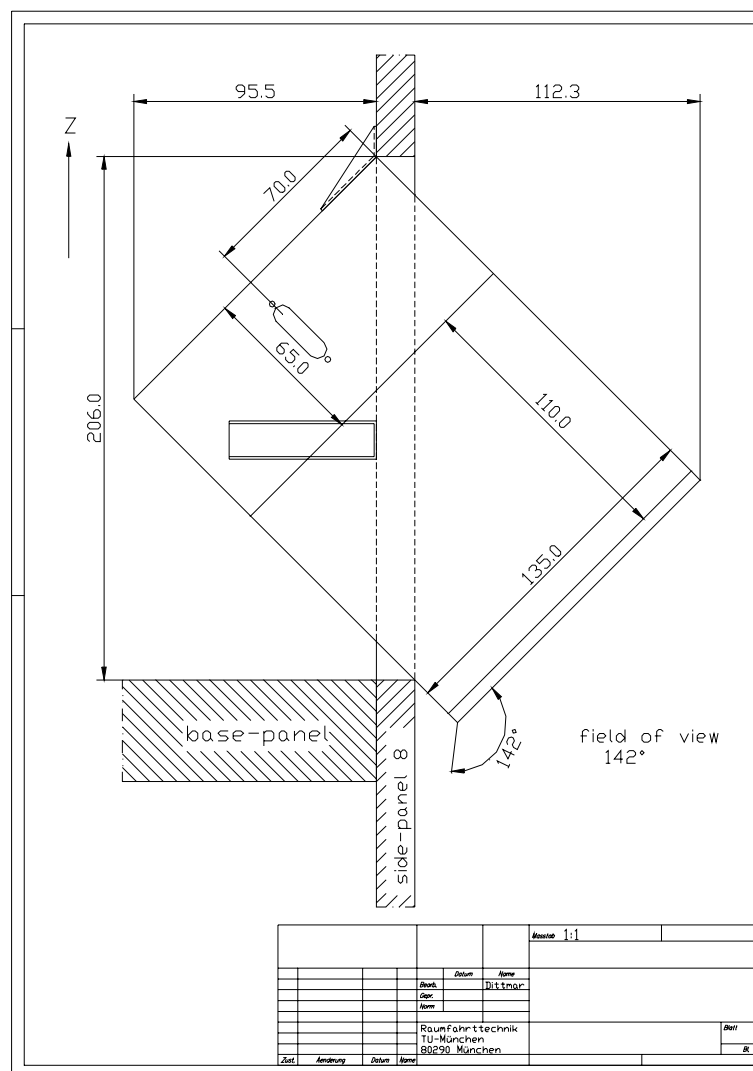


Figure 3-4: MDC integration, details

The MDC is mounted into NOZOMI side-panel #8, rotated 45° against the side-panel plane. The side panel restricts the MDC aperture angle to 142° in the z-direction.

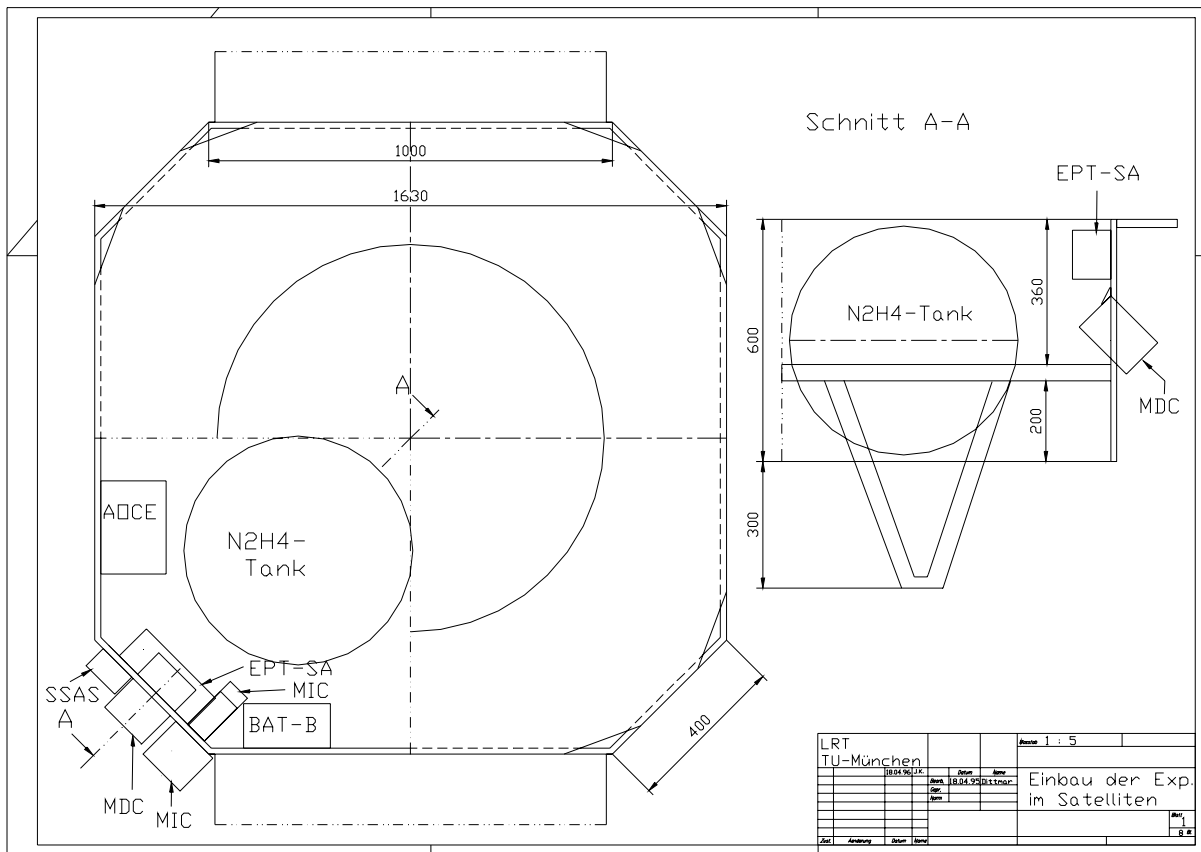


Figure 3-5: MDC integration, overview

The MDC is located on the NOZOMI side panel #8, next to the SSAS (Sun sensor). Unlike it is shown in this image, the MDC was later shifted towards side panel #1 (the neighboring panel, clockwise direction).

The field of view of the MDC can be described by the aperture angle and the effective solid angle, both depending on the instrument's and NOZOMI's geometric characteristics. While the aperture angle only gives a simple description of the field of view of the instrument itself without any consideration of possibly complex geometric characteristics, the effective solid angle is an exact value of the instruments detection capabilities. Determination of the effective solid angle requires detailed modeling of the geometric characteristics of the instrument and NOZOMI, and for complex configurations even numerical simulations. As an example, the effective solid angle of the Cosmic Dust Analyzer (CDA) on CASSINI was determined by a Monte-Carlo simulation of virtual impacting particles. For the MDC, this method is not practicable since the geometric conditions of the CDA and the MDC differ significantly. While the CDA target area is obscured only by parts of the instrument body that are located inside the sensor box, the MDC target area is obscured only by parts of the NOZOMI body that are located outside the sensor box at distances of several centimeters to meters.

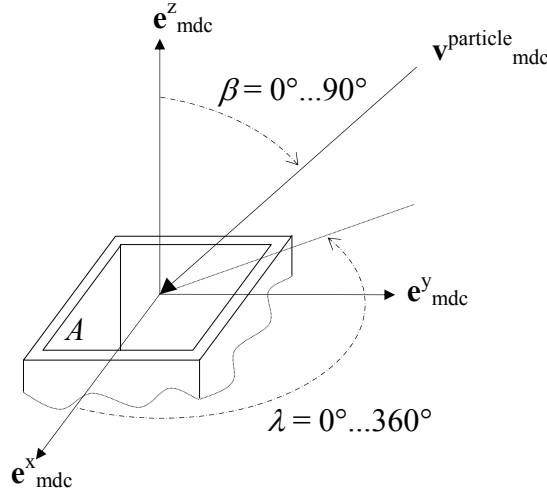


Figure 3-6: Latitude β and longitude λ of an impacting particle

Longitude λ of an impacting particle is measured in mathematically positive direction from the x-axis; latitude β is the angle between the z-axis and the particle direction.

Fortunately, the geometric conditions of the MDC instrument and the NOZOMI body are quite simple, analytical modeling and numerical integration is therefore feasible. Since the whole inner walls of the box build the instrument's sensitive area, the effective sensitive area or target area can be simply modeled as the aperture of the MDC's sensor box. Impacts with incident angles up to 90° can be detected by the MDC, the field of view of the instrument therefore is 180° and the aperture angle $\beta_{ap} = 90^\circ$ (if the target would be restricted to some smaller area inside the box, the aperture angle would be lower). These simple geometric conditions ease the further examinations.

Assuming a simple plain surface as sensitive area of the instrument, the effective sensitive area depending on the incident angle β is given by

$$A(\beta) = A_{total} \cos(\beta), \quad (3-3)$$

whereas A_{total} is the total surface area ($A_{total} = 116 \text{ mm} \cdot 125 \text{ mm} = 0.0145 \text{ m}^2$ for the MDC). Until now, the effects of the entrance grid are not considered. For a not obscured field of view, the solid angle element $d\Omega$ is given as

$$d\Omega = \int_0^{2\pi} d\lambda \sin(\beta) d\beta = 2\pi \sin(\beta) d\beta \quad (3-4)$$

in the case of axial symmetry (the rectangular shape of the MDC's sensor area does not affect this), and the effective solid angle Ω calculates to

$$\Omega = \int_0^{\beta_{ap}} 2\pi \sin(\beta) \cos(\beta) d\beta = 2\pi \left[-\frac{1}{2} \cos^2(\beta_{ap}) + \frac{1}{2} \right]. \quad (3-5)$$

This evaluates to $\Omega = \pi$. Thus, a detector like the MDC consisting (in principle) of a flat surface which detects particles passing through the surface in one defined fly-through direction covers $1/4^{\text{th}}$ of the whole hemisphere (a hemisphere's solid angle is given as 4π sr) and will detect $1/4^{\text{th}}$ of all particles (presumed an isotropic particle field).



Figure 3-7: Position of the MDC on NOZOMI's side panel #8

In this picture, the final position of the MDC on the NOZOMI side-panel #8 can be seen. Next to the MDC, the MIC instrument and the SSAS are located. The golden MLI (Multi-Layer-Insulation) was replaced by black *Kapton*[®] prior to launch.

This is only valid if the whole field-of-view of the MDC would not be obscured, which is not the case as can be seen in Figure 3-7. Parts of NOZOMI's body, of other instruments and the solar paddle mounted next to the MDC's side panel obscure the MDC's field of view. Also, the penetrability of the entrance grid must be considered. The determination of the effective solid angle of the MDC must be performed with respect to these obscuring parts of NOZOMI's body. In the following, the calculation method used by the author for effective solid angle determination is described. In principle, all obscuring parts of the NOZOMI body in the field of view were analytically modeled, except of the entrance grid whose obscuring effect was modeled as an averaged clouding of the MDC view.

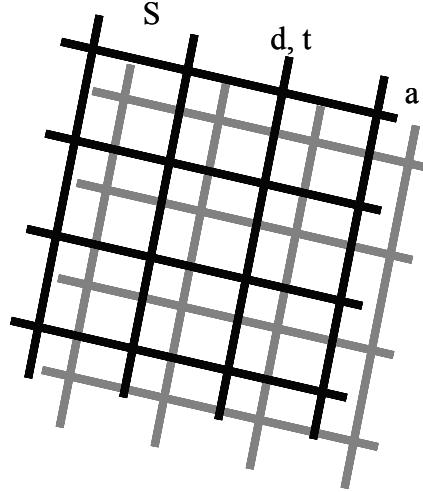


Figure 3-8: Illustration of the MDC entrance grid geometry.

The MDC sensor box is shielded by two identical grids (black and grey in this illustration) with a distance $a \approx 5$ mm. Distance between the bars is $S = 4$ mm, width of the bars is $d = 0.1$ mm and thickness of each grid is $t = 0.05$ mm.

The MDC entrance grid that shields the inner of the sensor box from outer electromagnetic disturbances had the following dimensions: distance between the bars $S = 4$ mm, width $d = 0.1$ mm, thickness $t = 0.05$ mm, symmetrically in x- and y- direction. According to Münzenmayer [Mün1995], the double entrance grid's penetrability η calculates to

$$\eta = \frac{(S - (d + t \cos \beta + D / \sin \beta))^2}{S^2}, \quad (3-6)$$

whereas D is the size of the impacting particle and $\beta = 0 \dots 90^\circ$ the impact angle. The shape of the penetrability $\eta(\beta, D)$ is shown in Figure 3-9. Assuming a mean particle density of 2.0 g/cm^3 [Lov1994], the particle sizes ($0.1 \text{ }\mu\text{m}$, $1 \text{ }\mu\text{m}$, $10 \text{ }\mu\text{m}$, $100 \text{ }\mu\text{m}$, $1000 \text{ }\mu\text{m}$) correspond to the masses (10^{-15} g , 10^{-12} g , 10^{-9} g , 10^{-6} g , 10^{-3} g). Since the MDC sensor box is shielded by two grids in series with a distance that is much higher than the grids' bar width and thickness, the effect of the grid can be considered by altering the solid angle element $d\Omega$ given by equation (3-4) to

$$d\Omega(D) = 2\pi \sin(\beta) \eta^2(\beta, D) d\beta, \quad (3-7)$$

which gives a particle diameter (or particle mass) dependent solid angle element $d\Omega(D)$ and an effective solid angle $\Omega(D)$. This is resulting from the fact that the order of magnitude of the grid parameters (millimeters and fractions of millimeters) and particle sizes (some micrometers to several 10-100 micrometers) are close to each other. This comes into charge especially for high latitudes β (for the other obscuring areas, whose sizes are in the order of magnitude of centimeters to meters, the sizes of the particles are not relevant).

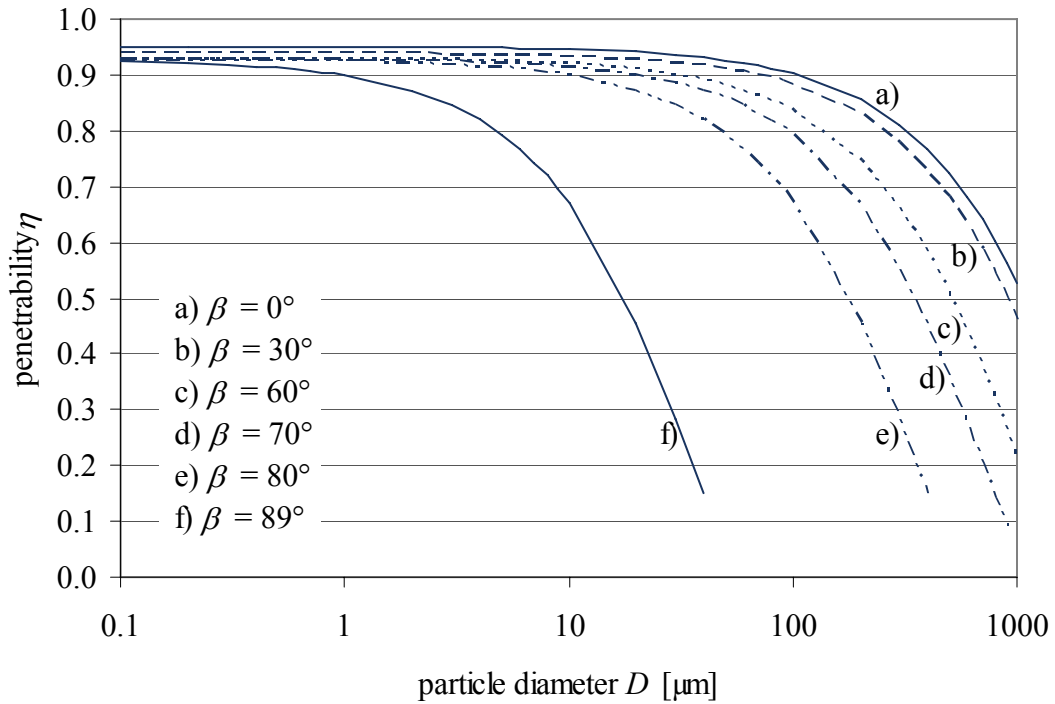


Figure 3-9: Penetrability of the MDC entrance grid over particle size.

For impact angles β greater than 10° , the penetrability of the grid is nearly constant for particle sizes from $0.1 \mu\text{m}$ to $10 \mu\text{m}$ at around 95% to 90%. For impact angles β lower than 10° or particle sizes greater than some tens of micrometers, the penetrability decreases fast. The curves d), e) and f) stop where the bracketed, not squared numerator of equation (3-6) gets negative for the next discrete value D_{max} , hence $\eta(D \geq D_{\text{max}}) = 0$.

All calculations were performed using *Microsoft® Excel®*. First, it must be considered that the dimensions of the MDC sensor box and the obscuring areas as well as the distance of the obscuring areas from the MDC sensor area are all in the order of magnitude of decimeters. Therefore, the effective solid angle is significantly different for every position on the MDC sensor area. While the NOZOMI solar paddle PDL-B is located sufficiently far away from the sensor box (in the magnitude of meters, the resulting differences of view-angles for different positions on the MDC sensor area are therefore very small), the MDC side panel #8 is located very near the sensor box and thus produces different rates of obscuration for different positions on the sensor area. Hence, the MDC sensor area was divided into 81 smaller sensor areas ($n = -4 \dots 4$, $m = -4 \dots 4$) and the effective solid angle was calculated for each of the different positions. The results were then averaged to calculate the final effective solid angle of the MDC on NOZOMI.

For each position (n, m) , a 90×360 matrix \mathbf{O}_{nmij} was created that represents all possible view directions from the center of the MDC effective sensor area, described by latitude $\beta_i = 0^\circ \dots 89^\circ$ ($i = 0 \dots 89$) and longitude $\lambda_j = 0^\circ \dots 359^\circ$ ($j = 0 \dots 359$) in steps of 1° each, see also Figure 3-6. Each cell of this matrix contained either the value +1 (free view direction) or 0 (obscured view direction). The solid angle element for a given latitude β_i was then calculated by

$$\Delta\Omega_{nmi}(D) = 2\pi \sin(\beta_i) \eta(\beta_i, D) \left(\frac{1}{360} \sum_{j=0}^{359} \mathbf{O}_{nmij} \right) \Delta\beta, \quad (3-8)$$

whereas $\Delta\beta = 1^\circ$ is the step-width used. From this, the final effective solid angle Ω was then calculated by

$$\Omega_{nm}(D) = \sum_{i=0}^{89} \Delta\Omega_{nmi}(D) \cos \beta_i. \quad (3-9)$$

For a completely free field of view ($\mathbf{O}_{nmij} = +1$ for all i, j, n, m ; $\eta = 1$) this evaluates to an effective solid angle of $\Omega = 0.99989 \pi$ sr rather than the exact analytical value of 1π sr. The accuracy of this method can therefore be seen as proven to be sufficient for the calculation of Ω , presumed correct modeling of the NOZOMI parts.

In the next step, the cells of the matrix \mathbf{O}_{nmij} must be filled with the appropriate values +1 or 0, respectively. To perform this, the obscuring areas had to be modeled and each individual line of view described by (λ_j, β_i) had to be tested whether it crosses at least one of these areas or not. First, the center of the MDC effective sensor area was placed in the origin of a Cartesian coordinate system with the positive z-axis perpendicular to the sensor area. The obscuring areas or planes, respectively, were modeled as planes using the vectorial representation for the k^{th} plane ($k = 1 \dots N$)

$$\mathbf{q}_k = \mathbf{q}_{k,0} + \mu \mathbf{x}_k + \nu \mathbf{y}_k, \quad (3-10)$$

where $\mathbf{q}_{k,0}$ is the center point of the k^{th} area, and the linear independent unit vectors \mathbf{x}_k and \mathbf{y}_k span the plane ($\mathbf{x}_k \perp \mathbf{y}_k$, $|\mathbf{x}_k| = |\mathbf{y}_k| = 1$). The dimensions of the k^{th} rectangular area are given by dx_k and dy_k for rectangular areas, or dr_k for circular areas (and spheres modeled as circles), respectively.

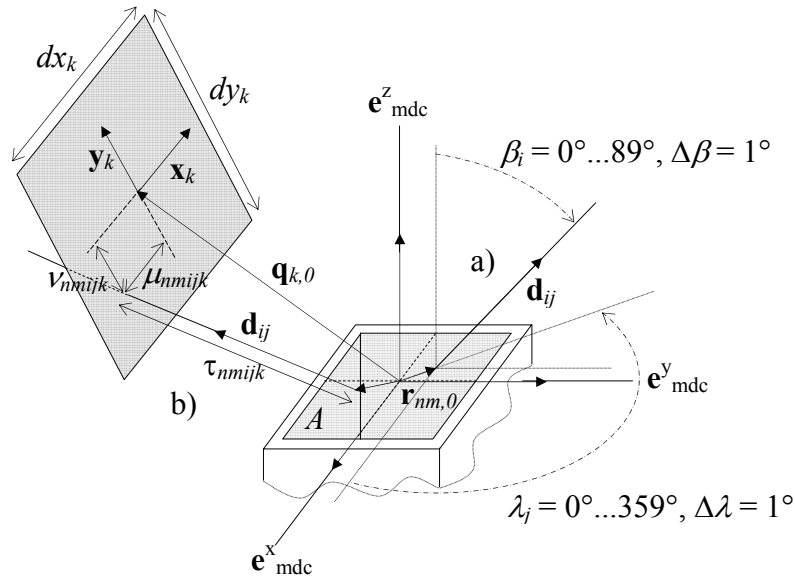


Figure 3-10: Illustration of the geometry for the calculation of Ω

The geometry of the models of the MDC sensor area, the view directions and the obscuring areas is shown here. In case a) the line of view is not obscured, the angles β and λ are illustrated. In case b), the line of view crosses the obscuring area, the values μ_{nmijk} , v_{nmijk} and τ_{nmijk} are illustrated that are used to determine if there is a point of intersection and if it's located within the area's boundaries. All vectors but $\mathbf{q}_{k,0}$ and $\mathbf{r}_{nm,0}$ are unit vectors.

The NOZOMI parts that obscure the MDC field-of-view were modeled from the available technical drawings as follows (all dimensions in millimeters):

$k = 1$, NOZOMI side-panel #8, rectangular area¹

$$\mathbf{q}_{1,0} = \begin{pmatrix} 25.1 \\ 100 \\ -66.2 \end{pmatrix}, \mathbf{x}_1 = \begin{pmatrix} 0.707 \\ 0 \\ 0.707 \end{pmatrix}, \mathbf{y}_1 = \begin{pmatrix} 0 \\ 1 \\ 0 \end{pmatrix}, dx_1 = 600, dy_1 = 400 \quad (3-11)$$

$k = 2$, NOZOMI solar paddle PDL-B, rectangular area

$$\mathbf{q}_{2,0} = \begin{pmatrix} -497 \\ 1446 \\ 31.7 \end{pmatrix}, \mathbf{x}_2 = \begin{pmatrix} -0.5 \\ 0.707 \\ 0.5 \end{pmatrix}, \mathbf{y}_2 = \begin{pmatrix} 0.5 \\ 0.707 \\ -0.5 \end{pmatrix}, dx_2 = 2240, dy_2 = 1000 \quad (3-12)$$

¹ Unlike it is shown in the technical drawings (see Figure 3-4 and Figure 3-5), the MDC was finally not mounted in the middle of the side panel #8, but shifted towards side panel #1. Since no drawings were available that could give more information, the value $q_{1,0}^y = 100$ mm was estimated from photographs (see Figure 3-7) of the final NOZOMI configuration where the MDC seems to be mounted in or near the middle of one half of the side panel #8.

$k = 3$, NMS instrument on side-panel #1, circular area, not modeled due to lack of data

$$\mathbf{q}_{3,0} = \begin{pmatrix} \text{N/A} \\ \text{N/A} \\ \text{N/A} \end{pmatrix}, \quad \mathbf{x}_3 = \begin{pmatrix} \text{N/A} \\ \text{N/A} \\ \text{N/A} \end{pmatrix}, \quad \mathbf{y}_3 = \begin{pmatrix} \text{N/A} \\ \text{N/A} \\ \text{N/A} \end{pmatrix}, \quad dr_3 = \text{N/A} \quad (3-13)$$

The line of sight defined by (λ_j, β_i) was also modeled using the vectorial representation

$$\mathbf{r}_{nmij} = \mathbf{r}_{nm,0} + \tau \mathbf{d}_{ij}, \quad (3-14)$$

whereas $\mathbf{r}_{nm,0}$ is the center of the $(n, m)^{\text{th}}$ part of the MDC sensor area as described above and $\mathbf{d}_{ij} = (\cos \lambda_j \sin \beta_i, \sin \lambda_j \sin \beta_i, \cos \beta_i)^{\text{T}}$ is the current view direction. The point of intersection of the $(i, j)^{\text{th}}$ line of view and the k^{th} plane is then given by the equation

$$\begin{aligned} \mathbf{q}_k &= \mathbf{r}_{nmij} \\ \mathbf{q}_{k,0} + \mu \mathbf{x}_k + \nu \mathbf{y}_k &= \mathbf{r}_{nm,0} + \tau \mathbf{d}_{ij} \\ \mu \mathbf{x}_k + \nu \mathbf{y}_k - \tau \mathbf{d}_{ij} &= \mathbf{r}_{nm,0} - \mathbf{q}_{k,0} \end{aligned} \quad (3-15)$$

which represents an inhomogeneous 3×3 system of linear equations with three independent variables that can be solved directly (there is always exactly one real solution for linear independent vectors \mathbf{x}_k , \mathbf{y}_k and \mathbf{d}_{ij} , the case of linear dependence (the line of view is parallel to the given k^{th} area) is rather unlikely in this approximation and even would have been trapped by the *Excel*[®] engine). For the calculation of μ_{nmijk} , ν_{nmijk} and τ_{nmijk} , the rule of Cramer was used. For the given system of linear equations,

$$\begin{pmatrix} x_k^1 & y_k^1 & -d_{ij}^1 \\ x_k^2 & y_k^2 & -d_{ij}^2 \\ x_k^3 & y_k^3 & -d_{ij}^3 \end{pmatrix} \cdot \begin{pmatrix} \mu_{nmijk} \\ \nu_{nmijk} \\ \tau_{nmijk} \end{pmatrix} = \begin{pmatrix} r_{nm,0}^1 - q_{k,0}^1 \\ r_{nm,0}^2 - q_{k,0}^2 \\ r_{nm,0}^3 - q_{k,0}^3 \end{pmatrix}, \quad \text{or } \mathbf{A}_{ijk} \cdot \mathbf{p}_{nmijk} = \mathbf{i}_{nmk}, \quad (3-16)$$

the values μ_{nmijk} , ν_{nmijk} and τ_{nmijk} are given by

$$\mu_{nmijk} = \frac{\det(\mathbf{A}_{nmijk}^{\mu})}{\det(\mathbf{A}_{ijk})} \quad (\nu_{nmijk} \text{ and } \tau_{nmijk} \text{ alike}), \quad (3-17)$$

where the matrix \mathbf{A}_{nmijk}^{μ} is derived from the matrix \mathbf{A}_{ijk} by replacing the accordant column by the right side vector \mathbf{i}_{nmk} . Given μ_{nmijk} , ν_{nmijk} and τ_{nmijk} , the point of intersection could be easily calculated from the linear or planar equations (3-10) and (3-14) described above, but this is not required here. It must only be determined whether the point of intersection is located in the positive view direction and within the boundaries of the given area k . This can be checked by applying the following conditions:

$\tau_{nmijk} > 0$ (the point of intersection is located in positive direction of the line of view), AND

for rectangular areas:

$\mu_{nmijk} < \frac{1}{2} dx_k$, (the point of intersection is located within the x-dimension of the area), AND
 $v_{nmijk} < \frac{1}{2} dy_k$, (the point of intersection is located within the y-dimension of the area),

for circular areas:

$\sqrt{(\mu_{nmijk})^2 + (v_{nmijk})^2} < dr_k$ (the point of intersection is located within the circle's dimensions).

If all three (or two for circular areas) conditions are fulfilled, the correspondent cell in the 90×360 matrix \mathbf{O}_{nmijk} is set to 0 (obscured by the k^{th} plane), otherwise to +1 (not obscured by the k^{th} plane). The final matrix \mathbf{O}_{nmij} is then build by a logical AND operation over all \mathbf{O}_{nmijk} , $k = 1 \dots N$.

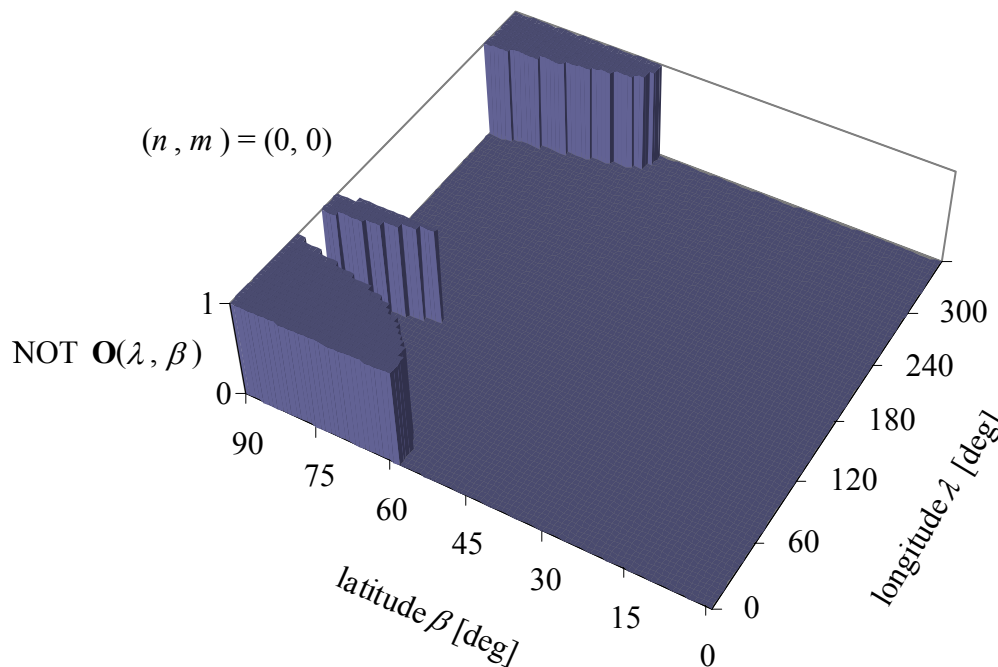


Figure 3-11: Visualization of the MDC view area

In this picture, the inverse of the matrix \mathbf{O}_{00ij} (NOT \mathbf{O}_{00ij}) is visualized, $(n, m) = (0, 0)$. From left to right, the impact angle $\beta = 0^\circ \dots 90^\circ$ is displayed where 0° means vertical impact and 90° striped impact, from bottom to top the longitude angle $\lambda = 0^\circ \dots 360^\circ$ is displayed. The bottom area with NOT $\mathbf{O}_{00ij} = 0$ represents directions of free view. The exalted area with NOT $\mathbf{O}_{00ij} = 1$ and $\beta = 59^\circ \dots 90^\circ$, $\lambda = 313^\circ \dots 73^\circ$ represents the NOZOMI side panel #8, the area with NOT $\mathbf{O}_{00ij} = 1$ and $\beta = 71^\circ \dots 90^\circ$, $\lambda = 103^\circ \dots 124^\circ$ represents the NOZOMI solar paddle PDL-B attached to side panel #7.

Using the method described above with the orientations and best guess dimensions of the two obscuring areas, the effective solid angle of the MDC evaluates to $\Omega_{00} = 0.9398 \pi$ sr as seen

from the center point of the MDC sensor area, $(n, m) = (0, 0)$ without considering the grid ($\eta = 1$).

The final effective solid angle $\Omega_{\text{MDC}}(D)$ is then averaged from the 81 values $\Omega_{nm}(D)$ by

$$\Omega_{\text{MDC}}(D) = \frac{1}{81} \sum_{n,m=-4}^4 \Omega_{nm}(D). \quad (3-18)$$

Figure 3-12 shows the effective solid angle $\Omega_{nm}(D)$ for $D = 5 \mu\text{m}$, Figure 3-13 shows the final effective solid angle $\Omega_{\text{MDC}}(D)$. The discrete values are shown in Table 3-1. For latter calculations of dust flux measured by the MDC, these values were used.

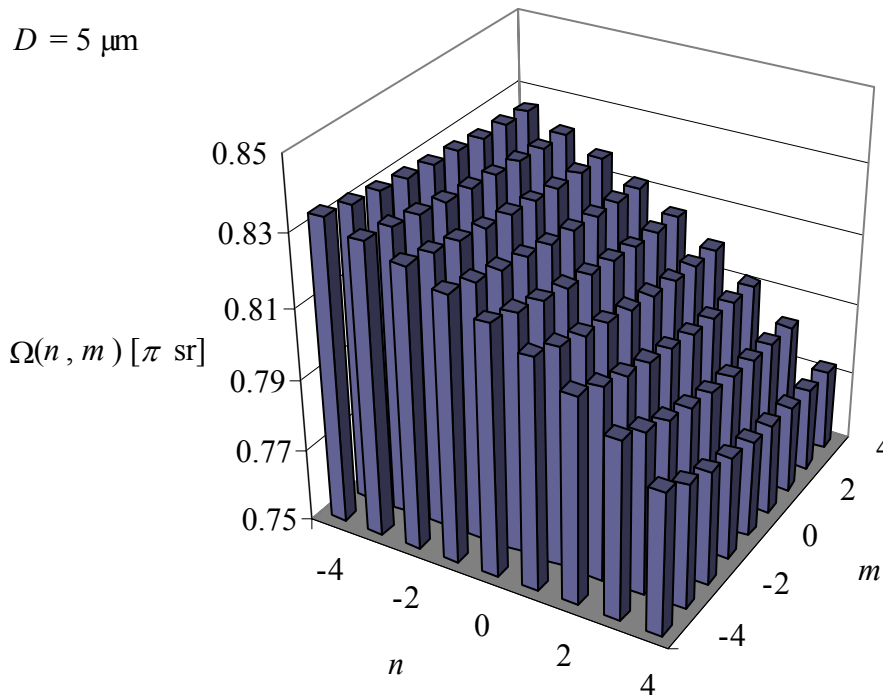


Figure 3-12: Effective solid angle $\Omega_{nm}(D)$ for a particle size of $D = 5 \mu\text{m}$
The 81 values $\Omega_{nm}(D)$ are displayed as bars over the MDC sensor area (grey area). Maximum value is $0.834 \pi \text{ sr}$ at $(n, m) = (-4, -4)$, minimum value is $0.773 \pi \text{ sr}$ at $(n, m) = (4, 4)$. Mean value is $0.808 \pi \text{ sr}$.

The calculation of the final values shown in Table 3-1 and Figure 3-13 took about 25 minutes on an 800 MHz *Intel*[®] *Pentium*[®] III desktop PC, due to the large number of 3×3 determinants that had to be evaluated and the limited computing efficiency of *Microsoft*[®] *Excel*[®] and VBA scripting.

Table 3-1: Effective solid angle $\Omega_{\text{MDC}}(D)$, final values

D [μm]	0.1	0.2	0.3	0.4	0.5	0.6	0.7	0.8	0.9
Ω [π sr]	0.817	0.817	0.816	0.816	0.816	0.816	0.816	0.816	0.815
D [μm]	1	2	3	4	5	6	7	8	9
Ω [π sr]	0.815	0.814	0.812	0.810	0.808	0.807	0.805	0.803	0.802
D [μm]	10	20	30	40	50	60	70	80	90
Ω [π sr]	0.800	0.784	0.768	0.753	0.738	0.723	0.709	0.695	0.682
D [μm]	100	200	300	400	500	600	700	800	900
Ω [π sr]	0.669	0.552	0.457	0.379	0.314	0.259	0.214	0.176	0.144

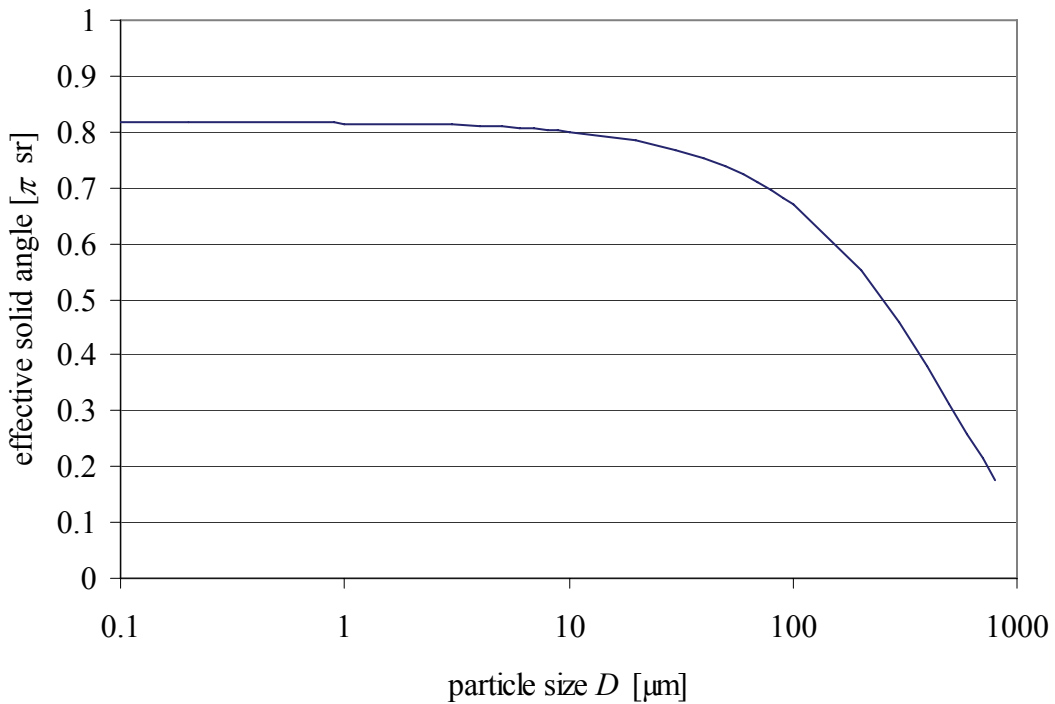


Figure 3-13: Particle size dependence of the effective solid angle $\Omega_{\text{MDC}}(D)$. For particle sizes from 0.1 μm to 10 μm , the effective solid angle is nearly constant around 0.82 to 0.80 π sr, while it decreases fast for particle sizes greater than some tens of micrometers.

Another interesting characteristic of the MDC/NOZOMI system is the spin-averaged sensitivity of the instrument, or average area of the instrument depending on the angle to the spin-axis, respectively (see Figure 3-14). Based on the method described above, the spin-averaged sensitivity was calculated as described in the following.

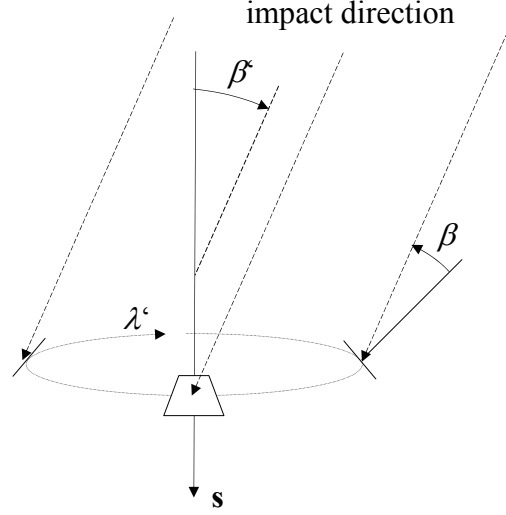


Figure 3-14: Geometry of the calculation of the spin-averaged sensitivity
The effective detector area of the MDC varies with the spin angle for
particles that arrive at a certain angle β to the NOZOMI spin axis s .

First, the matrices \mathbf{O}_{nmijk} were enlarged to 180×360 matrices as required by the range of (λ'_i, β'_j) . Instead of rotating the satellite or the MDC, respectively, the view directions were rotated around the negative NOZOMI spin-axis. The view directions were calculated from the angles (λ'_i, β'_j) as $\mathbf{d}'_{ij} = (\cos \lambda'_j \sin \beta'_i, \sin \lambda'_j \sin \beta'_i, \cos \beta'_i)^T$. The resulting view directions were then transformed from the NOZOMI reference system (λ'_i, β'_j) to the MDC reference system (λ_i, β_j) by the transformation

$$\mathbf{d}_{ij} = \begin{pmatrix} \cos \delta' & 0 & -\sin \delta' \\ 0 & 1 & 0 \\ \sin \delta' & 0 & \cos \delta' \end{pmatrix} \mathbf{d}'_{ij}, \quad (3-19)$$

whereas $\delta' = -45^\circ$ is the angle of the MDC z-axis to the negative NOZOMI spin-axis. From these view directions, the lines of sight were modeled as described in equation (3-14). Now, the calculation of the matrices \mathbf{O}_{nmijk} was performed exactly as described above. From these matrices, the final matrix \mathbf{O}_{nmij} was again built by a logical AND operation over all matrices \mathbf{O}_{nmijk} , $k = 1 \dots N$ and the matrix \mathbf{O}_{nmij0} that contains information about whether the given view direction is pointing to the outside of the sensor box ($d^z_{ij} > 0$). Then, the average area a_{nmi} for a given latitude β_j and position (n, m) was calculated by

$$a_{nmi} = \frac{A}{81} \sum_{j=0}^{359} \mathbf{O}_{nmij} d^z_{ij} \Delta\beta, \quad (3-20)$$

whereas A is the total MDC sensor area, $\Delta\beta = 1^\circ$ is the step width and the factor d^z_{ij} is the sine of the angle between the view direction and the MDC z-axis. The total average area for a given latitude β_i was summed up as

$$a_i = \sum_{n,m=-4}^4 a_{nmi}. \quad (3-21)$$

These values are visualized in Figure 3-15. The effect of the grid was not considered here since the quantitative values are not used for any further calculations. The integral of the spin-averaged sensitivity is shown in Figure 3-16. On an 800 MHz *Intel® Pentium® III* desktop PC, the calculation of the final values a_i took about 1 hour with *Microsoft® Excel®* and VBA scripting.

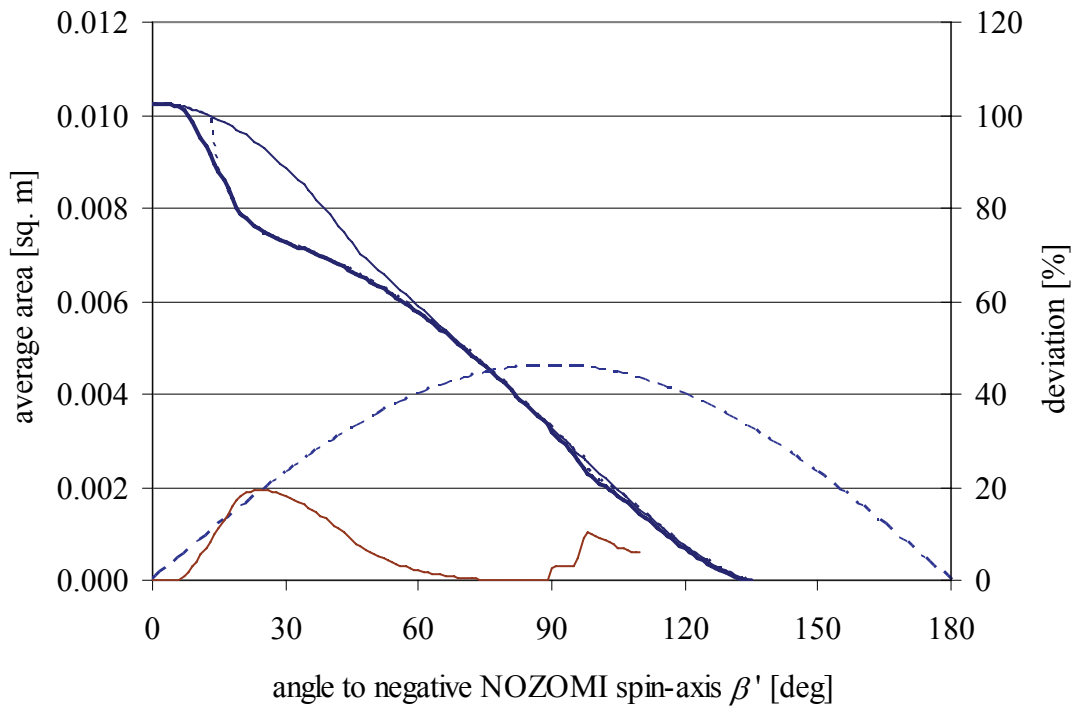


Figure 3-15: Spin-averaged sensitivity of the MDC on NOZOMI

The thick blue line represents the spin-averaged sensitivity of the MDC/NOZOMI system. See text for details.

The final spin averaged sensitivity of the MDC/NOZOMI system is shown in Figure 3-15. The thin blue solid line represents the spin-averaged sensitivity of the MDC without considering the obscuration by the side-panel and the solar-paddle, while the thick blue solid line represents the final spin-averaged sensitivity with consideration of the obscuration. The thin red solid line represents the effects of the obscuring areas as percentage (from $\approx 110^\circ$ onwards, the percentage values become invalid due to arithmetic errors caused by very small operands). The side panel affects the average area from 7° to around 65° (deviance $> 1\%$), maximum deviance is 19.3% at 24° . The solar panel has only little effect at around $98^\circ \pm 10^\circ$, maximum is 10.3%. From 135° to 180° , the average area is exactly zero. For illustration, the dotted blue line shows the average area for the single position $(n, m) = (0, 0)$. As can be seen, the effect of the side panel starts later at 14° , but with a much sharper edge. Also for illustration purpose, the dashed blue line represents the spin-averaged sensitivity of a fictitious detector mounted at an angle of 90° to the spin axis with completely free view area.

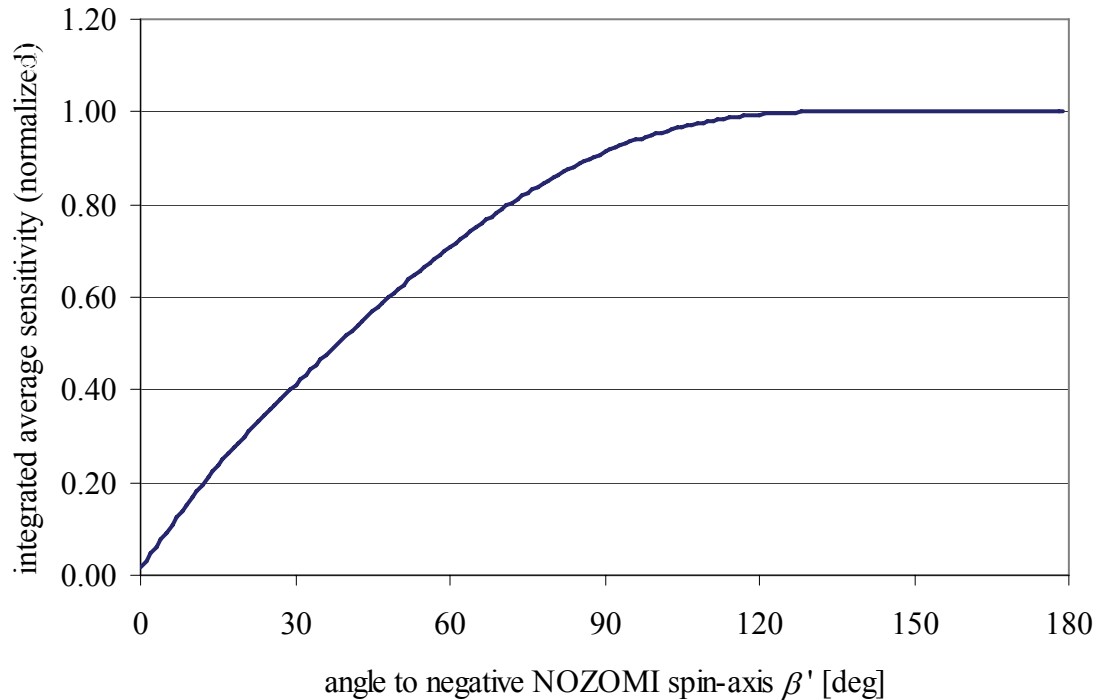


Figure 3-16: Integrated spin-averaged sensitivity

50% of all detected particles have impact directions within a cone with 39° aperture angle, 66% within 55°, 75% within 65° and 90% within 88°.

3.2.4 Instrument detection capabilities

To understand and interpret the results of the MDC, the characteristics and dynamics of high velocity impacts and the instrument's sensitivity must be taken into account. The MDC charge amplifiers and A/D converters are designed to measure and process charges up to 10^{-10} C. Impacts that produce higher charge in either channel will overload the charge amplifiers and important parts of the signal are lost. In this case, rise time and amplitude cannot be determined, and a further analysis is not possible anymore. This usually happens for particles with high mass and high impact velocity. On the other hand, impacts must produce enough charge to be separated from the instruments background noise. As estimation, it can be said that impacts that produce less than 10^{-15} C will not be recognized as impacts any more. Furthermore, any signal has to exceed a certain trigger level to be recorded by the MDC electronics at all. This trigger level must be chosen at a level, which is high enough to discard most noise events prior to processing in order to protect the MDC onboard computer from overload. On the other hand, the trigger level must not be chosen too high, otherwise signals that represent real impacts of low mass and low velocity particles will get lost.

During the whole interplanetary cruising phase (except for the phase where the “autotrigger” software patch was enabled), the instruments trigger level was set to a binary value of 143, which corresponds to a charge of $\approx 10^{-13}$ C, both for the ion channel and the electron channel. Impacts that produce less than 10^{-13} C of positive and/or negative charge are not even triggered and therefore lost.

Summarized, the instruments detection capabilities are limited to impacts that produce charge between 10^{-13} and 10^{-10} C. The charge gain of high velocity impacts is discussed in paragraph 3.1 and depends on the particle's mass as well as on its impact velocity. Figure 3-17 shows the calculated measuring range of the MDC for a given trigger level of 143. It can be estimated that the best detection capabilities of the instrument are at particle masses between 10^{-12} and 10^{-11} g. Above and below this interval, dust flux determinations do not give any reliable results.

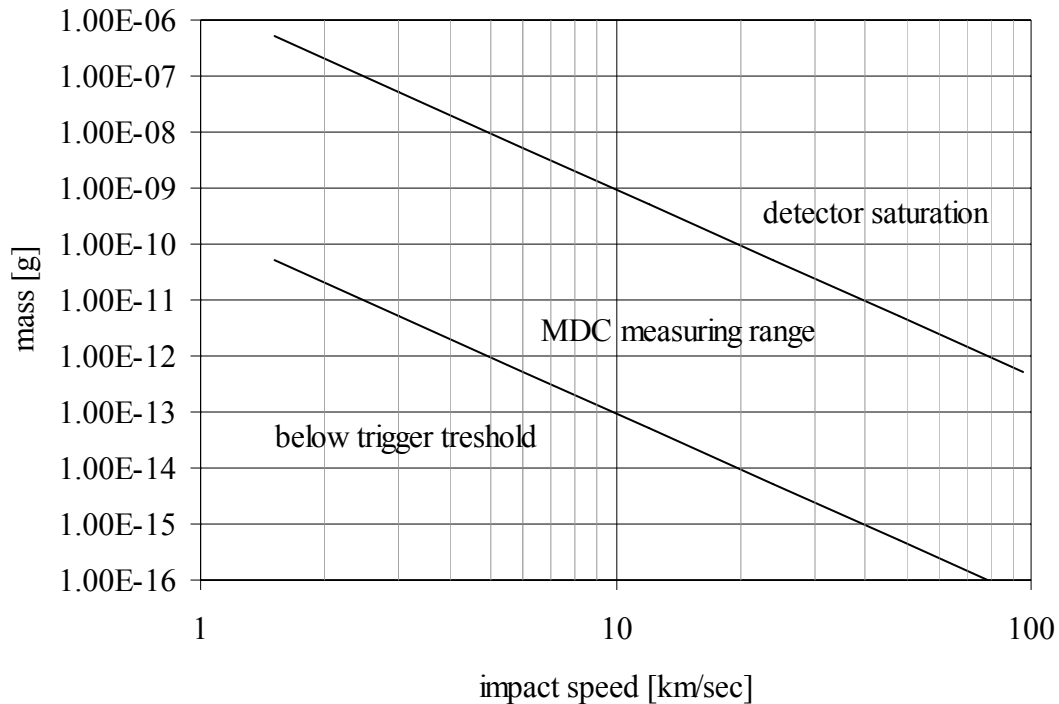


Figure 3-17: MDC measuring range

The MDC measuring range is limited towards low particle mass and low impact speed by the trigger threshold and towards high particle mass and high impact speed by the saturation of the detector electronics.

3.3 Data processing on ground

In this paragraph, MDC-NOZOMI calibration and data analysis are described briefly. For a detailed description of the calibration process, the determination of the required parameters for the data analysis process, and the data analysis itself, see Naumann [Nau2000].

3.3.1 Calibration

As already mentioned in paragraph 3.1, no quantitative mathematical model of the charge generation of hypervelocity impacts is available until today. Thus, every detector based on the physical effects of hypervelocity impacts has to be calibrated individually.

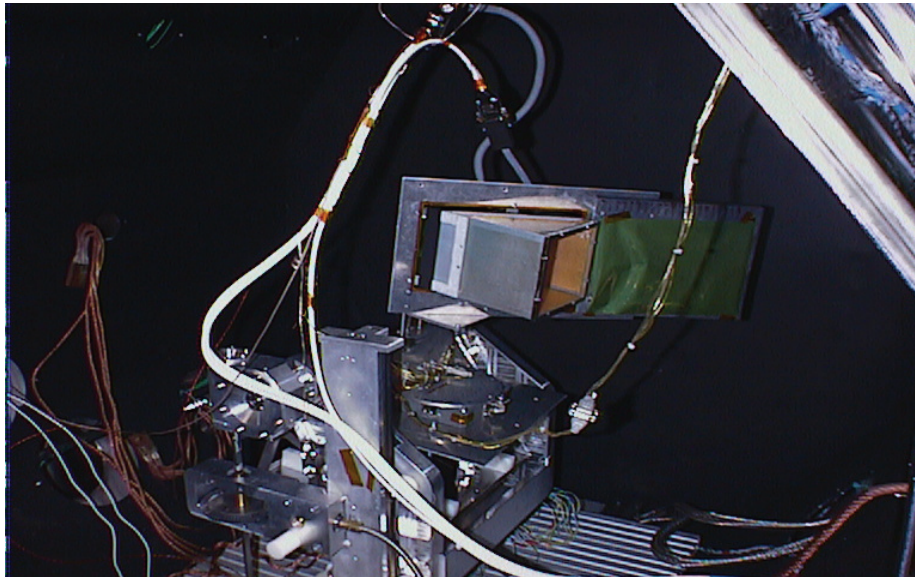


Figure 3-18: The MDC inside the calibration setup

For calibration experiments, particles of known mass and speed were shot into the MDC's target area.

Calibration of the MDC-NOZOMI was carried out in the electrostatic van-de-Graaf dust accelerator of the Max-Planck Institut für Kernphysik (MPI-K) at Heidelberg, Germany. Only ferrous dust particles of a size between 10^{-9} g and 10^{-15} g were used as projectiles, and shot onto different positions of the sensor box of the three available units of the MDC (Prototype, Flight Model 1 and Flight Model 2) at a speed range of 1.2 km/sec to 60 km/sec. Altogether 3713 good impact signals were used for the MDC calibration. Mass and speed range of the calibration particles is shown in Figure 3-19. Calibration of the MDC-NOZOMI in the low speed and high mass range in the plasma-dynamic accelerator at the LRT was not possible due to the strong light flash produced by this accelerator, which caused massive interference in the MDC sensor box and prevents the MDC from recording a good impact signal.

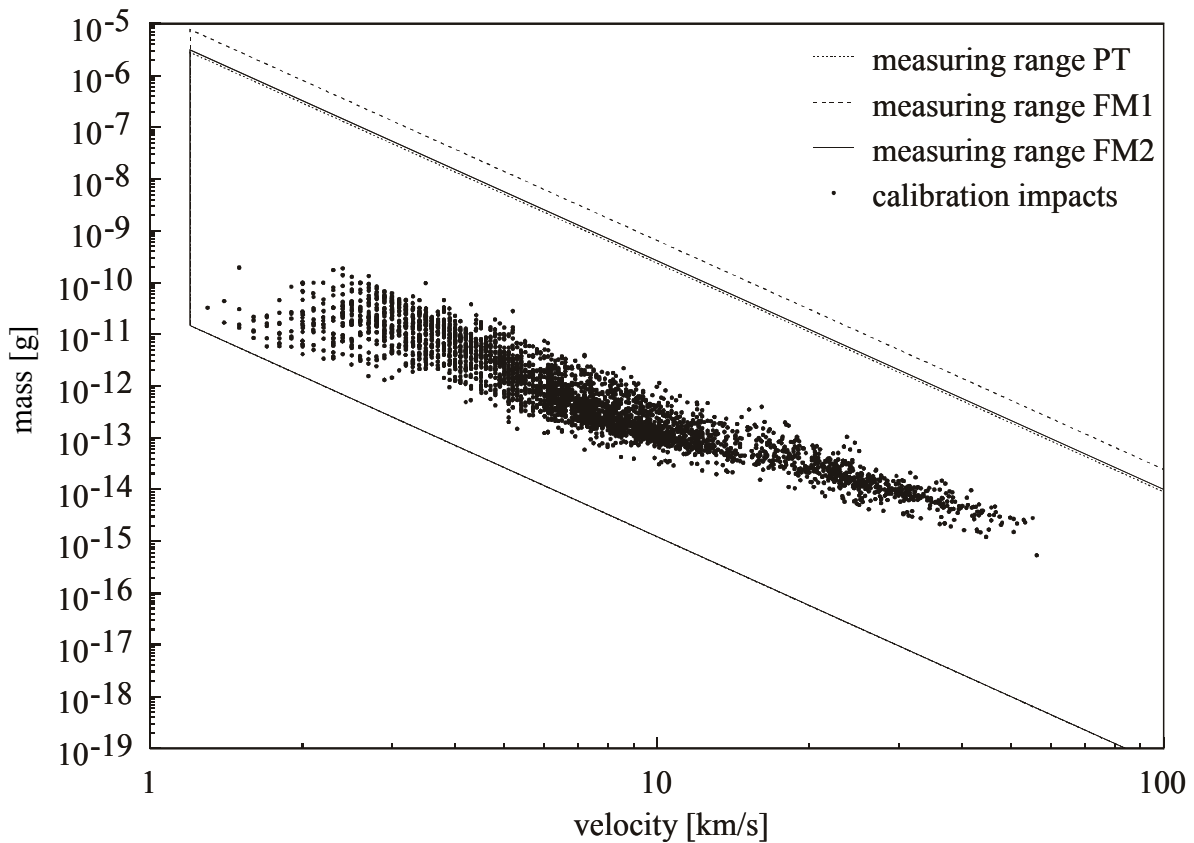


Figure 3-19: Calibration impacts

Particle mass vs. impact speed of the about 3713 calibration shots. All calibration particles have mass and speed within the boundaries of the measuring range of the three MDC models. PT = Prototype, FM1 = Flight Model 1, FM2 = Flight Model 2.

During calibration, particles were shot onto 51 positions inside the sensor box and outside the box on the satellite's MLI (Multi Layer Insulation). These positions are shown in Figure 3-20. The MDC sensor box was divided into 6 areas inside and 2 areas outside the box. From the 3713 calibration signals, the parameter sets needed for the determination of particle mass and impact speed were determined for each of these areas individually (see next paragraph for a description of the parameter sets and the determination of particle mass and impact speed).

MDC-HITEN calibration was also carried out at the Max-Planck Institut für Kernphysik (MPI-K) at Heidelberg, Germany, and is described by Münzenmayer [Mün1997].

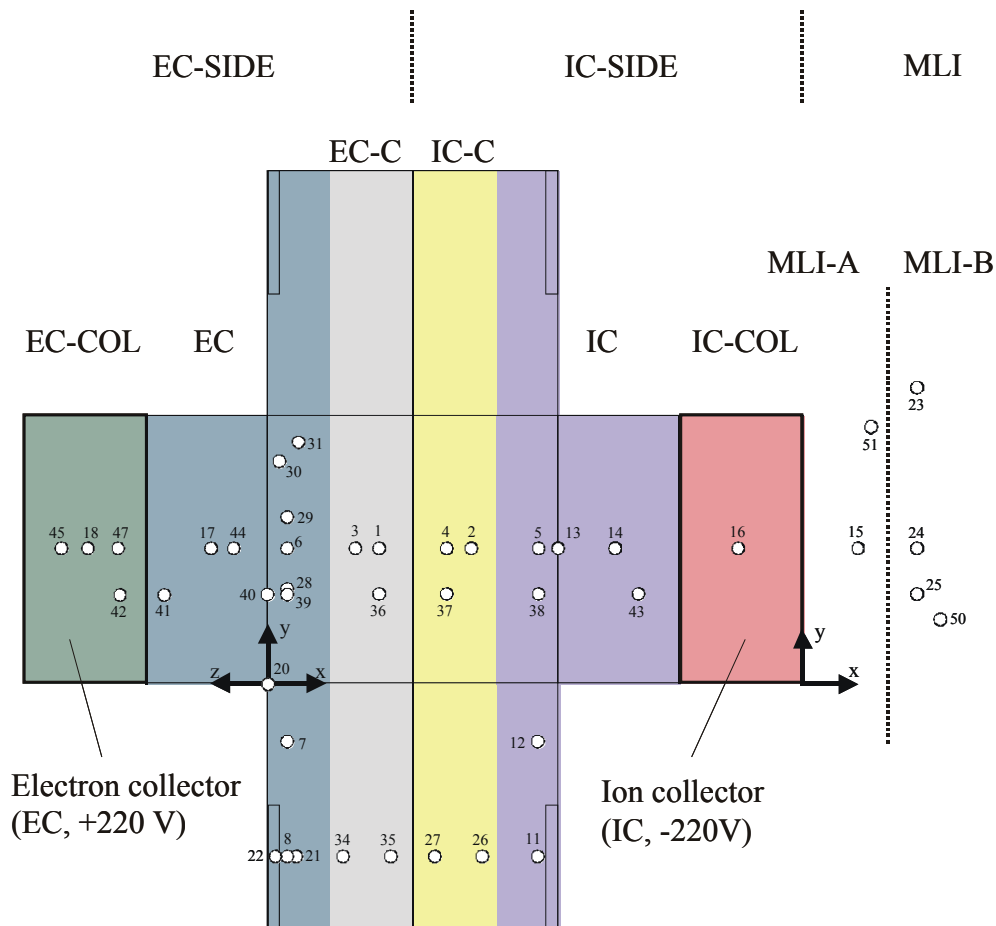


Figure 3-20: Impact positions inside the sensor box

During calibration, particles were shot onto 51 positions inside the sensor box (positions 48 and 49 (MLI-B) not shown in this graph). The sensor box was divided into 6 different areas, EC-COL, EC-C, EC, IC, IC-C and IC-COL, impacts outside the sensor on the areas MLI-A and MLI-B box were also calibrated.

3.3.2 Data analysis

The analysis of the downloaded impact signals was carried out on ground with the MDC data analysis software as described by Naumann. Data analysis is carried out in four subsequent steps:

1. Qualification, the selection of impact signals from the total amount of MDC signals
2. Classification, determination of the impact position inside or outside the sensor box
3. Curve analysis, determination of rise time and amplitude of the impact signal
4. Determination of particle mass and impact speed from the signal's rise time, charge amplitude and impact position

Step one is carried out manually by the experimenter (see chapter 4 for a discussion of methods that can be used for automation). Once a signal is qualified as an impact signal rather

than noise, its impact position must be determined in step two of the analysis process. This is currently done by a routine that compares the new signal that has to be classified with all 3713 calibration signals, whose impact position is known. The impact position of the calibration signal with the highest similarity to the new signal is then taken as the impact position of the new signal. Knowledge of the impact position is required for the later determination of particle mass and impact speed, as the correct parameter set has to be chosen.

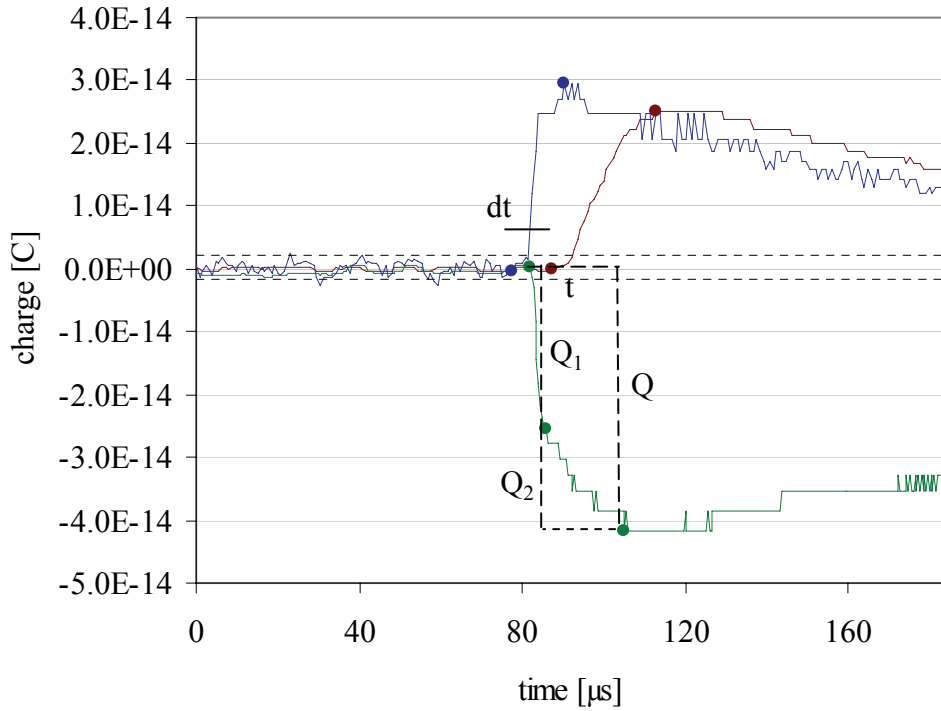


Figure 3-21: Typical calibration signal with characteristic points

In this figure a typical impact signal and its characteristic values rise time t , charge Q , primary and secondary charge Q_1 and Q_2 (all from the electron channel, green curve) and time delay dt between neutral channel and ion channel (red and blue curves) are displayed.

In step three of the analysis process, rise time and the charge amplitudes of primary and secondary charge (if available) are determined from the signal shape for each individual channel. From the characteristics of hypervelocity impacts and the MDC sensor box characteristics, impact speed v and particle mass m are determined in step four by the following equations:

$$\left. \begin{aligned} v^{ch} &= C_t^{ch} t^{\eta^{ch}} \\ v^{ch1,ch2} &= C_{dt}^{ch1,ch2} dt^{\kappa^{ch1,ch2}} \\ v^{EC} &= C_{12}^{EC} (Q_1 / Q_2)^{\delta^{ch}} \end{aligned} \right\} v_{mean}; \quad ch = IC, EC, NC \quad (3-22)$$

$$m_{ch} = \frac{Q^{ch}}{C_{\rho}^{ch} v_{mean}^{\beta^{ch}}} \Rightarrow m_{mean}$$

whereas v = impact speed and m = particle mass are the results of the calculation, $Q_{(1,2)}$ = charge, t = rise time, dt = time delay are the characteristic values determined from the signal shape, and C_i , η , C_{dt} , κ , C_{12} , δ , C_ρ , β are the parameters which are determined during calibration for each impact position (EC, EC_C, EC_COL, IC_COL, IC_C, IC, MLI-A, MLI-B). First, the impact speed is determined from the rise time t of each channel (top equation for impact speed v). Either all three values derived from the three channels can be used for the calculation of the mean value, or the experimenter can neglect uncertain values. For MLI impacts, the delay time of the beginning of signal rise of two different channels can be used for impact speed determination (middle equation for impact speed v). For impacts inside the sensor box, the ratio of primary to secondary charge of the electron channel EC can be used for impact speed determination (bottom equation for impact speed v). Once a mean value v_{mean} of the impact speed is determined, the particle mass m can be determined for each channel individually from the total charge Q of the channel, from these up to three values the final mean value m_{mean} is calculated.

According to Naumann, impact speed v and particle mass m can be determined by this analysis process with an accuracy of a factor of 2 and 5, respectively.

4 Signal screening

Any analog sensor device, especially nonlinear devices like the MDC, not only produces wanted signals but also random noise that must be separated from the final data. Several methods are used by the MDC electronics to perform this and are described in this chapter. In paragraph 4.2, a routine used by the MDC onboard software to qualify all new-recorded signals and an upgrade that enables much better separation of noise data from impact data is described. In paragraph 4.3, a new method that enables even better separation of noise data based on artificial neural networks is described and evaluated.

4.1 Basics and motivation

The overall ratio of real impact signals in the downloaded MDC data files was lower than 1% for the whole MDC-NOZOMI mission. This has two main disadvantages for the operation of the MDC. First, the high amount of noise data must be downloaded to the Earth to be processed further, which requires large resources of the limited telemetry capacities of the NOZOMI spacecraft. Second, for a further analysis of impact data, all downloaded noise data must be separated from the impact data by manual signal screening by the experimenter. An automated identification of noise signals onboard the MDC would therefore disburden the NOZOMI telemetry as well as the human experimenter on ground. The MDC electronics and onboard software already provide some methods that reduce noise data or can be used for a further reduction of noise data. An optimization of one of these methods that enables significant reduction of noise data downloaded to the Earth is described in this chapter. On ground, with much more computing power available, a further automated screening of the remaining data becomes possible that disburdens the experimenter from browsing thousands of signals.

4.2 Improvement of the onboard qualification

The MDC electronics provides two methods that reduce noise and one method that can be used for further selection of real impact signals.

First, any signal must exceed a certain trigger level to be recorded by the MDC electronics at all. The implementation of such a trigger is necessary to protect the MDC electronics from overload, otherwise every interference would be recorded and stored by the MDC and would cause overload of the limited computing capacity. The level to which this trigger has to be set must be selected carefully. A very low trigger ensures that even small real signals can be recorded and analyzed, but with the price of high noise ratio. On the other hand, a high trigger level would give a low noise ratio, but would also prevent the sensor from recording of small real impact signals. Therefore, a compromise must be found.

The second method performed by the MDC to select real impacts from noise is a very crude analysis of any new-recorded signals, the so called KO-criteria, see Naumann [Nau2000] for

details. A fast and straightforward analysis of certain criteria that have to be fulfilled by a signal is performed right after triggering and recording. If the signal fails these criteria, it is assumed to be noise and discarded.

A much more sophisticated method to analyze new signals is performed by the qualification routine described in this chapter. The qualification routine performs a more detailed analysis of recorded signals and as a result provides them with a numerical value, the quality key, which describes the quality of the signal, or the probability that it represents real data, respectively. The qualification routine takes about three seconds to run for every new signal; hence, the signals that have to be processed by this routine must be pre-selected by the other two methods, trigger and KO-criteria. In the basic version of the MDC, the quality keys are only used to determine the memory segment that will be overwritten if a new signal is recorded and no unused memory segment is available for storage. The new signal will then be stored in the memory segment that holds the signal with the lowest quality key. It would be a great benefit if a certain minimum quality key can be defined which separates noise from real impacts without losing any real impact signal but rejecting a high number of noise signals. This is discussed in the following paragraph. References for this paragraph are the monographies from Mitchell [Mit1998] and Heistermann [Hei1994] and the thesis work from Kyritsis [Kyr2003].

4.2.1 The qualification routine

In a first step, the qualification routine calculates a set of 7 criteria $v_{j,ch}$ for each channel $ch = IC, EC, NC, j = 0 \dots 6$ ($max, \mu_{pre}, \mu_{post}, \Delta\mu, \Delta max; s_c, \Delta t_n; m_c, \Delta t_i$, see Fischer [Fis1998] for a detailed description of these values) that represent some characteristics of the signal shape, e.g. difference of mean pre trigger and mean post trigger value, maximum post trigger value etc. Out of these 21 values, a weighted sum qu (the quality number) is calculated using the 21 qualification parameter set values $p_{j,ch}$, as follows (simplified):

$$qu_{ch} = \sum_{j=0}^6 p_{j,ch} \cdot v_{j,ch}; \quad ch = IC, EC, NC \quad (4-1)$$

$$qu = qu_{IC} + qu_{EC} + qu_{NC}$$

The original parameter set $p_{j,ch}$ used for the calculation of the quality key qu was determined by guess from the calibration impacts to give the higher values the better the signal is. It is obvious that this determination method of the qualification parameter set can only be a first pre-flight estimation since no optimization was performed and no information about the shape of noise signals was available, of course. Therefore, it can be expected that a systematic optimization of the qualification parameter set could improve the capabilities of selection of signals by the quality key as described above. Now, enough real impacts and noise signals are available to look on the qualification parameter set.

The intention is to find a parameter set that produces quality keys that separate real impact signals from noise signals in the best possible manner. This would allow the definition of a certain quality key threshold that determines the minimum quality key value a signal must

have to be kept in memory and/or downloaded. All signals with quality keys below that threshold value are discarded or marked as free segments that can be overwritten, respectively.

The current parameter set does not allow an effective selection by the definition of a threshold value. The threshold value must be chosen in a manner that only a minimum of real impact signals with low quality number gets lost and a maximum number of noise signals can be discarded. Since the quality keys of real impacts and noise signals overlap in a very wide range, a threshold value would allow only about half of the noise signals to be discarded. An optimized parameter set will give a minimal overlap of quality keys.

Since there are 21 parameters $p_{j,ch}$ that are used for the quality key calculation, the optimal parameter set cannot be determined analytical at all. Other sophisticated methods are available and can be used to determine at least a local optimum of the parameter set concerning the intended results, e.g. genetic algorithms or simulated annealing. For the optimization of the qualification parameter set, genetic algorithms are used.

4.2.2 Genetic algorithms

The main problem finding the optimum of a function in a high dimensional space is that any straight forward method would require a huge amount of computing time, in certain cases this time could exceed the age of the universe even when using today's fastest available computers. For the MDC qualification routine, 21 parameters with a range of 150 give $150^{21}=5 \cdot 10^{45}$ possible different parameter sets that had to be tested; the age of the universe is $4.5 \cdot 10^{17}$ seconds. Genetic algorithms (also called evolutionary algorithms) provide a method for the determination of an at least local optimum which comes close to the then still unknown global optimum.

In biological science, evolution is understood as the process of formation of different species and their optimization with respect to their given environment. This process is characterized by recombination, mutation and selection. Each individual carries a set of attributes (the genes) that determines the individual's performance in its environment (e.g. its capability to compete with other species about a limited environmental resource like food, its ability to escape or hide from predators, and its performance in reproduction). The optimization of the species' performance is coupled to the optimization of the genetic code of its individuals (its genotype). Recombination of the genetic code of two different individuals produces new child individuals with a different performance that is close to that of its parents, while random mutation allows larger, random changes in genetic code and performance and may open up new biological niches that can be occupied by the new branch of the species. Most important for a target-oriented evolution process is the selection of high-performance individuals as preferred parents for new child generations. In nature, this selection process is carried out by the environment of the species itself, which gives high-performance individuals a slightly better chance to reproduce than low performance individuals. From generation to generation, the adaptation of the species to the properties of the given environment increases.

Genetic algorithms are based on similar principles. The genes of an individual are identified with numerical a set of parameters whose performance has to be optimized with respect to a performance goal that has to be reached by the optimization process. Starting with a

population of individuals with random (or guessed) numerical sets of parameters, the performance (normally one numerical value) of each of these different individuals is determined with respect to the goal by a defined objective function. A set of high-performance individuals is then selected from the population by a selection function or operator (e.g. take only the best 10% of individuals). These selected individuals become the parents of the next generation; each member of this new child generation gets new parameter sets (or genes) that are combinations of the parameter sets of two individuals from the parental generation; a previously defined recombination operator defines the method of recombination (e.g. crossing over, a strategy where a random number of parameters are swapped between the two parents). In this stage, random mutation can be performed with a defined, but low probability to allow larger jumps in genotype. After the new generation is created, the genetic iteration process continues with testing the performance of the individuals and selecting the new parents for the next generation and so on. The optimization process continues until a predefined performance goal is reached or no significant improvement of performance can be achieved for a defined number of generations. Several different strategies of recombination, mutation, selection were described in literature, see Heistermann [Hei1994] for a discussion.

4.2.3 Optimization of the qualification parameter set

The optimization of the quality routine parameters was implemented in *MATLAB*[®]. The quality key routine was rebuilt in *MATLAB*[®] to compute the quality keys for any given parameter set. The input values (max , μ_{pre} , μ_{post} , $\Delta\mu$, Δmax ; s_c , Δt_n ; m_c , Δt_i) were determined once from the whole set of ≈ 20000 signals. The optimization run was carried out as described in the following.

At first, a set of set of reference impact signals was defined that was required for the determination of the performance of the different qualification parameter sets. This reference set was built from the previously identified real impact signals from the reviewed 1998 data, plus the already identified real impact signals of the 1999 and later data, and thus represents a minimum set of wanted signals that must be identified as possible impact signals from the optimized qualification routine.

A simple, self-developed genetic algorithm was used for optimization of the quality routine parameter set. The 21 individual values of the parameter set $p_{j,ch}$ are the “genes” of the individual parameter set, which determine its “performance”, that means, the capability of the individual parameter set for separation of noise signals from impact signals. To determine this performance, the quality numbers of the whole available MDC data (noise and possible impact signals) were calculated by the qualification routine using the parameter set to be tested. From the obtained list of quality numbers, a threshold value Q was set to the 4th but smallest quality key of the set of reference signals, to ensure that only a minimum number (four) of reference signals get lost by the separation. All signals with a higher quality key than this threshold value are then identified as possible impact signals. The performance of the given parameter set was determined as the ratio of the number of reference impact signals having quality key higher than the threshold value to the full number of signals passing the threshold value, $r_{imp} = (\text{No. of reference signals with quality} > Q) / (\text{No. of all signals with quality} > Q)$. A performance value of $r_{imp} = 0.25$ therefore means that 25% of all signals

passing the threshold value are reference impact signals, while the rest is noise. The higher the value of r_{imp} , the better the performance of the given parameter set is.

The optimization of the qualification routine parameter set was then carried out as follows. Starting with a single parameter set (the original one or a random one) a fixed number of $n = 1000$ initial parental parameter sets was created by mutation only (random variation of the parent's parameter set). Now the optimization routine entered an endless loop. First, the performance of the individual parameter sets was tested (the values r_{imp} were calculated), and the members of the population were sorted according to their performance r_{imp} . The worst 50% of parameter sets was then discarded from this generation. From the remaining members of this parental generation, an equal number of child parameter sets was created by combination of the parameters $p_{j,ch}$ (the "genes") of two randomly selected members of the parental generation in each case. The random selection of the two parents was designed to give parameter sets with high performance a greater chance to recombine than those with low performance. Recombination of parameters was carried out by building a new value from the two corresponding single parameters that was lying preferably closer to the value of one of its parents. Next, child and parental parameter sets were merged and used as new parental generation. This process was iterated until new generations did not show any more improvement in performance, Figure 4-1 shows the development of the performance r_{imp} of the best parameter set for each generation over the iteration process. The parameter set with the highest achieved value of r_{imp} was then chosen as the optimum parameter set. Since in most cases this optimum is one of a number of local optimums rather than the one and only global optimum, and may vary depending on the first parent used, this optimization must be performed several times using different random parent parameter sets.

The optimization process can be summarized as follows:

1. Create an initial parental generation of size $n = 1000$ from the single starting parameter set by mutation only
2. Calculate the performance r_{imp} of each member of the parental generation
3. Sort parental generation according to performance r_{imp}
4. Discard the worst 50% of parameter sets
5. Create child generation of equal size from the members of the remaining parental generation by recombination and mutation of the parental parameter sets
6. Merge parental and child generation
7. Proceed with step 2., with the merged population as new parental generation

No fixed stop criterion was defined, the iteration was stopped by the experimenter after no further increase in performance r_{imp} of the best parameter set of each generation could be observed over a number of generations.

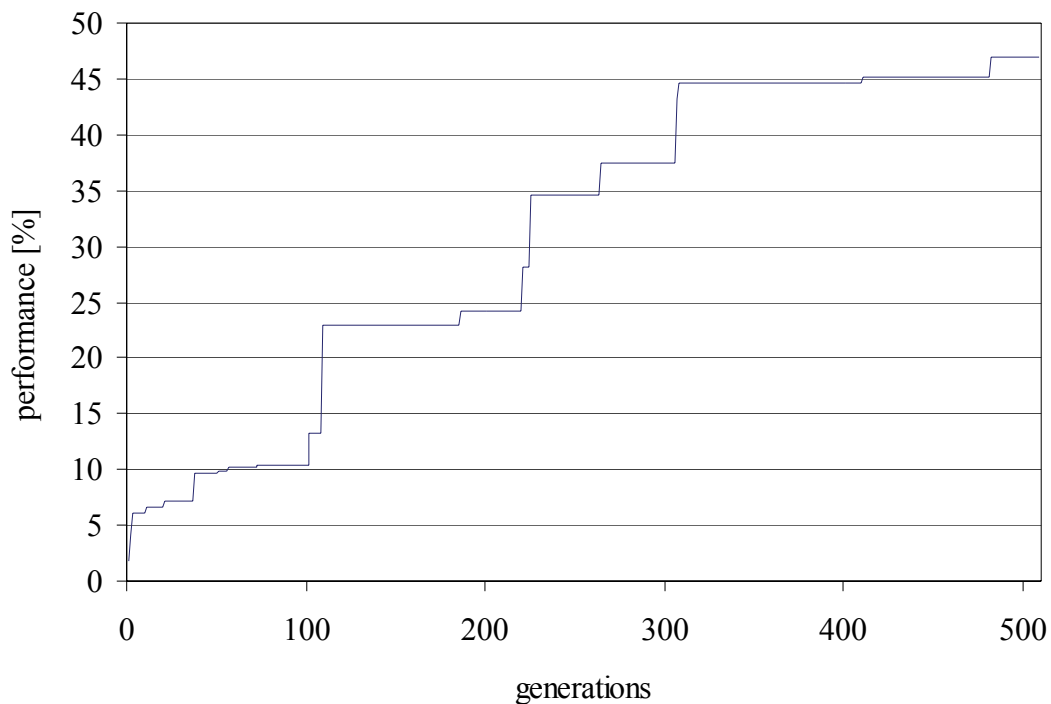


Figure 4-1: Evolution of the performance r_{imp} of the parameter sets.

Starting with the original parameter set with a performance of 3.51%, the performance rises with increasing generations. The experimenter stopped the optimization after 500 generations; achieved performance was 46.9%.

The results are shown in Figure 4-2 and Figure 4-3. The quality numbers of the full available MDC data were calculated from the original parameter set and from the best one found by the optimization routine. The frequency of these quality numbers is displayed over the full range, black bars represent reference signals, grey bars other signals. A threshold value was defined so that the four reference impact signals with the lowest quality key are rejected. The value p_Q defines the ratio of signals that pass the threshold, while the value r_{imp} defines the ratio of real impact signals in the set of signals that have passed.

Figure 4-2 shows the result of the original quality routine parameter set. A threshold value set at $Q = 102$ separates 87% of noise data from the whole set of data while $p_q = 13\%$ pass. The ratio of real impact signals in the set of passed signals is $r_{imp} = 3.51\%$.

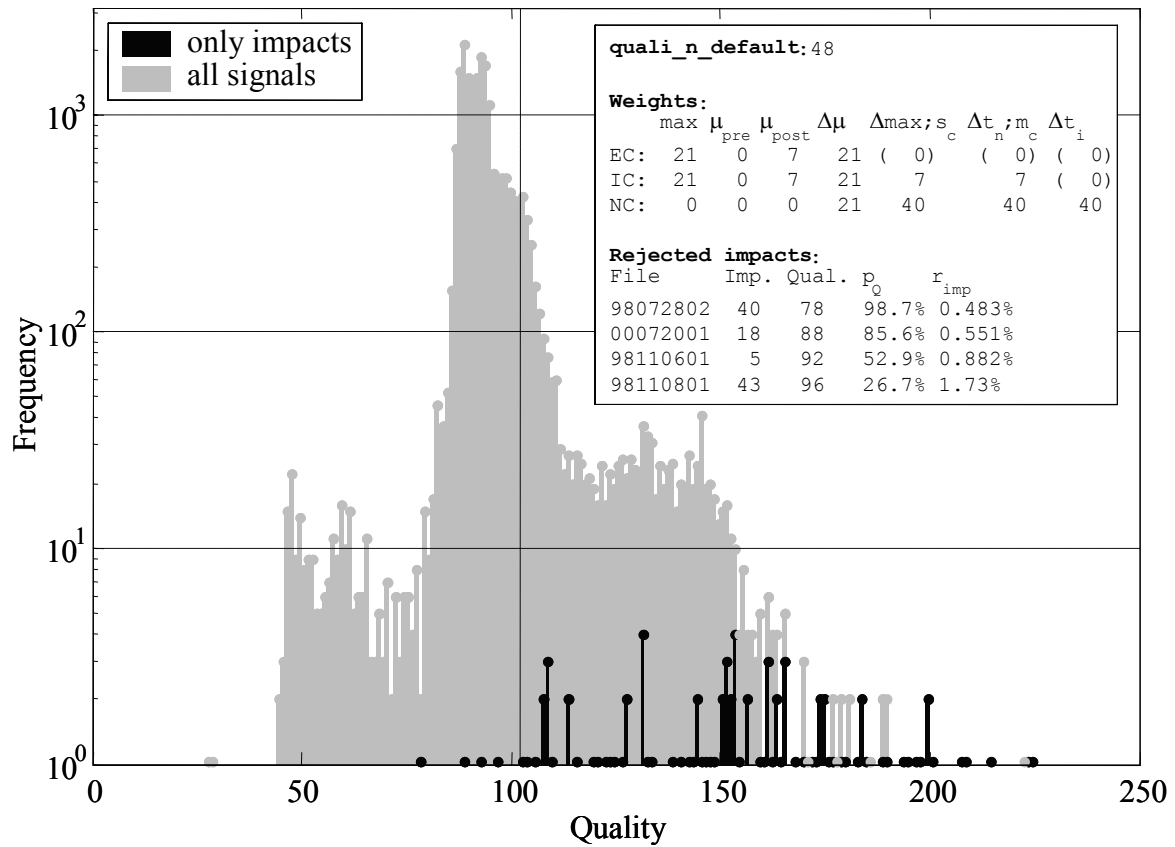


Figure 4-2: Separation capabilities of the original parameter set

Using the original parameter set for qualification, and a quality threshold of $Q=102$, $p_Q = 13\%$ of all signals pass the threshold; the impact ratio within the signals with $Q > 102$ is $r_{imp} = 3.51\%$.

The improvement that can be achieved by optimization of the quality routine parameter set is shown in Figure 4-3. Given a threshold value of $Q = 117$, only $p_Q = 0.903\%$ of signals pass the threshold, and the ratio of real impact signals in this set of data rises to $r_{imp} = 50.5\%$.

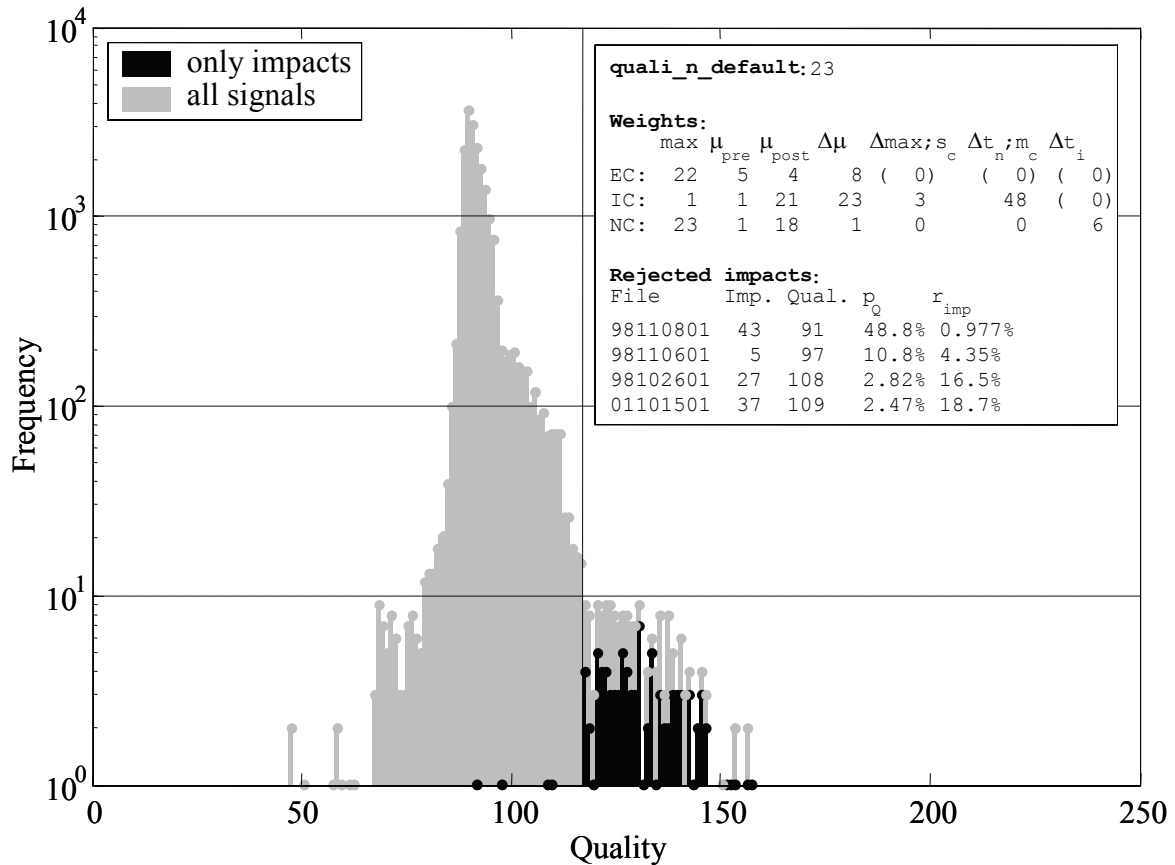


Figure 4-3: Separation capabilities of the best resulting parameter set
 Using the original parameter set for qualification, and a quality threshold of $Q=117$, only $p_Q = 0.9\%$ of all signals pass the threshold; the impact ratio within the signals with $Q > 117$ is $r_{imp} = 50.5\%$.

Thus, a great reduction of the overall amount of data can be achieved by determining and uploading an optimized set of quality routine parameters. The results are summarized in Table 4-1.

Table 4-1: Results of the optimization of the quality routine parameter set

Parameter set	p_Q	r_{imp}	reduction factor
Original	13%	3.51%	≈ 7.5
Best guess	0.903%	50.5%	≈ 110

In summary, an optimized quality routine parameter set could give a reduction of the amount of data to be downloaded to Earth by a factor of about 100. To benefit from these capabilities, a modification of the memory readout routine must be implemented that finally carries out the separation by skipping all signals with quality numbers lower than the threshold. Even without a further modification of the memory readout routine, a reduction of data can be achieved by simply performing less frequent memory readouts. As described in paragraph 3.2.2, new-recorded signals are stored in the memory segment with the lowest quality key. A parameter set with good separation capabilities therefore gives much more security that real impact signals will not be overwritten during long periods where no readout is performed.

4.3 Signal screening by neural networks

The following method of signal screening cannot be performed onboard the current MDC model since it requires more computing power and memory, but can be used in future models' onboard software or on ground to unburden the experimenter from time consuming work. A selection of signals from noise by an artificial neural network was implemented and tested. For long missions like the MDC, this would reduce the time consuming and troublesome selection of impact signals from a huge amount of (mostly noise) data by the experimenter and would enable some kind of automation of the whole data analysis process.

The first intention was to develop a method that is able to sort out real impact signals from noise signals automatically to create a basis for further automation of the whole data analysis process. Additionally, the experimenter can be unburdened from browsing several thousands of signals by hand, as it was necessary during the first year of the mission and would have been necessary if NOZOMI will enter Mars orbit with its full functionality. Finally, neural networks can replace the routines used in the MDC onboard software data processing in future experiments, when more computing power may be available.

References for the following paragraphs are the monographies from Scherer [Sch1997] and Zell [Zel1994], and the thesis work from Glas [Gla2003].

4.3.1 History and basics

First introduced in 1943 as a mathematical model that is able to solve any logical and arithmetical problem, neural networks soon caused a hype in mathematical science. After a backstroke in 1969, when an article challenged in principle their logical skills, neural networks became more popular again in the mid 1980s when computing power became broadly available and cheap. New techniques were developed and new fields of application were opened up. Today neural networks are used in a wide field of applications such as simulation of biological nervous systems, parallel information processing, control techniques, and pattern recognition. The latter application of neural networks is used here to create a procedure that recognizes real impact signals and separates them from noise signals produced by the MDC sensor device. Another possible application of neural networks could be a cluster analysis performed on the mass of noise signals to filter out certain patterns of reproducible noise signals that were recognized in the MDC data stream, see also paragraph 6.2.1.

In principle, neural networks consist out of a set of simple mathematical units, called neurons, which are interconnected in a special way. In these terms, the mathematical neural network corresponds to the biological nervous system that consists out of comparatively simple units (the cells) that are interconnected to a quite complex network, which shows much more abilities than the sum of the basic units does. The intelligence, or the mathematical and logical abilities, respectively, is represented in the connections between the neurons. The overall "shape" of a neural network, e.g. the number of neurons and the pattern of interconnection, is called the topology of the neural network. Neural networks are characterized by learning aptitude, parallelism, robustness and fault tolerance.

4.3.2 Components and functionality of neural networks

A neural network like the one used here for pattern recognition can be seen as a system (a “black box”) that is presented a certain pattern as input and, after processing the presented information, creates an output that is identified as the networks answer. The number of input parameters as well as the number of possible answers strongly depends on the problem that has to be solved with the help of the neural network.

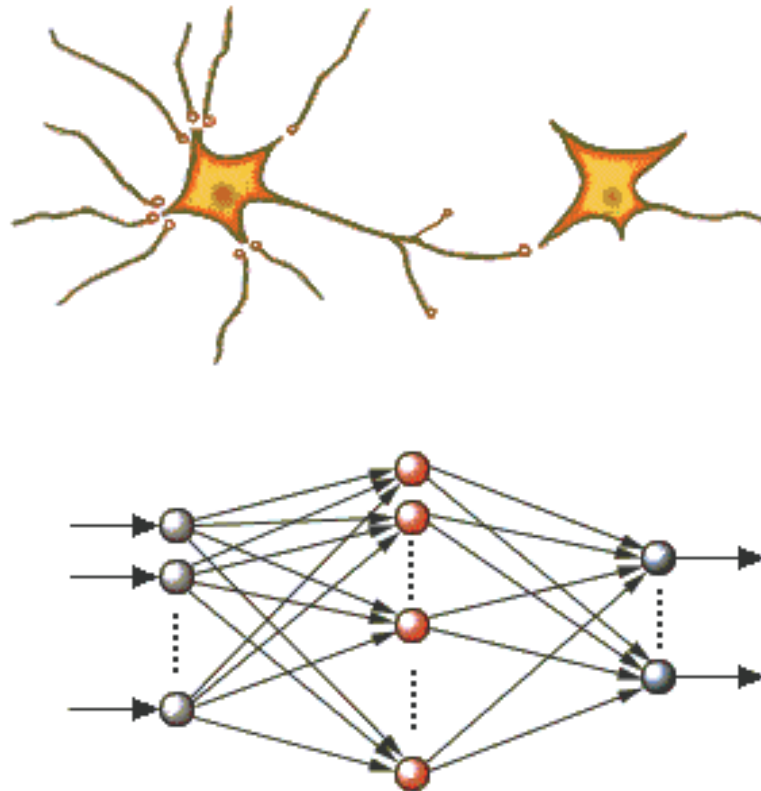


Figure 4-4: Biological and artificial neurons and related networks

The basic topology of biological neural networks (brains etc., top image) and artificial neural networks (bottom image) is very similar. Every neuron gets input from a number of other neurons, and creates one single output. The output is determined from the input, the network’s knowledge and the current state of the neuron by rules that are implemented as functions inside every neuron. In artificial neural networks, the network’s knowledge is represented in weights of the connections. These initially random weights have to be adjusted during the training of the neural network.

Here, the artificial neural network ought to be used to distinguish real impact signals from noise signals. Therefore, the input parameters must represent the overall characteristics of the signal in a unique way. To optimize the performance of the pattern recognition process, it is recommended to minimize the number of input parameters and avoid any redundancies. The desired output for the given problem reduces to a simple “yes/no” answer, either the presented signal is identified as a real impact signal or not.

The neuron itself is represented as a quite simple mathematical unit. In principle, the neurons can be seen as local processing units that create one certain output from a random number of inputs. The inputs can either be identical with the input of the neural network itself (the neuron then belongs to the “input layer”) or may be output from other neurons. The output of a certain neuron can already be part of the neural network’s answer (the neuron then belongs to the “output layer”) or become input of other neurons. If the neuron is connected to other neurons on the input and on the output side, it belongs to a “hidden layer” that has no connections to the outside of the network. Commonly, all neurons are combined in certain layers. Every network consist of one input layer, one or more (or, for simple applications, even no) hidden layers and one output layer. If the connections are directed and always point from one certain layer to the following one, the network is called a “feed forward” network.

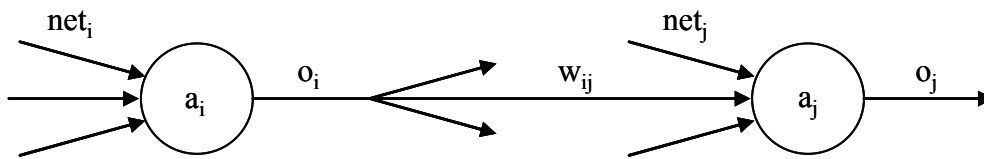


Figure 4-5: Input, attributes and output of neurons.
Attributes of single neurons (see text for details) and weight matrix w_{ij}

Any neuron holds the following attributes:

Propagation function net_j that represents the neurons input and is buildt from the output o_i of the previous neutrons and the weight matrix w_{ij}

$$net_j(t) = \sum_i o_i(t)w_{ij} . \quad (4-2)$$

Activation state a_j at time t

$$a_j(t) \in R . \quad (4-3)$$

Activation function f_{act} that determines the new activation state $a_j(t+1)$ from the input net_j

$$a_j(t+1) = f_{act}(a_j(t), net_j(t)) . \quad (4-4)$$

Output function f_{out} that determines the neurons output o_j from its new activation state a_j

$$o_j(t+1) = f_{out}(a_j(t+1)) . \quad (4-5)$$

For neurons on the input layer, the input net_j consist of a single input value from the pattern that is presented to the neural network for classification. The output o_j of neurons in the output layer is one single value of the networks answer.

Every connection inside the neural network holds a certain “weight” w_{ij} , the weights of the connection structure are represented by the weight matrix \mathbf{W} . This weight matrix represents the “knowledge” of the neural network and must be determined by initial training of the neural network. The training procedure strongly determines the later capabilities of the neural

network. Initially, all weights are set to random values and the network does not hold any kind of specific knowledge. The training itself is performed by presenting the network a set of training data that consists out of a representative part of the possible input data, and adjusting the weight matrix depending on the answers that are given by the untrained neural network. The adjustment of the weights is depending on the learning strategy used.

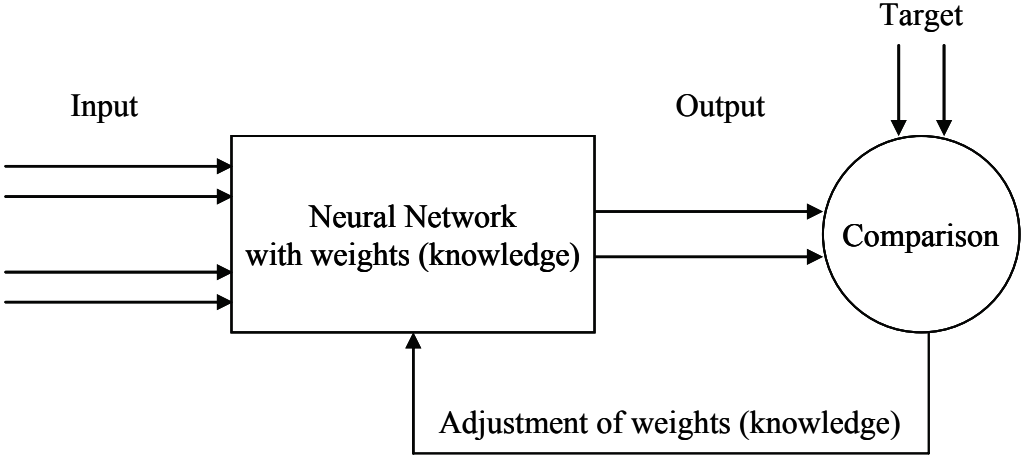


Figure 4-6: Illustration of the basic learning strategy

The training of a network is carried out iteratively by presenting the network a known input, comparing the network’s output to the target (the true answer) and adjusting the weight factors (the knowledge) of the network depending on the difference of the output and the target.

Different kinds of learning strategies were developed and are described in literature. During the learning process of a neural network, the weight matrix w_{ij} must be adjusted to increase the networks ability for giving correct answers. Most strategies are based on the general strategy introduced by Hebb in 1949:

$$\Delta w_{ij} = \eta h(o_i, w_{ij}) g(o_j, t_j) \tag{4-6}$$

whereas Δw_{ij} is the change that is applied to the certain weight w_{ij} . The value t_j is the target output value that is expected from the neuron, while the value o_j is the actual output value. The functions g and h and the parameter η determine the correction factor Δw_{ij} from the difference $g()$ between target and actual output and the relation $h()$ of the output value to the actual weight w_{ij} , and differ depending on the specific learning strategy.

Networks that contain hidden layers require more sophisticated training methods. Since the teaching input can only be applied to the output layer because no teaching input is available for neurons in hidden layers, a rule must be defined to propagate this teaching input from the output layer back to the hidden layers. This strategy is called “back propagation” and is based on the following rules:

$$\Delta w_{ij} = \eta o_i \delta_j \tag{4-7}$$

whereas

$$\delta_j = \begin{cases} f_j'(net_j)(t_j - o_j) & j \text{ is an output neuron} \\ f_j'(net_j) \sum_k (\delta_k w_{jk}) & j \text{ is a hidden neuron} \end{cases} \quad (4-8)$$

The function $f_j'()$ is an analogon to the activation function. With this strategy, the teaching input is back propagated through the network and an adjustment of all weights w_{ij} in the network becomes possible.

4.3.3 Implementation

The neural network that shall be implemented and tested for the classification of the MDC data must meet the following requirements:

- All segments that contain real impact signals must be recognized
- The number of segments that are falsely identified as real impacts should be minimal
- The network itself should be as slim as possible
- The number of input parameters should be as small as possible

The parameters of the neural network, namely number of input parameters, size of the network (number of neurons and hidden layers) and the teaching algorithm, are confined by the structure of the problem, but not defined strictly. Only the number of output neurons is fixed to two since the desired answer is a simple yes/no decision. The other parameters are subject to optimization that was performed by implementing different possible networks and evaluating their classification capabilities.

The answer of the neural network is read from the activation of the two output neurons a_1 and a_2 after a certain input was presented to the networks input layer. A signal is classified as a real impact signal if the activation of neuron 2 (a_2) succeeds the activation of neuron 1 (a_1)

As input parameters, the signal itself or the whole set of digitized data, respectively, was not concerned as a practical approach since that would require more than 800 input neurons and lead to a very huge neural network. Instead, a set of 56 parameters that represent the characteristics of the signal was used as input parameters. These parameters include a reduced set of data points, calculated parameters like mean-pre-trigger or total amplitude of the signal, and environmental data.

In a first approach, the network was designed quite large, using all the 56 input parameters that describe the signal shape, two hidden layers with 14 and 12 neurons, respectively, and two output neurons (56x14x12x2). Although this network showed only a weak classification performance, it was used as a basis for the following optimizations.

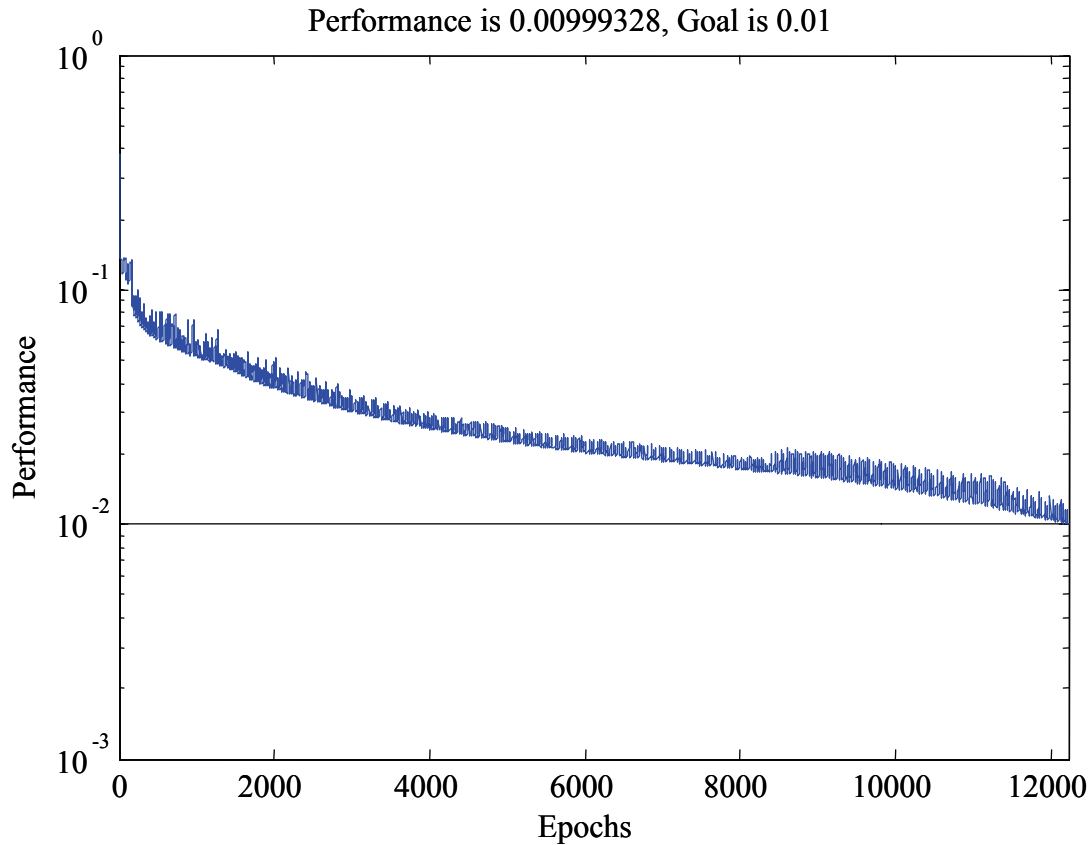


Figure 4-7: Training process of the neural network

This graph shows a typical training progression of a neural network containing two hidden layers with 15 and 11 neurons. Training goal of 0.01 (which means, an accuracy of higher than 99% in classification performance) was reached after 12225 epochs (training cycles).

4.3.4 Reduction of the input parameters

As mentioned before, the number of input parameters should be reduced to a minimum without losing classification performance. To carry out this reduction in a systematic way, the basic network described above was used to determine the significance of the input parameters. The numerical significance of each parameter can be calculated from the weight matrix of the trained network by the equation

$$f_{sig,i} = \begin{cases} \sum_j |w_{ij} f_{sig,j}| & j \text{ is a hidden neuron} \\ \sum_j |w_{ij}| & j \text{ is an output neuron} \end{cases} \quad (4-9)$$

It must be mentioned here that the significance of certain parameters differs widely for different instances of the network; therefore, the selection of parameters that are discarded must be carried out carefully. Also, parameters that represent the same characteristic value but are calculated from different channels do not show any correspondence in significance, as one

would expect. Finally, the input parameters were reduced to a set of the 16 most significant parameters.

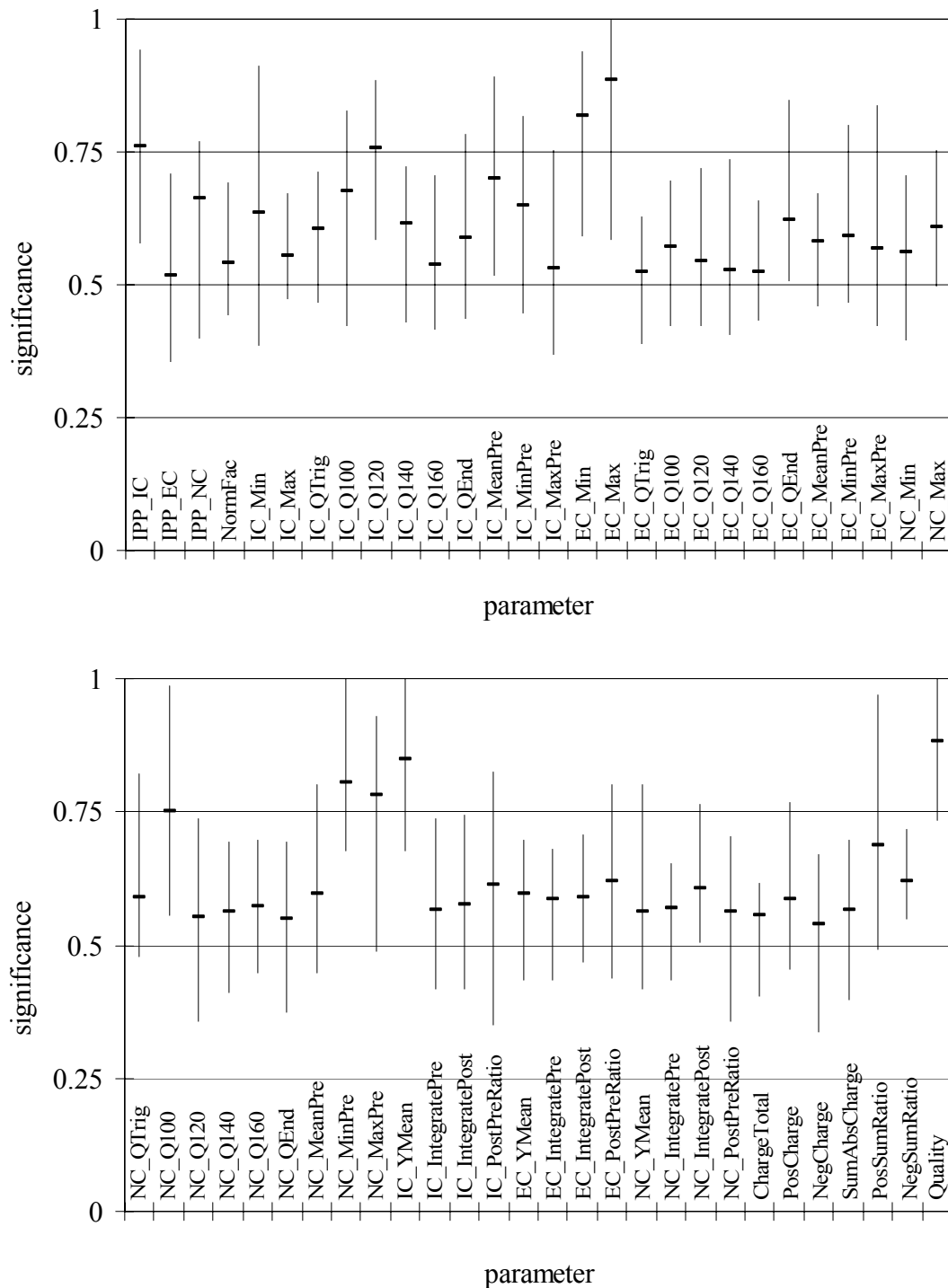


Figure 4-8: Significance of the input parameters

The significance of each input parameter calculated from the equation above is shown here. Values are mean values from 10 simulations; the bars represent the maximum and minimum value, respectively.

4.3.2. As the same network shows different performance for each new created instance, 5 runs for each topology were made to get a significant average. As reasonable topologies, networks with one hidden layer containing 3 to 17 neurons, and networks with 2 hidden layers containing 3/3 to 17/17 neurons were considered. Since the full test run of these configurations requires more than 24 hours on an average 800 MHz desktop PC, larger configurations were not considered as reasonable.

Table 4-2: Performance of neural networks with 1 HL

1st HL	PI mean	DI mean
6	261	2.8
11	265	2.4
17	269	1.2
10	272	1.6
5	275	3.2
8	279	2.6
14	285	0.6
16	289	0.8
7	300	1.4
13	302	1.6
15	317	1.6
9	319	0.6
12	327	2.0
4	361	1.2
3	368	1.6

1st HL = number of neurons in hidden layer,
 PI = Possible Impacts, DI = Dropped Impacts
 Mean values from 5 evaluation runs, PI rounded

Table 4-3: Performance of neural networks with 2 HL, best 15 topologies

1st HL	2nd HL	PI mean	DI mean
4	12	243	0.2
3	4	247	0.8
17	10	252	0.2
11	7	253	0.2
6	13	260	0.2
11	15	261	0.0
13	14	262	0.2
4	16	262	0.8
4	14	263	0.8
4	15	266	1.6
5	9	267	0.2
12	9	268	0.2
8	11	269	0.2
5	17	270	0.4
9	4	272	0.4

1st/2nd HL = number of neurons in 1st/2nd hidden layer,

PI = Possible Impacts, DI = Dropped Impacts

Mean values from 5 evaluation runs, PI rounded

The results are shown in Table 4-2 for networks with one hidden layer, and in Table 4-3 for networks with two hidden layers. An optimal neural network will identify a low number of signals as possible impacts for best noise reduction (parameter PI), but also drop a low number of real impacts (parameter DI). Figure 4-10 shows the network with the best configuration for networks with one hidden layer.

As can be seen, the optimal topology comes out as a network with two hidden layers containing 11 and 15 neurons in the hidden layers. This network identifies 261 of the more than 20000 signals as impacts and drops none of the (at this time) 120 possible impacts identified by the experimenter (real impacts were later reduced to 98 after reviewing the data).

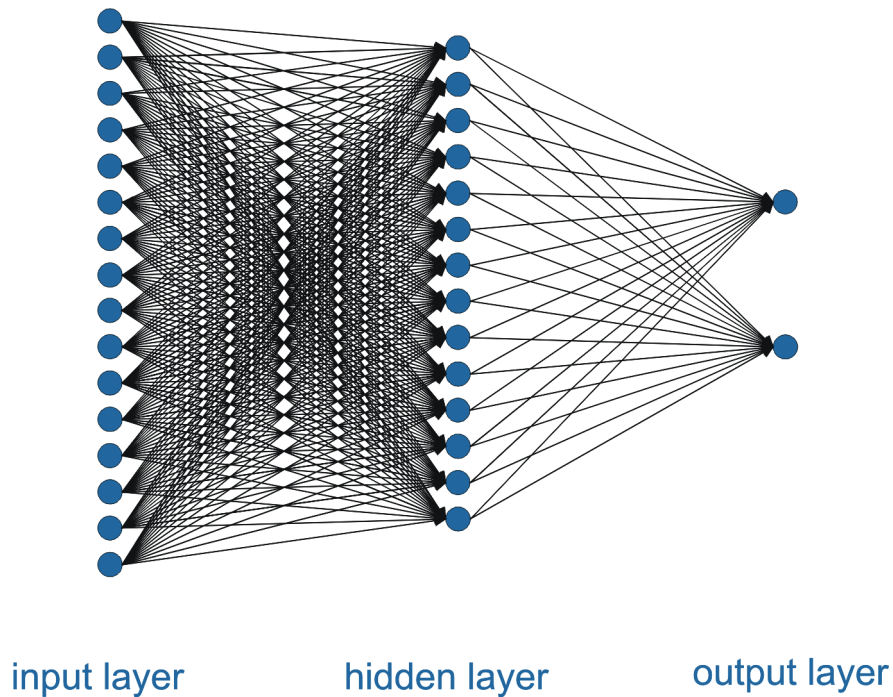


Figure 4-10: Final topology of the neural network with one hidden layer

The best topology of a neural network that is used for the classification of MDC signals is a network with 16 input neurons, one hidden layer containing 14 neurons and 2 output neurons.

4.3.6 Further potential applications

In this chapter, it was proven that neural networks are a powerful method for the classification of MDC signals. The classification efficiency (number of signals classified as possible impacts) of the neural networks described above is about in the same range as the classification capacity of the current qualification routine onboard the MDC (in case the new qualification parameter set is used), but neural networks show a much higher reliability with respect to the number of dropped impacts.

In this chapter, the neural network was used to recognize real impact signals in the MDC's data stream and separate them from unwanted noise signals. Further applications of neural networks on experiments like the MDC can be considered. The next step after identification of a real impact signal is the classification of the signal to determine the impact position inside the sensor box. Until now, this is done by a routine that simply compares the newly identified signal with several thousands of calibration signals with known impact positions, a method that requires much computing power and memory. A neural network that is designed and trained to determine the class of a new signal could reduce these expenses and even be implemented onboard a new designed experiment.

4.4 Summary and discussion

Intelligent pattern recognition methods like neural networks evaluated in this chapter provide a good alternative to the existing routine that is used by the MDC for the onboard identification of noise signals and the separation of wanted signals. Although it was shown that the existing onboard routine (the qualification routine) could achieve much better results in separating noise data from wanted data after optimization of the used parameter set, the artificial neural network showed even better performance. While the neural network reduces noise data to around 50% of the whole data without dropping a wanted signal erroneously, the qualification routine can only compete with this result by dropping at least three impact signals.

If NOZOMI was recovered from its system failure on April 24, 2002 and had finally reached Mars orbit, the new determined parameter set of the qualification routine would have enabled much longer time spans between MDC memory dumps without the risk of losing real impact signals due to overwriting. Therefore, telemetry time, which would have been a strictly limited resource on NOZOMI, could be saved.

An artificial neural network like the one described and evaluated in this chapter can be used in future instruments for an even better separation of noise data from wanted data.

Both methods require some kind of knowledge about the properties of wanted signals and noise signals prior to be deployed. While the properties of wanted signals that will be recorded in space can be estimated from the signals recorded during the calibration experiments, the properties of possible noise signals cannot be estimated prior to flight. Deployment of methods that discard unwanted noise signals without the possibility of intervention by the experimenter must be done with care. Training and optimization of the methods described in this chapter can be done during the first mission phase using recorded and downloaded noise and impact data as training data, until a satisfying level of pattern recognition capability of the instrument is reached. It is, however, essential that the experimenter can still trust in the data delivered by the experiment. An increasing level of experiment autonomy in separation of noise data means a decreasing knowledge of the experimenter about the discarded signals. If the environment of the spacecraft remains unaltered for a long period of time, and a high level of trust is achieved for the given environment, a high grade of autonomy can be accepted. Every alteration of the experiments environmental conditions (e.g. significant change of the spacecraft's orbit or even injection into a planetary orbit with a different dust environment and probably new sources of noise) needs a reconsideration of the level of autonomy granted to the experiment, and possibly intervention by the experimenter and new training of the experiments pattern recognition methods.

The possibilities of a full automation of the MDC data analysis process was discussed by Naumann [Nau2000]. It was shown that the further steps of the analysis process, which are the classification of an impact signal, the determination of the required signal characteristics (rise time, charge amplitude) and the final determination of particle mass and impact speed can be performed by an automated system with only a little loss of accuracy of the determined values of mass and impact speed. The biggest challenge in automation of the MDC (or a future similar) experiment is still the separation of noise signals from impact signals. While

possible errors in the further steps of the automated analysis process will produce deviations from the final values of particle mass and impact speed that are within the overall accuracy of the MDC experiment as shown by Naumann, a wrong qualification of noise signals as impact signals will falsify the overall results of the whole mission in an unacceptable manner. The good results of signal qualification by a simple artificial neural network as it was shown above are a basis for further investigation of this method to achieve reliable qualification results. It was shown by Heistermann [Hei1990] that a combination of conventional learning strategies and genetic algorithms as optimization technique for a neural networks knowledge gives an improved pattern recognition performance of the neural network for complex problems. Also, topology generation of neural networks by genetic algorithms provides better adaptation of a neural network to the given problem (see Scholz [Sch1995]) than simple straight-forward methods like the one used above for topology determination do. As both the optimization of the qualification routine parameter set by a genetic algorithm and qualification by an artificial neural network showed good performance, a further investigation of these technologies and their possible combination may allow full automation of future dust experiments.

5 Data compression onboard the MDC

For space missions, the amount of data that can be transferred back to Earth is limited not only by the nominal capacity of the transponders and antennas, but also by other factors as visibility and the pointing direction of the antenna or the attitude of the satellite, respectively. All these three factors take effect for a planetary deep space mission like NOZOMI. In principle, if downlink is possible at all, the available downlink capacity is limited by the power of the available transponders and decreases with increasing distance from Earth. NOZOMI's maximum nominal data rates vary from 2048 bps to 32768 bps. Not later than after injection into Mars orbit, this data rates will only be available for strictly limited time spans since NOZOMI will be hidden behind Mars at regular intervals, and additionally the remaining high gain antenna will not point to Earth continuously due to the attitude requirements of the scientific instruments on board.

Consequently, the overall amount of data that has to be transferred to Earth must be restricted to the essential minimum. The actual version of the Mars Dust Counter does not implement any kind of data compression. Nevertheless, the basic MDC onboard software already provides different opportunities for the implementation of data reduction. One is already described in chapter 4, a simple optimization of the parameter set of the qualification routine gives to the possibility to implement a significant reduction of noise data by setting a threshold value in quality number for data segments selected for download.

In the following chapter, a routine that implements a compression of data segments by a factor of 10 is introduced. References are the monographies from Debnath [Deb2001] and Louis et al. [Lou1998], the technical report from Fischer [Fis1999] and the thesis works from Kyritsis [Kyr2003] and Rott [Rot2004].

5.1 Basics and motivation

As described in paragraph 2.3.2, NOZOMI's downlink capabilities were reduced in 1999 due to failure of the omni-directional S-Band transceiver. The X-Band downlink requires pointing of the antenna and thus the NOZOMI spin axis to Earth, which will not be given all the time. As a tribute to the reduced data transmission capabilities, a reduction of the amount of data that has to be transferred to Earth for MDC data analysis to a minimum is aimed, as the downlink capacity available for the MDC after insertion into Mars orbit will be strongly limited due to activation of the other scientific instruments onboard. In addition, if recovery of NOZOMI's damaged power supply unit and thus Mars insertion and switch back to normal telemetry fails, only a very limited downlink capacity will be available.

To achieve these aims, two possible modes of data compression were elaborated:

- A compression of the digitized signals by a lossy compression algorithm,
- A partly data analysis onboard to achieve a maximum data reduction

In the first case, compression of the signals by MDC's onboard computer makes it possible to reconstruct the original shape of the signal after download by applying the corresponding decompression algorithm. When using lossy compression algorithms, the compression rate has to be adjusted to give a maximum data reduction without losing the signal's relevant information. Basically, the high frequencies parts of the signal get lost, which mainly represent noise but also may represent sharp edges which are relevant for data analysis. The low frequency parts of the signal are kept for reconstruction of the original signal's shape. As shown later, the Discrete Wavelet Compression allows a reduction of the amount of data to 1/16 or less of the original data without losing relevant information.

In the second case, when performing a partial data analysis onboard, the original shape of the signal gets lost. Thus, this can only be seen as an emergency procedure for the case that recovery of NOZOMI's nominal telemetry fails and only the highly limited telemetry capabilities in ranging mode are available. The transmission of single data bits by the use of NOZOMI's beacon signals would be sufficient to download all of the collected data, as the dust flow in the interplanetary space was quite low during the first years of the mission. Indeed, a better qualification and thus pre-selection of data sets to be stored safely for transmission to Earth is required, as described in chapter 4.

5.2 Data compression

In this paragraph, first the principles of lossy compression techniques are illustrated on the example Fourier Transformation, a widely used and well-known technology in communications engineering (paragraph 5.2.1). In paragraph 5.2.2, the Discrete Wavelet Transformation technique (DWT), its difference from the Fourier Transformation and its special advantages for the compression of the MDC signals is explained in detail.

5.2.1 Lossy compression

The original data of the MDC consists of a sequence of numerical values representing the shape of the signal recorded by the MDC electronics. Mathematically, this defines a discrete function $f(k)$ consisting of N values, $k = 0 \dots N-1$, where N is 413 for the electron channel and 213 and 212 for the ion channel and the neutral channel, respectively. Physically, this is the representation of the signal in the time domain.

In some cases, this representation is rather unsuitable for further analysis of the signal. To circumvent these restraints, a transformation of the signal to some other representation can be performed. Generally, a transformation of a function

$$f(k), k = 0 \dots N-1 \quad (5-1)$$

gives a new function

$$F[m], m = 0 \dots N-1, \quad (5-2)$$

that represents the same data in a different way. As an example of a widely used transformation, the Discrete Cosine Transformation, a variety of the Discrete Fourier Transformation, will be mentioned here².

Mathematically, the function or the signal is folded with a series of N scaled basis functions, in the case of Cosine Transformation scaled cosine functions are used as basis functions. Strictly speaking, a N -dimensional scalar product is calculated from the discrete signal and the m^{th} basis function giving one single scalar value (in the case of continuous functions, the scalar product is calculated in the Hilbert space, a infinite dimensional vector space). All N values $F[m]$ fully represent the original signal $f(k)$ in a new domain, called frequency domain when Fourier Transformation is used.

$$F[m] = w_m \sum_{k=0}^{N-1} f[k] e^{j2\pi \frac{mk}{N}}, \quad w_m = \begin{cases} \frac{1}{\sqrt{N}}, & m = 0 \\ \sqrt{\frac{2}{N}}, & 1 \leq m \leq N-1 \end{cases} \quad (5-3)$$

² In case of Fourier Transformation, which is based on periodical basis functions, the signal $f(k)$ has to be periodical as well to get proper results. Non-periodic signals can be periodically extended by defining a function $f^*(k^*)$, $0 < k^* < 2N$ where $f^*(k+N) = f^*(k)$, $0 < k < N$. Here, this will not be regarded further.

By applying the appropriate inverse transformation, the original signal $f(k)$ can be restored exactly from the coefficients $F[m]$, as long as all N coefficients are available for the inverse transformation. After transformation, certain manipulations and analyses of the signal are much easier using the $F[m]$ representation, in particular filtering of the signal.

Analogue signals of sensitive instruments like the MDC show natural noise, superposing the mainly low frequent wanted signal in a wide frequency range. To eliminate disturbing noise, in many cases a high pass filter may be useful for further processing of the signal. Transformation into the frequency domain makes it easy to apply such a filter, since the coefficients $F[m]$ of low order (small m) represent the existence of low frequencies in the signal, and those of high order (high m) represent the existence of high frequencies. Simply setting of the coefficients of unwanted frequencies to zero will remove these frequencies in the retransformed signal.

In most cases, when removing high frequencies, the wanted signal is smoothed and better suitable for further analysis. In terms of data compression, lossless compression algorithms like LZW (Lempel-Ziv-Welch) or RLE (Run Length Encoding) will work much better (i.e., lead to better compression rates) when processing a smooth signal rather than a noisy one. Alternatively, the low order coefficients $F[m]$, $0 < m < m_{\max} < N$ themselves can be used as a compressed representation of the signal, where m_{\max} must be preset as a fixed value giving the fixed compression rate. This value must be chosen with respect to the required accuracy of the wanted signal. Signals that consist mainly from low frequency parts will not be substantially affected even if high compression is applied.

One drawback of compression techniques like those described above is that leaps and bounds occurring in the wanted signal are represented by high order coefficients in the frequency space, and thus will also be smoothed. In certain cases, like the signals produced by the MDC, this is not acceptable and sets strong boundaries to the achievable compression rates.

Advanced compression techniques like the Discrete Wavelet Transformation DWT described in the following paragraph are designed to avoid this behavior and thus are more suitable for certain applications, e.g. the compression of MDC signals.

5.2.2 Discrete Wavelet Transformation (DWT)

The Discrete Fourier Transformation and its variants described before are based on periodical basis functions. The transformation of the signal into the frequency domain provides information about which frequencies the signal comprises and how strong these frequencies are represented overall. As a tribute to the periodicity of the basis functions, information about the time at which a particular frequency is present or absent is missing in the frequency domain.

As mentioned before, leaps and bounds in the signal are represented by high frequencies and will be smoothed when the signal is compressed. There are some newer methods available, which avoid this drawback; one is the Discrete Wavelet Transformation.

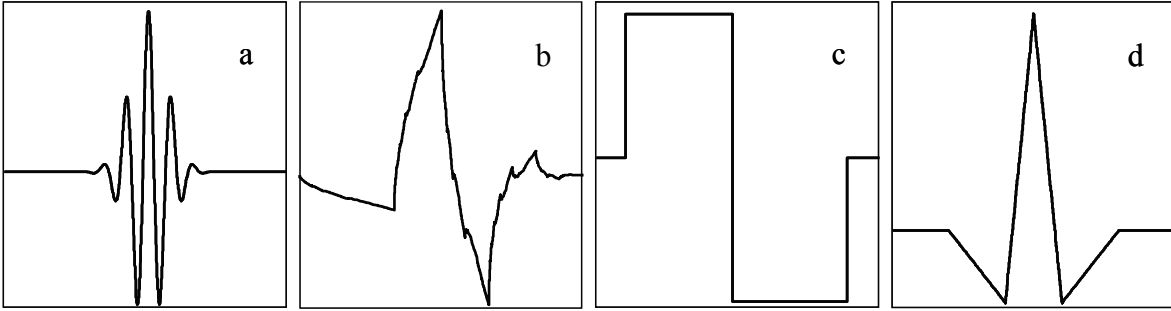


Figure 5-1: Some families of Wavelets

a) Morlet, b) Daubechies-4, c) Haar, d) Biorthogonal 2-2. Each family of Wavelets suites for different applications.

This method is quite similar to the Fourier Transformation, but is based on discontinuous basis functions rather than continuous ones. These basis functions are called Wavelets or Wavelet families, respectively. Many different wavelet families were developed which suite best for different applications like transformation and compression of speech, images etc. Some important Wavelet families are shown in Figure 5-1. For the transformation of the MDC signals, the Biorthogonal 2-2 was seen as best choice, because the simple construction of the Wavelet by a few straight lines allows fast integer addition, subtraction and left-shift operations which keep computing time short as it is required. First tests of transformation of MDC signals with the Biorthogonal 2-2 Wavelet family showed good results in achievable compression. Wavelet transformation is based on the following equation:

$$W[m, n] = \frac{1}{\sqrt{2^m}} \sum_{k=0}^{N-1} f[k] \Psi\left(\frac{k-n}{2^m}\right), \quad (5-4)$$

whereas the function $\Psi(x)$ describes the chosen Wavelet. Here, the scale is determined by the factor m , which is analogue to the frequency series used in the Fourier Transformation method, whereas the supplementary factor n defines the shift of the discontinuous basis function on the time axis (this makes no sense if continuous basis functions are used). Since there are now two parameters rather than one, the resulting coefficients are no longer one series of coefficients, but a number of individual series of coefficients.

The transformation method used for the MDC signals is based on the so-called Multiresolutional Analysis method. The original signal is decomposed systematically into approximations and details. An additional scaling function $\Phi(x)$, which must be orthogonal to the wavelet function $\Psi(x)$, is needed. Wavelet and scaling function are correlated by

$$\Phi(x) = 2 \sum_k h_k \Psi(2x - k); \quad \Psi(x) = 2 \sum_k g_k \Phi(2x - k), \quad (5-5)$$

with the low-pass coefficients h_k and high-pass coefficients g_k . For the transformation of the original signal, these low-pass and high-pass coefficients are needed. The transformation of a signal $f(k)$, $k = 1 \dots N$ is then carried out by

$$\begin{aligned}
a'(n) &= \sum_k h_k f(n-k) \rightarrow a(m) = a'(2m+1); & 0 < m < \frac{N}{2} - 1 \\
d'(n) &= \sum_k g_k f(n-k) \rightarrow d(m) = d'(2m); & 0 < m < \frac{N}{2} - 1
\end{aligned}
\tag{5-6}$$

which gives the approximations $a(m)$ of size $N/2$ and the details $d(m)$ of size $N/2$. Approximations and details together have the same size N as the original signal. Now, the detail part $d(m)$ is stored, and decomposition continues with the approximation part $a(m)$. This process is iterated until the size of the approximation and detail part becomes one single value (in case of the MDC signals, iteration was stopped when the size reached 4 values to save computing time). All approximation parts but the last one are discarded. The total size of approximations and details is then again N , which is the size of the original signal. The decomposition tree of a MDC neutral channel signal is shown in Figure 5-2.

After decomposition is finished, a compression of the signal can be carried out by removing (which means, setting to zero) transformation coefficients from the details parts obtained. This is described in the following paragraph.

Reconstruction of the original signal is carried out with the inverse transformation equations (not shown here, see Kyritsis [Kyr2003]). From the approximation part a_6 and the detail part d_6 , the approximation part a_5 can be reconstructed. This is iterated subsequently until the original signal is reconstructed from approximation part a_1 and detail part d_1 , see Figure 5-2.

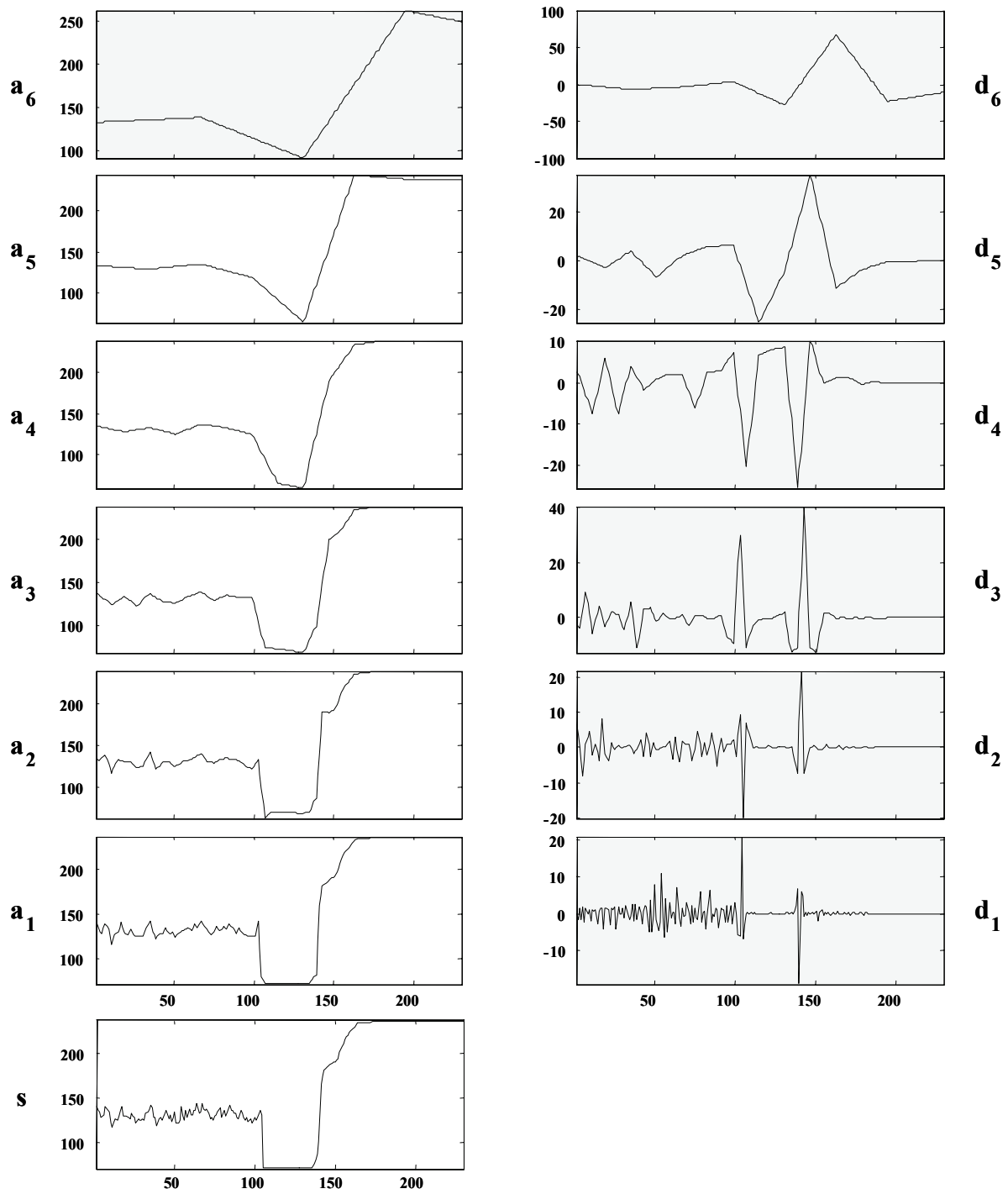


Figure 5-2: Decomposition tree of an MDC neutral channel signal

The original signal (s) is decomposed step by step into approximations (a_1 to a_6) and details (d_1 to d_6). For a complete reconstruction of the original signal, all detail parts d_1 to d_6 and the last approximation part a_6 need to be stored.

5.2.3 Compression of MDC signals

After transformation of the signal, the size of the data is still the same as before transformation. Now, coefficients that represent details that are not needed for the later analysis of the signal can be removed. To illustrate this, the coefficients of the detail parts of a transformed signal are shown in a two dimensional view in Figure 5-3 (approximation part a_6 is not shown here). In Figure 5-3 a), the full set of coefficients is shown, the values of the coefficients are indicated by colors (white: zero, black: maximum value). As a first step, all detail coefficients that are located below a zero value detail coefficient are removed, based on the assumption that a detail located below a zero detail represents a single peak, which is classified as noise and could be deliberately removed. This leads to Figure 5-3 b). Now, all details left of the trigger are removed since they are not needed for further data analysis. The pre-trigger shape of the reconstructed signal is then represented only by the remaining approximation part a_6 . Figure 5-3 c) shows the remaining coefficients. Next, coefficients are removed subsequently beginning with the smallest, until the desired compression rate (or, number of remaining coefficients) is reached. Figure 5-3 d) shows the final coefficients of the compressed signal. The desired compression rate for the MDC is set to a factor of 16, which means that only 6.25% of non-zero coefficients remain for later reconstruction of the original signal.

Now, as many coefficients as possible were set to zero with respect to the requirements of the data analysis regarding the shape of the reconstructed signal. No real compression at all is performed until now. Compression of the data is finally carried out by Differential Pulse Code Modulation, a well-established method of lossless compression of data streams. The more zero values are represented in the data that has to be compressed, the better the DPCM compression works.

The now compressed data of the signal shape is merged with a subset of the MDC memory segments housekeeping data and stored in the MDC memory as described in paragraph 5.3.2. A MDC memory segment of 1 kByte size can now hold 10 compressed signals rather than one uncompressed.

Figure 5-4 shows the overall performance of the data compression routine. Reconstruction error e (absolute difference of the reconstructed signal from the original signal, scaled by the signal range) is lower than 10% for 91% of all available MDC signals. Achieved compression factors are between 16 and ≈ 55 for all available MDC signals.

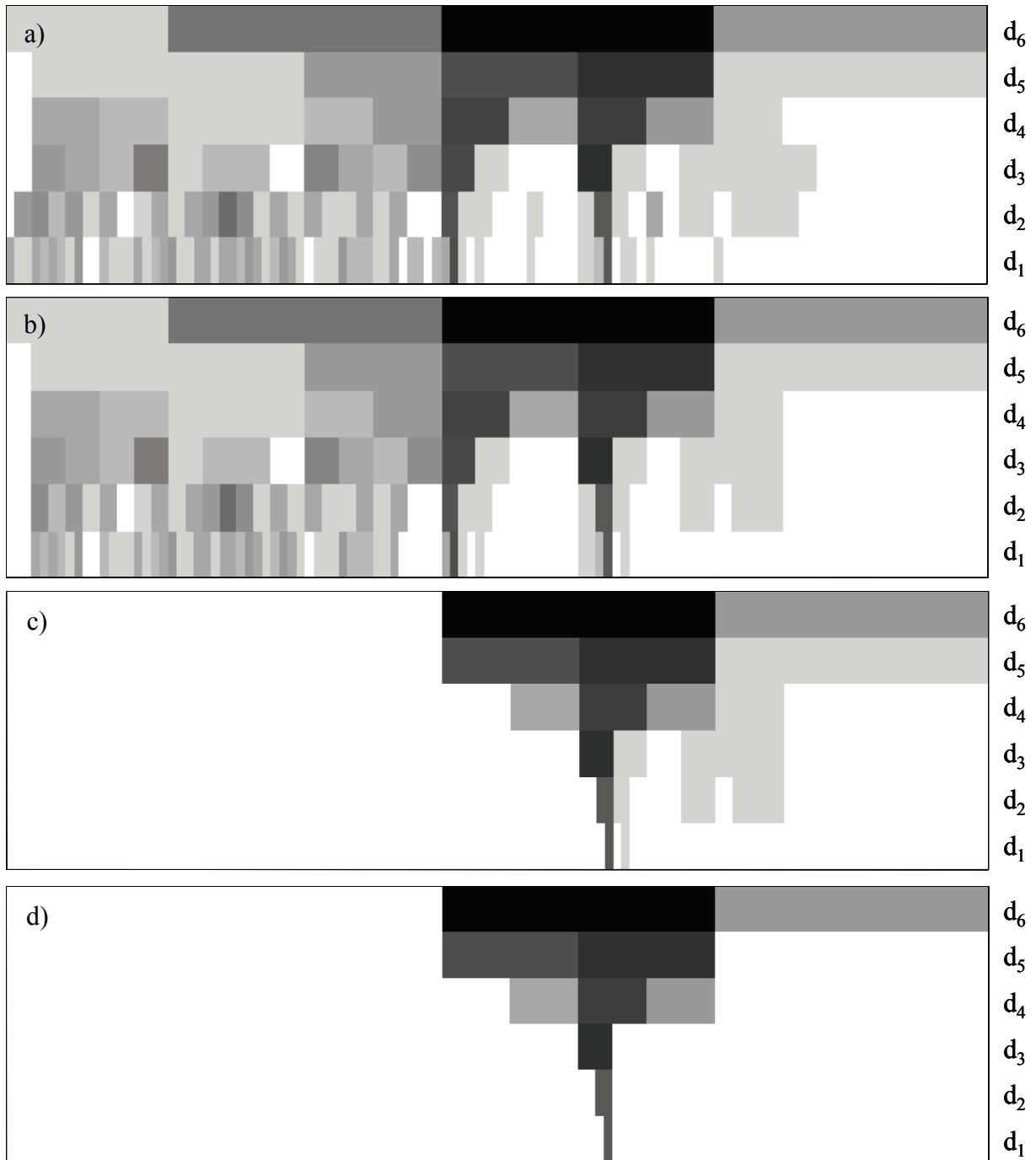


Figure 5-3: Compression of an MDC signal

a) Detail coefficients of the original signal; b) Detail coefficients after removal of small details without a large detail on top; c) Detail coefficients after removal of pre-trigger details; d) Detail coefficients after removal of small coefficients. Colors indicate the coefficients numerical value, white represents zero, black the maximum value of 56.

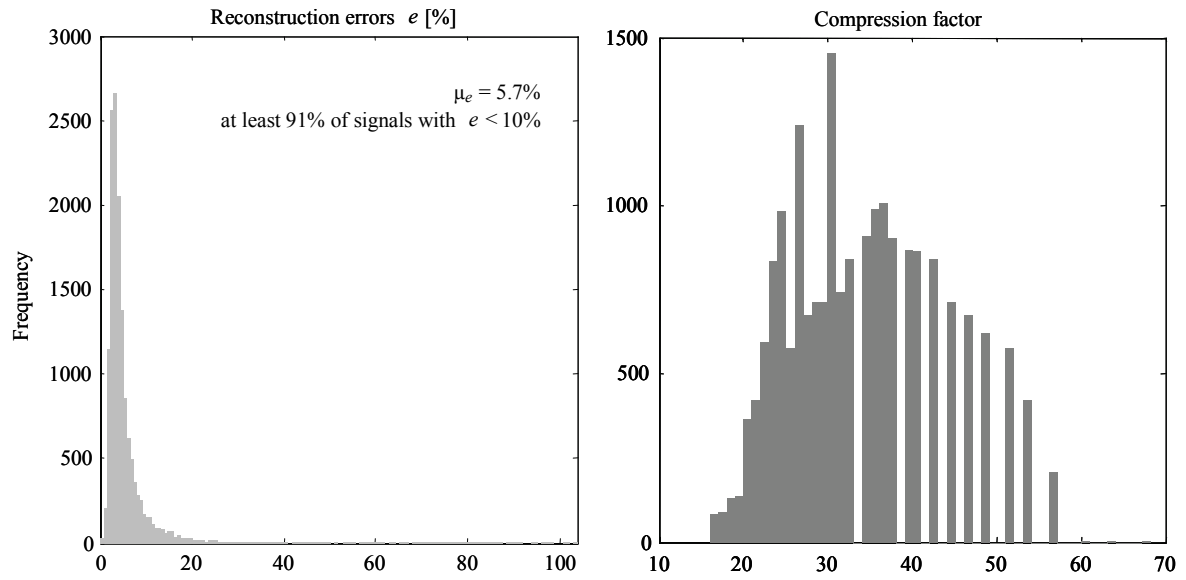


Figure 5-4: Performance of the data compression

Frequency of reconstruction errors and compression factors for all MDC signals.

5.3 Implementation and integration of the MDC onboard software upgrade

In this paragraph, the implementation and integration of the software upgrade that performs data compression onboard the MDC is described with respect to the limitations that are given by the MDC onboard data processing capabilities.

5.3.1 Hardware and software restrictions

Strong requirements have to be fulfilled when changing or upgrading a reliable and running system. The restrictions that have to be considered are discussed in this paragraph.

Due to the limited resources of the MDC onboard computer in memory and computing power (see paragraph 3.2.2), strict requirements have to be defined for a large software upgrade like the compression routine described here.

The limitations of the hardware enforce the following requirements:

- Any compression routine must be executable by the onboard processor in a time span of 1 to max. 3 seconds.
- All calculations must be implemented using integer arithmetic.
- The final code of the software upgrade must not require more than one KByte of RAM memory

The existing onboard software requires further restrictions regarding a software upgrade. During the MDC's operation since launch, the existing onboard software has proven to work stable and accurate. Therefore, it has to be ensured that the stability and functionality of the software will not be affected by the upgrade, even if the upgrade does not work properly or has to be removed.

In the case of the existing MDC software, the functionality of the existing memory management and the memory dump routines must not be affected by the software upgrade in any way. This is a strong requirement, since a possible deactivation of the upgrade caused by any case must not lead to any mismatch of memory segmentation. The following requirements must be fulfilled:

- The compression routine has to be integrated into the existing software without affecting the consisting operating sequence,
- The new memory management needed to store compressed data has to be implemented in a way that the existing memory management can operate as before and no adaptation is needed.

These requirements can be met by a smart exploitation of the provided extension options of the existing software.

5.3.2 Integration of the upgrade into the existing software

The qualification routine of the existing software provides the ideal integration point for the new compression routine. Any new-recorded signal will be qualified by a routine running as a background task. In principle, the qualification routine and the compression routine each perform an extensive calculation task, which creates new data from the original signal data, a qualification number and the compressed data, respectively.

Now, the branch table of the MDC software can be manipulated to call the new compression routine instead of the qualification routine after all other tasks are completed. The operation sequence of the preceding tasks is not affected by this manipulation, as described above this is a fundamental requirement. Indeed, the existing software provides several points for the integration of new routines into the original operation sequence; fortunately, this was not necessary for the software upgrade described here.

The compression routine itself first calls the original qualification routine, and subsequently performs the compression of the original data and the storage of the results. This should work without problems as long as the computing time of the compression routine does not exceed 1 to 2 seconds. A longer computing time is not acceptable since during phases of high dust flux or strong interferences (which cause a high rate of new signals to be qualified, compressed and stored) a proper completion of qualification and compression may not be guaranteed any more, which could result in loss of data.

After compression, the signal data is reduced to about 6.25% of the original amount of data. Added segment and housekeeping information, every new data set requires 10% of one 1 kByte segment. These new data sets have to be stored in memory in a different way than the original data, since every old 1 kByte segment can now hold 10 new data sets instead of one original data set. As mentioned before, the original memory management working with the 1 kByte segments must not be affected.

To achieve this, a new type of memory segment was defined which is designed to store the new compressed data sets, but shows up as a conventional 1 kByte memory segment when processed by the old memory management. Only the data structure inside these new segments differs from the conventional segment structure, while the original memory management identifies these new segments as segments that must not be manipulated in any way. The software identifies segments by their quality number, which is stored in the first byte of each segment. Quality numbers from 0 to 245 identify segments which can be used to store uncompressed (original) signal data, while quality numbers higher than 245 represent segments used as calculation space, code or parameter segments. As code segments will never be manipulated by the old memory management, the new segments, which contain compressed data sets, are marked as code segments with quality number 253. This enables the programmer to implement a new memory management handling the new compressed data sets without affecting the old memory management. The calculated quality number of a new data set is stored inside the data set, since the segment quality number of a new segment is fixed to be 253.

The original software stores new signals after qualification either in an unused memory segment or, if there are no more unused segments, in the segment presenting the lowest

quality number. This ensures that segments holding potentially good signals are relatively secured from being overwritten, if frequently memory readouts take place.

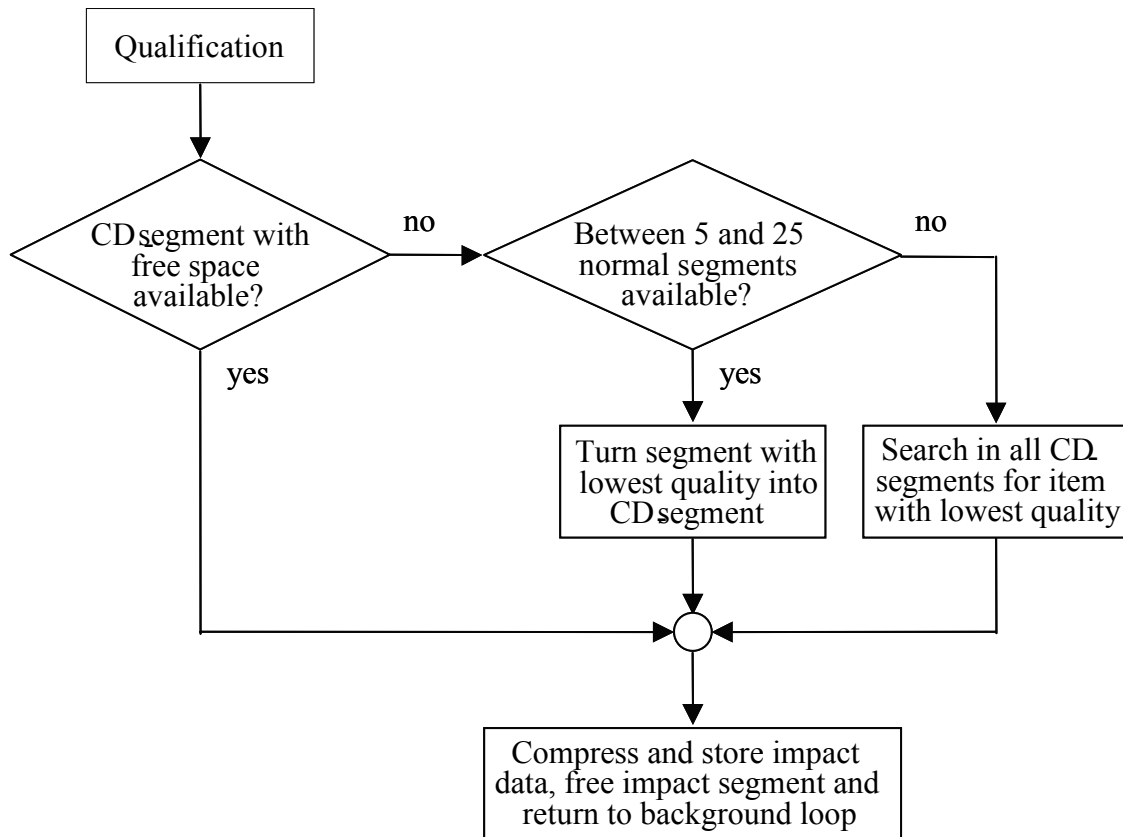


Figure 5-5: Flow chart of data processing of the new memory management
 After a new-recorded signal was processed by the qualification routine, the new MDC memory management looks for free space to store the compressed signal and calls the compression routine. CD segment = Compressed data memory segment.

The upgrade is working in a quite similar way. Instead of searching for the best 1 kByte segment to store a new signal, free memory places are searched inside the existing new segments already containing compressed data. If there is no more memory available inside the existing new segments, a free 1 kByte segment (or the one with the lowest quality number) is labeled and formatted as a new segment. The new compressed data set is then stored in the first memory place of this new segment. To ensure that enough conventional memory segments are available for the functionality of the old software, a limit of a maximum number of 35 to 40 new segments will be fixed ad hoc.

5.4 Verification of the new analysis process

As mentioned before, the resulting signal shape of MDC data after compression/decompression differs from the original signal shape, see Figure 5-6 for a comparison between the original and the compressed/decompressed signal shape. Although the difference is only slight, one can say that the required characteristic points used as input for the calculation of mass and velocity of an identified impact will be set to different coordinates, both by a human experimenter and by an automated routine. In the bottom chart of Figure 5-6, this can be seen directly. For the NC channel (blue line), the maximum of the charge is reached a few μs later on the compressed/decompressed curve than on the original one (thin black solid line next to the blue line). For the EC channel (green line), the maximum charge is higher on the compressed/decompressed curve than on the original curve (thin black solid line next to the green line). These differences influence the derived values of particle mass and impact speed, the magnitude of these induced errors in mass and impact speed is determined in the following.

To determine how much this difference of coordinates influences the final analysis results, test series were carried out. In principle, a set of original data that was analyzed previously using the uncompressed data was chosen, and the analysis was rerun using the same data sets after compression/decompression, giving new values for mass and impact speed for each data set.

Finally, the values resulting from the original analysis and the new analysis were compared and an overall deviation was calculated.

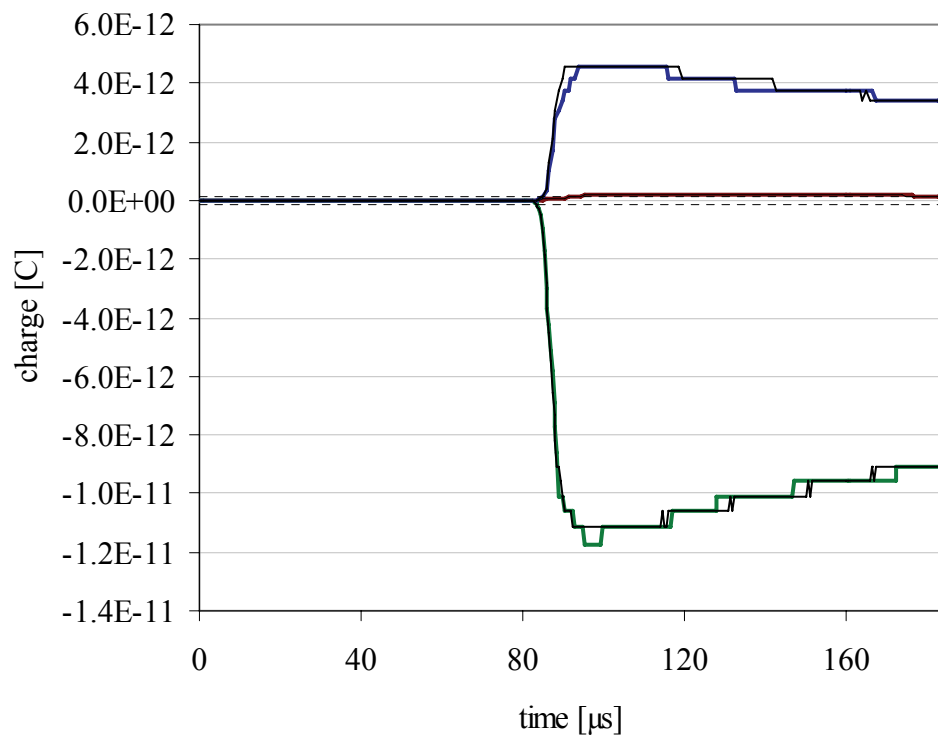
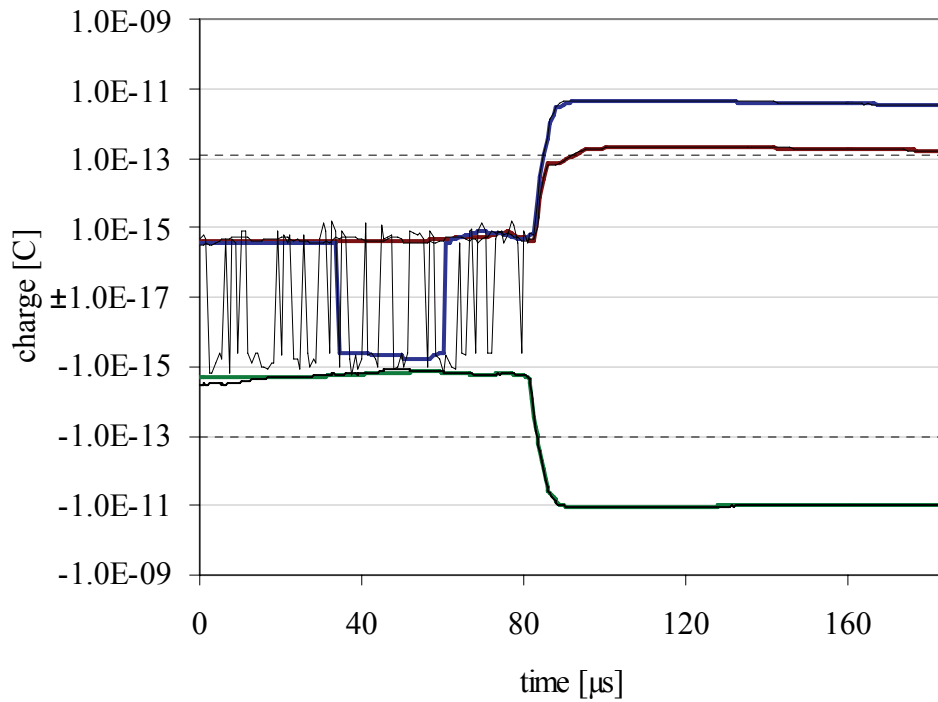


Figure 5-6: A typical MDC signal before and after compression

In this chart, a typical original MDC signal (solid black lines) is compared to the resulting signal after compression/decompression (solid colored lines), top: logarithmic view, bottom: linear view. As can be seen, the resulting signal is nearly identical to the original during the most important time period from 80 μ s to 120 μ s. Most information is lost in the time period from 0 μ s to 80 μ s, which is not relevant for MDC data analysis.

5.4.1 Analysis of MDC-NOZOMI data after compression/decompression

The analysis of MDC-NOZOMI signals is carried out using the *Microsoft® Windows®* MDCCDA program (Mars Dust Counter Control and Data Analysis) developed by Naumann [Nau2000] on the basis of the MS-DOS programs for MDC-HITEN and MDC-BREMSAT data analysis.

As the MDC data files that will be downloaded from NOZOMI after the software upgrade is installed will contain segments of compressed data, the MDCCDA program must be able to perform a decompression prior to the analysis of the data. Hence, the decompression routine was integrated into the existing MDCCDA. After decompression, the signals are analyzed in the same manner as before. To demonstrate that the analysis of compressed/decompressed signals gives accurate and unadulterated results, the compression routine used in the MDC software upgrade was also implemented into the MDCCDA. Thus, all the signals identified as impacts since launch of the NOZOMI mission and were already analyzed, can be compressed, filtered and decompressed and finally reanalyzed by the MDCCDA program. The algorithm used for compression onboard the MDC was mapped one-to-one from assembler to C++ code to ensure identical compressed data sets.

5.4.2 Analysis of MDC-HITEN data after compression/decompression

To get an even more reliable verification of the integrity of the new data analysis process, the compression routine designed for the MDC-NOZOMI data was also applied to the data of MDC-HITEN, the predecessor of the MDC-NOZOMI. Configuration, electronics and, most important, signal shape differ slightly from the more complex MDC-NOZOMI. Thus, if this verification also gives satisfying results, the developed method can be proven as generally applicable to future experiments based on similar configurations like the MDC-NOZOMI/MDC-HITEN configuration.

Unlike the MDC-NOZOMI, the compression/decompression was not integrated into the original data analysis software. Since this software was created parallel to the development process of the MDC-HITEN, and is now more than ten years old, it was decided that a reproduction of the analysis process using modern software can be performed much easier and more transparent than an extensive modification of the original software. Another reason for this decision was that the compression routines already existed in *MATLAB®*, and only the final calculation process had to be reproduced.

Nevertheless, some slight modification of the original software was necessary to convert the MDC-HITEN data files from the original (binary) telemetry format to a format that can be handled by *MATLAB®*, preferable text files. As a spin-off, the routines implemented for text export of the original data were used to create a universal XML (eXtensible Markup Language) representation of all MDC-HITEN data that can be easily used for future work, electronic publication and archiving (see chapter 7)

After importing the data into *MATLAB*[®], the analysis was carried out in the following way:

The chosen data set was compressed, filtered and decompressed by the previously developed *MATLAB*[®] routines. The resulting signal was displayed by the integrated *MATLAB*[®] data handling functionality in a way that the coordinates of the required data points could be easily determined by the user.

The resulting values Δt , Δq , q_e , q_i were carried over into a *Microsoft*[®] *Excel*[®] sheet, where the final calculation of mass and velocity was performed using the appropriate equations and parameters required for the chosen type of signal.

It must be pointed out here that the determination of the coordinates of the data points was performed without any knowledge of the position of these points according to the analysis made previously, to make sure that the experimenter is free of undue influence.

5.5 Summary and discussion

The results of the rerun analysis of MDC-HITEN data are summarized in the following figures, and in Table 5-1 and Table 5-2, broken down into the different signal types, see Münzenmayer [Mün1995] for a detailed description of the different MDC-HITEN signal types. In Figure 5-7, Figure 5-8, Figure 5-9 and Figure 5-10 mean values (solid red line) and standard deviation (dashed red lines) are visualized.

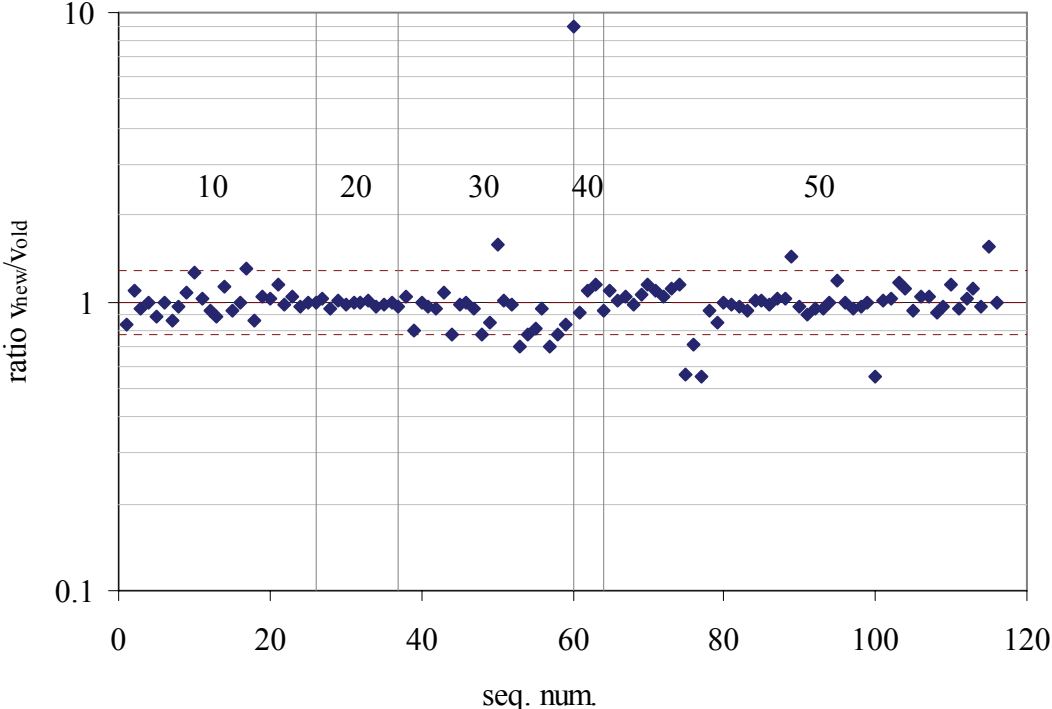


Figure 5-7: Impact speed ratio new/original analysis, MDC-HITEN
 Impact speed ratio of the 115 values determined by the rerun analysis based on compressed/ decompressed signals to the values of the original analysis. Numbers 10 to 50 indicate the MDC-HITEN signal types.

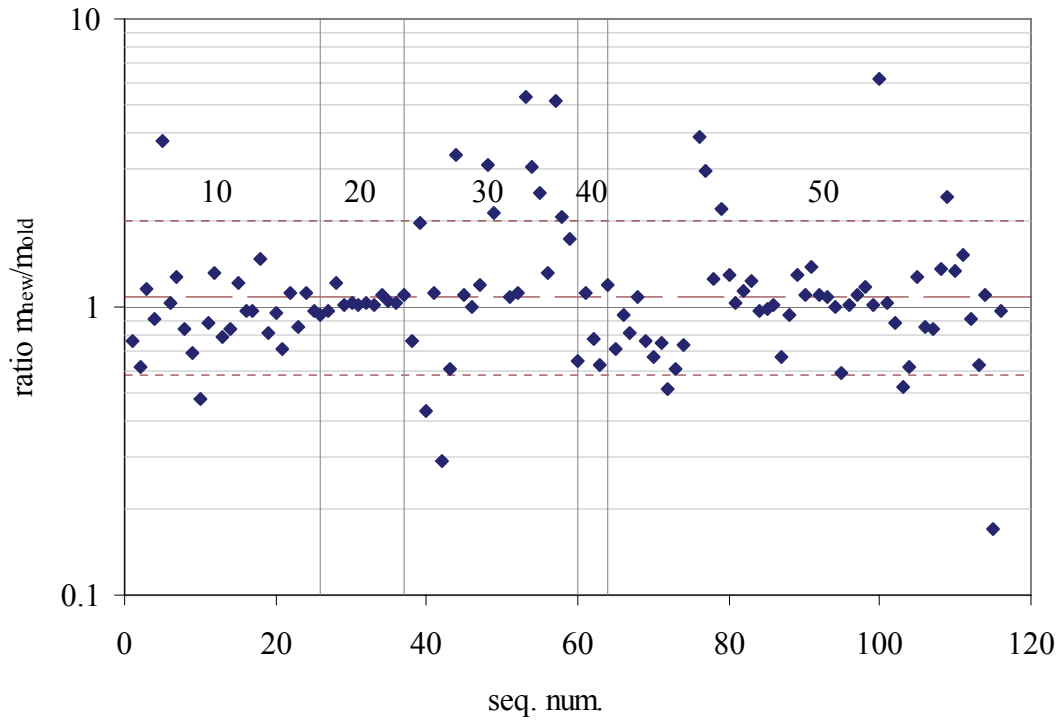


Figure 5-8: Particle mass ratio new/original analysis, MDC-HITEN

Particle mass ratio of the 115 values determined by the rerun analysis based on compressed/ decompressed signals to the values of the original analysis. Numbers 10 to 50 indicate the MDC-HITEN signal types.

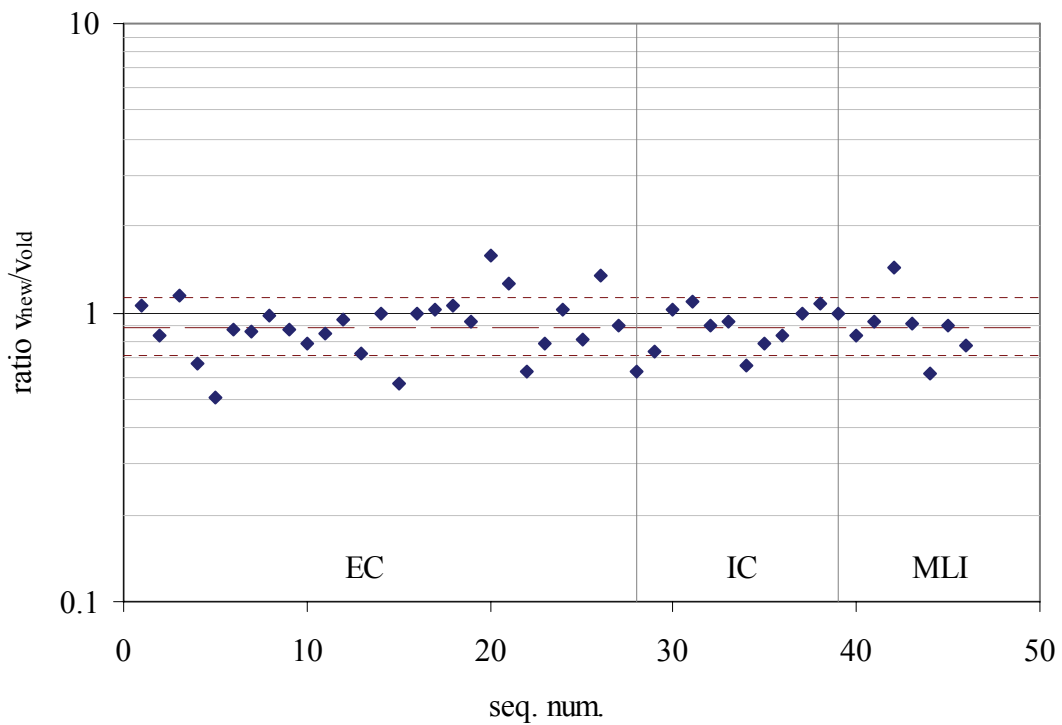


Figure 5-9: Impact speed ratio new/original analysis, MDC-NOZOMI

Impact speed ratio of the 45 values determined by the rerun analysis based on compressed/ decompressed signals to the values of the original analysis.

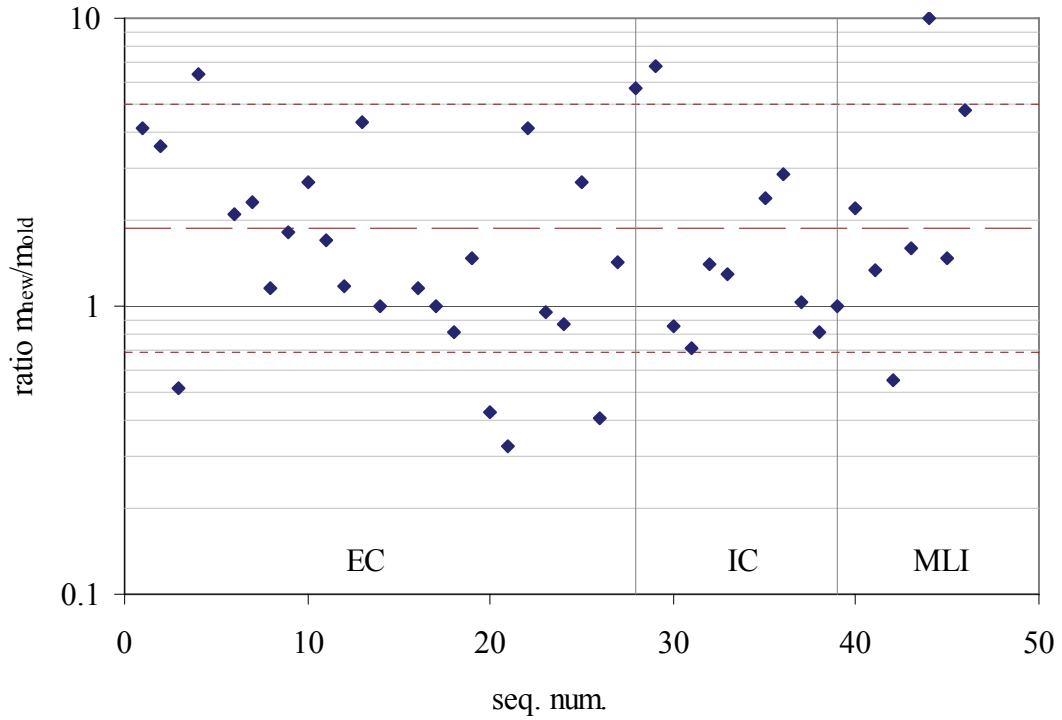


Figure 5-10: Particle mass ratio new/original analysis, MDC-NOZOMI
 Particle mass ratio of the 45 values determined by the rerun analysis based on compressed/ decompressed signals to the values of the original analysis.

The values shown in the following tables were calculated by the following equations:

$$\bar{m} = \exp\left(\frac{1}{N} \sum_{i=1}^N \log\left(\frac{m_{i,new}}{m_{i,old}}\right)\right) \quad (5-7)$$

$$\bar{v} = \exp\left(\frac{1}{N} \sum_{i=1}^N \log\left(\frac{v_{i,new}}{v_{i,old}}\right)\right) \quad (5-8)$$

$$\sigma_{m,\log} = \sqrt{\frac{1}{N} \sum_{i=1}^N \left(\log\left(\frac{m_{i,new}}{m_{i,old}}\right) - \log(\bar{m})\right)^2}, \bar{m}^{\pm} = \exp(\log(\bar{m}) \pm \sigma_{m,\log}) \quad (5-9)$$

$$\sigma_{v,\log} = \sqrt{\frac{1}{N} \sum_{i=1}^N \left(\log\left(\frac{v_{i,new}}{v_{i,old}}\right) - \log(\bar{v})\right)^2}, \bar{v}^{\pm} = \exp(\log(\bar{v}) \pm \sigma_{v,\log}) \quad (5-10)$$

where \bar{m} and \bar{v} are the mean values, and \bar{m}^{\pm} and \bar{v}^{\pm} are the upper and lower boundaries of the standard deviation.

Table 5-1: Validation of the compression on the MDC-HITEN data

Signals of type 10, 26 signals analyzed						
\bar{v}^-	\bar{v}	\bar{v}^+	\bar{m}^-	\bar{m}	\bar{m}^+	
0.90	1.00	1.12	0.67	0.97	1.41	
Signals of type 20, 11 signals analyzed						
\bar{v}^-	\bar{v}	\bar{v}^+	\bar{m}^-	\bar{m}	\bar{m}^+	
0.96	0.98	1.01	0.99	1.05	1.12	
Signals of type 30, 23 signals analyzed						
\bar{v}^-	\bar{v}	\bar{v}^+	\bar{m}^-	\bar{m}	\bar{m}^+	
0.60	1.00	1.66	0.50	1.28	3.26	
Signals of type 40, 4 signals analyzed						
\bar{v}^-	\bar{v}	\bar{v}^+	\bar{m}^-	\bar{m}	\bar{m}^+	
0.91	1.02	1.14	0.66	0.90	1.22	
Signals of type 50, 52 signals analyzed						
\bar{v}^-	\bar{v}	\bar{v}^+	\bar{m}^-	\bar{m}	\bar{m}^+	
0.82	0.98	1.18	0.58	1.07	1.99	
Overall results, 115 signals analyzed						
\bar{v}^-	\bar{v}	\bar{v}^+	\bar{m}^-	\bar{m}	\bar{m}^+	
0.76	0.99	1.29	0.58	1.08	2.00	

Table 5-2: Validation of the compression on the MDC-NOZOMI data

EC signals, 28 signals analyzed						
\bar{v}^-	\bar{v}	\bar{v}^+	\bar{m}^-	\bar{m}	\bar{m}^+	
0.76	0.96	1.20	0.58	1.36	3.19	
IC signals, 11 signals analyzed						
\bar{v}^-	\bar{v}	\bar{v}^+	\bar{m}^-	\bar{m}	\bar{m}^+	
0.60	0.77	0.97	1.07	3.67	12.59	
MLI signals, 6 signals analyzed						
\bar{v}^-	\bar{v}	\bar{v}^+	\bar{m}^-	\bar{m}	\bar{m}^+	
0.77	0.85	0.93	1.46	2.19	3.27	
Overall results, 45 signals analyzed						
\bar{v}^-	\bar{v}	\bar{v}^+	\bar{m}^-	\bar{m}	\bar{m}^+	
0.70	0.89	1.12	0.69	1.87	5.04	

For the MDC-HITEN data, the overall mean values of the ratios between the single results of the old analysis and the new analysis show only very low deviation in velocity, which is about a factor 0.99 towards lower velocity, and a deviation in mass of about a factor 1.08 towards higher mass. Since the appreciated accuracy of the analysis overall is about a factor 2 in velocity and a factor 5 in mass, the deviation caused by the compression/decompression is far below the accuracy that can be achieved with the instrument in principle.

Analysis of the MDC-NOZOMI control data shows an analog behavior. Velocity determined from the compressed data sets shifts about a factor 0.89 towards lower impact speed, while particle mass shifts by a factor 1.87 towards higher mass. A small number of mavericks cause most of this large deviation, while all other signals show much lower deviation from the old data. Since the analysis process of the MDC-HITEN and MDC-NOZOMI are similar besides the third channel in the MDC-NOZOMI data, it is most likely that the three-channel based MDC-NOZOMI analysis is much more sensible to small changes in signal shape than the more robust MDC-HITEN analysis. Nevertheless, the deviation of the impact speed is by far within the instruments accuracy. For further analysis and interpretation of the particle properties (orbital elements etc.), only impact speed is required.

It must be emphasized here that the shown values demonstrate the accuracy of the new analysis in comparison to the old analysis. They must not be interpreted as an absolute assessment of the new analysis process in comparison to any known, 100% reliable data.

The MDC software upgrade was ready for upload by the end of the year 2002, and the decompression routine was already implemented in the MDC analysis software. The assembler code for wavelet transformation and compression takes 555 bytes RAM for the code, plus one 1 kByte buffer segment for computations. The transformation of all three channels of a MDC signal is performed within 510000 clock cycles, which corresponds to 290 ms computing time.

If NOZOMI had been recovered from the system failure on April 24, 2002, and finally entered Mars orbit with its full functionality, there would have been three options for the analysis of MDC dust data downloaded in compressed format:

1. Leave the analysis process as it is with the only difference that compressed signals are used for the determination of mass and impact speed of the particles. This method was used above to validate the software upgrade. Resulting mass and speed are shown to be within the instrument's accuracy.
2. Determine correction factors for mass and impact speed for every MDC impact type (EC, IC and MLI) to minimize the deviation of the analysis results derived from the compressed signals from the results derived from the original signals, based on the results shown above. This method would give more accurate analysis results with a minimum effort.
3. Perform a complete recalibration of the MDC. This means, compress and decompress all calibration signals that were used for the determination of the parameter sets of the analysis process, and determine new parameter sets from these compressed calibration impact signals. This method would give the highest possible accuracy, but with a high effort.

For the MDC on NOZOMI, option 2 would have been the method of choice since it offers the best cost-value ratio.

For possible future dust experiments based on the MDC that require their own calibration anyway, option 3 is the method of choice. Integration of the compression and decompression routines into the calibration process, the onboard software and the data analysis process can be easily done during the development of the required software routines. The systematic changes in signal shape that are caused by the compression/decompression process are then integrated into the whole data handling process and do not have any effect on the final analysis results, as long as the required parameters (charges, rise time) can be determined from the resulting signal shapes, which is the case for signals compressed by the Wavelet compression routine discussed in this chapter.

6 Mission results

In this chapter, the scientific results of the MDC mission are presented and discussed. At first, paragraph 6.2 gives a closer look to the instrument's and NOZOMI's flight data, and a brief look at the noise data that was recorded by the MDC. Both the detector limits and the unusual high amount of noise data (compared with the previous mission MDC-HITEN) affect or may affect the final interpretation of the MDC impact data and thus were examined carefully. Finally, interpretation and determination of NOZOMI flight data that is required for further data analysis is described.

Although NOZOMI and the MDC could not fulfill their primary mission goals (see paragraphs 2.3 and 2.3.3), at least the MDC's measurements of cosmic dust in the vicinity of Earth and Moon and later in the interplanetary space yield interesting scientific results. To make allowance for the different environmental conditions, the discussion is separated into two sections. In paragraph 6.3, the results of the mission's first 6 months are discussed where NOZOMI resided in the vicinity of Earth and Moon. In paragraph 6.4, the results of more than 3 years in the interplanetary space are discussed. A detailed description of NOZOMI's mission can be found in paragraph 2.3.

Analysis of all data presented in the following paragraphs was performed as described in paragraph 3.3.2.

6.1 Overview

The detection capabilities of an instrument like the MDC as well as the interpretation of the measured dust data are strongly dependent not only on the instrument's principal properties, but also on the pointing directions of the instrument which in turn is determined by the attitude data of the hosting spacecraft. Very careful examination of the spacecraft's flight data (orbital position, attitude, flight direction) with special respect on the pointing directions of the MDC is required for correct interpretation of the measured dust data, to avoid wrong conclusions from observed patterns in impact data that are not of natural origin but are caused by the spacecraft's and the MDC's pointing direction. NOZOMI flight data and the vast amount of noise data recorded by the MDC are investigated prior to the final analysis of the impact data at the end of this chapter.

6.2 Noise signals and flight data interpretation

For the further interpretation of the MDC impact data, the instrument's characteristics have to be discussed first. Since the measuring range of the MDC electronics (charge amplifiers and A/D converters) is limited, every statistical analysis of the impact data must be related to the MDC detection capabilities. The MDC detection capabilities are already discussed in paragraph 3.2.4, but also the huge amount of noise data recorded by the MDC may influence the detection capabilities since every single signal triggered and processed by the MDC electronics causes some instrument dead time, and may therefore affect statistical analysis of dust flow. The effects and characteristics of the recorded noise rate and noise signals are discussed in paragraph 6.2.1. Interpretation of the absolute direction of the identified particles requires an exact determination of the MDC view axis at a given impact time, and a detailed examination of the spacecraft's attitude and thus spin-averaged sensor pointing directions for statistical analysis of particle flight directions. In paragraph 6.2.2, the calculation of the MDC view axis and the absolute particle velocity from the given NOZOMI flight data is described in detail, in paragraph 6.2.3 the NOZOMI flight data are examined in detail.

6.2.1 Noise signals and instrument dead time

Unlike the previous experiment on the mission HITEN, the MDC-NOZOMI recorded a huge amount of noise data that either was discarded onboard by the KO-criteria and can only be recognized by the instrument's rapidly rising noise count NC, or has passed the KO-criteria and can be seen in the downloaded raw data files.

Many of these noise signals are not shaped randomly as it could be expected for noise caused by random electromagnetic background from different possible sources like radiation in space or the satellite's electrical systems. Several nearly identical signal shapes were identified which occur in certain patterns.

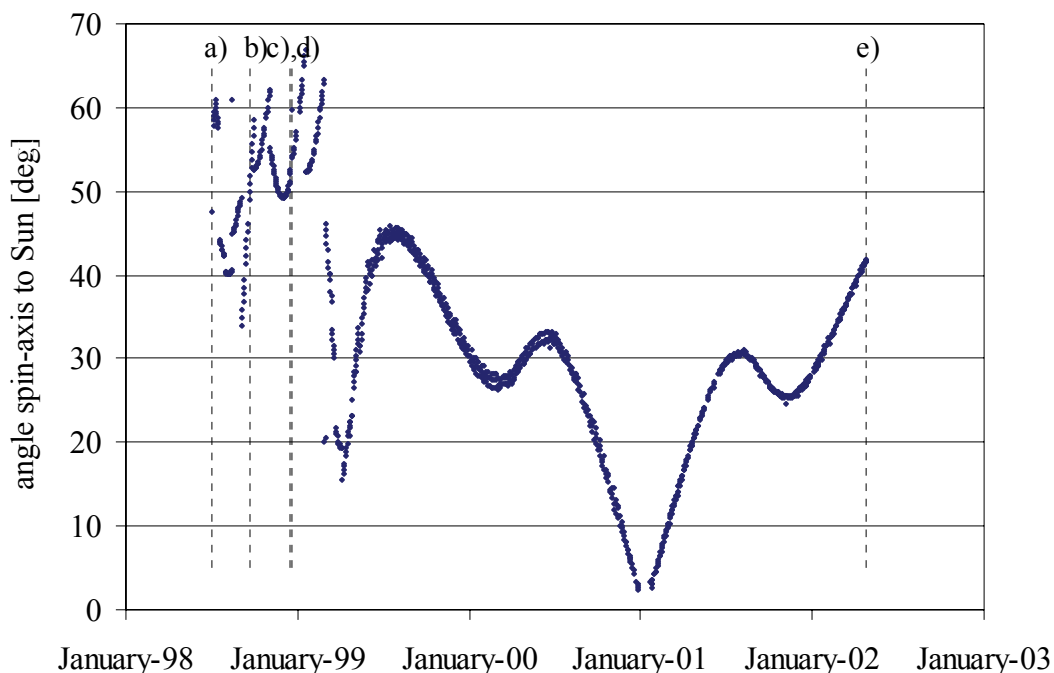


Figure 6-1: Angle of the NOZOMI spin-axis to the Sun over mission time

For most of the mission time, the angle between the NOZOMI spin-axis to the Sun was lower than 45° , which was necessary to ensure sufficient power generation by the solar panels. For angles higher than 45° , like in 1998 and early 1999, direct sunlight was falling into the MDC sensor box due to NOZOMI's spatial configuration and may have produced noise signals due to photo-ionization of the inner sensor box surfaces. The double and even triple lines since March 1999 are a result of the frequently (every 3-4 days) conducted attitude maneuvers that were necessary to keep the NOZOMI spin-axis and thus high-gain antenna pointing to Earth.

Every noise signal triggered has to be processed by the MDC electronics as described in paragraph 3.2.2. As shown in Figure 3-3, noise signals triggered and discarded by the KO-criteria cause an instrument dead time of 65 ms, while signals passing the KO-criteria cause an even higher instrument dead time of 120 ms. During periods of high noise rates, the total

instrument dead time must eventually be considered for further quantitative analysis and determination of dust flux.

Several periods of very high noise rates (steep rise of the noise count NC) were identified during the whole mission, as shown in Table 6-1. The origin of these sporadic interferences remains unclear. As one possible source, solar eruptions were taken into account since such events cause a very high proton flux and therefore may be recorded by the MDC as a series of noise events (as mentioned in paragraph 2.3.2, a solar eruption and the following very high proton flux was made responsible for the fatal NOZOMI system failure). In addition, the time span of the MDC high noise periods of several hours to a couple of days meets the usual time span of solar events. To verify this assumption, coincidences between scientifically proven solar eruptions observed by the SOHO spacecraft and periods of high noise recorded by the MDC were examined. This only makes sense for orbital configurations during which SOHO and NOZOMI are located within the same Sun centered solid angle interval, which is given e.g. during NOZOMI's first six months mission time where NOZOMI was in Earth orbit. SOHO is located around the Lagrange point between Earth and Sun. During this time span, none one of the five identified solar events observed by SOHO could be associated clearly to a certain period of high noise recorded by the MDC. Therefore, solar events must be excluded as a possible source of high noise recorded by the MDC. Other possible sources of high noise rates like the NOZOMI electrics and electronics itself were not examined due to missing information.

Table 6-1: Detector dead time

Period	dNC	dEC	max. / min. / av. dead time [%]
02/06/99-14/06/99	83000	2156	5.6 / 0.7 / 3.2
08/11/99-28/11/99	572000	29405	14.5 / 1.3 / 5.3
22/08/00-28/11/00	727000	23562	7.1 / 0.3 / 2.7
16/08/01	9000	105	1.7 / 1.7 / 1.7

Nevertheless, the total detector dead time caused by the high noise rates was determined for the most significant high noise periods, for details see Hübner [Hüb2003]. The results of this analysis are shown in Table 6-1. The highest determined detector dead time during the whole mission is 14.5% and occurs only once on November 8, 1999 for a period of about six hours, while during the other analyzed high noise periods the detector dead time varies between less than 1% and nearly 6%. For the latter analysis of dust flux, the detector dead time needs not to be considered in any way since the overall dead time was much lower than 1%.

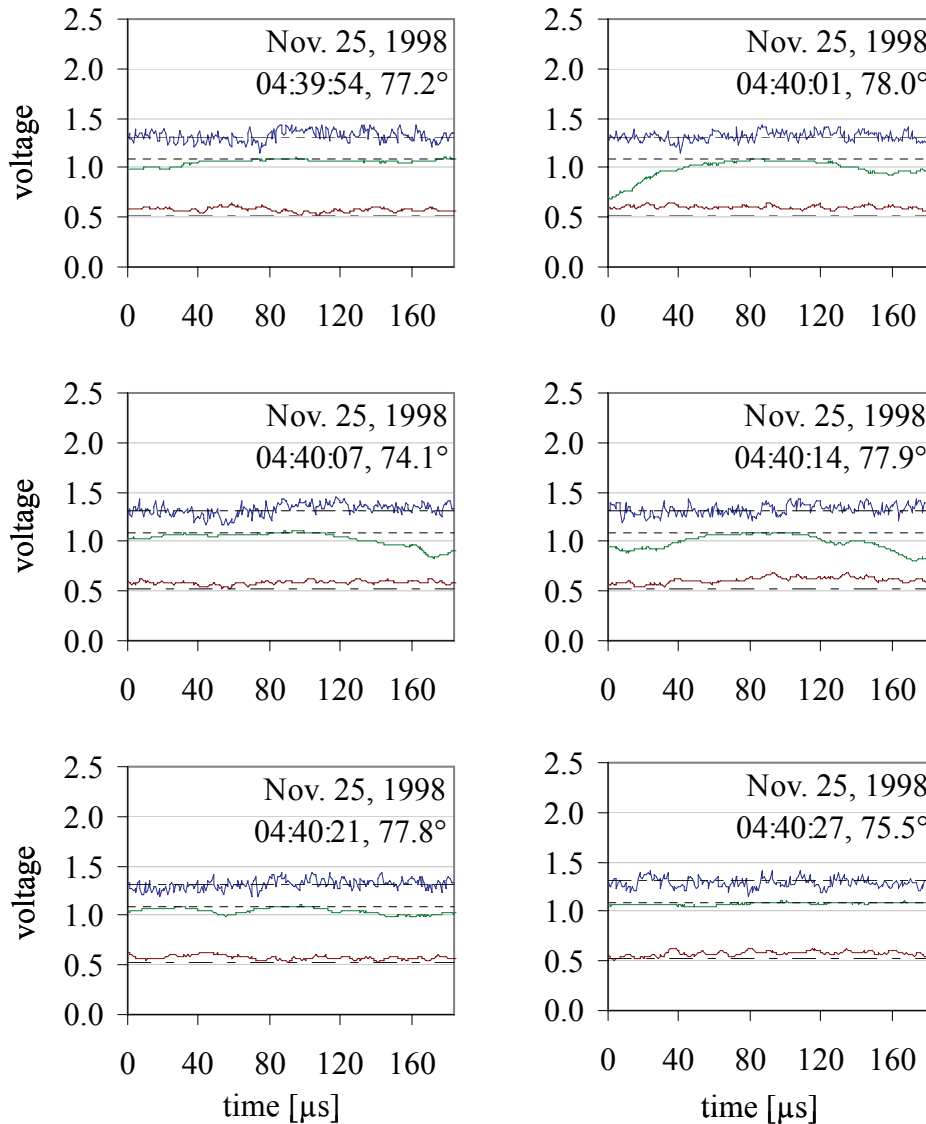


Figure 6-2: A series of noise signals with period \approx NOZOMI spin-period
 Signal series like the one shown here with nearly equal signal shape and time intervals of one or more NOZOMI spin periods were identified throughout the NOZOMI mission time. Mean interval between the signals shown is 6.67 sec, NOZOMI spin-rate on Nov. 25, 1998 was 9.16 rpm or 6.55 sec/revolution, respectively, as derived from NOZOMI attitude data. Signal identifiers from top left to bottom right are 98112506-3 to 98112506-8. For all these signals, housekeeping data showed good experiment condition.

A first look at the noise data showed that many groups of noise signals with similar shape and at time intervals of about the NOZOMI spin rate can be identified, see Figure 6-2 for an example. Because of this observation, the spin dependency of the noise signals was investigated further.

In a first approach, all 20538 signals recorded by the MDC during the mission were sorted into one-degree spin angle intervals. The result is shown in Figure 6-4 (top chart). As can be seen, the noise signals are not equally distributed over the spin angle. Around spin angles of

0° to 60°, a higher number of noise signals were recorded than around spin angles of 180° to 240°. This behavior can ad hoc be explained as being caused by an interference of the MDC experiment with radiation or particle streams originating from the Sun, e.g. sunlight, since at a spin angle of 0° the NOZOMI side panel #8 where the MDC is mounted points towards the sun for most orbital configurations. From previous missions, it is known that direct sunlight causes noise events when entering the MDC sensor box. In contrast, the strong peak at about 128° to 130° degrees cannot be explained in this manner since at those spin angles the MDC experiment is protected from sunlight by the NOZOMI body.

To separate spin-dependent noise signals from spin-independent noise signals, a simple filter algorithm was applied on the whole set of noise signals that identifies all signals as spin-dependent that have temporal neighbors (up to the fifth neighbor) with time differences of whole-numbered multiples (up to five) of the actual NOZOMI spin rate within a 5° interval. The result is shown in Figure 6-4 (middle and bottom chart). By this simple analysis, about a third of all noise signals are identified as being spin-dependent. While the principal distribution of the remaining spin-independent noise signals is constant over the whole angular range, the peak at 128° to 130° can not completely separated from the spin-independent noise data by this simple filtering method.

In Figure 6-3, the noise signals are again sorted into intervals of 1° width in spin-angle, but were separated into time spans of half-years previously. This analysis shows that the peak at 128° to 130° is not present during the whole mission time but vanishes during the periods I/2000, I/2001 and II/2001.

With the available information, it can only be assumed that the peak originates from some reflections of sunlight on parts of the NOZOMI body. A detailed analysis would require a three dimensional model of the completely integrated NOZOMI body with unfolded solar panels, and a simulation of the reflections that can occur with respect to the real NOZOMI attitude. This was not performed for the MDC-NOZOMI mission since no detailed model including surface characteristics of the MLI was available for the NOZOMI body. Thus, the origin of the noise peak at 128° to 130° still remains unclear.

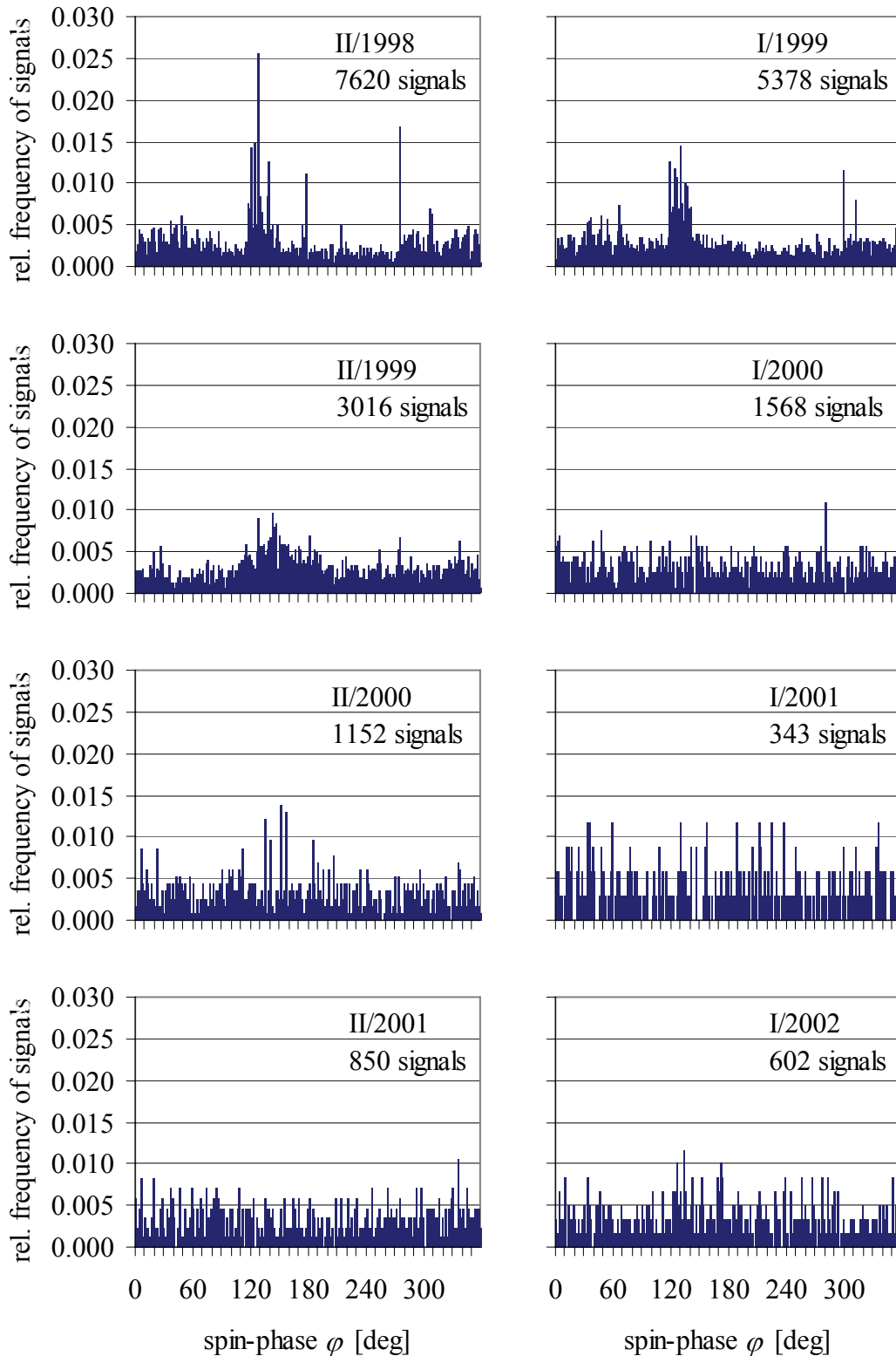


Figure 6-3: Distribution of noise signals over spin-phase, half years

Relative frequency of noise signals over spin-angle, separated into time spans of half years. During 5 of these time spans, a peak of noise data can be identified at 128° to 130° spin angle. During time spans that lack this peak, the overall distribution of the noise signals is nearly constant.

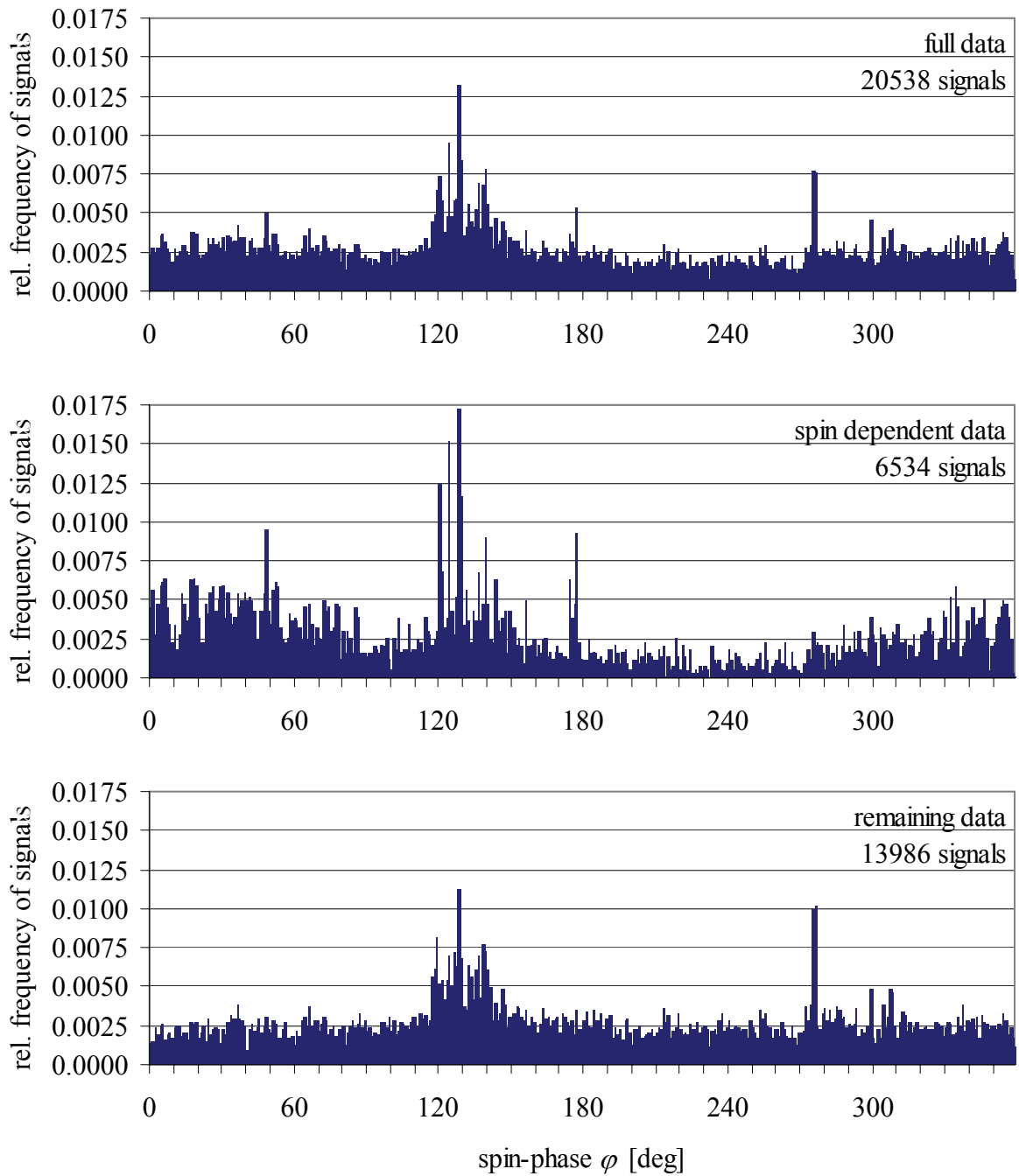


Figure 6-4: Distribution of noise signals over spin-phase, spin-dependency

The top chart was created from the whole set of noise data, while the middle and bottom chart represent the spin-dependent (one third) and spin-independent (two third) component of the noise data as identified by a simple filtering algorithm (see text for details)

To get a deeper understanding of the patterns and the origin of the noise signals recorded by the MDC, a hierarchical cluster analysis was performed on the MDC noise signals. Cluster analysis is a powerful standard method to identify groups (or clusters, respectively) of data sets that belong together due to certain similarities in a large amount of data sets, see Deichsel

& Trampisch [Dei1985] for more information. While in a two- or three-dimensional space clusters can easily be identified by a human experimenter (see also Figure 6-5), this is impossible for higher dimensions due to the limits of visualization options and human imagination, thus an analytical method is required. As an example, in archaeological science cluster analysis is used to identify vessels or shards from archaeological excavation sites by associating them to clusters of already identified vessels whose cultural, temporal and regional origin is known (the author was involved in a research project on this subject that was carried out at the nuclear research reactor of the Technische Universität München in Garching, Germany). As specific properties of the shards, the chemical composition of the material was used, which was determined non-destructive by neutron activation analysis. The rates of selected chemical elements in the chemical composition of a certain shard were used to describe the properties of the shard and can be seen as a multi-dimensional state vector of the certain shard.

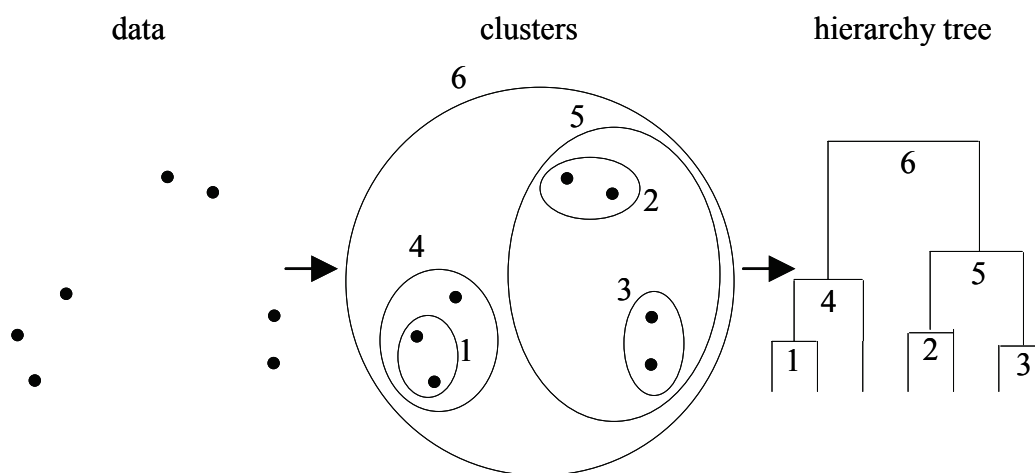


Figure 6-5: 2-Dimensional illustration of the principles of cluster analysis
A two-dimensional set of data points (left) is successively combined to clusters of data points (middle) that are ordered in a certain hierarchy (right). The result depends on the distance metric used for calculating the distance of two data points or data clusters, respectively, and the linkage method that defines what coordinate is used for a cluster containing more than one data point, see text for details.

In case of the MDC noise signals, a set of 55 values that were determined from the signal shape is used to describe a certain signal's properties. These 55 values can be interpreted as the state vectors of the signals in a 55-dimensional space. Like in any space of any dimension, a metric can be defined that enables the calculation of distances between certain coordinate points in that space, see below for description of some metrics used in cluster analysis. Also, scalar products (but not vectorial products which are defined in 3-dimensional space only) can be defined, that are calculated similar to the 3-dimensional scalar product by

$$\mathbf{a} \cdot \mathbf{b} = \sum_{i=1}^N a_i \cdot b_i, \quad (6-1)$$

whereas N is the dimension of the coordinate system.

Remark: In quantum mechanics, even infinite-dimensional state vectors in the infinite dimensional Hilbert space are used to describe the state of a physical particle or system, the scalar product is then given by

$$\langle a|b\rangle = \int_{x=-\infty}^{\infty} a(x) \cdot b(x) dx. \quad (6-2)$$

For cluster analysis, the distance of the coordinates or state vectors is required and can be calculated using different metrics.

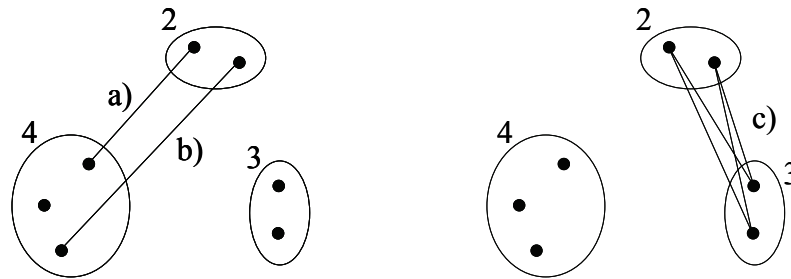


Figure 6-6: 2-Dimensional illustration of linkage methods

Three different linkage methods are available for the distance calculation of non-single clusters. a) Single linkage, the distance between the clusters #2 and #4 is the minimum distance of two data points. b) Complete linkage, the distance between the clusters #2 and #4 is the maximum distance of two data points. c) Average linkage, the distance between the clusters #2 and #4 is the mean distance of all data points.

For a given number M of data sets, a distance matrix of size $M \times M$ is calculated that contains the distances of each data set to every other data set. The two data sets closest to each other are then linked together to give a new data set that replaces the two original data sets. Different methods are available to determine the new coordinates of such a merged data set (cluster), see below. Then, the distances of this new data set to the now remaining $M-2$ data sets are calculated with respect to the metric and the coordinate determination method. These steps are iterated until there is only one top data set (cluster) left that contains all smaller data sets (clusters) down to the original single data sets. This linkage builds a hierarchical tree that is then analyzed to identify a reasonable number of clusters of reasonable size, the decision of what is reasonable number and size of the clusters must be made with respect to the given problem.

The cluster analysis described in the following was performed using the *MATLAB*[®] statistics toolbox. First, a cluster analysis was performed on a subset of all MDC noise data (all signals contained in the telemetry data files that were downloaded in the first six months of the year 2000) to evaluate the best distance metric and linkage method (coordinate determination method for non-single clusters for the distance calculation) for the given problem. All 55 values of the noise data were rescaled to give a absolute sum of 1 for each row in the full noise data set (this was necessary since the scale of the different values ranges from magnitudes of $\approx 10^{-16}$ for charge values and of ≈ 1000 for integrated values). From the available and established metrics and methods, three standard metrics (Euclidean, Minkowski and Chebychev) and three standard linkage methods (Single Linkage, Average Linkage and

Complete Linkage, see Figure 6-6) were chosen for evaluation. Also, for testing the significance of the cluster analysis result, a control data set of same size and dimension like the evaluation noise data set, but containing random data, was created and undertaken the same cluster analysis.

The distance between two coordinate points is calculated in the three different metrics by

$$\text{Euclidean distance: } d_{ij} = \sqrt{(x_i^1 - x_j^1)^2 + (x_i^2 - x_j^2)^2 + \dots + (x_i^N - x_j^N)^2}, \quad (6-3)$$

$$\text{Minkowski distance: } d_{ij} = \left[\sum_{k=1}^N |x_i^k - x_j^k|^p \right]^{\frac{1}{p}}, \quad (6-4)$$

$$\text{Chebychev distance: } d_{ij} = \max(|x_i^1 - x_j^1|, |x_i^2 - x_j^2|, \dots, |x_i^N - x_j^N|), \quad (6-5)$$

whereas N is the dimension of the coordinate system. In fact, the Euclidean distance is a special case of the Minkowski distance with $p = 2$, and the Chebychev distance is a special case of the Minkowski distance with $p \rightarrow \infty$ ($p = 1$ would give the so called City Block distance). In the following, $p = 3$ is used as exponent for the Minkowski distance.

The linkage methods that determines which cluster coordinates are used for later distance calculations are defined as

- Single Linkage: The distance between two non-singular clusters is the minimum of all distances between the members of the two clusters.
- Average Linkage: The distance between two non-singular clusters is the average of all distances between the members of the two clusters.
- Complete Linkage: The distance between two non-singular clusters is the maximum of all distances between the members of the two clusters.

For singular clusters (clusters that contain only one data set), the three linkage methods become identical. Three metrics and three linkage methods give nine different cluster analyses that need to be evaluated. The results are shown in Figure 6-7 and Table 6-2.

There were three steps from the source data set to the final clustering result. First, the distance matrix has to be calculated by the *MATLAB*[®] command

```
Dist=pdist(SpecVal_norm, 'euclid');
```

whereas the $M \times 55$ matrix variable `SpecVal_norm` contains the scaled source data. Next, the leaf nodes (singular clusters) have to be connected to higher nodes to build the hierarchy tree by the command

```
Link=linkage(Dist, 'complete');
```

Finally, the desired number of clusters is created by going down the hierarchy tree from the single top node until the maximum cluster number is reached, this is performed by the command

```
Clust=cluster(Link, 'maxclust', 100);
```

whereas the maximum number of clusters to be created is set to 100 in this example. Now, the vector variable `Clust` contains the cluster number each original signal was assigned to in the order of the original data set.

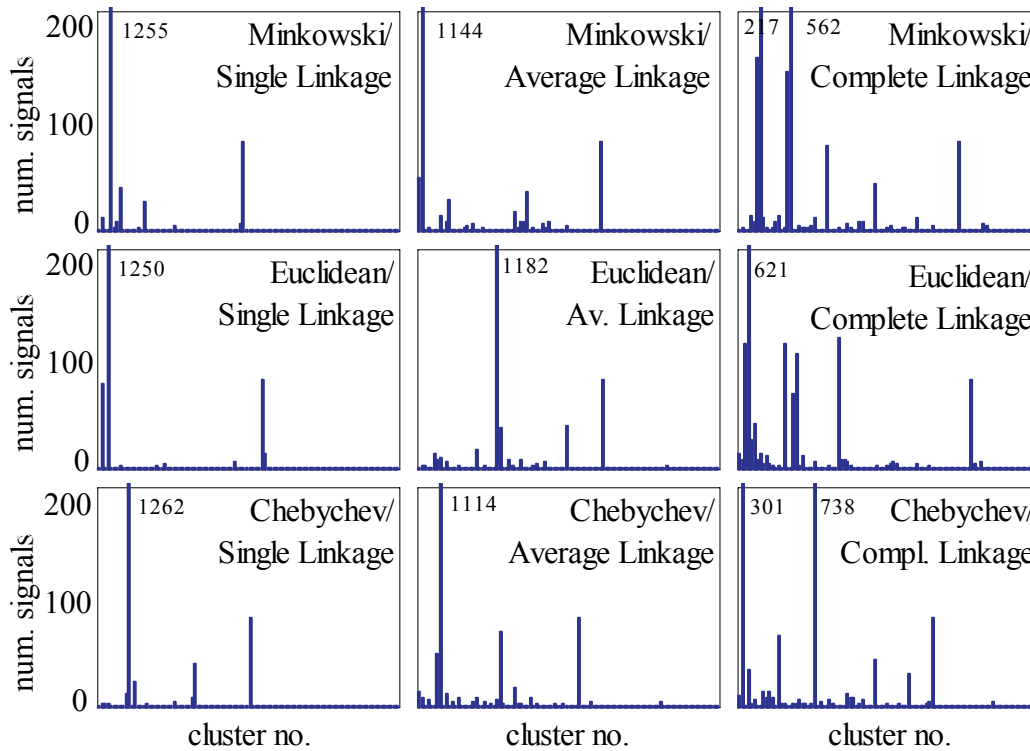


Figure 6-7: Results of the evaluation of metric and linkage method

For the given problem, the best choice of distance metric and linkage method is a combination that computes a large number of clusters that contain a large number of signals each.

Table 6-2: Results of the evaluation of metric and linkage method

Metric \ Linkage	Single Linkage	Average Linkage	Complete Linkage
Euclidean Dist.	6/1438	13/1433	27/1449
Minkowski Dist.	8/1440	15/1438	23/1436
Chebychev Dist.	7/1435	18/1439	22/1432

values given as: number of clusters containing ≥ 5 signals / number of signals in these clusters
total number of signals: 1556

Reasonable cluster size for the given problem is about 5 signals per cluster to several hundred signals per cluster as can be assumed by manual investigation of MDC noise data. A

reasonable number of identified clusters of the given reasonable size can be assumed to be 20 to 30, since by (time consuming and unreliable) manual analysis, 16 clusters were identified in the noise data recorded during first half year of the mission, see Hübner [Hüb2003] (collegiate thesis work on the MDC noise data). It can be assumed that automated cluster analysis will identify some more clusters that may have been overseen during manual analysis.

As can be seen in Figure 6-7 and Table 6-2, the combination of Euclidean metric and Complete Linkage gives the best fitting cluster analysis result with respect to the mentioned cluster size and cluster number mentioned above. Based on these results and some intuition (which, as in life, may not give the best choice but at least a good one), this combination was used in the following for a cluster analysis on the complete MDC noise data.

The significance of the cluster analysis can be seen in Figure 6-8 and Figure 6-9 on the following pages. Both, the identified clusters and the hierarchy tree derived from MDC noise data differ significantly from those derived from the random control data set.

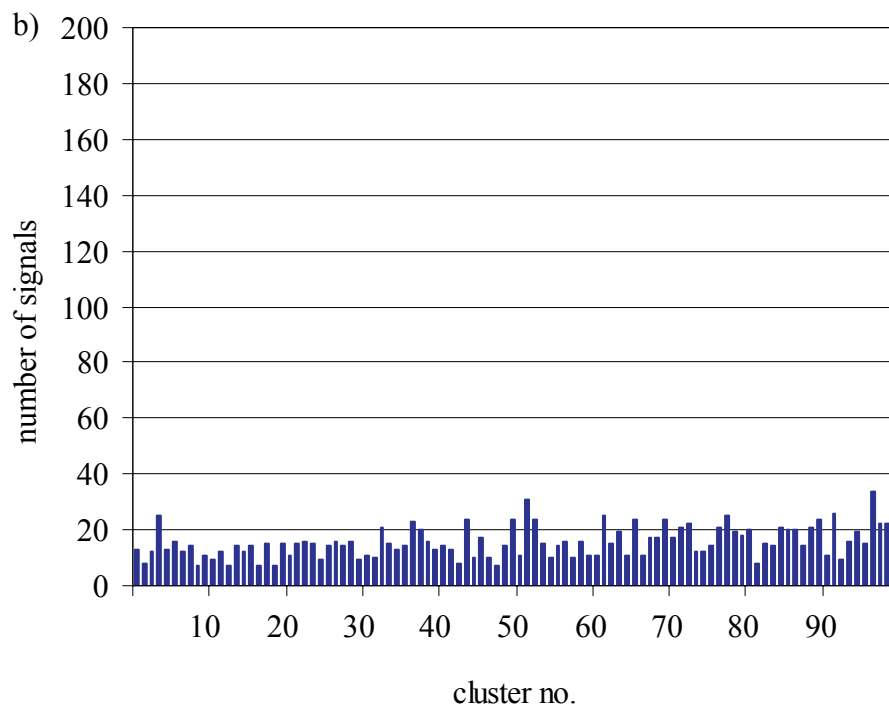
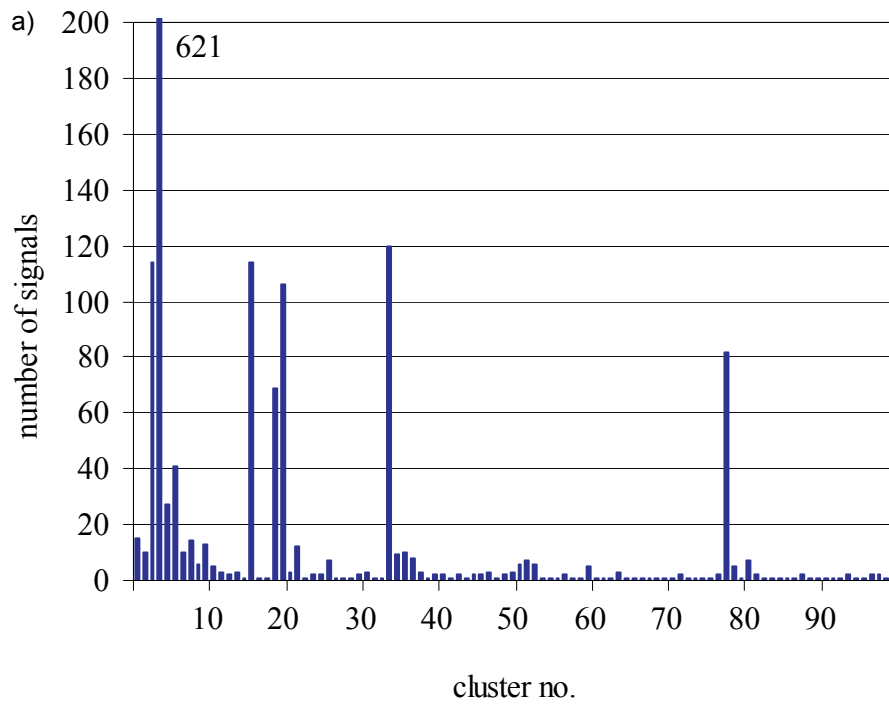


Figure 6-8: Cluster analysis result of MDC eval. noise data and control data
 While the random control data set b) does not show any pattern, the real data set a) shows a number of well defined clusters.

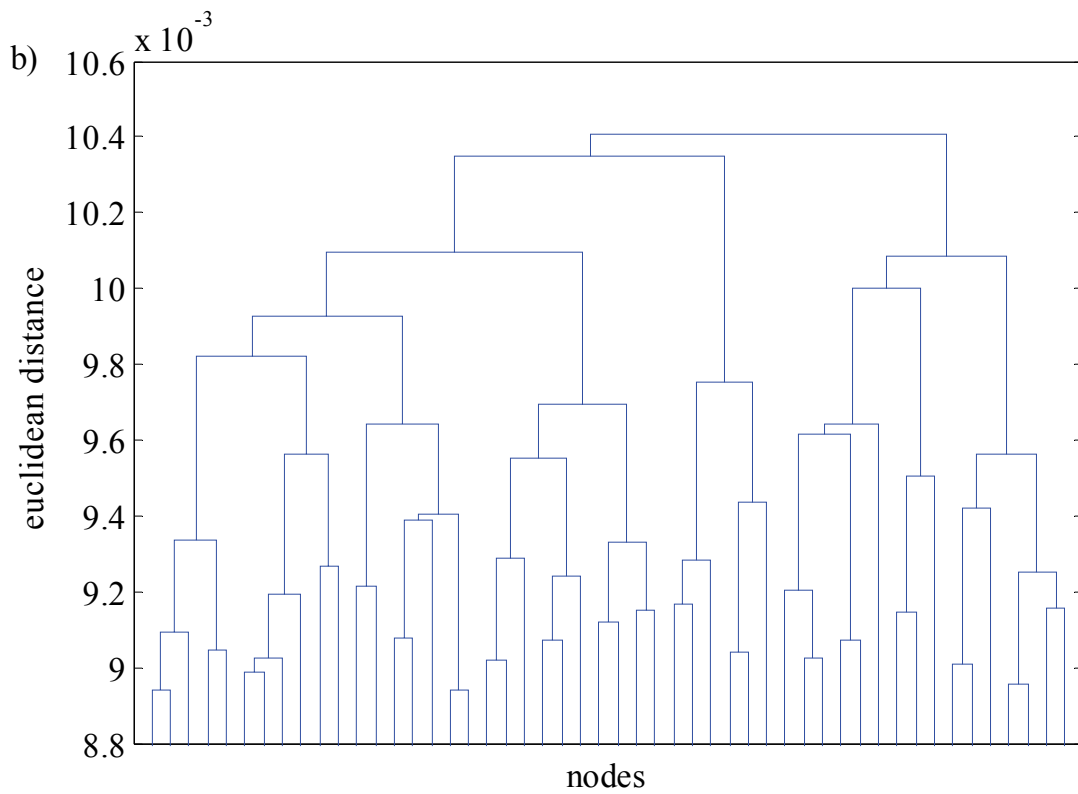
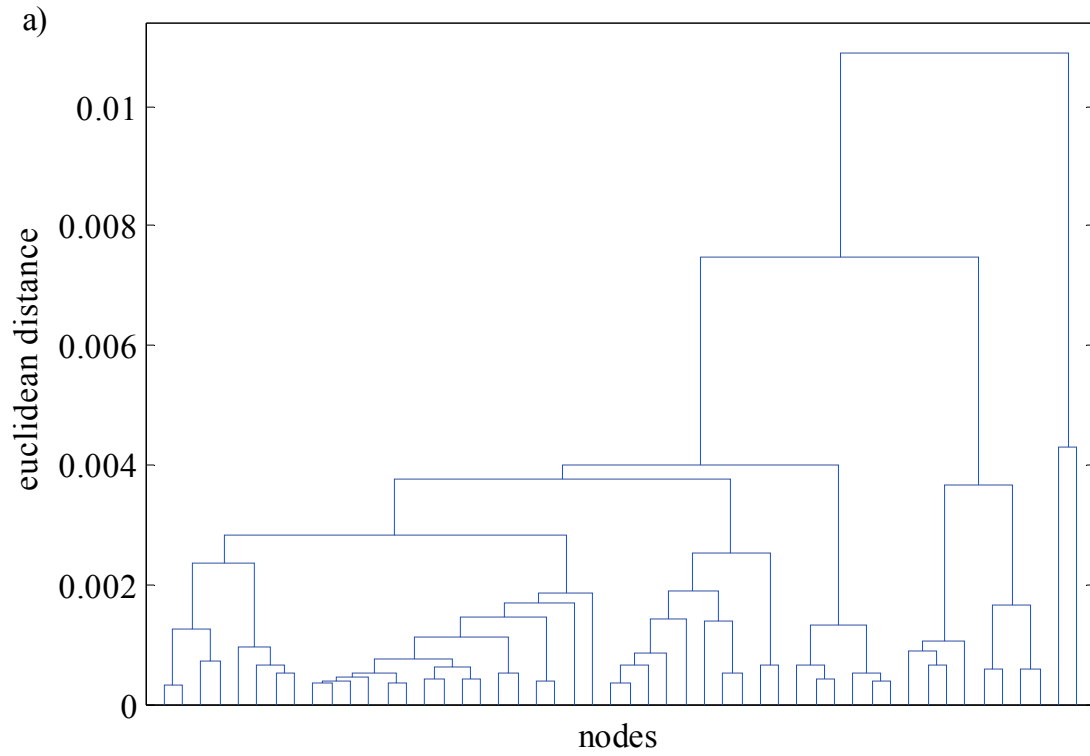


Figure 6-9: Hierarchy tree of MDC evaluation noise data and control data
 Also, the hierarchy tree of the control data set b) differs significantly from the
 hierarchy tree of the real noise data set a).

Further analysis of the noise signals could give evidence of the origin of the noise signals that are combined into one certain cluster. This was not performed for the NOZOMI mission due to a lack of information about possible sources of noise (e.g. electromagnetic interferences caused by the NOZOMI electrics and electronics itself).

The primary result of the cluster analysis performed on the full MDC data of 20538 signals is shown in Figure 6-10 (due to the large number of signals, this analysis had to be performed on a high performance system at the Leibniz Rechenzentrum LRZ; hierarchy tree visualization could not be created from this large data set with the available computer systems). Most conspicuous result is that more than two third of all signals can be found in one single cluster (no. 42) containing 15683 signals. For further analysis of the data contained in this cluster, the data had to be extracted from the remaining data and clustered separately a second time, since a simple increase of the number of clusters did not give a better separation of the large cluster, but resulted in further disintegration of smaller clusters.

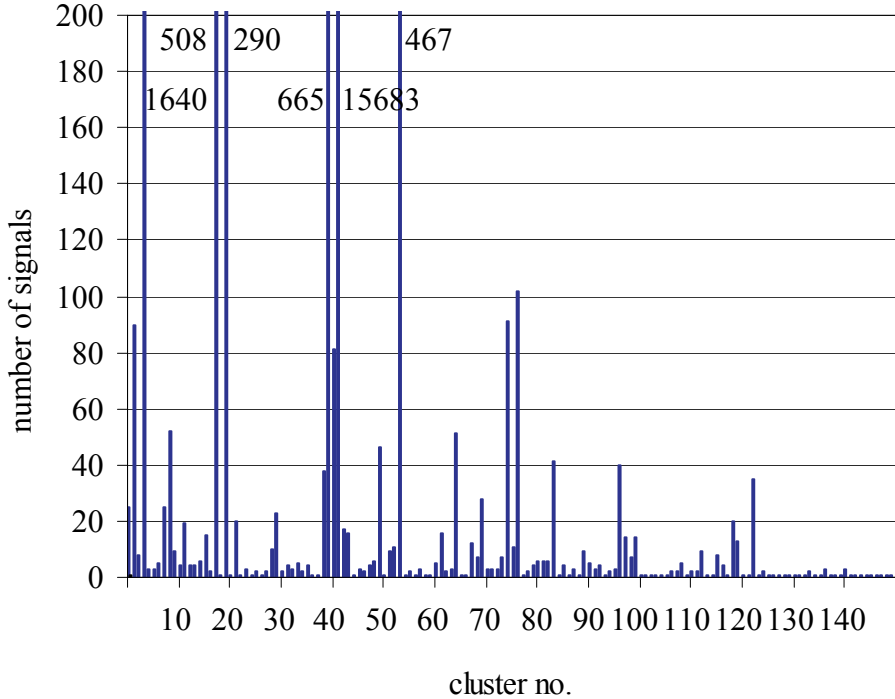


Figure 6-10: Cluster analysis result of the full MDC data

Clustering of the full MDC data gave the result shown above. The numbers next to the bars exceeding a value of 200 indicate the number of signals in the specific cluster. 15 clusters consist of 40 signals or more. From the 20538 signals, about two third (15683 signals) are sorted into one single cluster. The data in this large cluster was extracted from the full data and clustered separately.

In Table 6-3, the identified impact signals during the year 1998 are crosschecked against the size of the clusters they were assigned to. Since a real impact signal is a result of a single, individual impact event, it can be assumed that real impact signals will be most likely found in clusters containing only a few signals. Most impact signals are indeed assigned to clusters

containing 12 signals or less, from the eight remaining impact signals, three are assigned to the large cluster no. 42. In clusters no. 86 and 73, all signals are real impact signals.

Table 6-3: Clustering results, real impact signals

Imp. No.	Cluster No.	Σ signals
98071101-26	49	6
98071601-3	40	665
98073001-5	47	2
98073101-29	86	4
98080701-3	50	46
98082201-8	68	12
98090501-14	68	12
98092201-9	73	3
98092201-23	73	3
98101401-21	113	9
98102701-37	50	46
98110901-17	42	15683
98110901-29	73	3
98111001-1	42	15683
98111701-8	48	4
98111801-1	125	2
98111801-6	86	4
98112101-6	86	4
98120201-17	42	15683
98120301-9	113	9
98121801-35	86	4

As an example, cluster no. 2 was investigated further. Table 6-4 shows an excerpt of the signals assigned to cluster no. 2. Although this cluster contains signals from the whole mission time, 73 out of 90 signals in this cluster are found in series of more than four signals that occur within a few hours. Altogether, eight of such series were identified in cluster no. 2, three of them are shown in Table 6-4. Except of signal no. 99110404-44, all signals were assigned quality keys from 90 to 96. The spin angle of the signals shows a quite mysterious behavior within the series of signals, a nearly constant rise of the signal's spin angle can be observed from the first signal of a series to the last. Until now, this behavior could not be traced back to any known properties of the spacecraft/MDC system or its orbital attributes. In addition, no artifacts from data analysis could be identified that would explain this phenomenon.

Table 6-4: Signals assigned to cluster no. 2, excerpt

Imp. No.	Cluster No.	Date	Time	Quality	Spin Angle
...
98112502-35	2	25-Nov-98	04:09:31	95	8.8
98112502-38	2	25-Nov-98	04:09:38	93	15.1
98112502-39	2	25-Nov-98	04:09:44	93	6.5
98112505-9	2	25-Nov-98	04:30:24	92	51.2
98112505-24	2	25-Nov-98	04:31:16	90	59.1
98112505-26	2	25-Nov-98	04:31:23	91	60.5
98112505-28	2	25-Nov-98	04:31:30	93	60.6
98112507-41	2	25-Nov-98	04:54:13	90	110
...
98120203-4	2	2-Dec-98	05:06:07	92	25.1
98120203-18	2	2-Dec-98	05:06:53	91	26.9
98120206-22	2	2-Dec-98	05:23:17	94	53.8
98120206-27	2	2-Dec-98	05:23:36	92	54
98120207-21	2	2-Dec-98	05:28:31	92	65.1
98120210-4	2	2-Dec-98	05:53:14	90	139.5
98120210-9	2	2-Dec-98	05:53:33	93	130.5
98120212-12	2	2-Dec-98	06:27:59	91	243.9
98120212-33	2	2-Dec-98	06:31:03	92	262.5
...
99110402-3	2	4-Nov-99	07:24:12	92	4.6
99110402-10	2	4-Nov-99	07:24:43	91	0.3
99110402-5	2	4-Nov-99	07:43:09	91	91.2
99110404-27	2	4-Nov-99	08:54:08	96	58.6
99110404-36	2	4-Nov-99	08:56:15	92	80.3
99110404-40	2	4-Nov-99	08:56:31	95	80.2
99110404-44	2	4-Nov-99	08:56:47	105	78.9
99110404-45	2	4-Nov-99	08:56:54	90	74.8
99110404-51	2	4-Nov-99	08:59:25	91	97.1
99110405-7	2	4-Nov-99	09:19:43	92	249.9
99110405-19	2	4-Nov-99	09:21:34	91	253.9
99110405-21	2	4-Nov-99	09:21:41	91	253.5
99110405-26	2	4-Nov-99	09:23:48	90	282.7
99110405-31	2	4-Nov-99	09:28:41	94	323.4
99110405-35	2	4-Nov-99	09:28:57	91	321.9
...

Two signals of each of the three series in Table 6-4 are shown in Figure 6-11. The similar signal shape can be seen easily. Housekeeping information for all these signals showed good experiment condition.

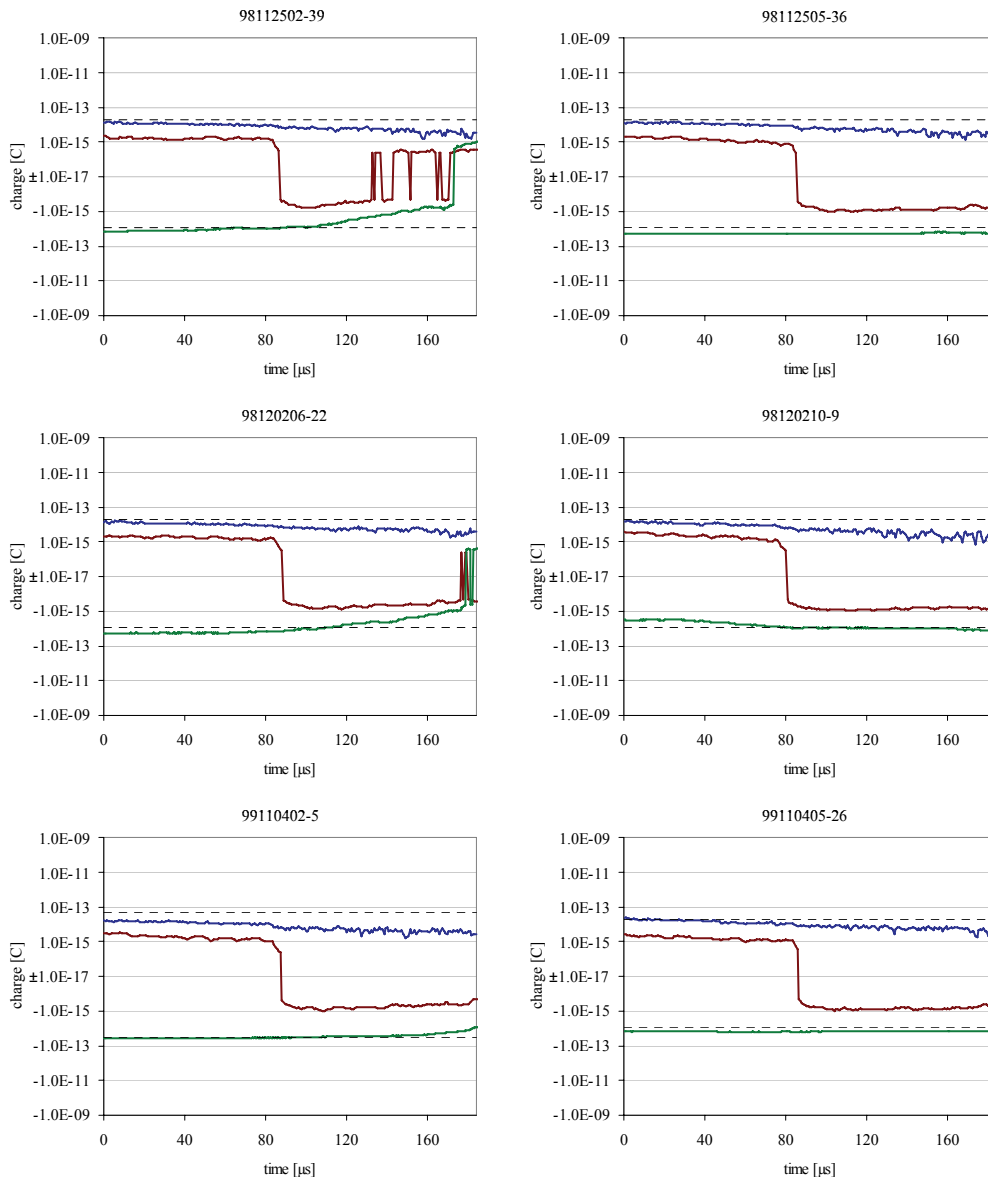


Figure 6-11: Signals assigned to cluster no. 2, signal shape

Signal shapes from cluster no. 2; top, middle and bottom pairs represent signals from the first, second and third series shown in Table 6-4, respectively. From each series, the third and the antepenultimate signal were chosen for this visualization.

Another attempt to classify noise data was made by Sauer [Sau2004] in her collegiate thesis work on the MDC noise data, where the noise signals were identified by a triple code (CIC, CEC, CNC) that describes the shape of the three signal channels and gives a unique identifier for clusters of signals of similar shape. Although this method could be automated by a self-developed proprietary software solution, cluster analysis as a standard method was favored.

In addition, since cluster analysis showed good results when performed on the MDC-NOZOMI noise data, clustering of the MDC-BremSat data can be assumed to give important help to understand the data and noise data produced by this MDC mission. As mentioned before, the MDC-BremSat mission suffered from a high amount of noise data that may have

been caused by atmospheric or charged particle disturbances. See Kellerer [Kel2004] (collegiate thesis work on the MDC-BremSat data) for a review of the MDC-BremSat data.

6.2.2 MDC view-axis determination from NOZOMI attitude

NOZOMI flight data were provided by ISAS/JAXA. Orbital data were given as Cartesian vectors $\mathbf{r}_{\text{nozomi}} = (r_1, r_2, r_3)^T$ based on the Earth-equatorial reference system (indexed as “eeq” in the following, with the Earth as center body) from launch until January 6, 1999, several data per day at different times, and the Earth-ecliptic reference system (indexed as “eec” in the following, with the Sun as center body) from January 6, 1999, one data per day at midnight (the index “nozomi” is omitted in the following for NOZOMI orbital data). Attitude data were given as tuples (λ, β) where λ is longitude (mathematically positive rotation around the z-axis) and β latitude (mathematically negative rotation around the y-axis) of the NOZOMI spin-axis, also one data per day at different times and based on the Earth ecliptic reference system. Since NOZOMI is spin-stabilized, the spin-angle φ is not given with the attitude data but, in case of the MDC, is provided by the satellite’s AOCs as a parameter of the housekeeping data attached to the scientific data.

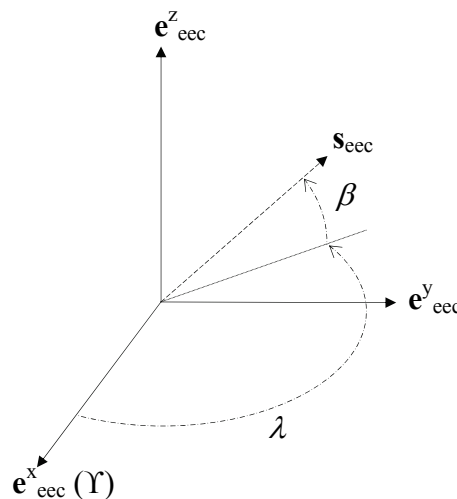


Figure 6-12: Illustration of NOZOMI attitude (λ, β) and spin-axis vector \mathbf{s}_{eec}
 NOZOMI attitude is given as (λ, β) , whereas β is measured from the positive x-axis in mathematically negative direction (rotation around y-axis) and λ is measured from the positive x-axis in mathematically positive direction (rotation around z-axis). The spin-axis vector \mathbf{s}_{eec} is calculated from λ, β as described in equation (6-9).

To allow easier handling of NOZOMI orbital data, all orbital data that were given in the Earth equatorial reference system were transformed to the Earth ecliptic reference system first. This can be performed by a simple rotation of the Earth equatorial coordinates of NOZOMI orbital data by the mean angle of the Earth’s spin axis to the ecliptic plane, given as $\varepsilon = 23.5^\circ$, and vectorial addition of the current Earth orbital position $\mathbf{r}^{\text{Earth}}$, see Figure 6-13. Higher orders of ε and further corrections that are caused by precession and nutation of the Earth’s spin axis, and perturbations by other celestial bodies are not concerned here since the mean value is sufficient for the required accuracy. The transformation from Earth equatorial to Earth ecliptic reference system of orbital coordinates is given by

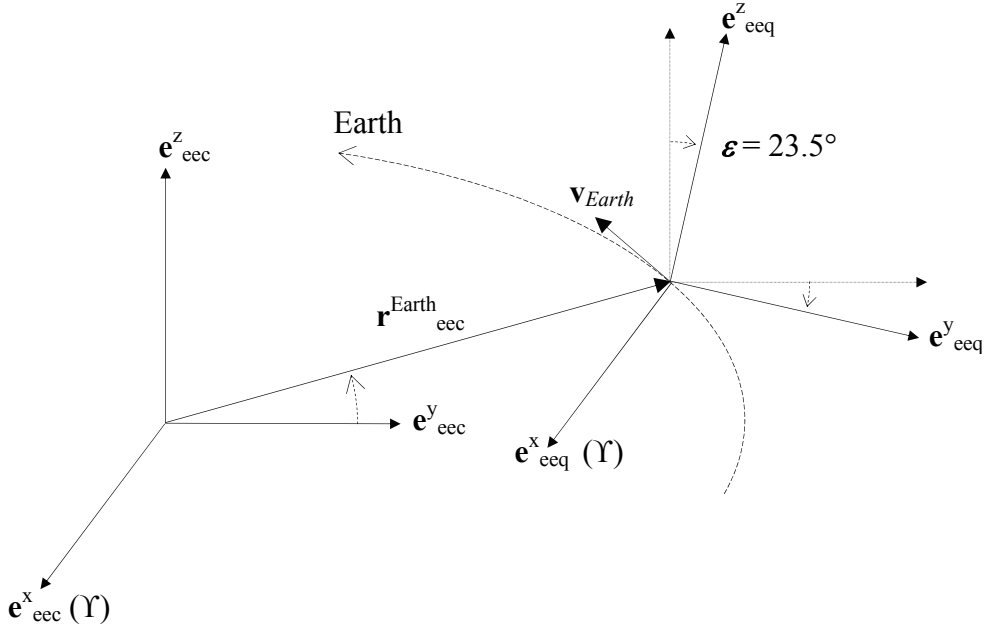


Figure 6-13: The Earth-ecliptic and the Earth-equatorial reference system
The Earth-equatorial reference system is tilted by $\varepsilon = 23.5^\circ$ against the Earth-ecliptic reference system, fixed to the center of the Earth and moving with the Earth. In both reference systems, the e^x -axis is pointing towards the vernal equinox (point of Aries Υ).

$$\mathbf{r}_{\text{eec}} = \mathbf{A}_{\text{eec,eeq}} \mathbf{r}_{\text{eeq}} + \mathbf{r}_{\text{eec}}^{\text{Earth}}, \quad (6-6)$$

whereas

$$\mathbf{A}_{\text{eec,eeq}} = \begin{pmatrix} 1 & 0 & 0 \\ 0 & \cos \varepsilon & \sin \varepsilon \\ 0 & -\sin \varepsilon & \cos \varepsilon \end{pmatrix}. \quad (6-7)$$

Earth and Mars orbital data $\mathbf{r}_{\text{eec}}^{\text{Earth}}$ and $\mathbf{r}_{\text{eec}}^{\text{Mars}}$ (from January 1, 1998 until December 31, 2004) that were needed for this transformation and for latter visualization were derived from the jpleph410 ephemeris data, which were provided by NASA's Johnson Propulsion Laboratory (JPL).

The positions \mathbf{r}_{eec} , directions of the spin-axis \mathbf{s}_{eec} and velocities \mathbf{v}_{eec} of NOZOMI at a given impact time t^{imp} were then determined from the provided flight data by the linear interpolations

$$\mathbf{r}_{\text{eec}} = \frac{\mathbf{r}_{\text{eec}}^{\text{f}} - \mathbf{r}_{\text{eec}}^{\text{p}}}{t^{\text{f}} - t^{\text{p}}} (t^{\text{imp}} - t^{\text{p}}) + \mathbf{r}_{\text{eec}}^{\text{p}} = \begin{pmatrix} \overline{r_1} \\ \overline{r_2} \\ \overline{r_3} \end{pmatrix} = \begin{pmatrix} \frac{r_1^{\text{f}} - r_1^{\text{p}}}{t^{\text{f}} - t^{\text{p}}} (t^{\text{imp}} - t^{\text{p}}) + r_1^{\text{p}} \\ \frac{r_2^{\text{f}} - r_2^{\text{p}}}{t^{\text{f}} - t^{\text{p}}} (t^{\text{imp}} - t^{\text{p}}) + r_2^{\text{p}} \\ \frac{r_3^{\text{f}} - r_3^{\text{p}}}{t^{\text{f}} - t^{\text{p}}} (t^{\text{imp}} - t^{\text{p}}) + r_3^{\text{p}} \end{pmatrix}, \quad (6-8)$$

$$\mathbf{s}_{\text{ecc}} = \begin{pmatrix} \bar{s}_1 \\ \bar{s}_2 \\ \bar{s}_3 \end{pmatrix} = \begin{pmatrix} \cos \bar{\lambda} \cos \bar{\beta} \\ \sin \bar{\lambda} \cos \bar{\beta} \\ \sin \bar{\beta} \end{pmatrix}, \quad \begin{pmatrix} \bar{\lambda} \\ \bar{\beta} \end{pmatrix} = \begin{pmatrix} \frac{\lambda^f - \lambda^p}{t^f - t^p} (t^{\text{imp}} - t^p) + \lambda^p \\ \frac{\beta^f - \beta^p}{t^f - t^p} (t^{\text{imp}} - t^p) + \beta^p \end{pmatrix}, \quad (6-9)$$

and

$$\mathbf{v}_{\text{ecc}} = \frac{\mathbf{r}_{\text{ecc}}^f - \mathbf{r}_{\text{ecc}}^p}{t^f - t^p}, \quad (6-10)$$

whereas the indices f and p define the temporally following and previous orbital and attitude data point, respectively. With respect to the much higher inaccuracy of the MDC data analysis process, this linear interpolation gives sufficient accuracy of the NOZOMI flight data for further data interpretation (e.g. in case of a circular orbit, the maximum deviation from the exact orbital position is $\hat{r}/r = \cos(2\pi/n) > 0.9999$ with $n = 500$ data points per orbit, where \hat{r} and r are the interpolated and real orbital radius, respectively). In most cases, the NOZOMI flight data around the impact time of the recorded and analyzed impacts show a low gradient, and linear interpolation will give reliable results. Only some impacts were recorded during or temporally near orbital maneuvers or a swing-by phase, both events lead to large gradients in orbital and attitude data and therefore unreliable interpolation results.

To determine the complete NOZOMI attitude at the given impact time t^{imp} , the directions of the NOZOMI x-axis, and y- or z-axis are needed. A reference system “noz” is defined that is fixed to the NOZOMI body, where the x-axis points in the direction of the NOZOMI spin-axis, and the y-axis points from the NOZOMI center of mass in the direction of the side panel #8 where the SSAS (Spin-type Sun Aspect Sensor) and the MDC are located (this is different from the NOZOMI engineering reference system, where the z-axis points in the direction of the NOZOMI spin-axis). Spin-phase $\varphi = 0$ is defined as the attitude when the Sun passes by the SSAS view-plane. The NOZOMI x-axis is given as $\mathbf{x}_{\text{ecc}} = \mathbf{s}_{\text{ecc}}$, while the direction of the y-axis can be calculated from the orbit position \mathbf{r}_{ecc} and the spin-axis \mathbf{s}_{ecc} for spin phase $\varphi = 0$ as

$$\mathbf{y}_{\text{ecc}} = \left[\frac{(\mathbf{r}_{\text{ecc}} \times \mathbf{s}_{\text{ecc}}) \times \mathbf{s}_{\text{ecc}}}{|\mathbf{r}_{\text{ecc}}|} \right]_{\varphi=0}. \quad (6-11)$$

For the determination of the flight direction of an impacting particle, the view axis of the MDC in the Earth ecliptic reference system must be calculated from the NOZOMI configuration, attitude data and orbital data. It is common sense in dust sciences that the flight direction of an impacting particle is defined as the opposite direction of a dust experiment’s view axis. In the MDC instrument’s reference system (indexed as “mdc” in the following), the flight direction of a particle is therefore given as $\mathbf{n}_{\text{mdc}} = (-1, 0, 0)^T_{\text{mdc}}$ if the positive x-axis is defined to be the view axis (the other axes need not to be defined here). First, this must be transformed to the NOZOMI fixed reference system “noz”. In this system, the NOZOMI spin-axis is given as $\mathbf{s}_{\text{noz}} = (1, 0, 0)^T_{\text{noz}}$, and the MDC view axis is rotated by $\gamma = 0^\circ$ around the NOZOMI x-axis (SSAS and MDC are having the same view axis), and $\delta = 135^\circ$ around the NOZOMI z-axis. The opposite view direction of the MDC in this system is given by the transformation

$$\mathbf{n}_{\text{noz}} = \mathbf{A}_\gamma \mathbf{A}_\delta \mathbf{n}_{\text{mdc}}, \text{ or } \mathbf{n}_{\text{noz}} = \mathbf{A}_{\text{noz,mdc}} \mathbf{n}_{\text{mdc}}, \quad (6-12)$$

whereas $\mathbf{A}_{\text{noz,mdc}}$ is the transformation matrix from the MDC fixed reference system to the NOZOMI fixed reference system.

$$\mathbf{A}_\gamma = \begin{pmatrix} 1 & 0 & 0 \\ 0 & \cos \gamma & \sin \gamma \\ 0 & -\sin \gamma & \cos \gamma \end{pmatrix}, \mathbf{A}_\delta = \begin{pmatrix} \cos \delta & \sin \delta & 0 \\ -\sin \delta & \cos \delta & 0 \\ 0 & 0 & 1 \end{pmatrix}, \quad (6-13)$$

$$\mathbf{A}_{\text{noz,mdc}} = \mathbf{A}_\gamma \mathbf{A}_\delta = \begin{pmatrix} \cos \delta & \sin \delta & 0 \\ -\sin \delta \cos \gamma & \cos \delta \cos \gamma & \sin \gamma \\ \sin \delta \sin \gamma & -\cos \delta \sin \gamma & \cos \gamma \end{pmatrix}. \quad (6-14)$$

Now the NOZOMI spin-phase must be considered. The spin-phase of NOZOMI is given as $\varphi = 0 \dots 359^\circ$, where $\varphi = 0$ is defined as the rotational angle where the SSAS points towards the Sun. The transformation into the rotated reference system “noz φ ” is given as

$$\mathbf{n}_{\text{noz}\varphi} = \mathbf{A}_\varphi \mathbf{n}_{\text{noz}}, \text{ or } \mathbf{n}_{\text{noz}\varphi} = \mathbf{A}_{\text{noz}\varphi, \text{noz}} \mathbf{n}_{\text{noz}}, \quad (6-15)$$

with the transformation matrix

$$A_{\text{noz}\varphi, \text{noz}} = \begin{pmatrix} 1 & 0 & 0 \\ 0 & \cos \tilde{\varphi} & \sin \tilde{\varphi} \\ 0 & -\sin \tilde{\varphi} & \cos \tilde{\varphi} \end{pmatrix}. \quad (6-16)$$

The angle $\tilde{\varphi}$ must be calculated from the spin-phase φ with respect to the NOZOMI attitude and orbit position, respectively, as described in the following.

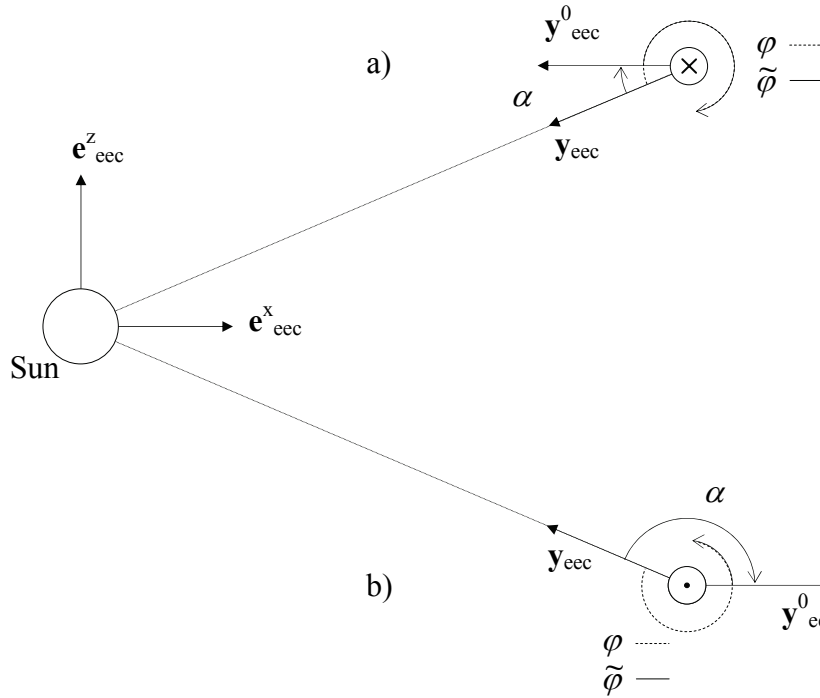


Figure 6-14: Illustration of correction angle α and spin-phase φ and $\tilde{\varphi}$

The determination of the correction angle α and the angles φ and $\tilde{\varphi}$ is shown for two different orbital configurations: a) NOZOMI is located north of the ecliptic plane, with the spin axis parallel to the positive y direction, and b) NOZOMI is located south of the ecliptic plane with the spin-axis parallel to the negative y direction. While the given spin-phase φ is measured from the y_{ecc} axis, the corrected spin-phase $\tilde{\varphi}$ is measured from the y^0_{ecc} axis. For configuration a) the angle $\tilde{\varphi}$ must be calculated by $\tilde{\varphi} = \varphi - \alpha$, for configuration b) by $\tilde{\varphi} = \varphi - (360^\circ - \alpha) = \varphi + \alpha$, because the rotation of the axis y_{ecc} is in mathematically negative direction for a) and in mathematically positive direction in b) as seen from the spin-axis.

The NOZOMI orbital plane is tilted against the Earth-ecliptic by about $\vartheta = 2.94^\circ$ during most of the interplanetary cruising phase until December 21, 2002, by $\vartheta = 6.21^\circ$ between the two Earth swing-by's on December 21, 2002 and June 19, 2003 and by $\vartheta = 0.06^\circ$ after June 19, 2003 (see Figure 2-15). These values were not given by ISAS/JAXA, but calculated from NOZOMI orbital data by

$$\vartheta = \frac{1}{n - (m - 10)} \sum_{t_n}^{t_{m-10}} \arccos \left[\left(\frac{\mathbf{r}(t_n)}{|\mathbf{r}(t_n)|} \times \frac{\mathbf{r}(t_{n+10})}{|\mathbf{r}(t_{n+10})|} \right) \cdot \mathbf{e}^z \right], \quad (6-17)$$

where the indices n and m define the first and last orbital data point for the desired period, respectively. These angles lead to a deviation of the direction of the y_{ecc} axis from the ecliptic plane, and require an additional coordinate transformation by a rotation around NOZOMI's x-axis that can be performed by a correction of the spin-phase φ , since the spin-phase is measured from the y_{ecc} axis. The direction of this axis is determined by $\varphi = 0^\circ$ when the Sun crosses the view-plane of the SSAS. To determine the correction angle α , first the NOZOMI y-axis y^0_{ecc} is determined from the given attitude data $(\bar{\lambda}, \bar{\beta})$ as

$$\mathbf{y}_{\text{ecc}}^0 = \begin{pmatrix} \cos \bar{\beta} \cos \bar{\lambda} & -\sin \bar{\lambda} & -\sin \bar{\beta} \cos \bar{\lambda} \\ \cos \bar{\beta} \sin \bar{\lambda} & \cos \bar{\lambda} & -\sin \bar{\beta} \sin \bar{\lambda} \\ \sin \bar{\beta} & 0 & \cos \bar{\beta} \end{pmatrix} \cdot \mathbf{e}_{\text{ecc}}^y = \begin{pmatrix} -\sin \bar{\lambda} \\ \cos \bar{\lambda} \\ 0 \end{pmatrix}_{\text{ecc}}. \quad (6-18)$$

The correction angle α is determined by

$$\alpha = \arccos(\mathbf{y}_{\text{ecc}}^0 \cdot \mathbf{y}_{\text{ecc}}). \quad (6-19)$$

The angle α already includes the possible discontinuous shift of the direction of the \mathbf{y}_{ecc} axis by 180° around \mathbf{s}_{ecc} (if \mathbf{s}_{ecc} is lying in the NOZOMI orbital plane), or fast move from $\approx 0^\circ$ to $\approx 180^\circ$ (if \mathbf{s}_{ecc} is not lying in the NOZOMI orbital plane) when the Sun passes by NOZOMI's stern or bow in longitudinal direction (see Figure 6-15), but not the direction into which the correction of φ has to take place.

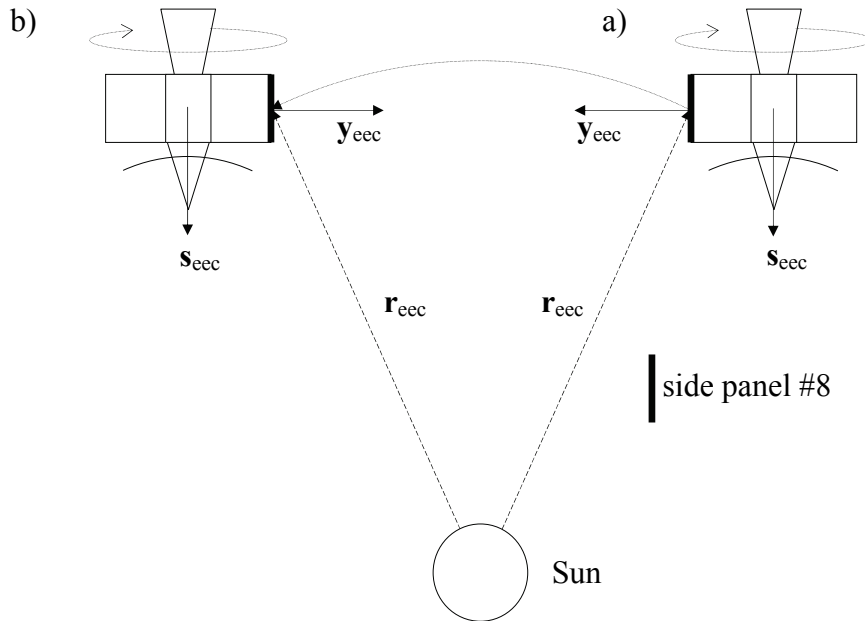


Figure 6-15: Illustration of the shift of the \mathbf{y}_{ecc} axis and the spin-phase φ
 Spin-phase $\varphi = 0^\circ$ occurs when the Sun passes by the view plane of the SSAS, the SSAS is located on the side-panel #8 like the MDC. If the Sun passes by NOZOMI's stern or bow, as it happens between positions a) and b), the \mathbf{y}_{ecc} axis defined by $\varphi = 0^\circ$ shifts about 180° .

The direction can easily be determined if an auxiliary vector

$$\mathbf{h}_{\text{ecc}} = \frac{\mathbf{y}_{\text{ecc}}^0 \times \mathbf{y}_{\text{ecc}}}{|\mathbf{y}_{\text{ecc}}^0 \times \mathbf{y}_{\text{ecc}}|} \quad (6-20)$$

is defined, that is either parallel or anti-parallel to the spin-axis \mathbf{s}_{ecc} . Then the angle $\tilde{\varphi}$ is finally given as

$$\tilde{\varphi} = \varphi + (\mathbf{h}_{\text{ecc}} \cdot \mathbf{s}_{\text{ecc}})\alpha, \quad (6-21)$$

where the scalar product of \mathbf{h}_{ecc} and \mathbf{s}_{ecc} evaluates either to +1 (\mathbf{h}_{ecc} parallel \mathbf{s}_{ecc}) or to -1 (\mathbf{h}_{ecc} anti-parallel \mathbf{s}_{ecc}). If the NOZOMI orbit and spin-axis were in the ecliptic plane, the angle α would always be exactly zero or 180°, respectively.

The last transformation is the transformation from NOZOMI's rotated reference system to the Earth ecliptic reference system, which is performed by

$$\mathbf{n}_{\text{ecc}} = \mathbf{A}_{-\bar{\lambda}} \mathbf{A}_{\bar{\beta}} \mathbf{n}_{\text{noz}\varphi} = \mathbf{A}_{\text{ecc,noz}\varphi} \mathbf{n}_{\text{noz}\varphi}, \quad (6-22)$$

$$\mathbf{A}_{\bar{\beta}} = \begin{pmatrix} \cos \bar{\beta} & 0 & -\sin \bar{\beta} \\ 0 & 1 & 0 \\ \sin \bar{\beta} & 0 & \cos \bar{\beta} \end{pmatrix}, \mathbf{A}_{-\bar{\lambda}} = \begin{pmatrix} \cos \bar{\lambda} & -\sin \bar{\lambda} & 0 \\ \sin \bar{\lambda} & \cos \bar{\lambda} & 0 \\ 0 & 0 & 1 \end{pmatrix}, \quad (6-23)$$

$$\mathbf{A}_{\text{ecc,noz}\varphi} = \mathbf{A}_{-\bar{\lambda}} \mathbf{A}_{\bar{\beta}} = \begin{pmatrix} \cos \bar{\beta} \cos \bar{\lambda} & -\sin \bar{\lambda} & -\sin \bar{\beta} \cos \bar{\lambda} \\ \cos \bar{\beta} \sin \bar{\lambda} & \cos \bar{\lambda} & -\sin \bar{\beta} \sin \bar{\lambda} \\ \sin \bar{\beta} & 0 & \cos \bar{\beta} \end{pmatrix}. \quad (6-24)$$

The different signs at λ and β result from the different mathematical directions in which λ and β are given. In summary, the opposite view axis direction of the MDC is calculated from the NOZOMI flight data at $t = t^{\text{imp}}$ ($\mathbf{r}_{\text{ecc}}, \bar{\lambda}, \bar{\beta}, \varphi$) and spatial configuration (γ, δ) by the transformation

$$\mathbf{n}_{\text{ecc}} = \mathbf{A}_{\text{ecc,noz}\varphi} \mathbf{A}_{\text{noz}\varphi,\text{noz}} \mathbf{A}_{\text{noz,mdc}} \mathbf{n}_{\text{mdc}}. \quad (6-25)$$

Finally, the absolute particle velocity \mathbf{u}_{ecc} is given by the vectorial subtraction

$$\mathbf{u}_{\text{ecc}} = u^{\text{imp}} \mathbf{n}_{\text{ecc}} - \mathbf{v}_{\text{ecc}}, \quad (6-26)$$

whereas u^{imp} is the scalar impact speed of the particle as derived from the impact data analysis, and \mathbf{v}_{ecc} is the current speed vector of NOZOMI at the given impact time t^{imp} .

If not specified, all vectors (coordinates and velocities) are given in the Earth-ecliptic reference system in the following paragraphs, and the index “ecc” is therefore omitted. MDC impact data during the Earth-Moon phase can easily be transformed back to the Earth equatorial reference system by the inverse of the transformation given in equation (6-6), and therefore can be analyzed and displayed in both reference systems.

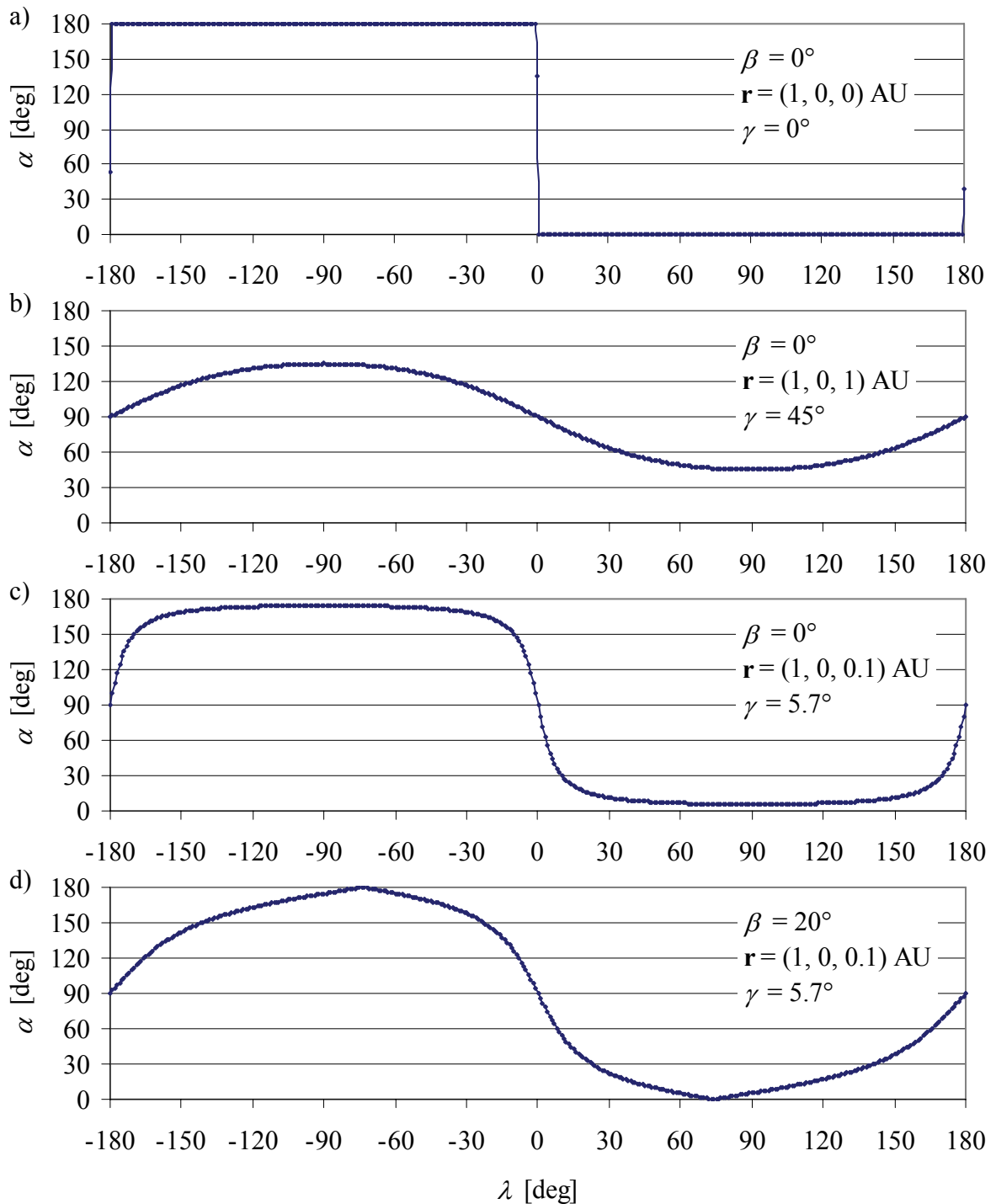


Figure 6-16: Spin-phase correction angle α for longitudes $\lambda = -180^\circ \dots 180^\circ$
 The correction angle α is displayed for two hypothetical a), b) (only for illustration) and two realistic c), d) orbital configurations over the NOZOMI spin-axis longitude λ . The NOZOMI orbital position \mathbf{r} and spin-axis latitude β are given for each configuration (the absolute value r is not relevant), the angle γ is the angle between the NOZOMI radius vector and the ecliptic plane and calculates from \mathbf{r} . As can be seen, the angle α varies between 0° and 180° with different shapes. For configuration a) and other thinkable configurations, there is a singularity at $\lambda = 0^\circ$ or $\pm 180^\circ$.

6.2.3 NOZOMI flight data and sensor pointing directions

For further interpretation of the primary analysis results of the MDC data, the characteristics of the spacecraft's flight data and the resulting sensor pointing directions over mission time must be taken into account. NOZOMI orbital data and attitude data were supplied by ISAS/JAXA as derived from the spacecraft's telemetry. Orbital position data and attitude data are shown and analyzed here with respect to the MDC instrument requirements.

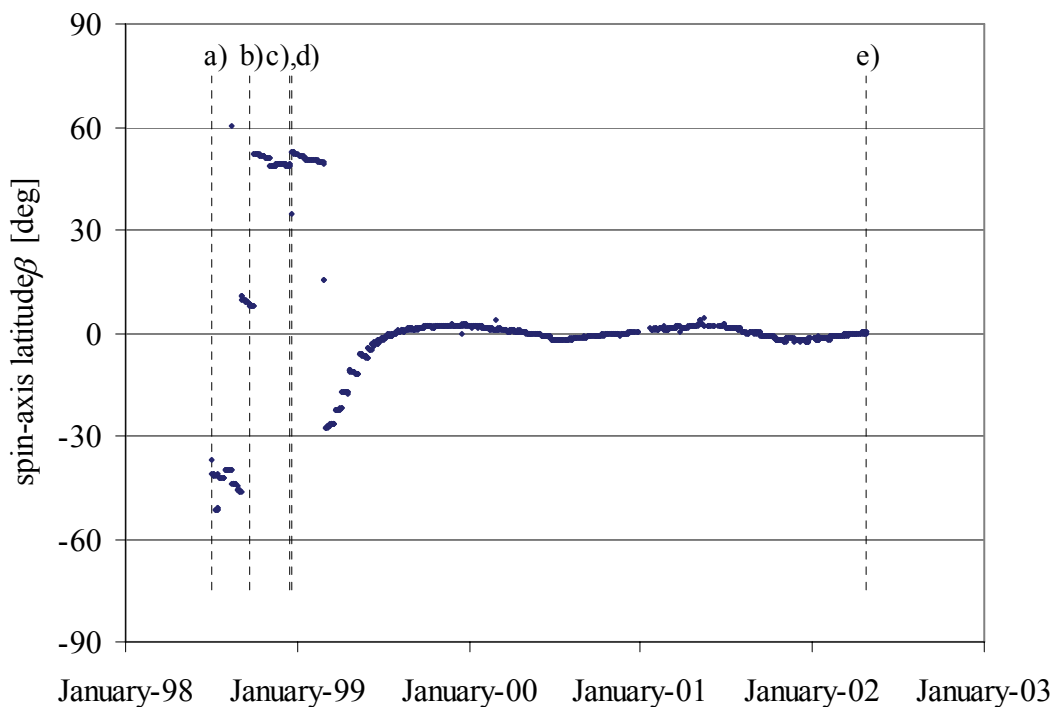


Figure 6-17: NOZOMI spin-axis latitude β over mission time, 1998-2002
Mission events: a) Launch July 4, 1998, b) Moon swing-by #1, September 24, 1998, c) Moon-swing-by #2, December 18, 1998, d) Earth swing-by, December 20, 1998, e) System failure, April 24, 2002.

Critical for the latter determination of dust flux and the statistical interpretation of particle characteristics are both the orbital position of the spacecraft and the overall sensor pointing directions. It is obvious that the MDC cannot measure any particle flux from directions it never looked at.

Latitude and longitude of the NOZOMI spin axis pointing directions over mission time are shown in Figure 6-17 and Figure 6-18. Spin-axis latitude varies between $+45^\circ$ and -45° during the first months of the mission and stabilizes at $+3^\circ$ for the rest of the mission time, while longitude covers the whole range from 0° to 360° for $2\frac{1}{2}$ times.

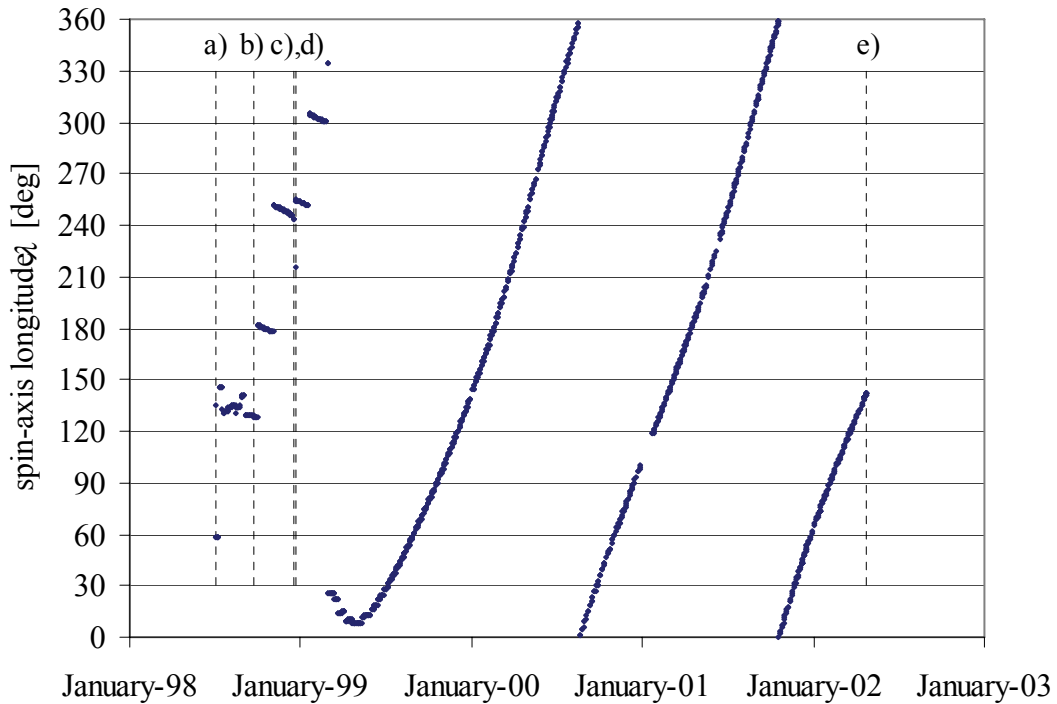


Figure 6-18: NOZOMI spin-axis longitude λ over mission time, 1998-2002

Mission events: a) Launch July 4, 1998, b) Moon swing-by #1, September 24, 1998, c) Moon-swing-by #2, December 18, 1998, d) Earth swing-by, December 20, 1998, e) System failure, April 24, 2002.

Figure 6-19 shows the overall heliospheric coverage of the MDC field-of-view during the full mission time. The coverage of each solid angle element $\Delta\lambda\Delta\beta$ was calculated from the MDC spin-averaged sensitivity and the NOZOMI attitude data for each single day, integrated over the whole mission time and normalized to 100%. Minimum value is 0.0011% for $\lambda = 76^\circ$ and $\beta = 41^\circ$, maximum value is 0.0021% for $\lambda = 259^\circ$ and $\beta = -2^\circ$. Mean value is 0.0015% (which is $100\%/(360 \times 180)$). In summary, the whole heliosphere was covered well by the MDC with maximum and minimum coverage deviating about 50% from the average value.

The coverage during the first six months in Earth orbit and the remaining mission time in the interplanetary space are shown separately in Figure 6-20 (lower left and lower right graphs, respectively). For illustration, the coverage of a single mission day (upper right graph) and a fictitious in-ecliptic spinning dust sensor (upper left graph) are shown. The shape of the coverage for a single mission day resembles the shape of the spin-averaged sensitivity of the MDC as shown in Figure 3-15.

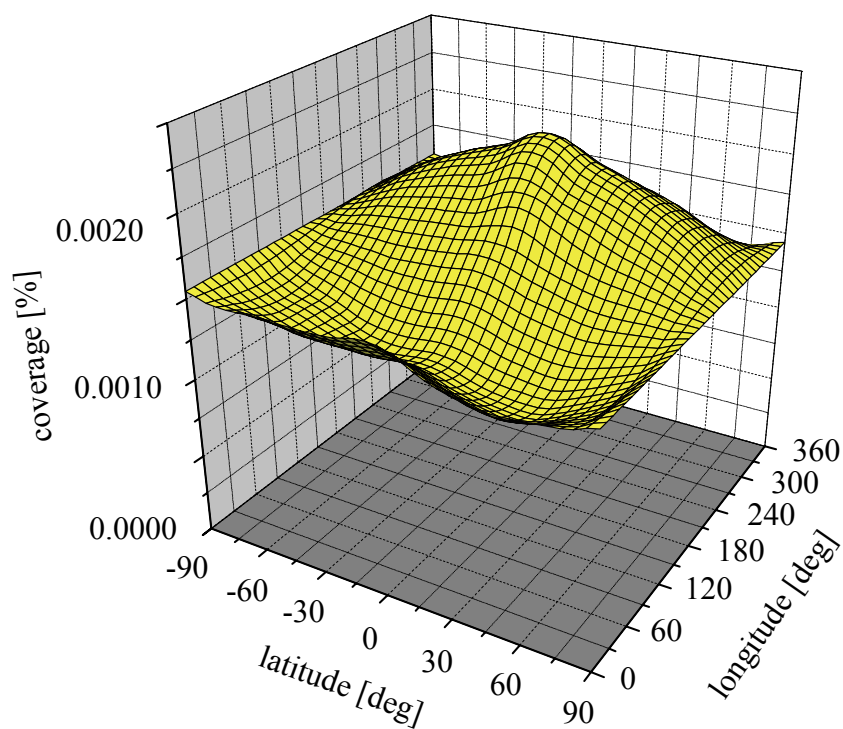


Figure 6-19: Overall heliospheric coverage of the MDC sensor view

Based on the spin-averaged sensitivity of the MDC on NOZOMI and the NOZOMI flight data, the overall coverage of the MDC sensor over longitude and latitude of the heliosphere is shown in this graph. Coverage is given in % per $\Delta\lambda\Delta\beta$ (1° step width each) interval and must be scaled to solid angle elements when used for further statistical analysis.

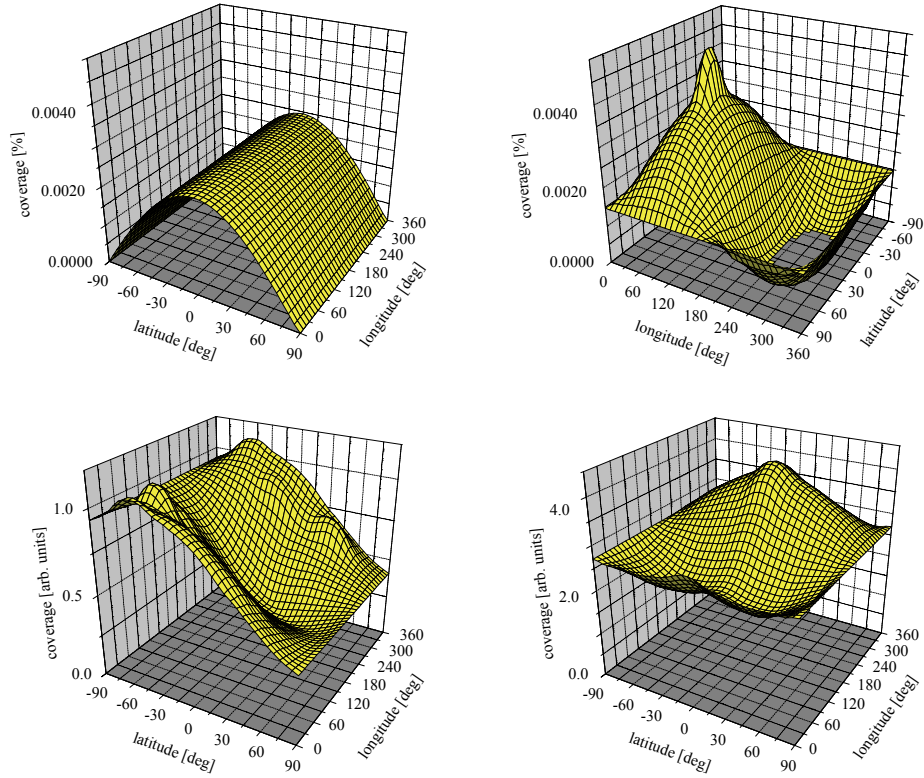


Figure 6-20: Heliospheric coverage, illustration

For illustration purpose, the heliospheric coverage of a flat, in-ecliptic spinning surface with solid angle 2π sr (upper left), the MDC sensor on NOZOMI for a fictitious single day with constant longitude -90° and latitude 0° (upper right) and the MDC sensor during the Earth-Moon mission phase with latitude $\approx +45^\circ$ and -45° (lower left) and the interplanetary cruising phase with latitude $\approx 0^\circ \pm 2^\circ$ (lower right) is shown here. Coverage was not normalized for intermediate results.

NOZOMI spin-rate over mission time is shown in Figure 6-21. Initially between 9 and 10.3 rpm, the spin rate was lowered to 7.7 rpm after injection into the interplanetary orbit and later to 6.9 to 6.8 rpm. The NOZOMI spin rate does not affect the analysis of impact data (rotation speed of the MDC is much lower than the orbital speed of the spacecraft and the nominal impact speed of dust particles, and therefore negligible), but was used for the analysis of the MDC noise data as described in paragraph 6.2.1.

Figure 6-22 shows the angle of the NOZOMI spin axis to the NOZOMI orbital radius vector in the Sun centered eec system. After injection into the transfer orbit to Mars, the angle never falls below 135°, which means that the minimum angle of the MDC bore sight direction to the radius vector is always lower than 90° and no direct sunlight was falling into the MDC sensor box (see also Figure 6-1 and paragraph 6.2.1 for a more detailed discussion).

Figure 6-23 shows the angle of the NOZOMI spin axis to the NOZOMI velocity vector in the Sun centered ecliptic coordinate system. During the mission period in the interplanetary space, the angle drops to a minimum of 45° and rises continuously to finally nearly 135°. For angles below 90°, the MDC sensitivity is enhanced into the spacecraft's anti-apex direction, while for angles above 90°, MDC sensitivity is enhanced into the spacecraft's apex direction. This has consequences for the dust detection capabilities of the MDC and is discussed later in this paragraph.

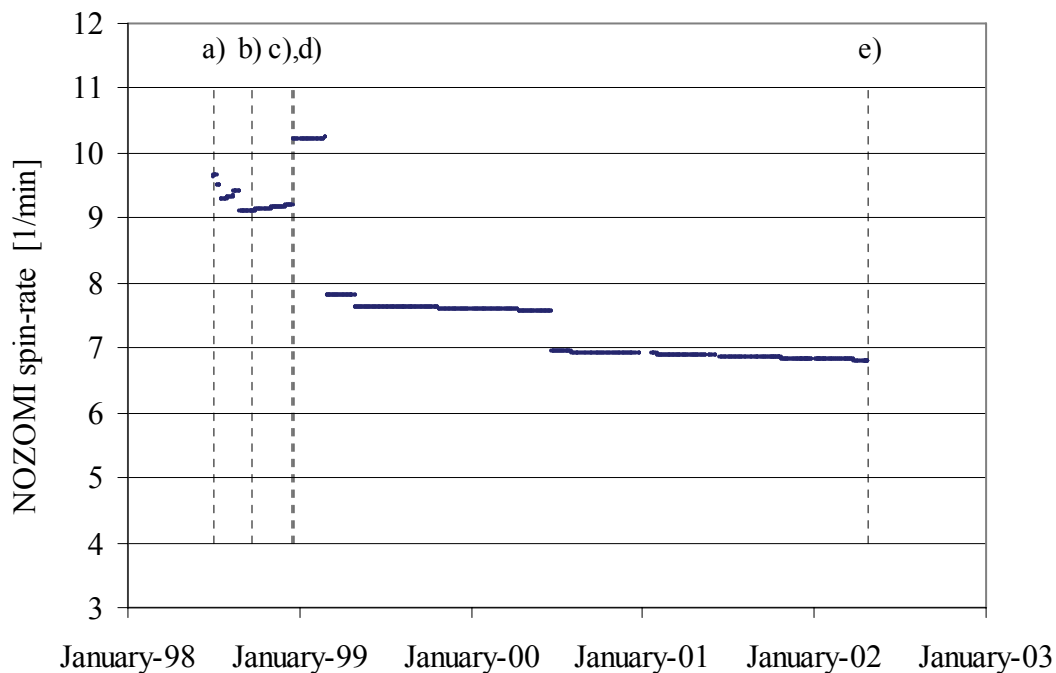


Figure 6-21: NOZOMI spin rate over mission time

Mission events: a) Launch July 4, 1998, b) Moon swing-by #1, September 24, 1998, c) Moon-swing-by #2, December 18, 1998, d) Earth swing-by, December 20, 1998, e) System failure, April 24, 2002.

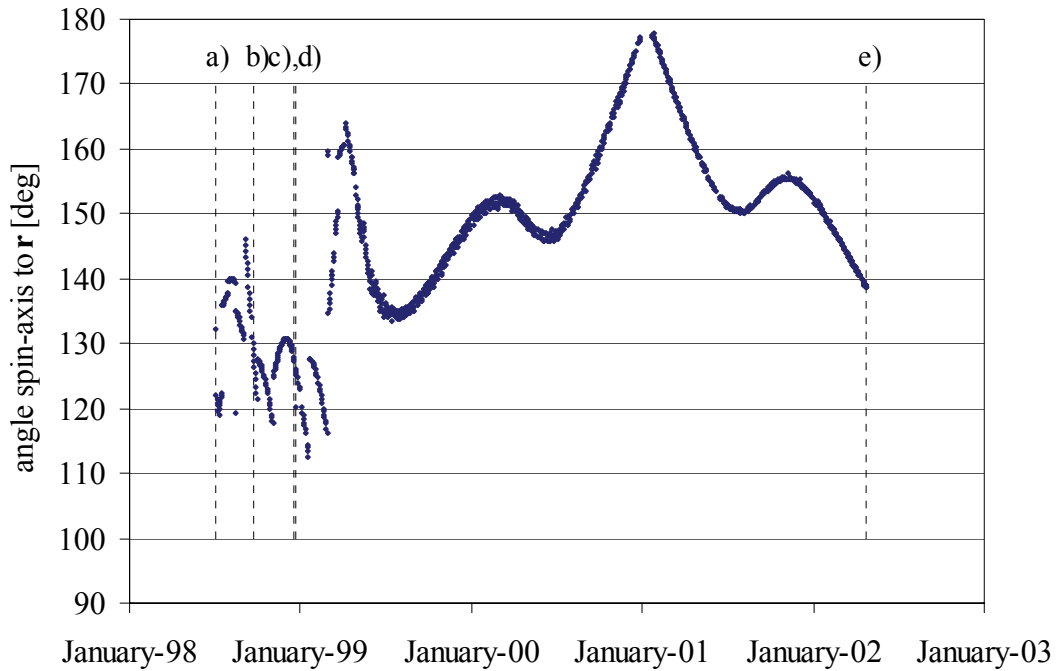


Figure 6-22: Angle of NOZOMI spin-axis to NOZOMI radius vector
 Mission events: a) Launch July 4, 1998, b) Moon swing-by #1, Sep. 24, 1998, c) Moon-swing-by #2, Dec. 18, 1998, d) Earth swing-by, Dec. 20, 1998, e) System failure, April 24, 2002.

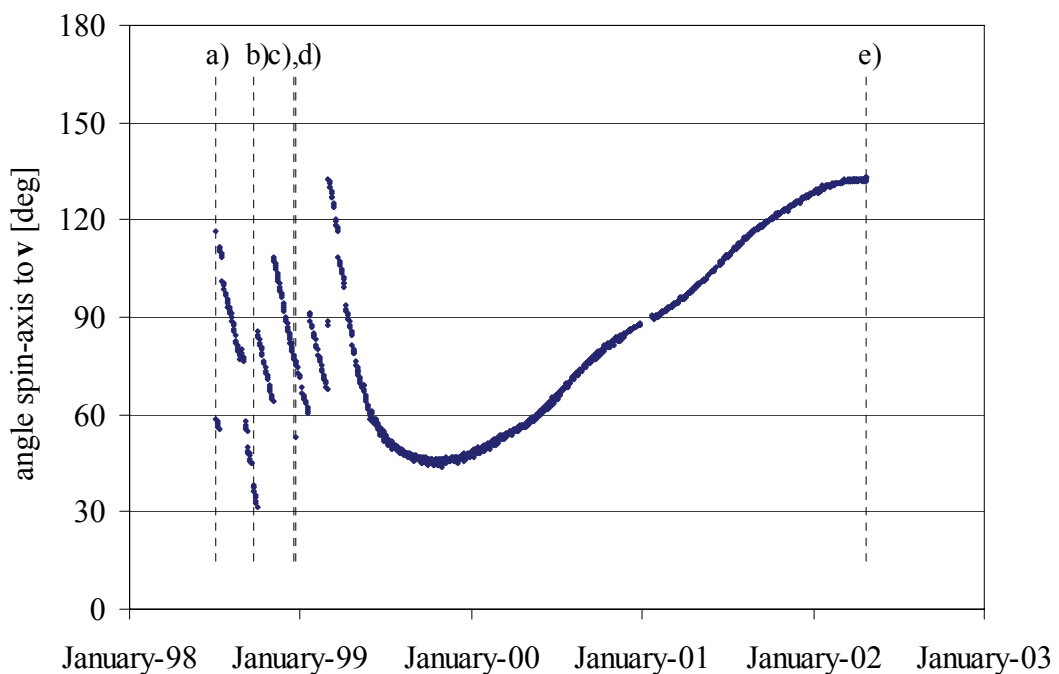


Figure 6-23: Angle of the NOZOMI spin-axis to the velocity vector
 Mission events: a) Launch July 4, 1998, b) Moon swing-by #1, September 24, 1998, c) Moon-swing-by #2, December 18, 1998, d) Earth swing-by, December 20, 1998, e) System failure, April 24, 2002.

NOZOMI distance from the Earth during 1998 (see Figure 6-24) and from the Sun (see Figure 6-26) during the whole mission is shown on the following pages. From launch until the first Moon swing-by on September 24, 1998 NOZOMI was in a high elliptic orbit around the Earth with perigee at around 8000 km and apogee at around 420000 km to 515000 km. Between the two Moon swing-bys, apogee was 1.7 million km.

After the Earth swing-by on December 20, 1998, NOZOMI was injected into an elliptic orbit around the Sun with perihelion at 0.98 AU and aphelion at 1.45 AU.

In Figure 6-25 and Figure 6-27, NOZOMI's duration of stay in different radius intervals is shown. Due to the elliptic characteristics of the orbits, the duration of stay is significantly higher at apogee and aphelion than at perigee and perihelion, respectively. This must be considered in later interpretation of measured MDC dust data, especially for the determination of dust flux measured by the MDC.

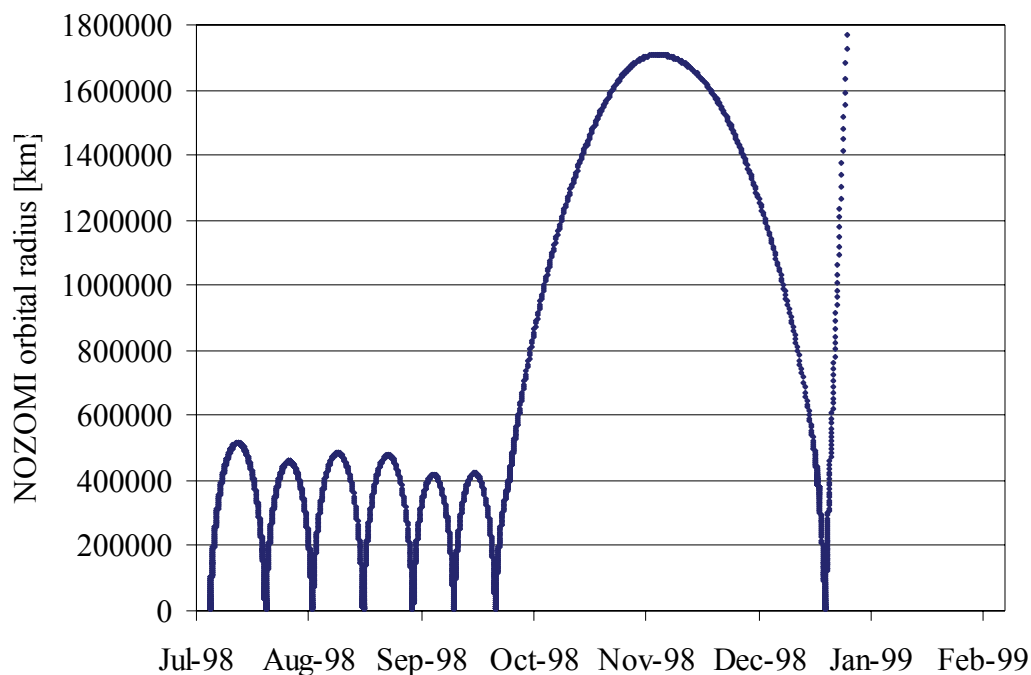


Figure 6-24: NOZOMI distance from the Earth 1998

After six high elliptical orbits with apogee beyond the Moon orbit (400000 to 500000 km), NOZOMI performed two Earth swing-by's that finally brought it on it's trajectory to Mars.

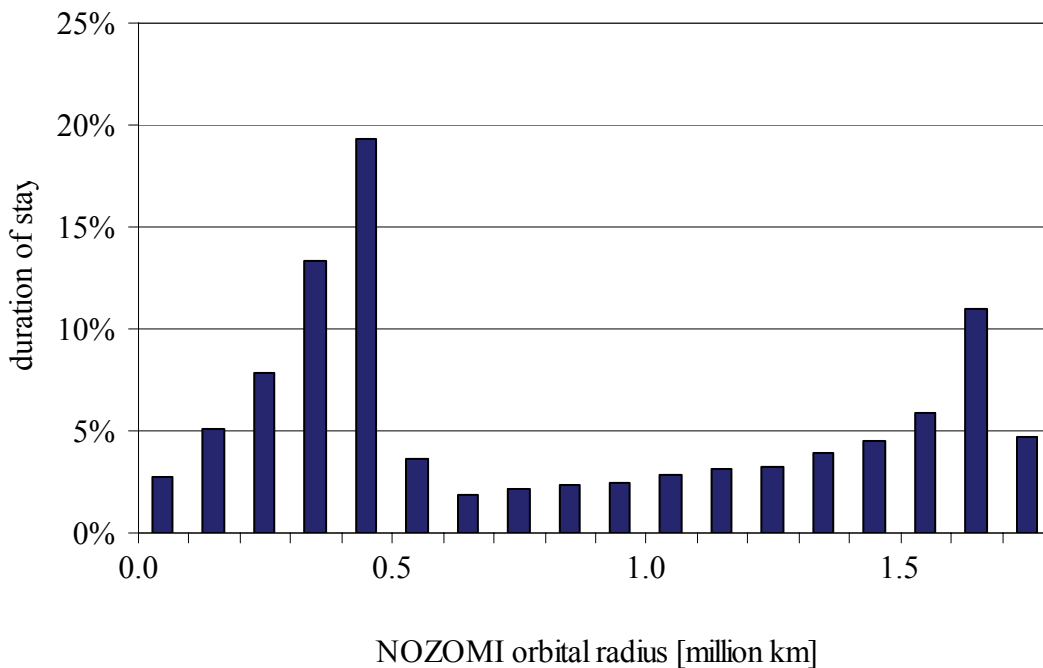


Figure 6-25: NOZOMI distance from the Earth, duration of stay

For further statistical interpretation of particle impacts, the duration of stay of the NOZOMI spacecraft at the different radius intervals was determined.

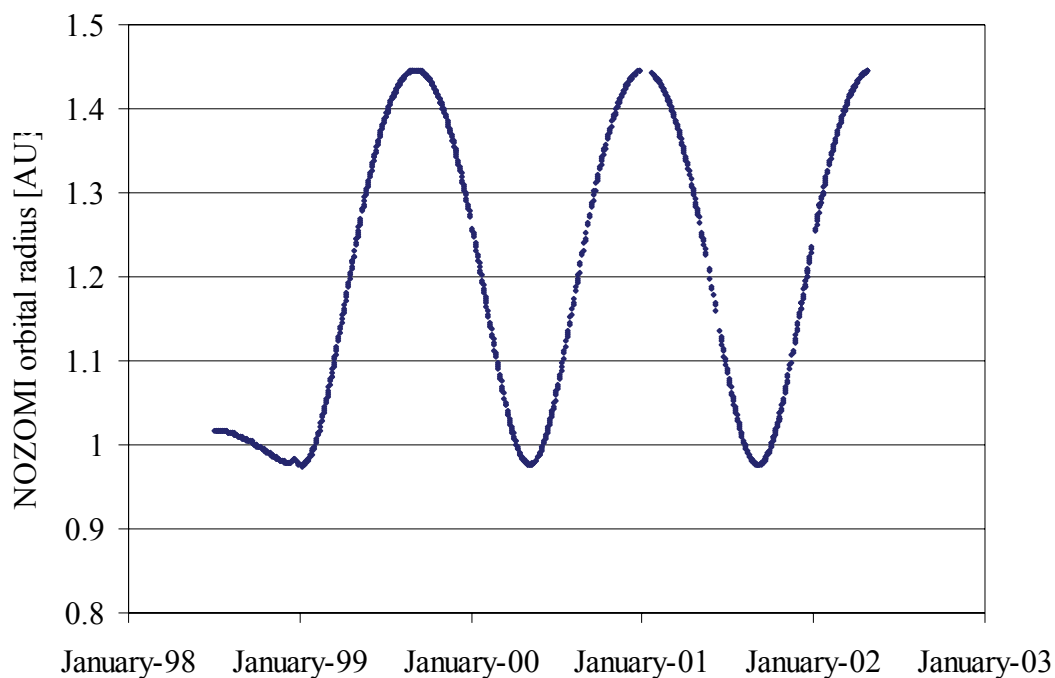


Figure 6-26: NOZOMI distance from the Sun

NOZOMI's distance from the Sun varies between 0.99 and 1.01 AU in 1998 (orbit around the Earth), and between 0.98 and 1.45 AU during the interplanetary cruising phase.

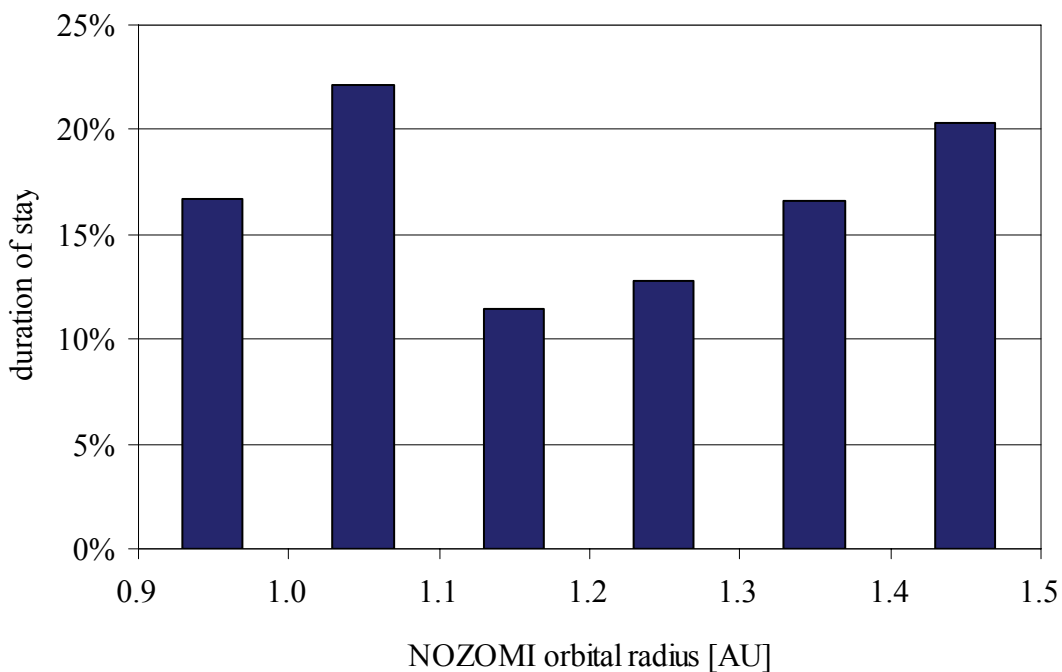


Figure 6-27: NOZOMI distance from the Sun, duration of stay

For further statistical interpretation of particle impacts, the duration of stay of the NOZOMI spacecraft at the different radius intervals was determined.

Based on the NOZOMI flight data and the MDC spin-averaged sensitivity, the MDC-NOZOMI detection capabilities for three specific populations of dust particles were estimated. The three populations investigated were apex-particles, β -meteoroids and interstellar dust grains.

The so called apex particles are a population of the interplanetary dust flux that are expected to orbit in nearly circular orbits with a lower circular speed than macroscopic objects due to the effect of radiation pressure, see paragraph 2.1.1. Because of this lower speed, such particles are expected to impact preferable from the apex direction of the spacecraft.

β -meteoroids are expected to travel on high-speed hyperbolic orbits that deviate only by a few degrees from the radial direction.

Interstellar dust grains are expected to have flight directions nearly similar to that of the interstellar gas flux. The interstellar gas flux is crossing the solar system at $\lambda = 79^\circ$ and $\beta = -5^\circ$ downstream direction.

The MDC's sensitivity for these three populations of particles was determined from the NOZOMI orbital position, NOZOMI flight direction, NOZOMI attitude data and the MDC spin-averaged sensitivity for each day of the mission. The results are shown and discussed in the following.

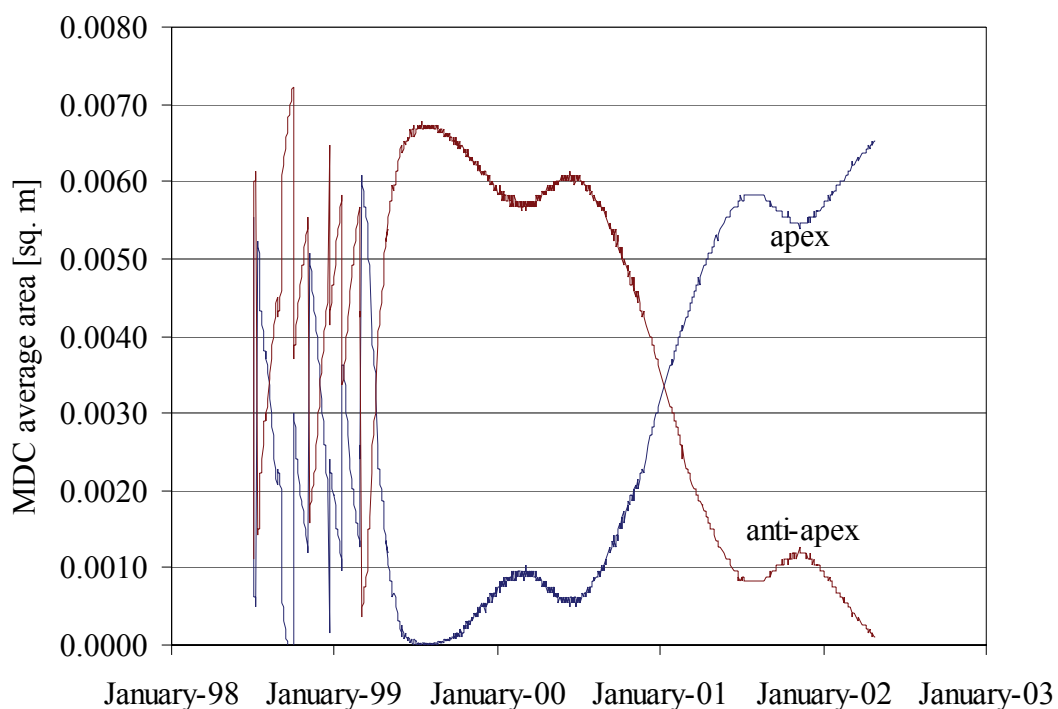


Figure 6-28: MDC sensitivity for apex-particles

Sensitivity of the MDC for apex (blue line) and anti-apex (red line) particles approaching exactly from the front of the spacecraft (apex) and at an angle of 0° to the spacecraft's flight direction (anti-apex).

In Figure 6-28, the average sensitive area of the MDC for apex (blue line) and anti-apex (red line) particles is shown. Sensitivity is fluctuating during the first months of the mission where the NOZOMI attitude was changed frequently due to orbital maneuvers, and Earth and Moon swing-by maneuvers. After NOZOMI spin-axis was set to Earth-pointing direction in March 1999, the sensitivity for apex particles was first falling to zero in July and August 1999 and afterwards rising discontinuously throughout the mission time with two local maxima. The average sensitive area for apex and anti-apex particles never reaches the maximum possible sensitive area of 0.01025 m^2 since the angle of the NOZOMI spin-axis to the NOZOMI flight direction never was lower than 45° .

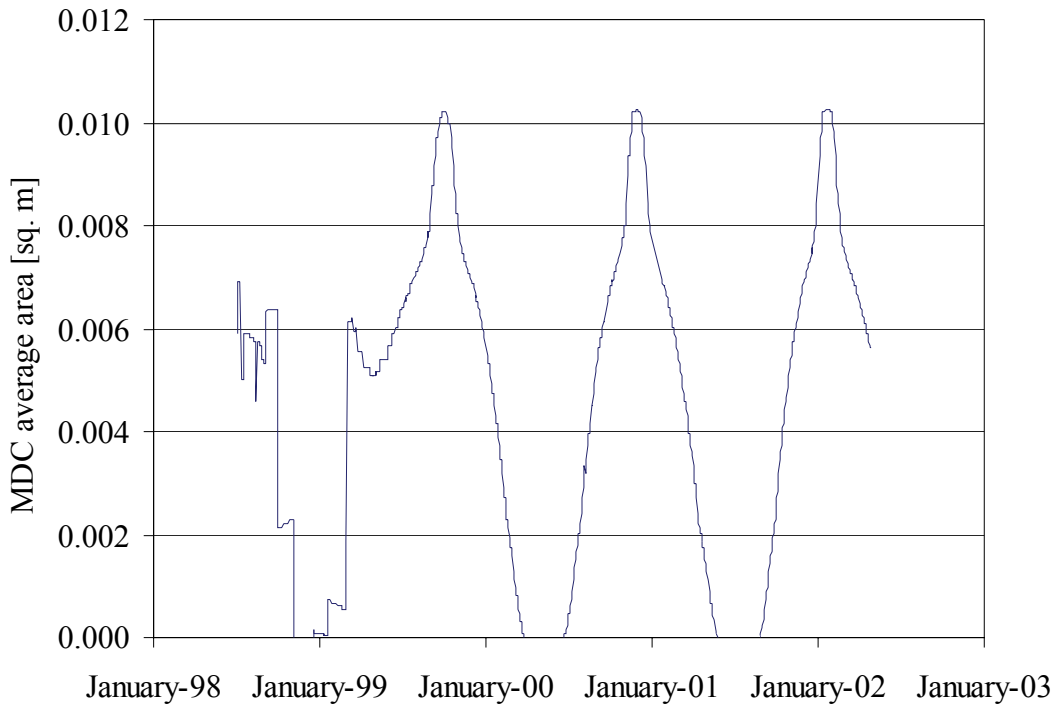


Figure 6-29: MDC sensitivity for ISD grains

Sensitivity of the MDC for particles arriving from the direction of the interstellar gas and dust flux.

In Figure 6-29, the average sensitive area for particles approaching from the direction of the interstellar gas and dust flow ($\lambda = 79^\circ$, $\beta = -5^\circ$ downstream direction) is shown. After a short period of medium sensitivity at the beginning of the mission, the sensitivity drops to zero until NOZOMI spin-axis was set to Earth-pointing direction in March 1999. Afterwards, the sensitivity fluctuates between a maximum value near the theoretical maximum of 0.01025 m^2 and zero depending on the NOZOMI spin-axis longitude. Maximum sensitive area was given on Oct. 7, 1999, Dec. 7, 2000 and Jan. 26, 2002.

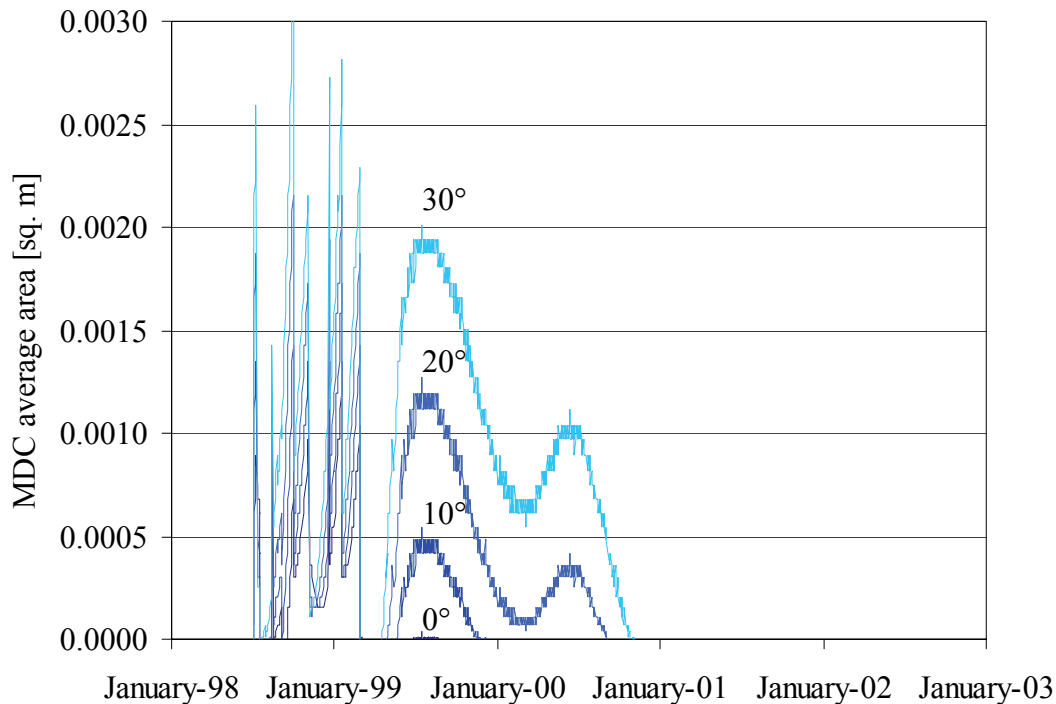


Figure 6-30: MDC sensitivity for β -meteoroids

Sensitivity of the MDC for particles traveling on a radial trajectory and on trajectories with different angles to the radial direction (in prograde direction).

In Figure 6-30, the MDC sensitive area for particles traveling on radial or near radial trajectories (with deviances of 10° , 20° and 30° from the exact radial direction in prograde direction) is shown. Deviances in the magnitude of tens of degrees for β -meteoroids were derived from theoretical calculations by Wehry and Mann [Weh1999] (9° to 24° at 2.5 AU for different conditions), and by Iglseider et al. [Igl1993b] from the MDC-HITEN data ($\approx 30^\circ$ in average at 1 AU). During the first months of the mission, where NOZOMI attitude was changed several times, the MDC was indeed pointing to the sun and detection of β -meteoroids traveling on an exactly radial trajectory (0° in the graph) was possible for a couple of days. For the rest of the mission, sensitivity for such β -meteoroids equals to zero with negligible non-zero values around July 16, 1999. For particles on trajectories with deviance from the exact radial direction, the MDC sensitive area has a maximum around July 16, 1999. The higher the deviance, the larger the maximum of the sensitive area is and the broader the time interval becomes during which the detection of such β -meteoroids becomes possible. The speed of the NOZOMI spacecraft was not considered in this estimation and will lower the shown sensitivities. The maximum sensitive area for particles with 30° deviation from the radial flight direction is 0.0020 m^2 , which is one fifth of the maximum sensitive area for particles approaching exactly in the direction of the NOZOMI spin-axis (anti-apex).

One question raised by the integration of the MDC on NOZOMI and the orbital configuration (the MDC is mounted at an angle of 135° to the NOZOMI spin-axis, the spin-axis of the NOZOMI spacecraft is mainly lying in the ecliptic plane) is: How would the distributions of orbital elements for special populations of dust particles look like? To get an impression about this, a simulation was run based on the true orbital data of the NOZOMI spacecraft (orbital

positions, direction of the spin-axis) and a fictitious population of dust particles orbiting on circular orbits with an orbital speed that is determined by the gravitational force and the Sun’s radiation pressure. A mass of 10^{-12} g and a resulting β -value of 0.4 were assumed for particles of this model population, hence the simulated particles have lower orbital speed than the NOZOMI spacecraft (as a macroscopic body that is not affected by radiation pressure) has. They are “overtaken” by the spacecraft and will impact from the apex direction of the spacecraft (so called “apex-particles”). Effects of the slightly inclined and elliptic shape of the NOZOMI orbit, and of the MDC entrance grid were neglected in this simple simulation. The simulation results are shown in Figure 6-31 and Figure 6-32, respectively. While the resulting distribution of inclination is close to the exact value of $i = 0^\circ$ for all particles (82% of the particles are assigned inclinations between 0° and 10°), the resulting distribution of eccentricity differs significantly from the exact value of $e = 0.0$ for all particles, and has a peak at $e = 0.3$ to 0.4 . This is an effect of the out-of-ecliptic spinning of the MDC sensor, and the limited accuracy in the determination of the particles’ flight direction (which is assumed perpendicular to the MDC sensor area, as best possible guess). Consequently, the distributions of the orbital elements derived from the real impact data recorded by the MDC (see paragraph 6.4) should be discussed with respect to the artifacts that are caused by the MDC’s and NOZOMI’s configuration as discussed here. Within the scope of this work, the distributions of orbital elements derived from the MDC impact data are discussed “as is”, that means, without respect to the mentioned artifacts.

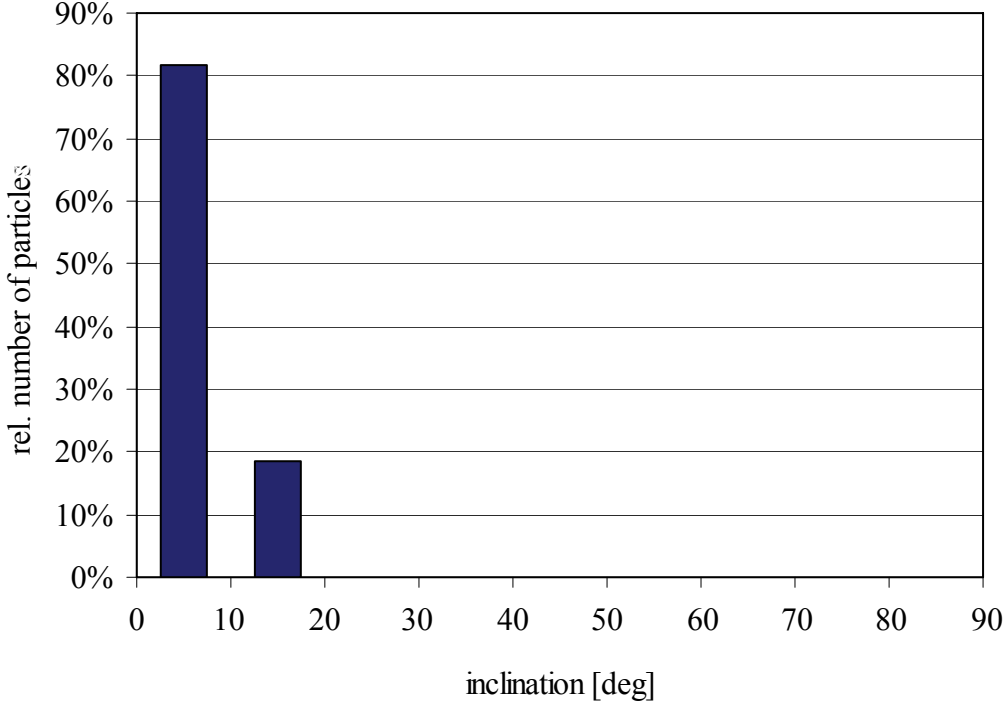


Figure 6-31: Simulation of inclination of a model particle population
Inclination distribution as it is derived from the MDC on NOZOMI for a model population of apex-particles having exact inclination $i = 0^\circ$.

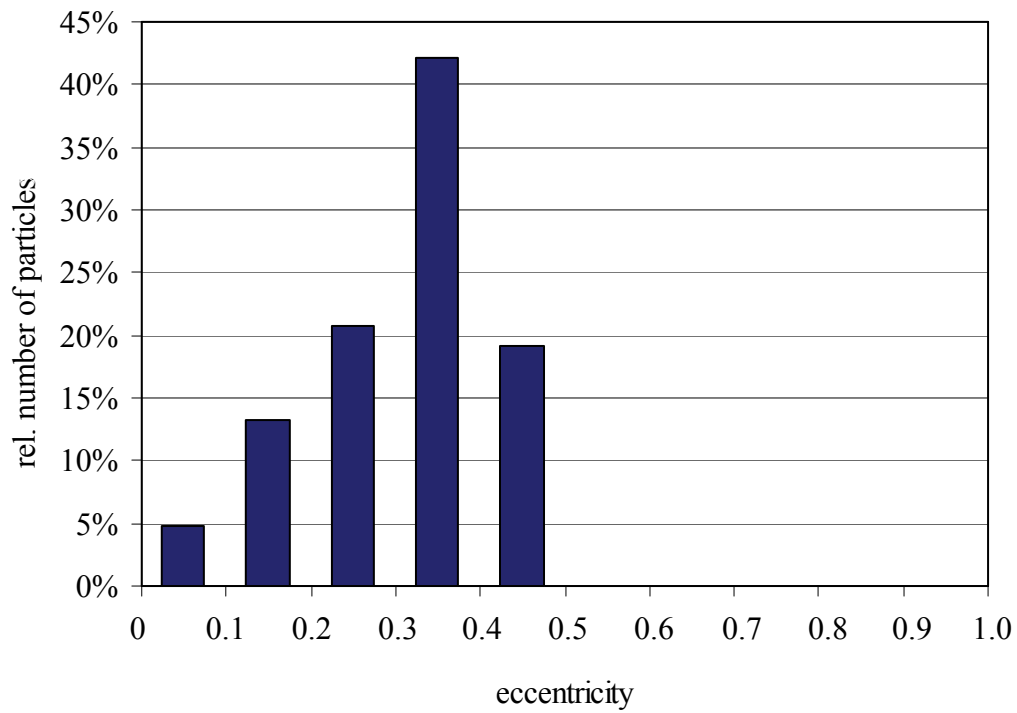


Figure 6-32: Simulation of eccentricity of a model particle population
Eccentricity distribution as it is derived from the MDC on NOZOMI for a model population of apex-particles having exact eccentricity $e = 0.0$.

6.2.4 MDC operating data

The MDC operating data that includes information about the state of the experiment can be derived either from the housekeeping telemetry data that contains full sets of MDC operating data, or from the impact housekeeping information that contains a subset of the MDC operating data and is attached to each single recorded signal data set.

Unfortunately, the housekeeping telemetry data contains many erroneous data sets that complicate further analysis.

The following voltage and temperature charts were created from the much more reliable impact housekeeping information.

As can be seen in Figure 6-33, the +5 V power supply voltage shows a very high stability around 5.0 V \pm 0.1 V during the whole mission time, while the \pm 12 V power supply voltage rose rapidly from 12.0 V right after launch to a means of 13.0 V and 13.5 V, respectively. The initial rise of these voltages and their fluctuation by 0.5 V in the order of months during the whole mission time are correlated well to the temperatures of the MDC electronics and sensor box as shown in Figure 6-34. These temperature fluctuations in turn are correlated well to the distance of the NOZOMI spacecraft from the sun (see Figure 6-26).

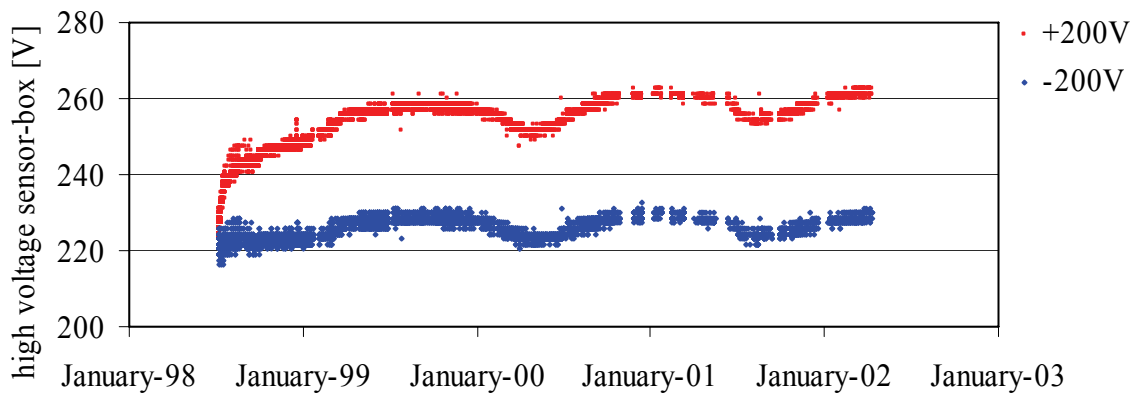
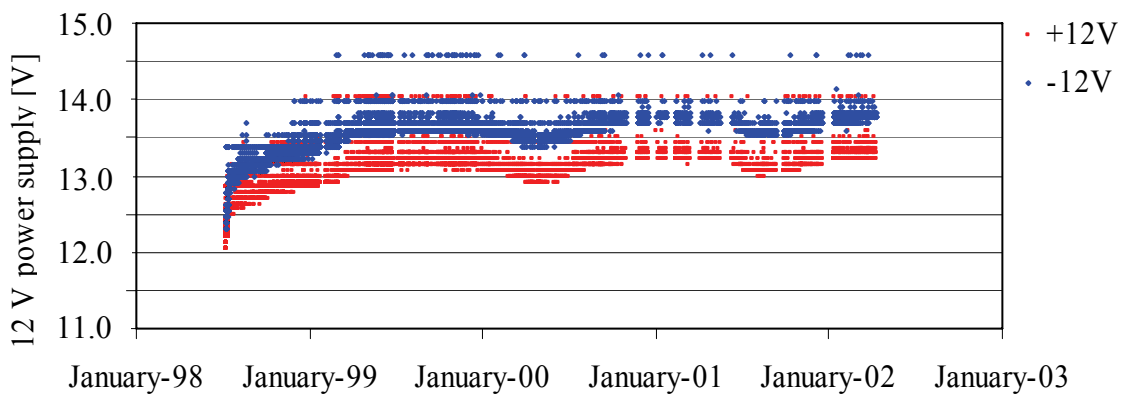
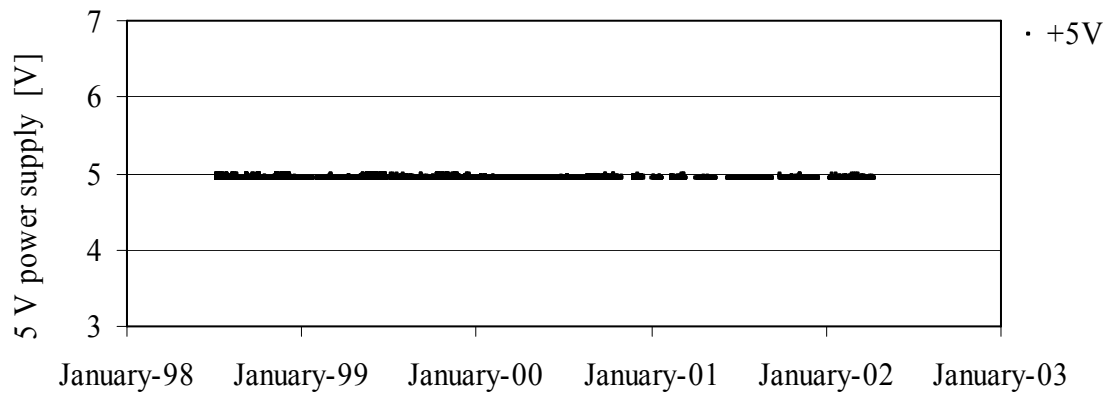


Figure 6-33: Power supply voltages and high-voltages

The power supply voltages of the MDC as derived from the impact housekeeping data. The MDC electronics box is powered by the +5 V voltages, while the ± 12 V voltage powers the MDC sensor box high voltages.

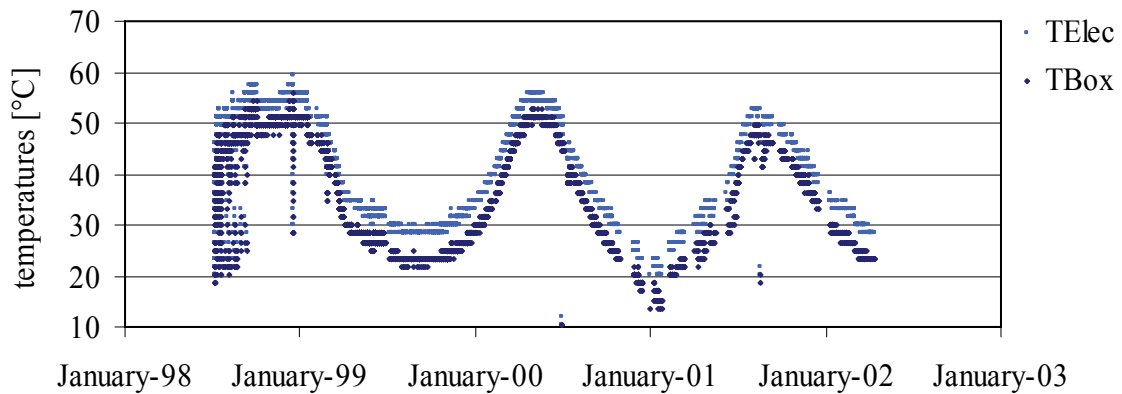


Figure 6-34: Temperatures of the MDC electronics- and sensor-box

The temperatures of the MDC experiment vary between 15°C and 60°C depending on the spacecraft's distance from the Sun.

Although the fluctuations of the ± 12 V power supply voltages cause even higher fluctuations of the sensor box high voltages and thus of the electrostatic field inside the box, these fluctuations have only little influence on the signal shape that is created by the charges an impacting particle produces. As it was mentioned in paragraph 3.1.2, the strength of the electrostatic field inside an impact ionization detector (and thus an MDC like sensor box) has measurable influence on the recorded signal until the high voltages reach ≈ 200 V. A further rise of the voltages, as it can be observed in the MDC operating data, has only very little influence on the charge signal and thus on the further analysis results. The large difference between the -200 V and the +200 V values was caused by erroneous monitoring electronics, as it was proven soon after launch by measurements on the spare flight model by Naumann [Nau2000].

In summary, all parameters of the MDC experiment are within the ranges that ensure reliable operation and dust detection. The observed fluctuations of the power supply voltages and experiment temperatures are therefore not considered in the data analysis process and the scientific results that are presented in the following paragraphs.

Table 6-5 shows the MDC command log for the first day of the mission. Refer to Fischer [Fis1998] for a detailed description of the different commands. From the MDC command log of the first 428 days of the mission, a total downtime of the MDC of 33 days was determined (by analyzing MDC_HV_OFF and MDC_HV_ON commands that switch the high voltage of the MDC sensor box), which gives a ratio of 7.7 % overall downtime for this time span. During the interplanetary cruising phase from January 1999 to September 1999, downtime was 3 %.

Table 6-5: MDC command log, first day of mission

Date	ComCode	ComName	Transmit	VerifyE	VerifyF	VerifyS
10.07.1998	80	MDC_HV_ENA	07:22:14	07:22:19	07:22:24	#NV
10.07.1998	C0	MDC_HV_ON	07:22:41	07:22:46	07:22:50	#NV
10.07.1998	01	MDC_RST	07:23:42	07:23:47	07:23:51	#NV
10.07.1998	30	MDC_CPU_RESET	07:24:29	07:24:34	07:24:39	#NV
10.07.1998	30	MDC_CLEAR_RAM	07:25:06	07:25:11	07:25:16	#NV
10.07.1998	30	MDC_TEST_PULSE	07:25:56	07:26:01	07:26:05	#NV
10.07.1998	31	MDC_TESTNCPOS	07:26:44	07:26:48	07:26:53	#NV
10.07.1998	30	MDC_TEST_PULSE	07:27:19	07:27:24	07:27:29	#NV
10.07.1998	30	MDC_TEST_PULSE	07:27:46	07:27:51	07:27:56	#NV
10.07.1998	30	MDC_TEST_PULSE	07:28:20	07:28:25	07:28:30	#NV
10.07.1998	31	MDC_TESTNC10P	07:28:54	07:28:59	07:29:04	#NV
10.07.1998	30	MDC_TEST_PULSE	07:29:17	07:29:22	07:29:26	#NV
10.07.1998	30	MDC_TEST_PULSE	07:29:46	07:29:50	07:29:55	#NV
10.07.1998	30	MDC_TEST_PULSE	07:30:07	07:30:12	07:30:17	#NV
10.07.1998	31	MDC_TESTNC10N	07:30:47	07:30:52	07:30:56	#NV
10.07.1998	30	MDC_TEST_PULSE	07:31:12	07:31:16	07:31:21	#NV
10.07.1998	30	MDC_TEST_PULSE	07:31:38	07:31:43	07:31:48	#NV
10.07.1998	30	MDC_TEST_PULSE	07:32:01	07:32:06	07:32:11	#NV
10.07.1998	31	MDC_TESTNCNEG	07:32:29	07:32:34	07:32:38	#NV
10.07.1998	30	MDC_TEST_PULSE	07:33:05	07:33:10	07:33:14	#NV
10.07.1998	30	MDC_TEST_PULSE	07:33:41	07:33:45	07:33:50	#NV
10.07.1998	30	MDC_TEST_PULSE	07:34:07	07:34:12	07:34:17	#NV
10.07.1998	30	MDC_PWSON	07:34:45	07:34:50	07:34:55	#NV
10.07.1998	31	MDC_SETTRM_12	07:43:31	07:43:36	07:43:41	#NV
10.07.1998	31	MDC_SETTRM_04	07:47:57	07:48:02	07:48:07	#NV
10.07.1998	22	DHU_MODE_CHNG	07:51:27	07:51:32	07:51:37	#NV
10.07.1998	30	MDC_PWSOFF	07:54:21	07:54:26	07:54:31	#NV
10.07.1998	30	MDC_PWSON	08:01:32	08:01:37	08:01:42	#NV
10.07.1998	31	MDC_SETTRM_03	08:02:28	08:02:32	08:02:37	#NV
10.07.1998	30	MDC_TEST_PULSE	08:03:33	08:03:38	08:03:42	#NV
10.07.1998	30	MDC_TEST_PULSE	08:04:04	08:04:09	08:04:14	#NV
10.07.1998	31	MDC_KO_CRITERIA_02	08:04:50	08:04:55	08:05:00	#NV
10.07.1998	31	MDC_KO_CRITERIA_03	08:10:29	08:10:33	08:10:38	#NV
10.07.1998	30	MDC_TEST_PULSE	08:12:45	08:12:50	08:12:55	#NV
10.07.1998	22	DHU_MODE_CHNG	08:13:58	08:14:03	08:14:08	#NV
10.07.1998	31	MDC_SETTRM_04	08:44:02	08:44:07	08:44:12	#NV
10.07.1998	30	MDC_PWSOFF	08:44:33	08:44:38	08:44:43	#NV
10.07.1998	31	MDC_KO_CRITERIA_04	08:45:26	08:45:31	08:45:36	#NV
10.07.1998	31	MDC_CAL_TP_MIX	08:46:01	08:46:06	08:46:11	#NV
10.07.1998	31	MDC_LIMIT12V	08:46:36	08:46:41	08:46:46	#NV
10.07.1998	22	DHU_MODE_CHNG	08:47:06	08:47:11	08:47:16	#NV
10.07.1998	31	MDC_KO_CRITERIA_02	08:48:47	08:48:52	08:48:57	#NV
10.07.1998	40	MDC_HV_OFF	10:54:24	10:54:29	10:54:33	#NV
10.07.1998	31	MDC_SETTRM_13	10:55:13	10:55:17	10:55:22	#NV
10.07.1998	22	DHU_MODE_CHNG	11:05:59	11:06:04	11:06:08	#NV
10.07.1998	80	MDC_HV_ENA	11:07:32	11:07:37	11:07:42	#NV
10.07.1998	C0	MDC_HV_ON	11:07:55	11:08:00	11:08:04	#NV
10.07.1998	31	MDC_SETTRM_04	13:10:37	13:10:42	13:10:46	#NV
10.07.1998	22	DHU_MODE_CHNG	13:10:54	13:10:59	13:11:04	#NV
10.07.1998	30	MDC_PWSON	13:12:24	13:12:29	13:12:33	#NV
10.07.1998	31	MDC_SETTRM_03	13:12:50	13:12:55	13:13:00	#NV
10.07.1998	22	DHU_MODE_CHNG	13:21:15	13:21:20	13:21:25	#NV
10.07.1998	31	MDC_KO_CRITERIA_05	13:33:49	13:33:54	13:33:59	#NV
10.07.1998	31	MDC_SETTRM_13	13:34:46	13:34:51	13:34:56	#NV
10.07.1998	22	DHU_MODE_CHNG	13:35:18	13:35:22	13:35:27	#NV
10.07.1998	30	MDC_PWSOFF	13:37:23	13:37:28	13:37:33	#NV
10.07.1998	30	MDC_PWSON	13:39:13	13:39:18	13:39:22	#NV
10.07.1998	22	DHU_MODE_CHNG	13:39:51	13:39:56	13:40:00	#NV
10.07.1998	31	MDC_KO_CRITERIA_04	13:42:32	13:42:36	13:42:41	#NV

6.3 Particles detected in the vicinity of Earth and Moon

During the first half year of the mission, NOZOMI was in a high elliptic orbit around Earth with perigee at around 8000 km and apogee beyond the orbital radius of the Moon. Therefore, it was expected that the MDC would detect interplanetary dust grains encountering the Earth as well as dust grains and space debris particles that are on bound orbits around the Earth. For this reason, the particles detected during the first half year of the mission were investigated separately from the particles that were detected during NOZOMI's interplanetary cruising phase. The results are presented and discussed in this paragraph.

The orbital elements inclination and eccentricity of the detected particles were calculated with respect to the gravitational force only, although most particles discussed in this paragraph experience additional forces like radiation pressure due to their size.

6.3.1 Overview

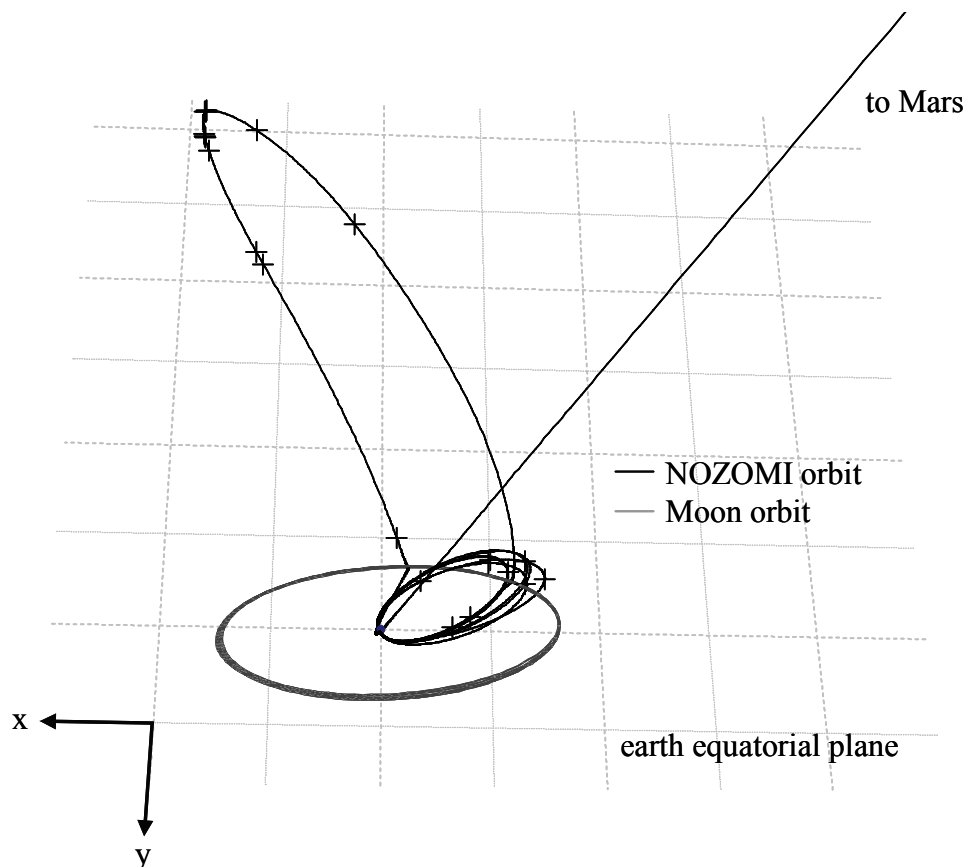


Figure 6-35: Spatial distribution of the particles in the Earth-Moon system
Plus signs indicate the orbital positions of the particles detected in the year 1998 when NOZOMI was in orbit around Earth.

NOZOMI's first mission phase lasted from July 1998 until January 1999. About 10000 signals were triggered, recorded, qualified and downloaded during this time. Manual

screening of these bulk signals was applied to separate noise signals from potential impact signals. 21 good signals were identified as impacts, 20 were analyzed and are discussed here, see Table 6-6. One signal (98111001-1) was identified as impact, but the electron channel EC was out of range, hence a correct determination of rise time and charge amplitude, both needed for further analysis, was not possible.

In Figure 6-35, the NOZOMI orbit during the first half-year and the orbital positions of the detected particles are shown. As can already be seen in this view, all particles were detected far away from Earth near the apogee of the NOZOMI orbits. This is discussed later in this paragraph.

Figure 6-36 shows mass vs. impact speed of the detected particles. Lowest impact speed was 7.7 km/sec, highest was 50.9 km/sec. The detector limits shown in this graph are mean values from all impact positions inside the MDC sensor box.

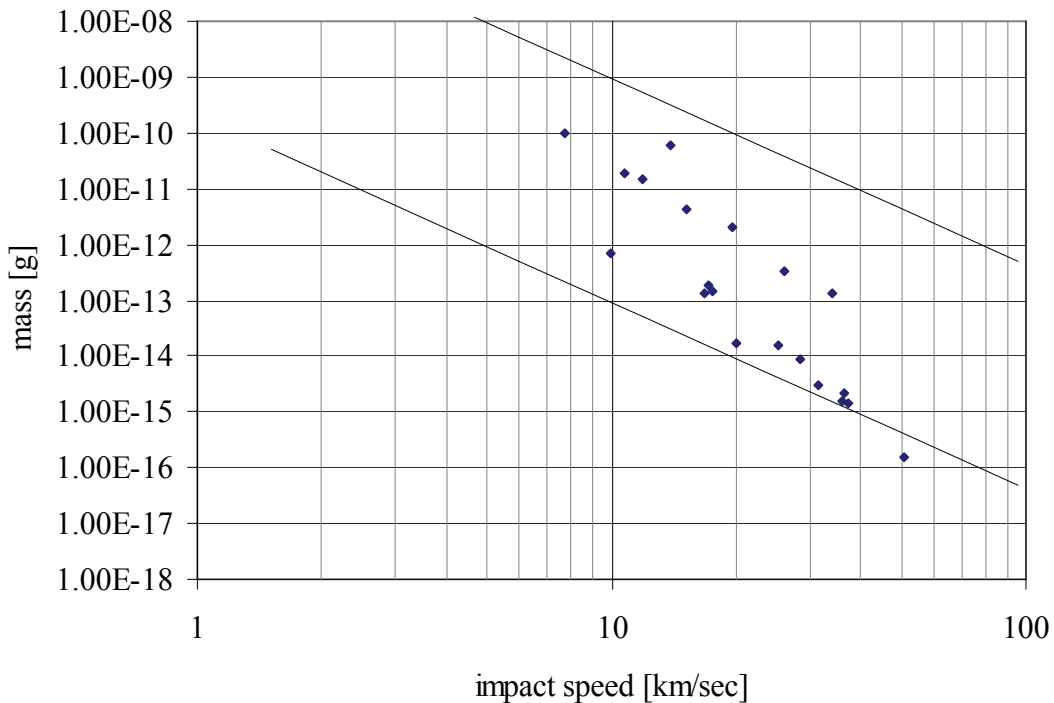


Figure 6-36: Mass vs. imp. speed of the particles in the Earth-Moon system
 The two lines show the detector limits. The upper limit is defined by the maximum charge that can be processed by the charge amplifiers and the A/D converters without overload; the lower limit is defined by the sensitivity of the instrument that is set by a certain trigger level. .

Table 6-6: Detected particles in the vicinity of Earth and Moon

File	Imp. No.	Date [UT]	Time [UT]	Pos. X [km]	Pos. Y [km]	Pos. Z [km]	Orb. Rad. [km]
Sp. X [km/s]	Sp. Y [km/s]	Sp. Z [km/s]	Abs. Sp. [km/s]	Imp. Sp. [km/s]	Mass [g]	Incl. [deg]	Ecc.
98071101	26	1998-07-10	15:08:21	47071711	-144794138	28784	152253372
54.31	12.79	-16.65	58.23	31.57	3.0E-15	16.67	2.88
98071601	3	1998-07-16	03:52:01	60278018	-139746168	63454	152192098
12.70	15.17	-2.74	19.97	15.24	4.4E-12	8.81	0.66
98073001	5	1998-07-28	23:23:54	88381925	-123617666	59061	151962809
22.49	24.85	-0.53	33.53	7.69	1.0E-10	0.92	0.35
98073101	29	1998-07-31	06:37:46	93191670	-119958656	49421	151903815
30.52	47.47	-18.68	59.45	34.14	1.3E-13	19.33	2.91
98080701	3	1998-08-05	11:14:40	102884667	-111488040	27355	151706423
23.22	25.17	-19.06	39.19	20.04	1.7E-14	29.18	0.76
98082201	8	1998-08-22	00:48:36	129049547	-78765918	55978	151188156
13.97	24.87	-25.21	38.07	25.34	1.6E-14	41.49	0.65
98090501	14	1998-09-02	21:28:35	141712211	-51326819	44935	150720918
7.19	25.25	-9.09	27.78	9.89	6.7E-13	19.14	0.14
98092201	9	1998-09-21	10:30:04	149955432	-4648768	-13433	150027474
-32.72	40.19	-15.35	54.05	37.41	1.4E-15	21.41	1.90
98092201	23	1998-09-22	00:23:40	149929104	-3207880	-4758	149963418
-1.13	57.53	21.78	61.52	35.85	1.6E-15	20.75	3.27
98101401	21	1998-10-13	03:45:06	140661832	48872548	470810	148911042
-9.00	14.04	33.99	37.86	36.46	2.1E-15	64.51	0.61
98102701	37	1998-10-26	10:07:48	125317767	79079706	597923	148184007
-14.26	18.65	27.95	36.50	28.64	8.5E-15	50.09	0.49
98110901	17	1998-11-08	23:02:03	102744228	105734878	623866	147433476
-13.78	15.62	14.26	25.24	17.15	1.9E-13	34.45	0.30
98110901	29	1998-11-08	11:38:43	103639158	104886737	624512	147454036
-16.60	18.92	15.88	29.76	16.82	1.3E-13	32.30	0.06
98111001	1	1998-11-09	10:35:00	101823105	106580827	623077	147403547
N/A	N/A	N/A	N/A	N/A	N/A	N/A	N/A
98111701	8	1998-11-17	04:23:19	86086726	119183754	591866	147023950
-33.15	8.81	1.77	34.34	11.86	1.5E-11	3.26	0.46
98111801	1	1998-11-17	17:02:59	84951085	119965169	588452	146998894
-33.33	17.81	10.99	39.36	13.92	6.0E-11	16.37	0.72
98111801	6	1998-11-18	00:35:19	84273081	120428155	586334	146987198
-44.83	0.58	5.17	45.13	26.09	3.3E-13	8.10	1.18
98112101	6	1998-11-20	10:39:41	78952092	123855597	568035	146880783
-20.16	10.53	7.40	23.92	10.80	1.9E-11	18.10	0.37
98120201	17	1998-12-01	18:58:50	52215696	136913926	431437	146533574
-33.56	13.15	16.36	39.58	17.46	1.5E-13	24.42	0.73
98120301	9	1998-12-02	18:41:39	49768815	137804201	415244	146516570
-13.20	4.69	47.96	49.96	50.90	1.6E-16	73.72	1.76
98121801	35	1998-12-17	10:17:34	12054841	146232969	65009	146729018
-30.69	4.83	19.20	36.52	19.65	2.0E-12	31.78	0.48

Table 6-6 shows the complete data of the 21 identified particles during the mission period from July to December 1998. More details for each data set/particle including signal shape and housekeeping information can be found in Appendix C.

In Figure 6-37 and Figure 6-38, mass vs. absolute speed of the detected particles in the eqq and eec system are shown. Absolute speed was derived from the particles' impact speed and NOZOMI orbital and attitude data as described in paragraph 6.2.3. Since the speed of the NOZOMI spacecraft in the eqq system (several km/sec down to 0.1 km/sec) is far below the impact speed of the particles (several km/sec up to 90 km/sec), Figure 6-37 differs only slightly from Figure 6-36.

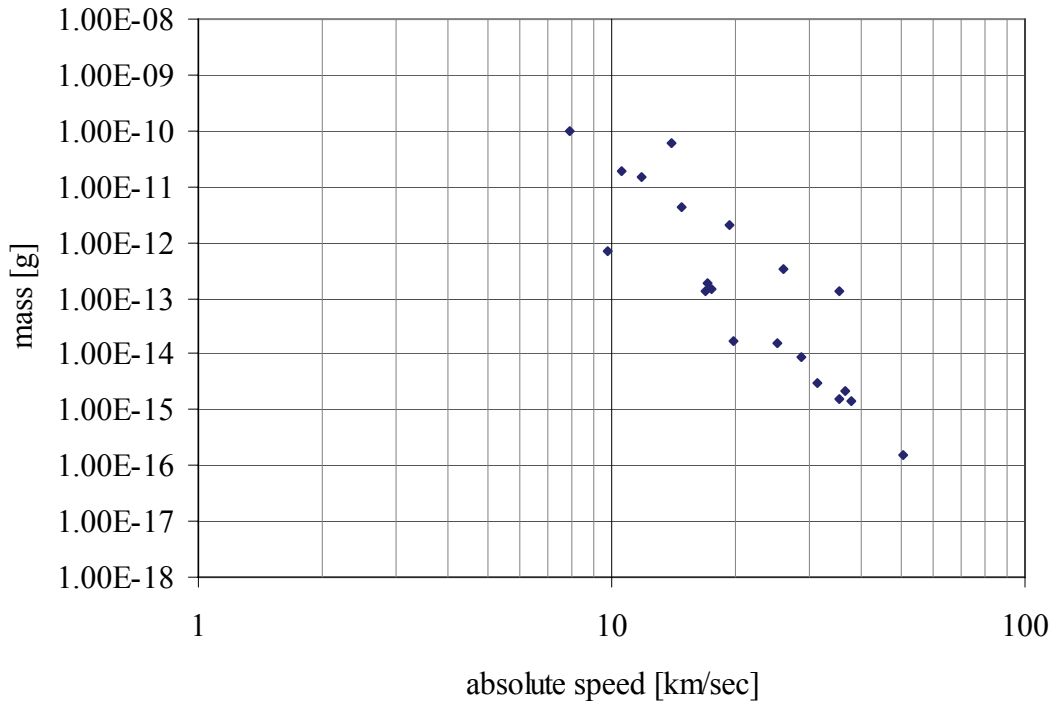


Figure 6-37: Mass vs. abs. speed of the particles in the Earth-Moon system
 The absolute speed vector of the particles was determined from the flight direction of the particles, impact speed and the NOZOMI attitude.

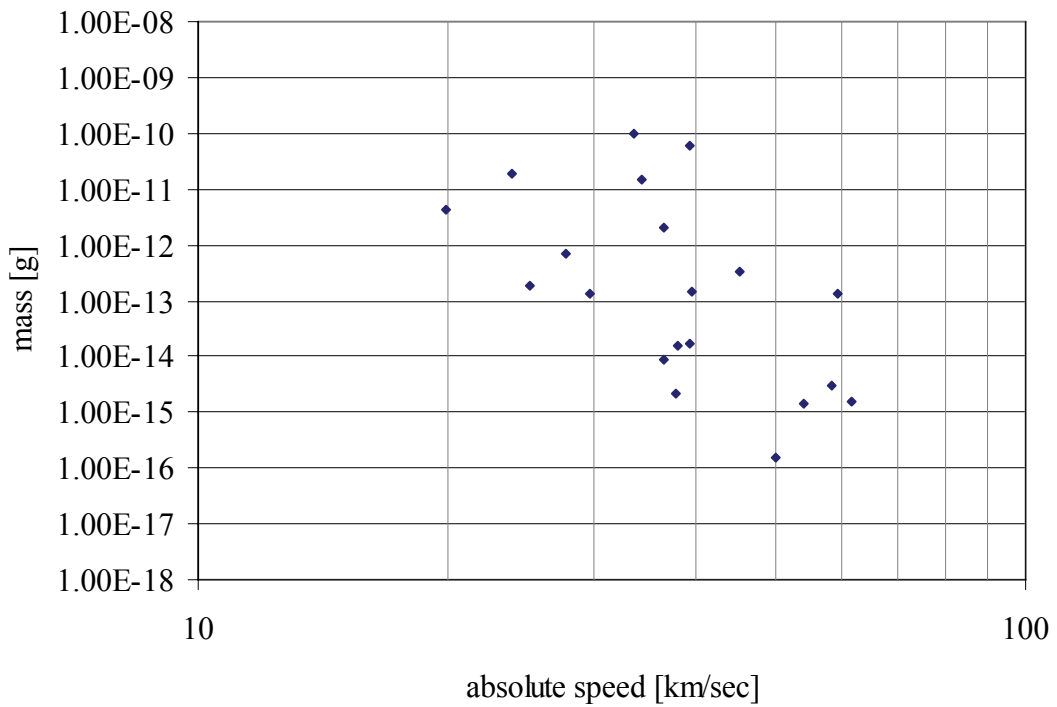


Figure 6-38: Mass vs. abs. speed of the particles in the eec system
 The absolute speed vector of the particles was determined from the flight direction of the particles, impact speed and NOZOMI attitude.

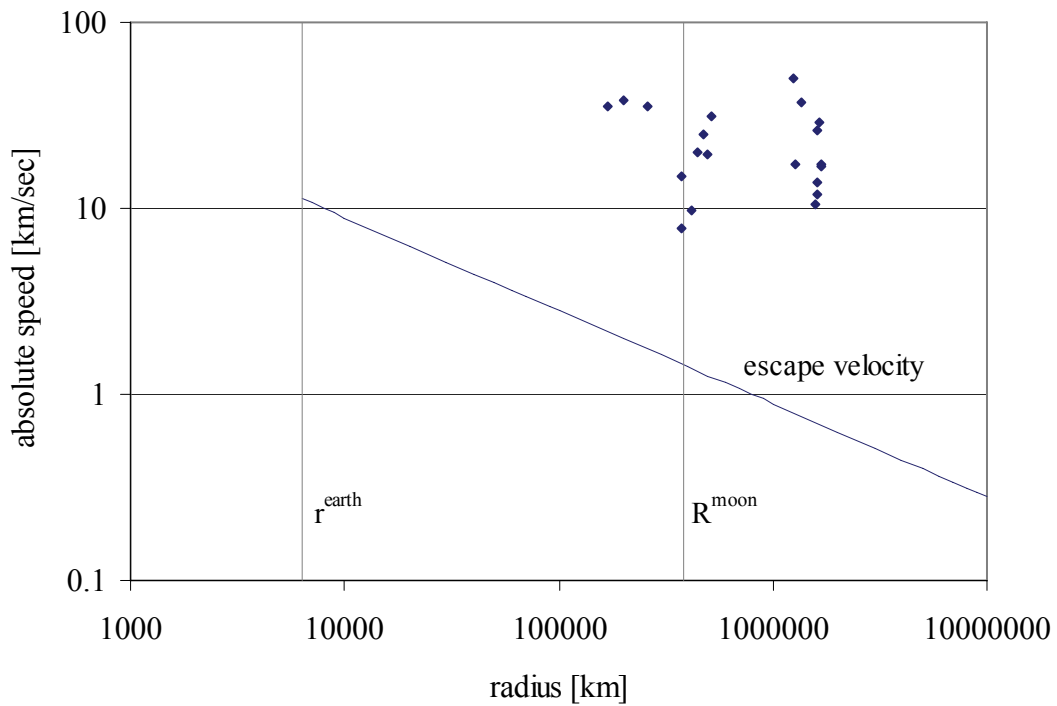


Figure 6-39: Orbital radius vs. abs. speed of the particles in the eeq system
 The absolute speed of all particles is far beyond the escape speed at the given distance of the particles.

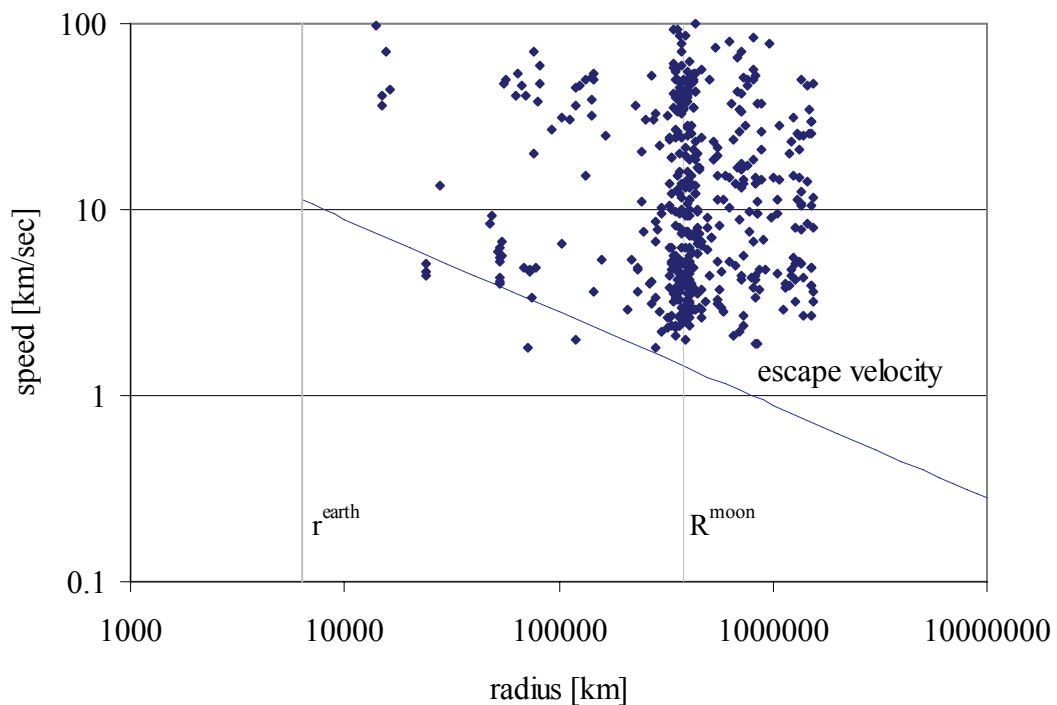


Figure 6-40: Orbital radius vs. abs. speed of the HITEN particles
 The speed of most particles detected by the MDC-HITEN is also beyond the escape speed at the given distance of the particles.

As can be seen in Figure 6-37, absolute speed in the eeq system is higher than 8 km/sec for all particles, and exceeds the escape speed from the Earth orbit for NOZOMI's all orbital distances from Earth. The absolute speed of the particles and the escape speed are compared in Figure 6-39. All particles' speed is far beyond the escape speed at the given orbital radius. For this reason, all particles detected during the first half year of the mission are of interplanetary or interstellar origin. Also, most particles detected by the MDC-HITEN during its three year mission in the Earth-Moon system are of interplanetary or interstellar origin, see Figure 6-40³.

Figure 6-41 shows the number of detected particles per radius interval during the first half year of the mission. All particles were detected at orbital radii between 100000 km and 600000 km, or between 1 million km and 2 million km, respectively. Although the accumulation of orbital radii of the particles around the mean orbital distance of the Moon (which is 384000 km) may suggest that there is some correlation of these dust particles with a possible dust ring around the Earth in the distance of the Moon, this cannot be the case because of the absolute speed of the particles discussed above. In addition, no increase of detection rate was registered during the two Moon swing-by maneuvers. The particles detected by the MDC-HITEN show a similar distribution due to comparable orbital characteristics, although the MDC-HITEN detected particles in nearly all radius intervals due to its much longer mission time in the Earth-Moon system, see Figure 6-42.

The explanation of the accumulated impact rates at the two orbital radius intervals is the duration of stay of NOZOMI in these specific intervals, see Figure 6-25. The duration of stay of NOZOMI in the radius interval from 100000 km to 600000 km is 49 % of the mission time, and 39 % in the interval from 1 million km to 2 million km. The duration of stay was only 3 % of the mission time below 100000 km, and 8 % of the mission time between 600000 km and 1 million km.

³ Speed is given as relative speed, since no absolute speed data in the Earth centered coordinate system was available for MDC-HITEN data. Absolute speed differs by the speed of the HITEN satellite at the utmost, which is 1.12 km/sec in average.

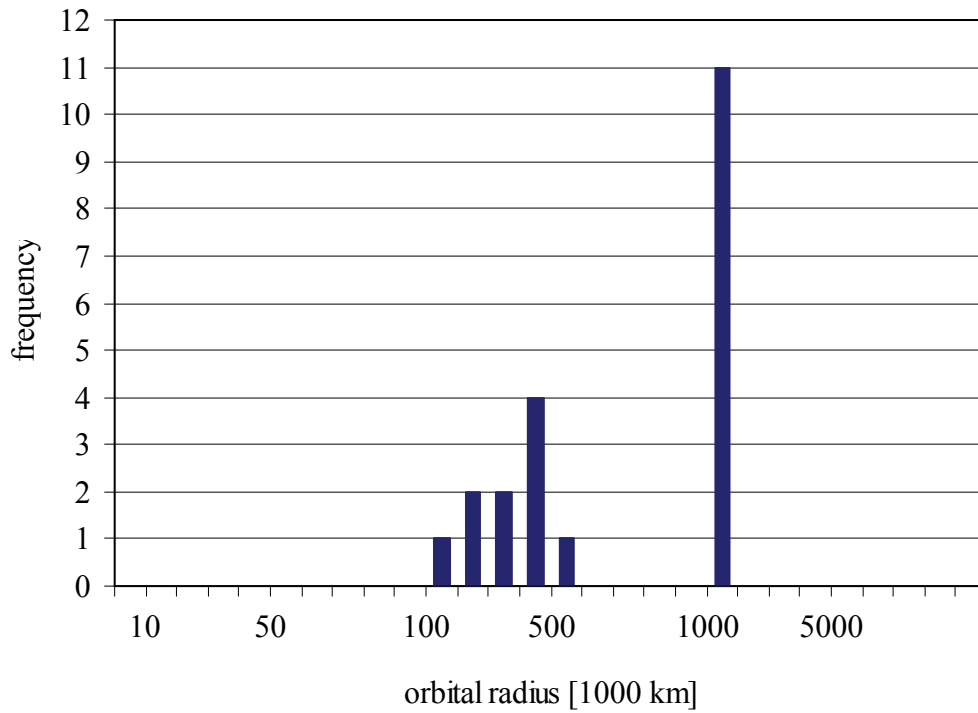


Figure 6-41: Number of particles per radius interval

All detected particles are located within two radius intervals, 100000 km to 600000 km and 1000000 km to 2000000 km, respectively.

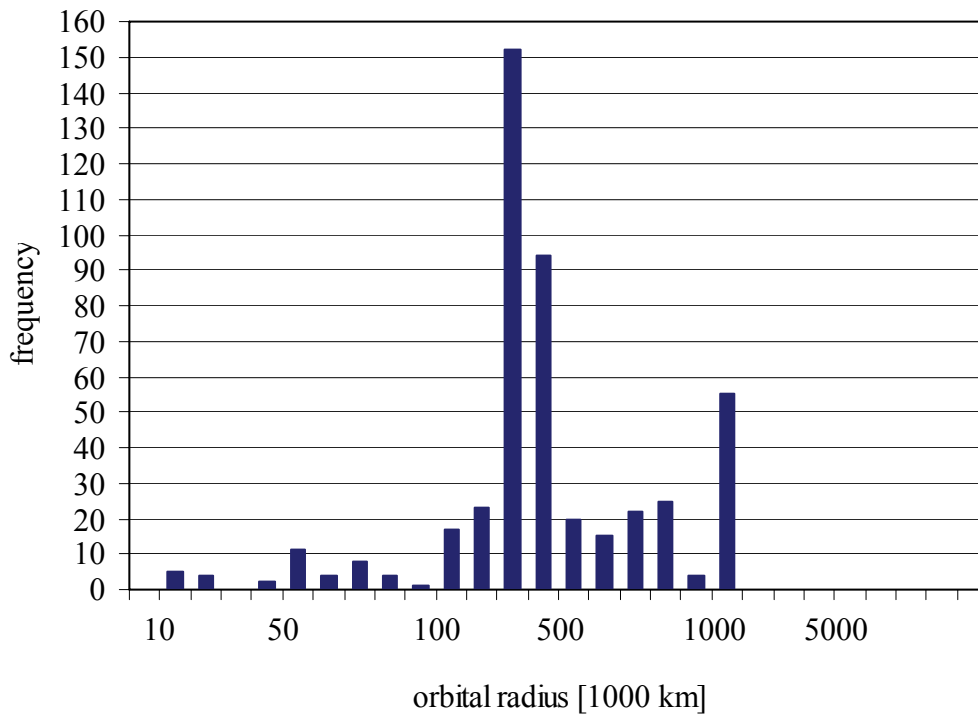


Figure 6-42: Number of particles per radius interval, HITEN

The number of particles detected by the MDC-HITEN has peaks at orbital radii from 300000 to 500000 km, and at 1000000 to 2000000 km.

In summary, all particles detected during the first half year of the mission where NOZOMI was in an orbit around the Earth must be of interplanetary or interstellar origin. Therefore, these particles are merged with the particles that were detected in the interplanetary space and that are discussed in paragraph 6.4.

The MDC on NOZOMI did neither detect dust particles of natural origin that are bound to the Earth, nor space debris.

6.3.2 Dust flux determination

Although the MDC-NOZOMI did not detect particles that are bound to the Earth or may originate from the Earth-Moon system, the overall dust flux measured by the MDC during the mission time in the Earth-Moon system was determined and compared to previous flux measurements by the MDC-HITEN.

Between July 10, 1998 and January 6, 1999, the MDC-NOZOMI detected 21 particles during $\Delta T = 180$ days measuring time. From these 21 particles, $N = 18$ can be used for dust flux determination (two MLI impacts outside the sensor box and one GRID impact were ignored). This gives a total rate of 0.12 particles per day. With the given values of the MDC-NOZOMI sensor area ($A = 0.145 \text{ m}^2$) and effective solidangle ($\Omega = 0.81 \pi \text{ sr}$) the total flux calculates to

$$\Phi = \frac{\pi}{A \cdot \Omega} \cdot \frac{N}{\Delta T}, \Phi_{\text{MDC}}^{1998} = \frac{\pi}{0.0145 \text{m}^2 \cdot 0.81\pi} \cdot \frac{18}{180\text{d}} = 8.51 \frac{1}{\text{m}^2 \cdot \text{d}} \quad (6-27)$$

Since the detection capabilities of the MDC-NOZOMI are strongly limited for small particles, dust flux was also determined for particles with mass heavier than 10^{-12} g , which calculates to 2.84 particles/($\text{m}^2 \cdot \text{day}$).

For the MDC-HITEN, a total dust flux of up to $5.5 \cdot 10^{-4}$ particles/($\text{m}^2 \cdot \text{sec}$) is given in literature, which is 48 particles/($\text{m}^2 \cdot \text{day}$), see Iglseider et al. [Igl1993a]. This value corresponds to $N = 498$ detected particles during $\Delta T = 1142$ days measuring time, with a sensor area of $A = 0.1 \text{ m}^2$ and an effective solid angle of $0.91 \pi \text{ sr}$ (calculated from $\beta = 145^\circ$ aperture angle). In a later review of the MDC-HITEN data by Münzenmayer [Mün1995], 231 of the 498 particles were identified as most likely noise rather than impacts. From the remaining 267 particles, the overall dust flux calculates to 25.7 particles/($\text{m}^2 \cdot \text{day}$). Dust flux for particles heavier than 10^{-12} g calculates to 16.7 particles/($\text{m}^2 \cdot \text{day}$).

The results of dust flux measurements of MDC-HITEN and MDC-NOZOMI in the Earth-Moon system are summarized in Table 6-7.

Table 6-7: Dust flux measurements by MDC-HITEN and MDC-NOZOMI

Particle mass	all	$m > 10^{-12}$
Flux MDC-NOZOMI	8.51	2.84
Flux MDC-HITEN ¹	48.0	33.5
Flux MDC-HITEN ²	25.7	16.7

Flux values given as particles/(m²·day)

¹ values by Iglseider

² values by Münzenmayer

Although the MDC-HITEN and MDC-NOZOMI instrument capabilities and measuring range are comparable, as well as the orbital trajectories of HITEN and NOZOMI with respect to the distances from the Earth, the dust flux determined from the MDC-HITEN data is significantly higher than the flux determined from the MDC-NOZOMI data. Even the more conservative values from Münzenmayer give a three to six time higher flux measured by MDC-HITEN than the values measured by MDC-NOZOMI. The sensitivity of the instruments is nearly equal, the trigger levels varied only slightly during the missions, for MDC-NOZOMI it was nearly constant around $1 \cdot 10^{-13}$ C, for the MDC-HITEN it was set from $2.3 \cdot 10^{-13}$ C to $4.0 \cdot 10^{-13}$ C after the first year in space. The mass distribution of the particles detected by the MDC-HITEN and the MDC-NOZOMI is also nearly similar to each other. The significant difference in dust flux can thus not be explained exclusively by the instrument capabilities.

There are two significant differences in the configurations of the satellites HITEN and NOZOMI that may be responsible for the difference in dust flux measurements. First, HITEN performed several Moon swing-by maneuvers and finally entered Moon orbit, while NOZOMI only performed two Moon and one Earth swing-by. Second, as already described in paragraphs 2.2.2 and 2.3.2, HITEN was a spin-stabilized satellite with spin axis perpendicular to the ecliptic plane, while NOZOMI was a spin-stabilized satellite with spin axis nearly parallel to the ecliptic plane. While the MDC-HITEN thus was scanning the whole latitude range of the ecliptic each revolution of the satellite, the MDC-NOZOMI scanning directions were determined mainly by the satellites attitude that was changed only a few times during the first half year of the mission. Within this work, it can not be proven if this difference in configuration can fully explain the difference in dust flux, since detailed information of the dust distribution in and around the Earth-Moon system would be necessary.

6.3.3 Characteristics of the detected particles

On Nov. 18, 1998, NOZOMI encountered the Leonid particle stream. The Leonid particles originate from the comet 55P/Tempel-Tuttle and, as viewed from Earth, seem to come from the Leo constellation ($\alpha = 153.67^\circ$, $\delta = 21.70^\circ$). The particles can be viewed as meteors from Nov. 14 to Nov 21 every year, with a maximum on Nov. 17. Leonid particles are expected to travel at high speed of around 70 km/sec, the average flight direction is longitude $\lambda = 327^\circ$ and latitude $\beta = -10^\circ$ in Sun centered ecliptic coordinates, width of the particle stream is around 35,000 km. NOZOMI crossed the Leonid particle stream about 1 day after the maximum flux was observed on Earth.

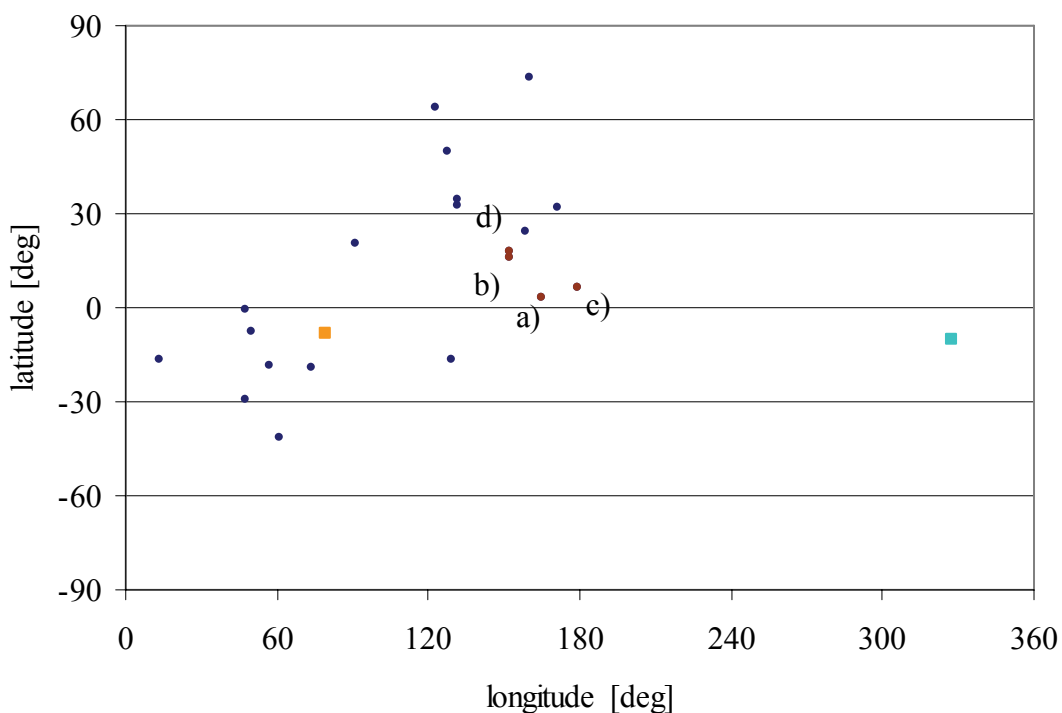


Figure 6-43: Flight direction of 1998 particles

Blue dots: Flight direction of particles detected in the first six months of MDC operation. Red dots: Flight direction of four particles detected during Leonid dust stream encounter on Nov. 18, 1998. Orange square: Mean flight direction of interstellar dust cloud particles. Turquoise square: Flight direction of Leonid dust stream particles.

Although the MDC high voltage was switched off during the encounter on Nov. 18, 4:00 UT to avoid possible damage to the experiment, a significant high number of particles were detected in Nov. 1998 that even show a correlation in flight direction, see Figure 6-43.

Table 6-8: Particles detected around Nov. 18, 1998

Label	File	Imp. No.	Date [UT]	Abs. Speed [km/sec]	Mass [g]	Latitude [deg]	Longitude [deg]
a)	98111701	8	17-Nov-98	11.78	1.5E-11	2.96	165.12
b)	98111801	1	17-Nov-98	13.89	6.0E-11	16.22	151.88
c)	98111801	6	18-Nov-98	26.01	3.3E-13	6.58	179.26
d)	98112101	6	20-Nov-98	10.61	1.9E-11	18.02	152.43

However, for all four particles detected by the MDC around Nov. 18, 1998 (see Table 6-8) neither traveling speed nor flight direction fit to the Leonid dust particle stream, see Figure 6-43. In contrary, the detected particles nearly show anti-Leonid direction, and thus cannot be identified as Leonid dust particles. Nevertheless, a significant influence of the Leonid particle stream on the lunar sodium tail during the 1998 encounter was observed [Smi1999]. This gives evidence that the significant high number of particles detected by the MDC may result from other environmental influences such as collisions of larger particles of the Leonid dust stream with the Moon that produce secondary dust particles, see Sasaki [Sas2002]. The orbital configuration of Earth, Moon and NOZOMI, where NOZOMI was located behind the Moon as seen in the direction of the Leonid particle stream and the Earth-Moon system was moving nearly against the direction of the Leonid particle stream, though makes this explanation unlikely.

6.4 Particles detected in the interplanetary space

After leaving Earth orbit on December 21, 1998, NOZOMI was in an orbit around the sun with perigee at 1.0 AU and apogee at 1.44 AU. The MDC was in operation during the whole mission time in the interplanetary space, and was expected to detect interplanetary and interstellar dust particles. Until the system failure on April 24, 2002, NOZOMI completed 3 ½ orbits.

6.4.1 Overview

NOZOMI's interplanetary cruising phase lasted from January 1999 until April 2002 (in fact, NOZOMI continued its interplanetary orbit, but in April 2002, telemetry was lost and data transmission stopped, see chapter 2.3). About 11000 signals were triggered, recorded, qualified and downloaded.

To separate noise signals from potential impact signals, a neural network as described in chapter 4.3 was used. The chosen topology was a network with two hidden layers containing 11 and 15 neurons, as it came out as optimal topology in the evaluation process described in chapter 4.3. As training data for this neural network, all during data review manually identified impacts from the year 1998, a number of signals identified as impacts during the first data analysis by Münzenmayer and Naumann from the 1999 and 2000 data, and a number of signals that could not be identified clearly as impact or noise signals were used (the latter signals were included into the training data to ensure that no potential impact signals are lost by the screening process). An equal number of noise signals required for training of the network was randomly chosen from the MDC noise data. In this configuration, the neural network identified 288 of the more than 11000 signals that were downloaded from the MDC during the years 1999 to 2002 as possible impacts. Since all training data signals from the years 1999 and 2000 were included in these 288 possible impact signals identified by the neural network, it can be assumed that these 288 signals contain all possible impact signals from the unreviewed 1999 and 2000 data and the previously not analyzed 2001 and 2002 data. Also, manual random examination and cross-checking of a number of downloaded data sets did not give any new possible impacts identified by the experimenter that were not included in the 288 possible impacts identified by the neural network. Finally, the 288 possible impact signals were examined carefully by the experimenter, and a remainder of 77 good signals was identified doubtlessly as impact signals.

Altogether 98 impacts signals (77 good signals plus all 21 signals detected during the Earth-Moon cruising phase which are all assumed to be of interplanetary origin due to the high distances from Earth and orbital speeds exceeding the escape speed from the Earth by far) were identified and analyzed and are discussed here. From these 98 signals, 13 were identified as impacts onto the MDC sensor box shielding grid (for these signals, no mass and speed determination was possible due to a lack of calibration data), and 5 were not analyzed due to charge overload in one or more channels. Particle mass and impact speed were determined for the remaining 80 signals. The results are summarized in Table 6-9, Table 6-10 and Table 6-11, see also Table 6-6 for the particles detected during the first half year.

All orbital coordinates and elements in the following paragraphs are given in the Sun centered Earth ecliptic (eec) coordinate system.

Again, the orbital elements inclination, eccentricity and semi major axis of the detected particles were calculated with respect to the gravitational force only, although most particles discussed in this paragraph experience additional forces like radiation pressure due to their size. The distributions of the orbital elements shown in this chapter are discussed without respect to the simulations shown in paragraph 6.2.3.

In Figure 6-44, the NOZOMI orbit during the interplanetary cruising phase and the orbital positions of the detected particles are shown. The higher number of particles detected north of the ecliptic plane results from the fact that the northern part of the orbit was flown through three times and the southern part only two times until data transmission stopped on April 24, 2002.

Figure 6-45 shows mass vs. impact speed of all detected particles including those from the first half year. Lowest impact speed was 3.0 km/sec, highest was 69.6 km/sec. The detector limits shown in this graph are mean values from all impact positions inside the MDC sensor box.

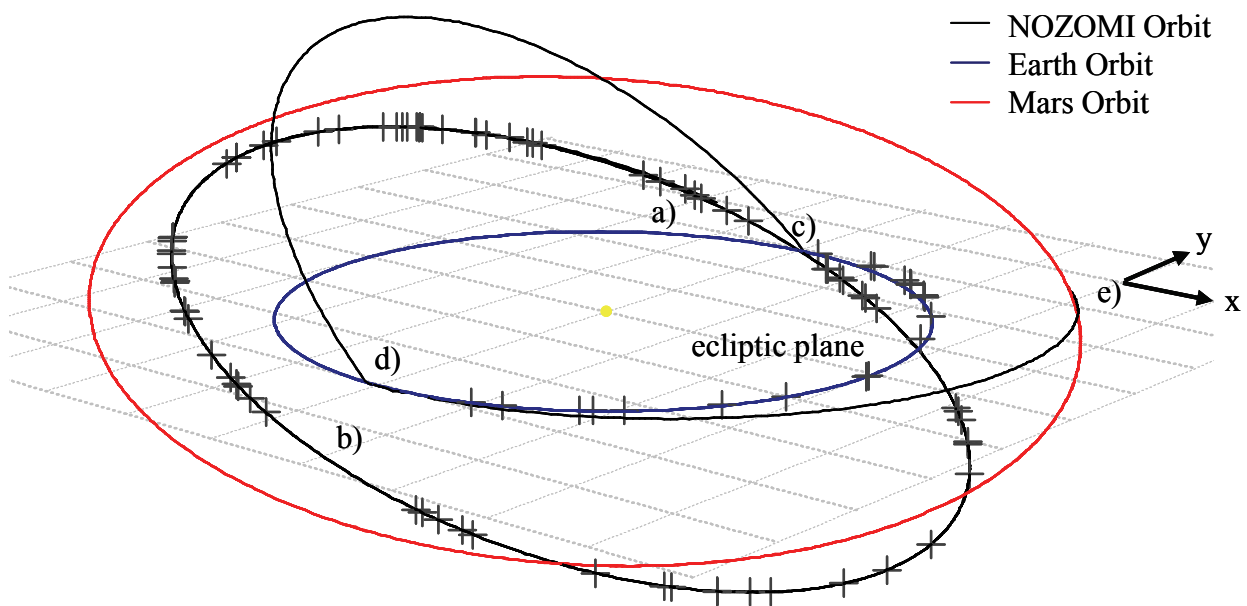


Figure 6-44: Spatial distribution of the particles in the interplanetary space
Mission events: a) Injection into Sun orbit, b) System failure (end of data transmission), c) 1st Earth swing-by, d) 2nd Earth swing-by, e) Mars fly-by.

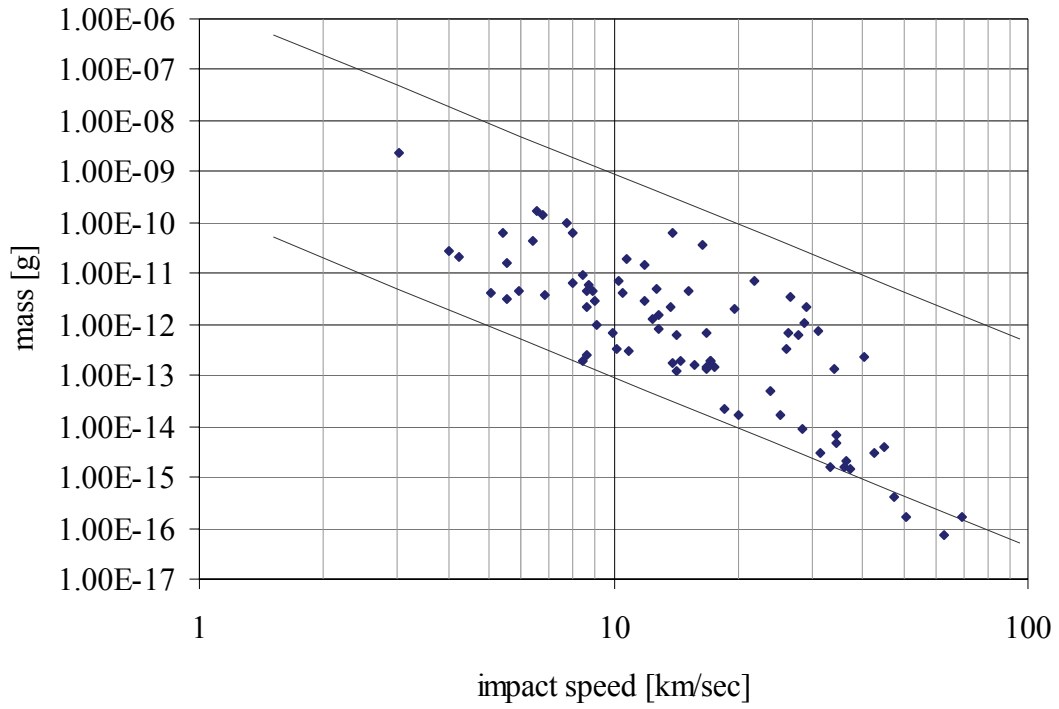


Figure 6-45: Mass vs. impact speed of the particles in the int. space

The two lines show the detector limits. The upper limit is defined by the maximum charge that can be processed by the charge amplifiers and the A/D converters without overload; the lower limit is defined by the sensitivity of the instrument that is set by a certain trigger level.

Table 6-9: Detected particles in the interplanetary space, Part 1

File	Imp. No.	Date [UT]	Time [UT]	Pos. X [km]	Pos. Y [km]	Pos. Z [km]	Orb. Rad. [km]
Sp. X [km/s]	Sp. Y [km/s]	Sp. Z [km/s]	Abs. Sp. [km/s]	Imp. Sp. [km/s]	Mass [g]	Incl. [deg]	Ecc.
99011201	43	1999-01-11	17:36:43	-60090702	133262786	3301958	146221631
-25.75	-19.00	5.91	32.54	8.89	4.6E-12	11.03	0.26
99021401	20	1999-02-12	03:47:27	-129195358	80347667	6705510	152289698
-14.13	-26.58	2.91	30.24	5.88	4.7E-12	6.22	0.08
99030104	29	1999-03-01	09:40:43	-152913439	40469814	7845675	158372600
-68.94	4.25	24.34	73.23	69.58	1.6E-16	57.20	2.07
99030901	3	1999-03-05	22:01:49	-157266956	29376881	8067958	160190476
31.34	-11.02	14.82	36.37	47.41	4.1E-16	72.88	0.93
99030901	31	1999-03-08	19:07:38	-159641635	22221957	8188819	161388735
-7.80	-24.77	-6.26	26.71	7.95	6.8E-12	14.46	0.20
99042001	29	1999-04-20	09:14:18	-160847494	-81802403	8235959	180641580
15.15	-20.76	3.25	25.91	10.18	3.3E-13	8.13	0.17
99052701	39	1999-05-27	00:50:57	-121929404	-153506611	6228099	196137320
27.58	-20.13	-13.39	36.68	16.78	1.5E-13	21.43	0.99
99060201	15	1999-06-01	18:55:49	-113496858	-162463142	5794150	198265936
19.41	-14.17	-2.78	24.19	4.23	2.1E-11	6.83	0.13
99071201	29	1999-07-11	08:00:29	-45209701	-205043548	2284434	209980933
26.48	1.79	5.83	27.18	12.45	1.3E-12	13.09	0.32
99072401	34	1999-07-21	16:10:04	-25529578	-210559673	1273877	212105535
26.26	-2.93	-5.64	27.02	6.38	4.2E-11	12.05	0.17
99091201	12	1999-09-11	13:53:33	73154780	-203522168	-3790628	216303637
37.73	14.96	-3.48	40.74	18.55	2.1E-14	5.03	1.70
99092401	7	1999-09-15	05:27:15	79662563	-200929557	-4124835	216184702
20.13	13.83	3.32	24.65	6.76	1.4E-10	7.77	0.22
99101901	45	1999-10-18	09:37:27	132995420	-165734631	-6863033	212609620
1.00	48.32	-27.55	55.63	44.83	3.8E-15	42.84	3.08
99112001	13	1999-11-20	03:51:16	170868118	-112651281	-8803966	204850517
9.71	23.82	-2.49	25.84	3.04	2.3E-09	6.59	0.19
99112501	3	1999-11-24	23:36:37	174817334	-103541015	-9005852	203378828
-15.37	31.53	5.02	35.43	26.72	3.6E-12	11.19	0.98
00040501	19	2000-04-02	15:23:17	50731385	142029583	-2592619	150840305
-48.18	8.82	1.96	49.02	17.18	1.9E-13	2.38	1.72
00041101	7	2000-04-05	16:51:25	42452439	143886305	-2166598	150033904
N/A	N/A	N/A	N/A	N/A	N/A	N/A	N/A
00041601	8	2000-04-12	01:28:10	24907116	146475307	-1264008	148583235
-29.54	-31.05	-3.49	42.99	34.44	4.5E-15	9.02	1.02
00052301	29	2000-05-20	04:29:12	-78913331	123954539	4072224	146998723
-24.52	-20.40	2.54	32.00	5.55	1.6E-11	5.04	0.18
00052301	36	2000-05-17	07:38:15	-71787710	127846302	3706283	146669318
-39.43	-31.41	-12.65	51.97	23.97	5.1E-14	14.11	1.97
00061301	19	2000-06-09	20:39:49	-123385600	87376625	6354660	151324362
N/A	N/A	N/A	N/A	N/A	N/A	N/A	N/A
00062101	4	2000-06-19	11:51:26	-139206255	66309094	7165354	154358737
-7.96	-30.02	5.73	31.58	10.88	3.1E-13	11.41	0.23
00062101	37	2000-06-19	08:42:39	-139013539	66608656	7155521	154313572
-12.12	-27.67	1.39	30.24	5.07	4.0E-12	3.80	0.07
00062101	42	2000-06-17	07:46:12	-135938575	71223534	6998044	153626367
N/A	N/A	N/A	N/A	N/A	N/A	N/A	N/A
00070701	22	2000-06-30	05:52:23	-152766946	40869640	7859392	158334574
-1.49	-30.94	6.98	31.75	12.71	5.1E-12	13.84	0.28
00070701	26	2000-06-30	18:13:38	-153307441	39615177	7886932	158539388
-3.62	-28.61	-0.34	28.84	8.60	2.6E-13	2.87	0.13

Table 6-10: Detected particles in the interplanetary space, Part 2

File	Imp. No.	Date [UT]	Time [UT]	Pos. X [km]	Pos. Y [km]	Pos. Z [km]	Orb. Rad. [km]
Sp. X [km/s]	Sp. Y [km/s]	Sp. Z [km/s]	Abs. Sp. [km/s]	Imp. Sp. [km/s]	Mass [g]	Incl. [deg]	Ecc.
00070701	29	2000-07-03	19:07:25	-156281040	32162643	8038908	159758640
-4.06	-31.92	-6.72	32.88	10.46	4.3E-12	11.96	0.31
00072601	17	2000-07-22	12:16:06	-167002683	-14687530	8584081	167866930
5.54	-26.32	-2.07	26.97	9.02	2.8E-12	5.02	0.15
00081301	3	2000-08-06	12:18:13	-166716711	-51676975	8564725	174752184
9.95	-23.56	-2.06	25.66	8.39	2.0E-13	5.18	0.17
00081801	37	2000-08-15	18:50:25	-163003944	-73553807	8370791	179026586
11.00	-22.61	-1.57	25.19	6.49	1.7E-10	4.40	0.15
00092901	3	2000-09-25	15:04:09	-121162129	-154420890	6208188	196378752
20.83	-2.97	1.41	21.08	16.39	3.5E-11	5.75	0.58
00101201	16	2000-10-07	17:52:39	-102758167	-172353058	5259521	200729868
21.82	4.72	5.76	23.05	21.79	7.3E-12	20.73	0.67
00101501	37	2000-10-13	14:04:38	-93199460	-179901458	4766798	202665725
21.72	-7.86	4.29	23.49	8.62	2.3E-12	10.87	0.20
00103001	13	2000-10-27	00:45:25	-69838166	-194489332	3563473	206678900
19.99	-5.41	-2.27	20.84	5.55	3.2E-12	6.28	0.33
00103001	22	2000-10-24	14:48:28	-74153607	-192156991	3785745	206003394
20.10	-5.18	-3.36	21.03	6.81	3.7E-12	9.19	0.33
01012501	8	2001-01-09	06:44:50	70699447	-204417263	-3665361	216329064
21.30	10.61	1.42	23.84	3.99	2.7E-11	3.45	0.15
01012501	19	2001-01-19	13:17:01	88861867	-196719539	-4598394	215907743
-3.31	46.49	43.78	63.94	62.40	7.4E-17	69.39	4.10
01012501	29	2001-01-21	19:41:04	92751876	-194750035	-4798212	215762623
24.30	34.16	-11.27	43.41	26.36	6.5E-13	17.79	1.89
01030701	32	2001-03-02	17:23:13	151659347	-144638115	-7821226	209718653
-4.70	45.71	-27.42	53.51	42.48	3.1E-15	43.93	2.80
01030701	42	2001-03-04	04:39:46	153407310	-142285263	-7910657	209383565
2.37	16.94	-4.25	17.62	11.86	2.8E-12	18.35	0.69
01031401	28	2001-03-14	03:56:34	164272640	-125429220	-8467062	206856667
5.26	29.21	-7.72	30.67	12.86	1.6E-12	17.54	0.60
01031401	30	2001-03-14	04:32:27	164297309	-125385114	-8468330	206849571
N/A	N/A	N/A	N/A	N/A	N/A	N/A	N/A
01042801	43	2001-04-25	18:20:58	187835874	-39757497	-9667764	192240577
N/A	N/A	N/A	N/A	N/A	N/A	N/A	N/A
01042801	49	2001-04-13	05:21:54	185210475	-66819656	-9536246	197126169
N/A	N/A	N/A	N/A	N/A	N/A	N/A	N/A
01051701	6	2001-05-12	03:53:34	185013498	-3160239	-9517613	185285096
-20.86	-8.85	12.60	25.93	40.38	2.3E-13	128.56	0.82
01070201	1	2001-06-29	09:35:55	130348109	98285898	-6692786	163387700
-22.57	13.19	8.33	27.44	10.29	7.0E-12	18.30	0.39
01070201	6	2001-06-11	06:08:30	159342208	63034534	-8188596	171552747
-16.68	17.61	-3.57	24.52	7.93	6.0E-11	10.43	0.42
01070201	40	2001-06-22	08:06:52	142835370	85253451	-7336723	166505019
N/A	N/A	N/A	N/A	N/A	N/A	N/A	N/A
01070201	50	2001-06-21	12:59:31	144147630	83721769	-7404466	166861320
N/A	N/A	N/A	N/A	N/A	N/A	N/A	N/A
01071101	3	2001-07-02	05:38:10	124917369	103219225	-6412911	162171770
-21.18	12.28	-3.16	24.69	8.72	6.2E-12	8.93	0.42
01071101	14	2001-07-03	08:32:53	122701224	105114802	-6298786	161692259
N/A	N/A	N/A	N/A	N/A	N/A	N/A	N/A
01080701	35	2001-08-06	13:30:43	40249764	144297129	-2053286	149819628
N/A	N/A	N/A	N/A	N/A	N/A	N/A	N/A

Table 6-11: Detected particles in the interplanetary space, Part 3

File	Imp. No.	Date [UT]	Time [UT]	Pos. X [km]	Pos. Y [km]	Pos. Z [km]	Orb. Rad. [km]
Sp. X [km/s]	Sp. Y [km/s]	Sp. Z [km/s]	Abs. Sp. [km/s]	Imp. Sp. [km/s]	Mass [g]	Incl. [deg]	Ecc.
01081601	8	2001-08-14	17:42:07	17568823	147008013	-886524	148056764
-31.95	-10.70	-9.37	34.97	16.72	7.1E-13	17.25	0.53
01081601	14	2001-08-14	23:33:07	16885348	147047013	-851363	148015755
-29.44	-22.47	-21.12	42.63	33.47	1.6E-15	38.56	1.02
01081601	39	2001-08-11	06:49:33	27219203	146222479	-1382973	148740751
-25.03	-0.60	-0.88	25.05	8.59	4.7E-12	2.22	0.36
01091201	4	2001-09-04	04:37:18	-39704522	140557870	2058017	146072583
N/A	N/A	N/A	N/A	N/A	N/A	N/A	N/A
01091201	24	2001-09-08	22:14:27	-52485293	136371100	2714743	146147708
-25.69	-11.09	0.19	27.98	5.40	6.4E-11	1.15	0.14
01091201	33	2001-08-31	01:13:26	-28290410	143408893	1471372	146180104
-25.41	-14.07	-7.99	30.13	13.66	2.2E-12	15.94	0.30
01091201	35	2001-09-10	04:43:43	-55854359	135073123	2887877	146194384
N/A	N/A	N/A	N/A	N/A	N/A	N/A	N/A
01101501	15	2001-10-07	06:07:38	-118445072	92784313	6100892	150583481
0.11	-17.25	-16.57	23.92	28.96	1.1E-12	50.08	0.57
01101501	37	2001-10-08	20:27:08	-121445047	89542857	6254968	151016381
-10.17	-16.33	-1.93	19.33	13.84	1.7E-13	6.05	0.58
01102601	47	2001-10-25	20:22:45	-147692924	51559764	7599835	156618538
-3.70	-29.54	9.99	31.40	14.26	1.2E-13	19.65	0.24
01110301	8	2001-11-01	18:22:40	-155260426	34800106	7986757	159313011
N/A	N/A	N/A	N/A	N/A	N/A	N/A	N/A
01110301	43	2001-10-29	16:13:37	-152106974	42349726	7825425	158086268
-7.44	-23.83	-4.51	25.37	8.45	9.2E-12	10.70	0.23
01110301	50	2001-10-30	06:59:05	-152762671	40854760	7858999	158326590
7.91	-1.62	-9.16	12.20	34.64	6.5E-15	93.10	0.91
01112101	3	2001-11-16	12:16:52	-165364919	-2030892	8501495	165595762
N/A	N/A	N/A	N/A	N/A	N/A	N/A	N/A
01120901	40	2001-12-02	22:06:35	-167460239	-42873428	8603767	173075380
N/A	N/A	N/A	N/A	N/A	N/A	N/A	N/A
01121801	31	2001-12-15	17:18:10	-163047897	-73317671	8373146	178969850
7.11	-1.35	11.18	13.32	27.87	6.0E-13	70.08	0.81
02020501	2	2002-01-26	20:50:42	-119420615	-156340981	6118480	196827898
8.61	-7.41	-4.43	12.20	14.15	6.4E-13	21.46	0.78
02020501	30	2002-02-01	04:10:21	-111524003	-164433827	5711383	198767972
9.78	-6.04	4.54	12.35	14.51	1.9E-13	21.68	0.77
02021501	14	2002-02-12	00:27:34	-94200049	-179153738	4818354	202467103
22.52	-3.10	-11.50	25.47	15.72	1.6E-13	27.92	0.31
02021501	31	2002-02-10	19:09:15	-96222343	-177623575	4922522	202072029
1.55	4.60	-13.95	14.77	29.10	2.2E-12	93.42	0.72
02022501	25	2002-02-23	05:15:40	-74917678	-191727021	3825042	205879916
8.84	8.41	-22.29	25.41	31.35	7.4E-13	76.82	0.45
02032301	8	2002-03-19	17:27:36	-29441565	-209681925	1483941	211743990
N/A	N/A	N/A	N/A	N/A	N/A	N/A	N/A
02032301	12	2002-03-22	20:37:50	-23430977	-211023843	1174685	212323933
N/A	N/A	N/A	N/A	N/A	N/A	N/A	N/A
02033101	7	2002-03-27	05:49:45	-14980509	-212550436	739853	213078978
14.11	-1.18	-4.31	14.80	9.11	9.5E-13	16.92	0.65
02041401	34	2002-04-01	13:17:15	-4703522	-213835193	211179	213887020
12.48	1.60	-8.34	15.10	12.84	8.4E-13	33.82	0.64

Table 6-9, Table 6-10 and Table 6-11 show the complete data of the particles detected during the interplanetary cruising period from January 1999 to April 2002. More details for each data set/particle can be found in Appendix C.

6.4.2 Determination of interplanetary dust flux

During the whole mission time, 98 particles were detected by the MDC. From these, 17 particles were identified as MLI impacts outside the sensor box, 13 particles were identified as grid impacts and were not analyzed due to lacking calibration data, and 5 particles were identified as impacts but were not analyzed due to charge overload. In the following, only the remaining 63 particles were used for the determination of interplanetary dust flux. Between July 10, 1998 and April 14, 2002 (last memory dump sent to Earth), the MDC was recording data for altogether 1374 days. This gives a total rate of 0.047 particles per day, or one particle every 3 weeks. For the determination of the instrument independent total dust flux, the instruments characteristics must be taken into account. Commonly, dust flux is given as particles per area per time interval, as in Table 6-12 as particles/(m²·day). Hence, the calculated rate of 0.046 particles per day must be corrected by the instruments sensor area ($A = 0.0145 \text{ m}^2$) and effective solid angle ($\Omega = 0.81 \pi \text{ sr}$), these characteristics are discussed in chapter 3.2.3. Also, the instruments measuring range must be regarded carefully to get reliable results for dust flux. The total dust flux Φ is therefore given by

$$\Phi = \frac{\pi}{A \cdot \Omega} \cdot \frac{N}{\Delta T}, \Phi_{\text{MDC}}^{\text{int}} = \frac{\pi}{0.0145 \text{m}^2 \cdot 0.81\pi} \cdot \frac{63}{1374 \text{d}} = 3.90 \frac{1}{\text{m}^2 \cdot \text{d}} \quad (6-28)$$

whereas N is the number of particles detected during the time interval ΔT .

Applying the instrument characteristics, the total flux of interplanetary particles detected by the MDC calculates to 3.90 particles/(m²·day), the cumulated flux of particles heavier than 10⁻¹² g (29 particles) calculates to 1.80 particles/(m²·day), for particles heavier than 10⁻⁹ g (1 particle) to 0.06 particles/(m²·day). These results are summarized and compared to the model by Grün et al. [Grü1985] in Table 6-12.

Table 6-12: Comparison of the MDC results and the Grün model.

Particle mass	$m > 10^{-15} \text{ g}$	$m > 10^{-12} \text{ g}$	$m > 10^{-9} \text{ g}$
Flux MDC	3.72	1.80	0.06
Flux Grün model	92	2.98	0.26

Flux values given as particles/(m²·day)

The cumulated dust flux measured by the MDC lies far below the predictions of the Grün model for particle masses greater than $m = 10^{-9} \text{ g}$ and $m = 10^{-15} \text{ g}$, while the cumulated flux for particle masses greater than $m = 10^{-12} \text{ g}$, which is 1.80 particles/(m²·day), meets the predicted value of 2.98 particles/(m²·day) by a factor of ≈ 1.5 . Since the measuring range of the MDC allows a reliable dust flux determination only for particle mass around 10⁻¹¹ g to 10⁻¹² g, this good consistency confirms the reliability of the MDC dust data measurements.

Unlike it is presumed by the model, the MDC sensor area's normal is not rotating in the ecliptic plane, this was not taken into account for the calculations. Detector dead time caused by processing noise signals was neglected. Also, detector down time, which can be assumed to a few percent of mission time (see paragraph 6.2.4), was not considered in the determination of dust flux. The calculated values are mean values over the whole mission time. A further breakup into smaller time intervals (months or half years) is possible but was

not regarded to give meaningful results, due to the small number of detected particles that are available for flux determination and the varying sensitivities of the MDC caused by the attitude of the NOZOMI spacecraft (see paragraph 6.2.3).

6.4.3 Characteristics of the detected particles

In this paragraph, the characteristics of the detected particles are discussed. First, some statistical analyzes of mass, speed and orbital elements of the particles are presented. Subsequent, patterns were identified within the whole set of detected particles and discussed separately.

The orbital elements eccentricity e , inclination i and semi-major axis a discussed in this paragraph were calculated from the radius vector \mathbf{r} and the speed vector \mathbf{v} of a particle as follows (see Steiner & Schagerl [Ste2004]):

$$\begin{aligned}
 i &= \arccos\left(\frac{\mathbf{r} \times \mathbf{v}}{|\mathbf{r} \times \mathbf{v}|} \mathbf{e}_z^{ecc}\right) \\
 e &= \frac{|\mathbf{q}|}{\mu}; \quad \mathbf{q} = \mathbf{v} \times (\mathbf{r} \times \mathbf{v}) - \mu \frac{\mathbf{r}}{|\mathbf{r}|}; \quad \mu = GM_{Sun} \\
 a &= \frac{(\mathbf{r} \times \mathbf{v})^2}{\mu(1 - e^2)}
 \end{aligned} \tag{6-29}$$

whereas G is the gravitational constant and M_{Sun} the mass of the Sun.

In Figure 6-46, mass vs. absolute speed of the detected particles is shown. A clear tendency towards smaller mass with increasing orbital speed can be seen for the speed range of 20 km/s upwards. A number of medium sized particles from 10^{-11} g to 10^{-14} g does not show this behavior and has low orbital speed between 10 and 20 km/s. 16 particles have orbital speed higher than 40 km/s, which is about the mean escape speed at the orbital radius range from 1.0 AU to 1.4 AU.

The absolute speed of the particles in relation to the escape speed is shown in Figure 6-47. Escape speed (with respect only to the gravitational force) decreases from 44 km/s at 0.9 AU to 35 km/s at 1.5 AU. Again, 16 particles have orbital speed greater than the escape speed, which is shown as a dashed line. The solid line represents the orbital speed of bodies on a circular orbit (again with respect only to the gravitational force). A majority of the detected particles has orbital speed below this circular speed, which indicates that these particles are either on elliptical orbits and were detected near the aphelion of their orbits, or, if they are on circular orbits, are affected by the Sun's radiation pressure (which decreases the circular orbital speed of such particles). Most particles detected by the MDC are within the mass (and therefore size) range of particles that have β -values greater than zero and thus are affected by solar radiation pressure.

As can also be seen in Figure 6-47, a high number of particles were detected at orbital radii of around 1.0 AU and 1.4 AU, while in between the number of detected particles is significantly

lower. Since the duration of stay of NOZOMI (see Figure 6-27) also is higher at 1.0 AU and 1.4 AU due to the orbital configuration, the detected number of particles was scaled by the duration of stay. Since the high detection rate during the first six months where NOZOMI was in an orbit around the Earth may be a result of some effects caused by the Earth (e.g. gravitational focusing) or the Moon, all 1998 particles were removed from the data for this analysis. During the remaining time span, NOZOMI never encountered Earth or Mars. The result is shown in Figure 6-48. As can be seen, there is still a significantly higher detection rate at around 1.0 AU and 1.4 AU than in between.

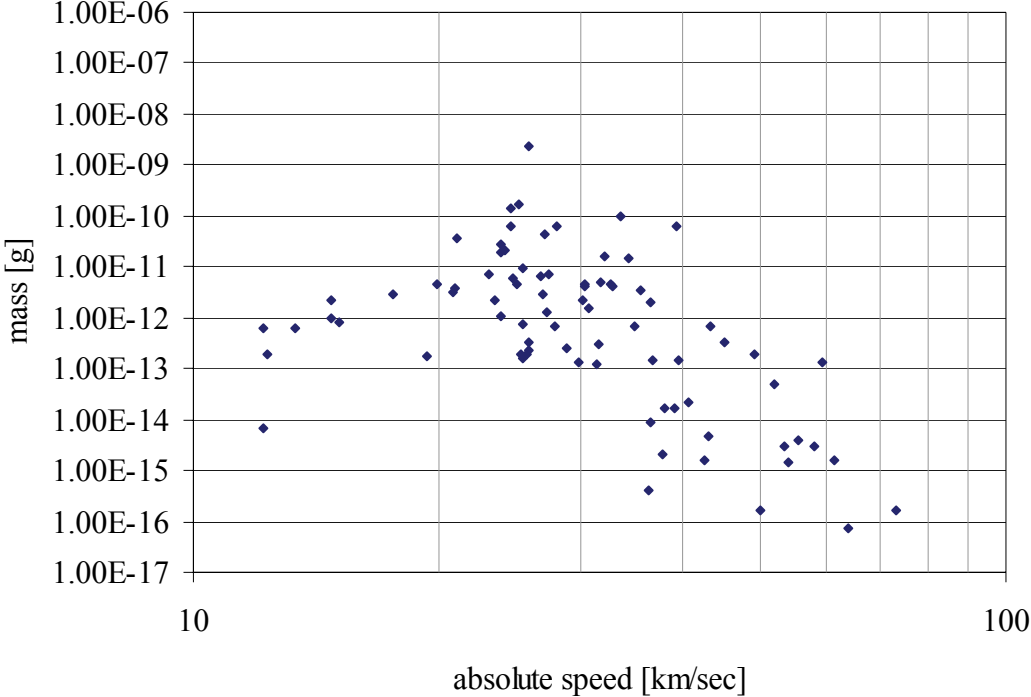


Figure 6-46: Mass vs. absolute speed of the detected particles

The absolute speed vector of the particles was determined from the impact speed and the NOZOMI orbital position and attitude.

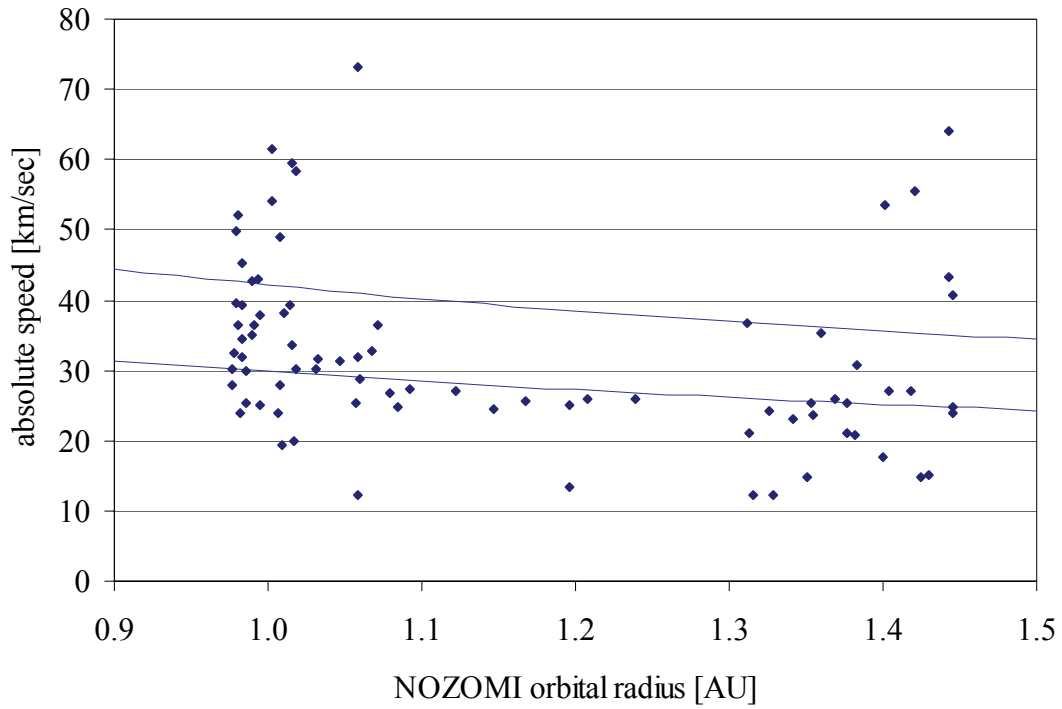


Figure 6-47: Orbital radius vs. abs. speed of the particles

The two lines represent the circular orbital speed (lower, solid line), and the escape speed (upper, dashed line).

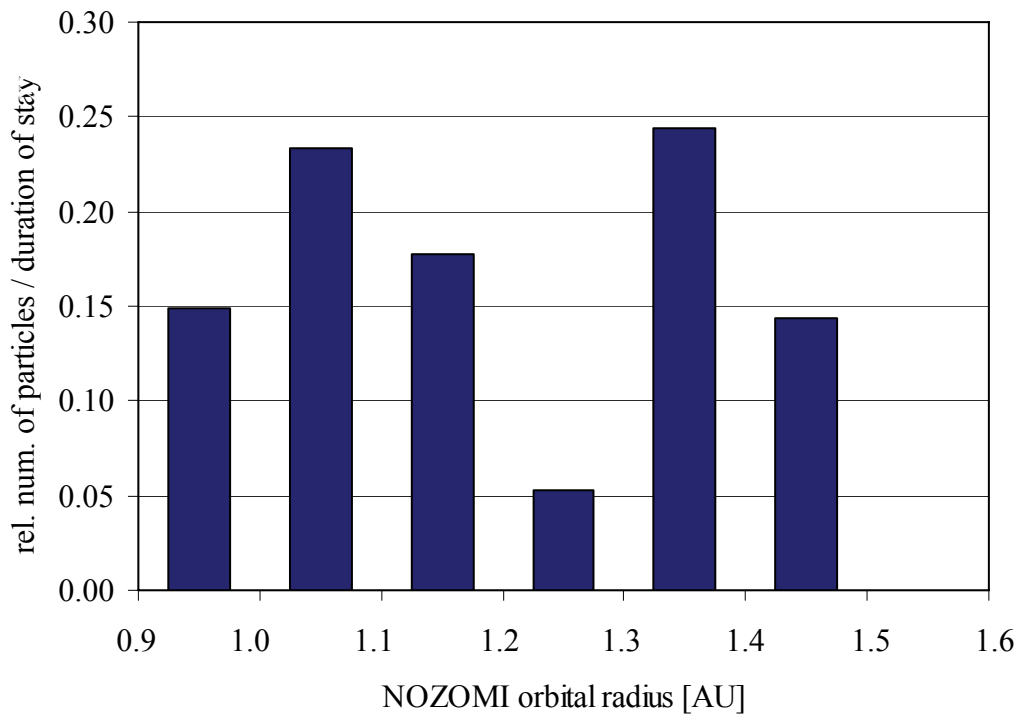


Figure 6-48: Number of particles per radius interval, corrected

The number of particles detected around 1.0 AU (R^{Earth}) and 1.4 AU (R^{Mars}) after correction by the duration of stay of the NOZOMI spacecraft (see Figure 6-27) is still higher than between the orbits of Mars and Earth.

On the following pages, the distributions of mass and orbital speed and of the orbital elements inclination and eccentricity of the detected particles are shown.

The distribution of orbital speed of the particles detected by the MDC is shown in Figure 6-49. Orbital speed ranges from 12.2 km/s to 73 km/s with a strong peak at 25 km/s to 30 km/s. 67% of all particles have an orbital speed in the range from 20 km/s to 40 km/s.

The distribution of mass of the particles detected by the MDC is shown in Figure 6-50. Particle mass ranges from $2.3 \cdot 10^{-9}$ g down to $7.4 \cdot 10^{-17}$ g with a peak at 10^{-11} g to 10^{-13} g.

The shown distributions of speed and mass of the detected particles are determined mainly by the MDC measuring range, see Figure 3-17. They must not be interpreted as absolute speed and mass distributions of dust particles in the interplanetary space. To get information about the real distributions of mass and speed of the dust particles, similar data from several in-situ and remote sensing instruments with different measuring ranges must be combined, as described in paragraph 2.1.2.

The distributions of inclination and eccentricity of the detected particles are shown in Figure 6-51 and Figure 6-52, respectively. The inclination distribution of the detected particles has a strong peak to 0° to 20° , and falls rapidly for higher inclination (one retrograde particle with inclination 128° is not included in this graph). The eccentricity distribution of the detected particles has a strong peak at 0.1 to 0.2, and falls for rising eccentricity until $\varepsilon \approx 1$. There are two populations of unbound particles with eccentricities from 1.7 to 2.1 and from 2.7 to 3.

The number of detected particles per month over the whole mission time is shown in Figure 6-53. After a period of high detection rate during the first half year of the mission, where 21 particles were detected (extrapolated ≈ 42 particles/year), the detection rate falls down to 15 particles/year during 1999 and rises to 20 particles/year in the year 2000 and 33 particles/year in the year 2001. In the year 2002, 9 particles were detected from January to March, which gives an extrapolated value of ≈ 36 particles/year. These detection rates correspond well with the calculated sensitivity of the MDC for apex particles (which represent the main constituent of the interplanetary dust cloud) as shown in Figure 6-28. None of the strong peaks in June 2000, June 2001, August 2001 and October 2001 can be associated with a particle stream since the detected particles during these months do not show any similarities in speed or flight direction. The November 1998 peak is discussed in paragraph 6.3.3. The mentioned peaks and the gaps from December 1999 to February 2000 and in November/December 2000 can only be explained by statistical fluctuations of the detection rate.

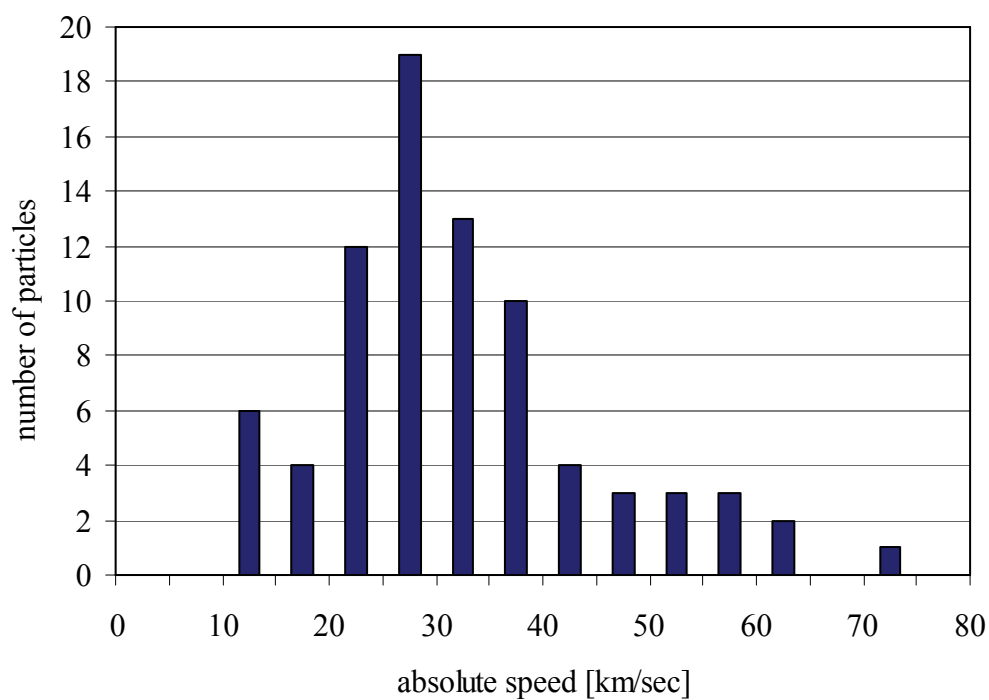


Figure 6-49: Number of particles vs. absolute speed

The absolute speed of the detected particles ranges from 10 km/sec up to 75 km/sec, with a peak at 25 to 30 km/sec.

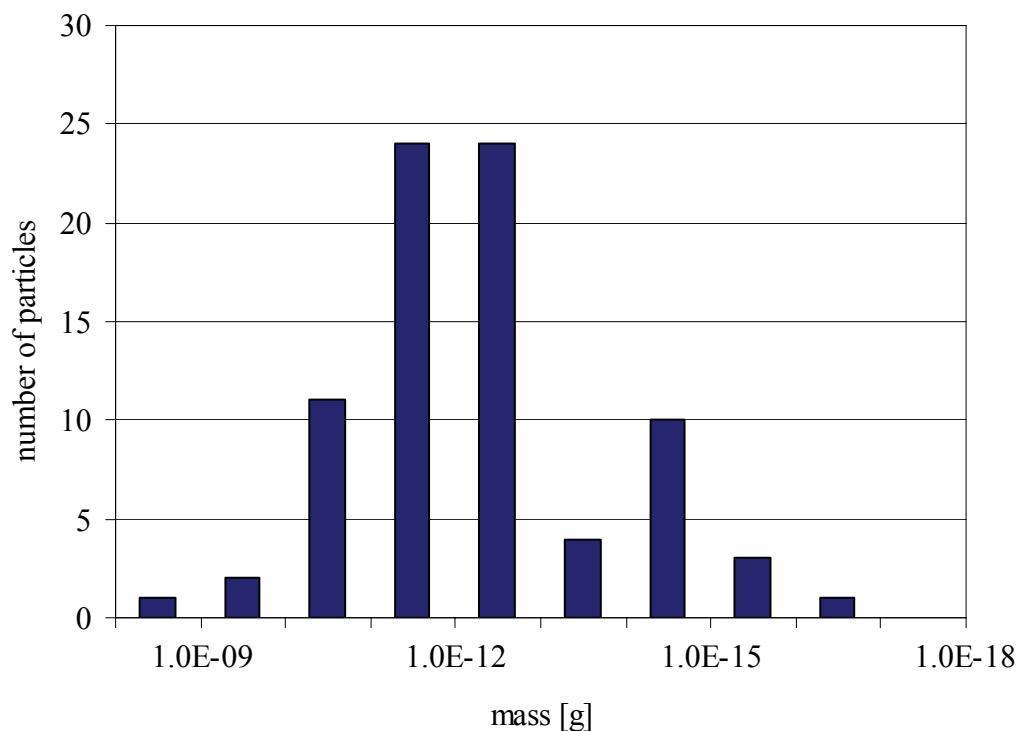


Figure 6-50: Number of particles vs. mass

The mass of the detected particles ranges from 10^{-8} g to 10^{-17} g, with peaks at 10^{-11} to 10^{-13} g.

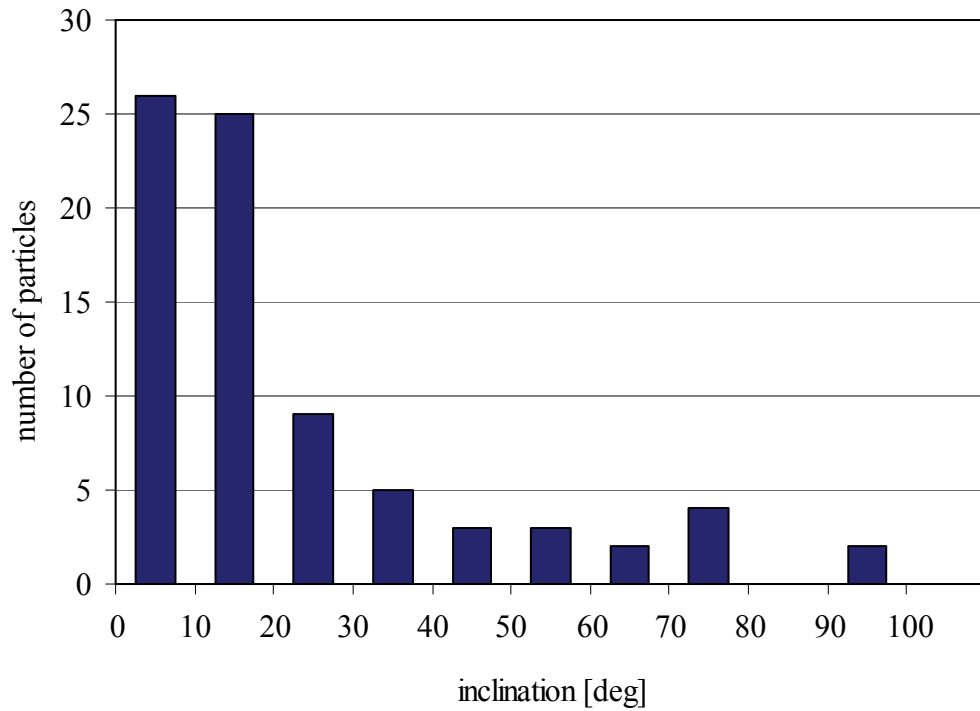


Figure 6-51: Number of particles vs. inclination

Inclination of the detected particles ranges from 0° up to 93° (with one retrograde particle, $i = 128^\circ$, not included), with maximum at 0° to 20° .

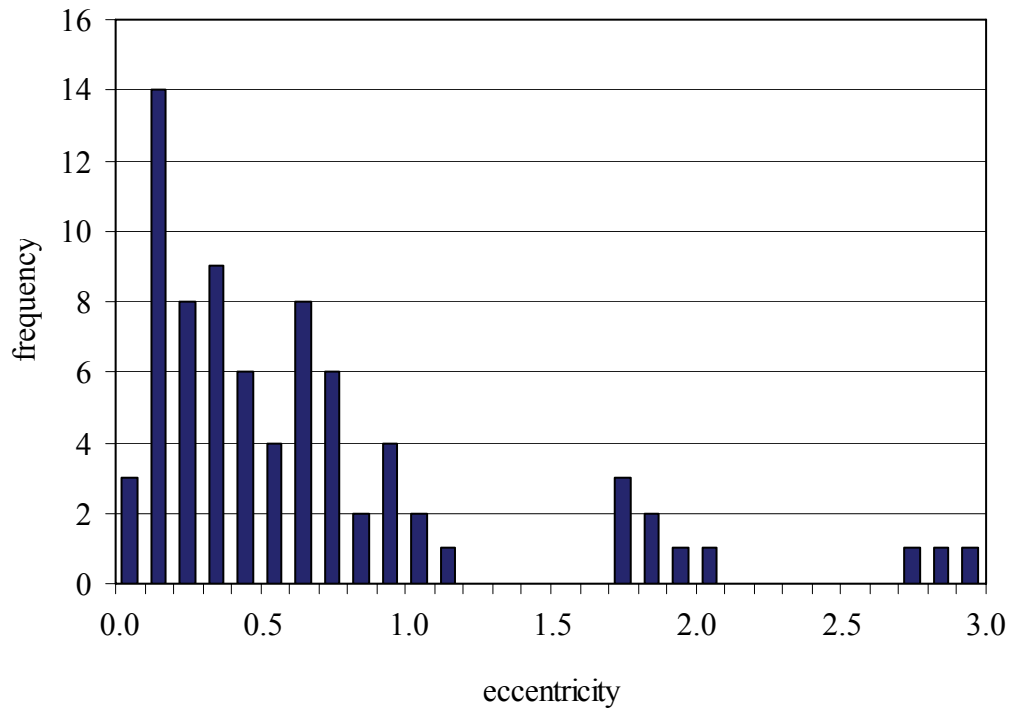


Figure 6-52: Number of particles vs. eccentricity

The eccentricity of the detected particles splits into one elliptical and two hyperbolic populations. Elliptical eccentricities have a peak at 0.1 to 0.2.

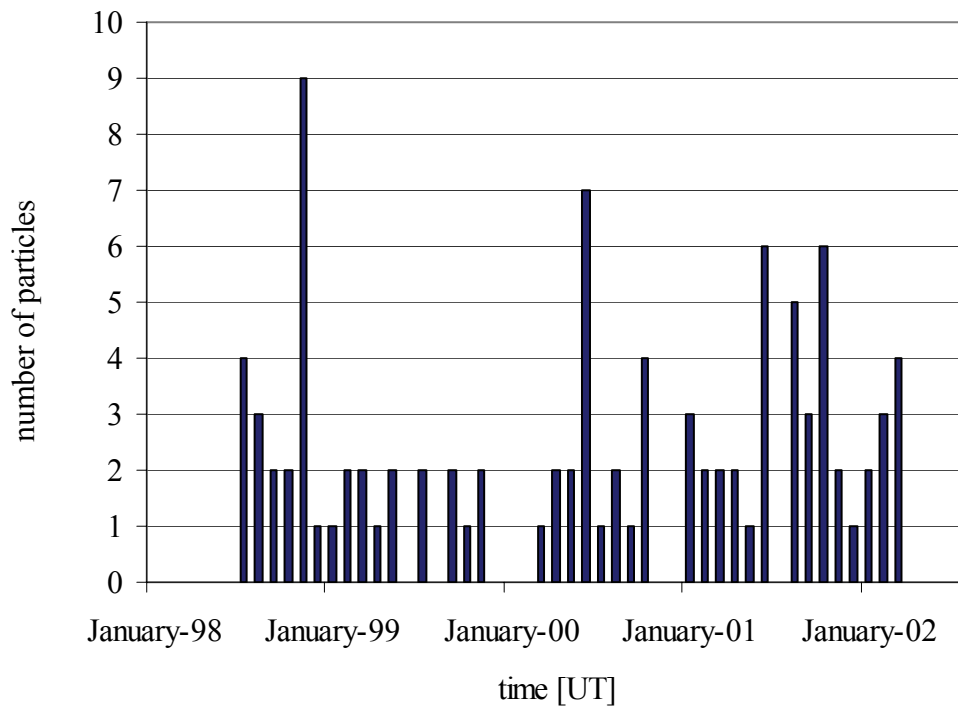


Figure 6-53: Number of particles over mission time

Distribution of the number of detected particles per month over mission time. Peaks and gaps are not assigned to particle streams or caused by orbital configuration.

To identify possible separable populations of particles in the measured MDC data, a cluster analysis was performed on the individual characteristic attributes of the particles: Mass m , eccentricity e and inclination i . Again, a standard cluster analysis method as described in paragraph 6.2.1 was used (with the parameters Complete Linkage, Euclidean distances). Based on the three populations of bound particles identified by Grün et al. [Grü1997], a fixed number of nine clusters was chosen to have sufficient space for all possible populations of bound and unbound particle populations, and also mavericks (like one previously identified retrograde particle). The results of this analysis are shown and discussed in the following.

Table 6-13: Dust populations according to Grün et al.

Population	Asteroidal	Core	A	B	C
mass distribution maximum	10^{-3} g	10^{-5} g	10^{-11} g	10^{-13} g	5×10^{-15} g
Eccentricity					
0.00	0.572	0.572	1.628	0.975	0.627
0.10	2.078	2.078	1.864	0.975	0.266
0.25	1.753	1.753	1.791	0.878	0.140
0.45	1.110	1.110	0.225	1.244	0.063
0.65	0.898	0.898	0.011	0.078	0.063
0.80	0.155	0.155	0.326	0.780	1.198
0.98	0.000	0.000	3.016	5.384	7.678
Inclination					
0°	2.809	2.809	1.684	0.525	0.513
10°	2.809	2.809	2.020	2.707	1.566
20°	1.039	1.039	1.347	1.998	2.278
30°	0.286	0.286	0.673	0.608	1.109
45°	0.073	0.073	0.337	0.112	0.154
60°	0.000	0.000	0.002	0.001	0.026
90°	0.000	0.000	0.000	0.000	0.001

Altogether five populations of bound particles were identified, with different but overlapping mass range, and different distributions in eccentricity and inclination. These populations were named E1, E2, E3, E4 and E5 (“E” for bound populations on “e”lliptic orbits). “Population” E5 contains only one particle on a bound, but retrograde orbit.

Also, four populations of unbound particles were found, also with different mass range, inclination and eccentricity, named H1, H2, H3 and H4 (“H” for unbound populations on “h”yperbolic orbits). Populations H3 and H4 contain only two and one particle of very low mass, respectively.

On the following pages, the different characteristics of the identified populations are analyzed statistically. In Figure 6-54 and Figure 6-55, the eccentricities and inclinations of the larger populations E1, E2, E3, H1 and H2 are shown; all populations are displayed in a different color. Statistical analyses of the larger populations are shown subsequently.

Population E1 (blue dots) consists of particles with mean mass around $1 \cdot 10^{-10}$ g on low inclination, low eccentricity orbits.

Population E2 (green dots) consists of lighter particles with mean mass around $7 \cdot 10^{-13}$ g on low inclined orbits and a different, bimodal distribution in eccentricity.

Population E3 (turquoise dots) consists of light particles with mean mass around $6 \cdot 10^{-15}$ g, on high inclined orbits and with high eccentricity (> 0.5 and < 1.0).

Population E4 (not shown) consists of three particles with mean mass around $1.2 \cdot 10^{-12}$ g, on very high inclined orbits and with medium eccentricity.

Population E5 (not shown) consists of one particle with mass $2.3 \cdot 10^{-13}$ g, on a retrograde, high inclined orbit and with high eccentricity 0.82 (single value).

Population H1 (red dots) consists of particles with mean mass around $1.8 \cdot 10^{-13}$ g, on low inclined orbits with mean eccentricity around 1.6 (mean value).

Population H2 (orange dots) also consists of light particles with mean mass around $2.9 \cdot 10^{-14}$ g, with higher inclination and very high eccentricity around 3.0 (mean value).

Population H3 (not shown) consists of two very light particles with mass $1.6 \cdot 10^{-16}$ on high inclined orbits with eccentricity around 1.9 (mean value).

Population H4 (not shown) consists of one very light particles with mass $7.4 \cdot 10^{-17}$ on a high inclined orbit with eccentricity 4.1 (single value).

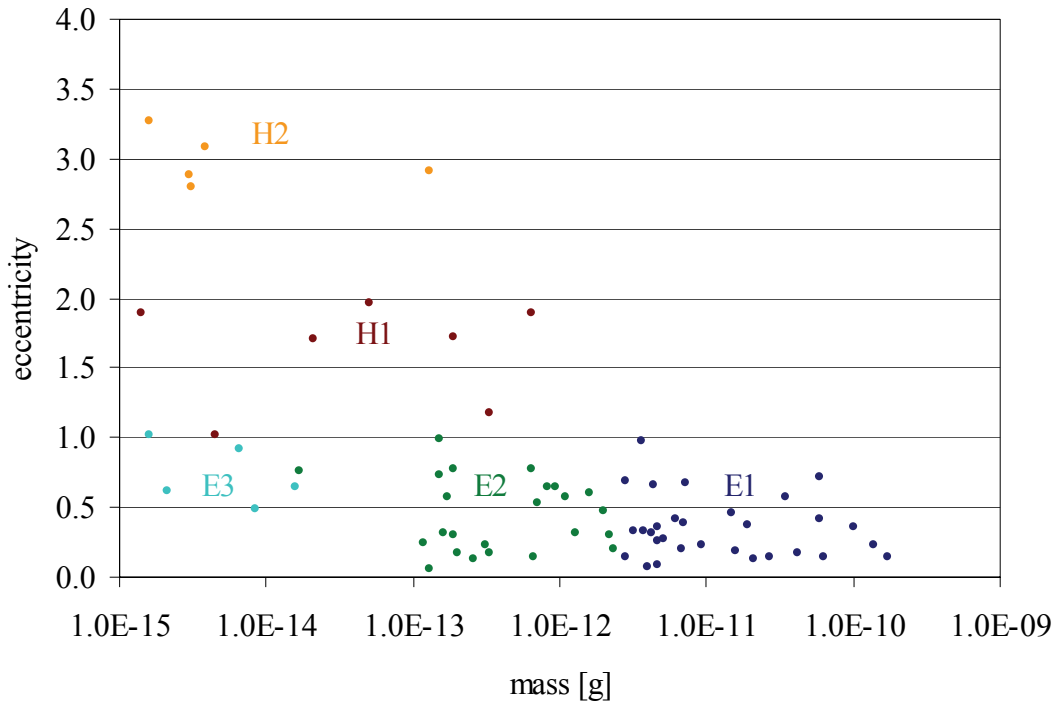


Figure 6-54: Eccentricity over mass, identified populations

Population E1, blue dots; Population E2, green dots; Population E3, turquoise dots; Population H1, red dots; Population H2, orange dots.

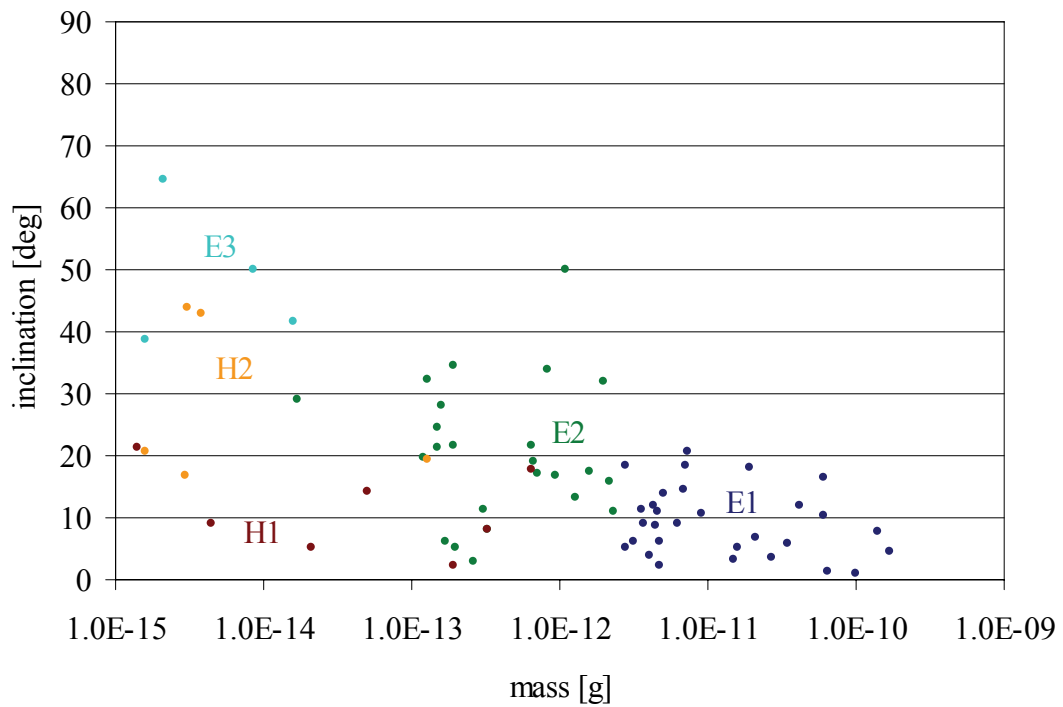


Figure 6-55: Inclination over mass, identified populations

Population E1, blue dots; Population E2, green dots; Population E3, turquoise dots; Population H1, red dots; Population H2, orange dots.

The main properties of the 31 population E1 particles are summarized in Table 6-14. Flight directions of the particles are shown in Figure 6-56.

Population E1 particles show some similarities to population A particles described by Grün et al. The mass distribution of population E1 particles is shown in Figure 6-57. The mean mass of population E1 particles of $1.02 \cdot 10^{-10}$ g fits to the maximum of the mass distribution of Grün's population A ($1 \cdot 10^{-10}$ g). Also, the distributions of eccentricity and inclination of population E1 (see Figure 6-59 and Figure 6-60) fit well to the corresponding distributions of population A, besides that the distribution of eccentricity does not show the second peak at high eccentricities near 1 and the distribution of inclination has a maximum at 0° to 10° instead of 10° for Grün's population A particles.

Population E1 particles preferable impact from the apex direction of the spacecraft (see Figure 6-58). This is the expected behavior for particles of non-negligible β -value orbiting in nearly circular orbits, since the circular orbit speed for particles experiencing radiation pressure is lower than the circular orbit speed with respect only to gravitational force.

Table 6-14: Properties of the 31 population E1 particles

Pop. E1	Mass [g]	Eccentricity	Incl. [deg]	Sm. ax. [AU]
Max	2.30E-09	0.98	20.73	3.45
Min	2.80E-12	0.07	0.92	0.66
Mean	1.02E-10	0.34	9.13	1.18

One maverick value omitted in semimajor axis mean value

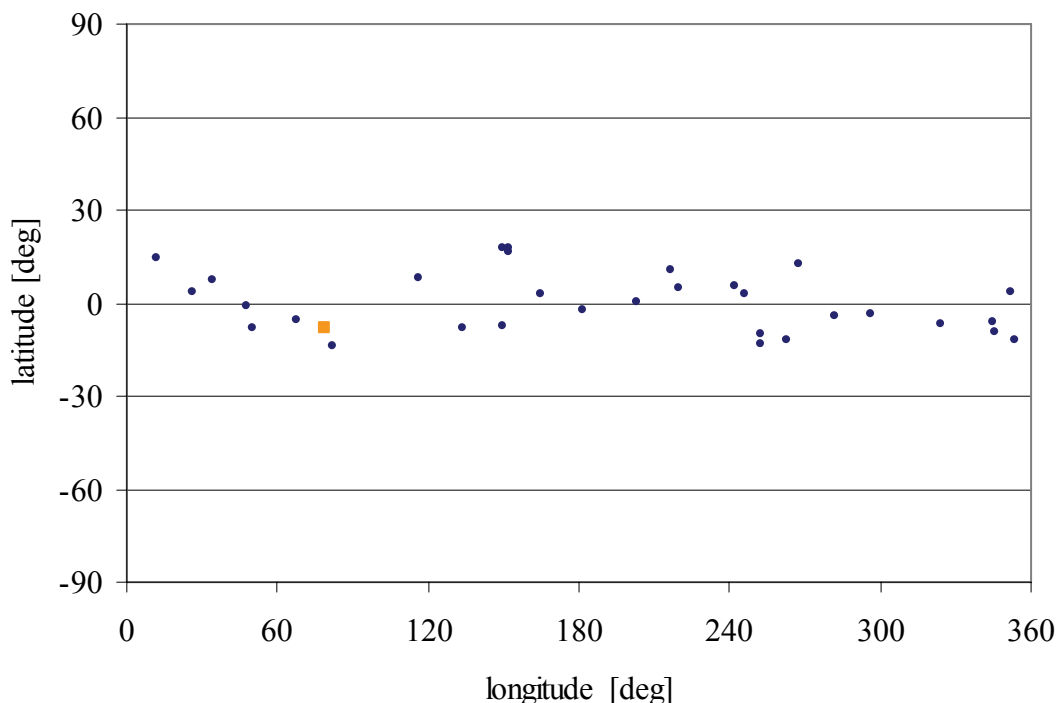


Figure 6-56: Latitude vs. longitude of population E1 particles

Population E1 particles do not show a preferred flight direction. The orange square marks the downstream direction of interstellar dust flux.

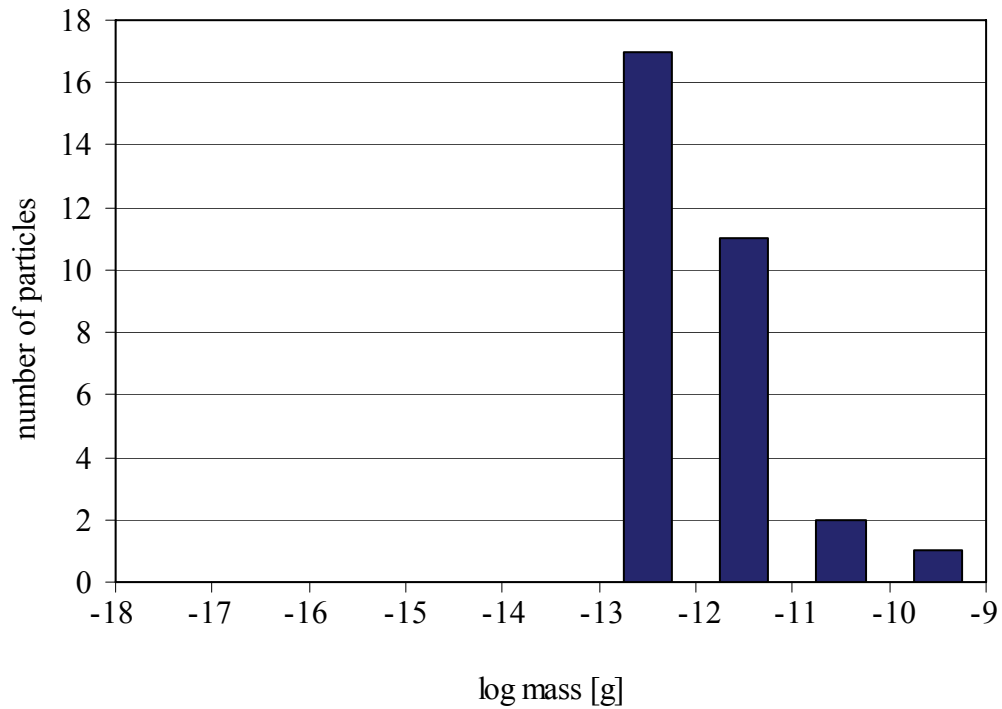


Figure 6-57: Mass distribution of population E1 particles

Population E2 particles have high mass from 10^{-9} g to 10^{-13} g, with a peak at 10^{-13} g.

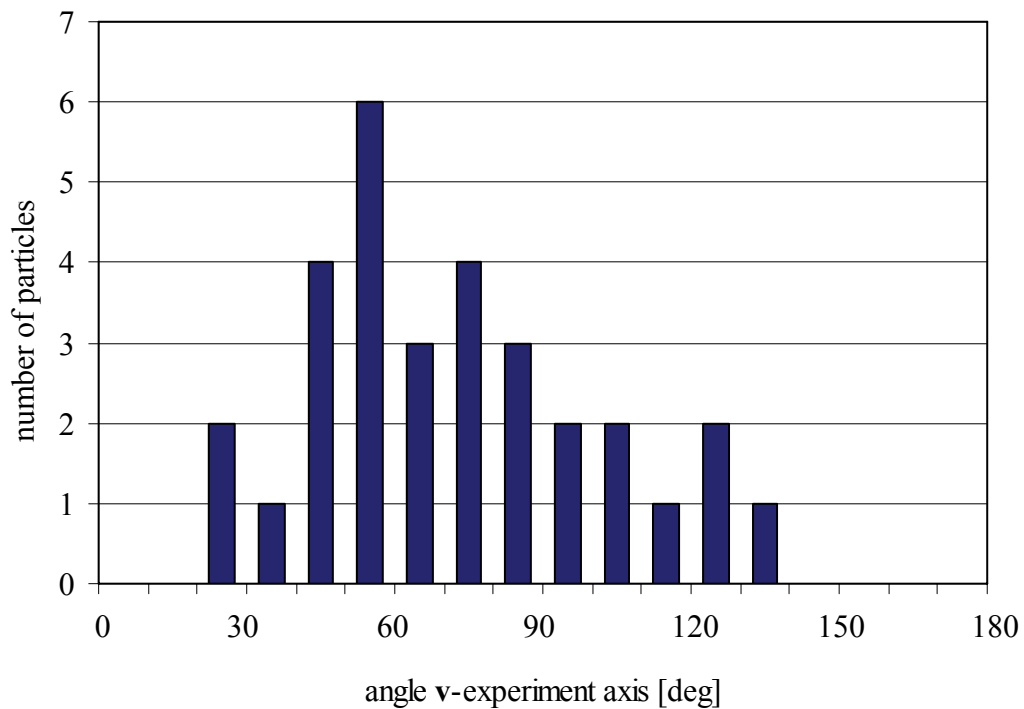


Figure 6-58: Impact direction distribution population E1 particles

Population E1 particles mainly arrive from the spacecrafts apex direction (angle experiment axis – flight direction $< 90^\circ$).

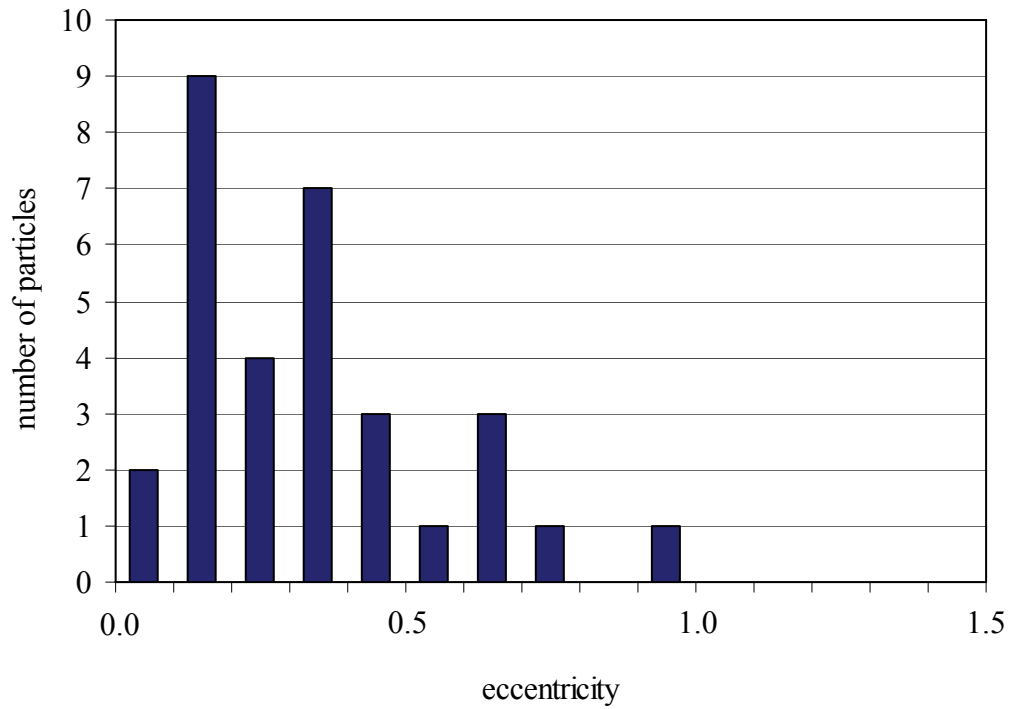


Figure 6-59: Eccentricity distribution population E1 particles

Population E1 particles mainly have low eccentricities with a peak at 10° to 20° .

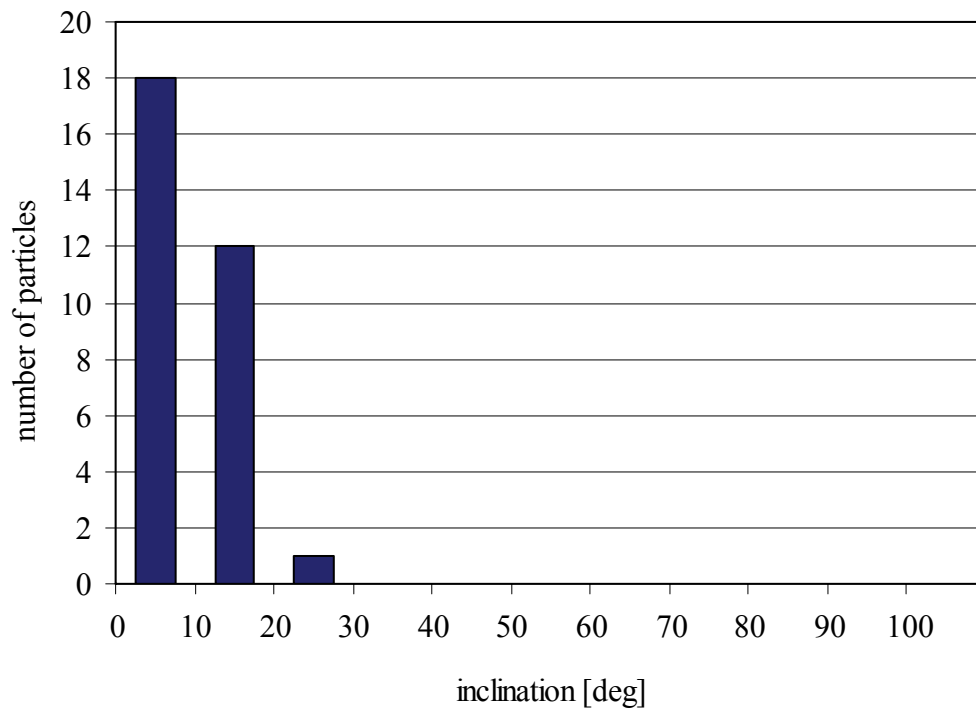


Figure 6-60: Inclination distribution population E1 particles

Population E1 particles have low inclinations ($< 30^\circ$) with a peak at 0° to 10° .

The main properties of the 24 population E2 particles are summarized in Table 6-15. Flight directions of the particles are shown in Figure 6-61.

Population E2 particles have lower mass, but broader distributions in eccentricity and inclination towards higher eccentric and higher inclined orbits. In addition, population E2 particles show some similarities to Grün's model. The mass distribution of population E2 particles is shown in Figure 6-62 and has a mean value of $6.95 \cdot 10^{-13}$ g, which fits to the maximum of the mass distribution of Grün's population B ($1 \cdot 10^{-13}$ g) within the limits of the accuracy in mass determination. Also, the distributions of eccentricity and inclination of population E2 (see Figure 6-59 and Figure 6-60) fit well to the corresponding distributions of population B, the distribution of eccentricities of population E2 particles even shows the bimodal characteristic like Grün's population B particles do, but with the second peak at lower eccentricity than population B particles.

Like population E1 particles, population E2 particles preferable impact from the apex direction of the spacecraft (see Figure 6-63).

Table 6-15: Properties of the 24 population E2 particles

Pop. E2	Mass [g]	Eccentricity	Incl. [deg]	Sm. ax. [AU]
Max	2.30E-12	0.99	50.08	4.15
Min	1.70E-14	0.06	2.87	0.64
Mean	6.95E-13	0.44	20.52	1.39

One maverick value omitted in semimajor axis mean value

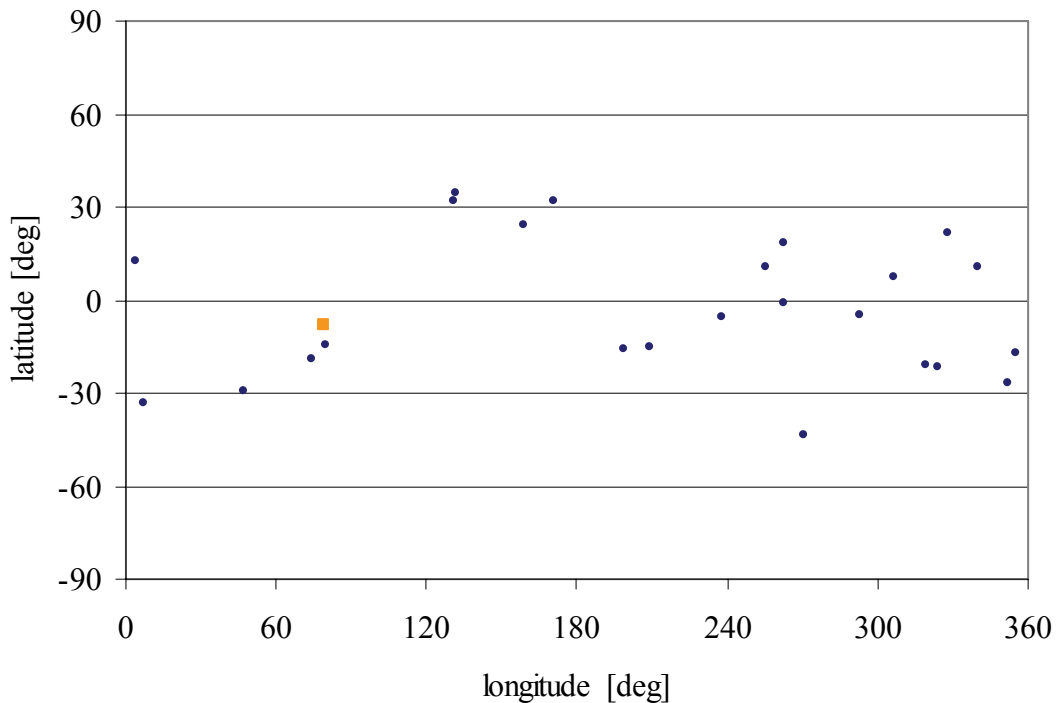


Figure 6-61: Latitude vs. longitude of population E2 particles

Population E2 particles do not show a preferred flight direction. The orange square marks the downstream direction of interstellar dust flux.

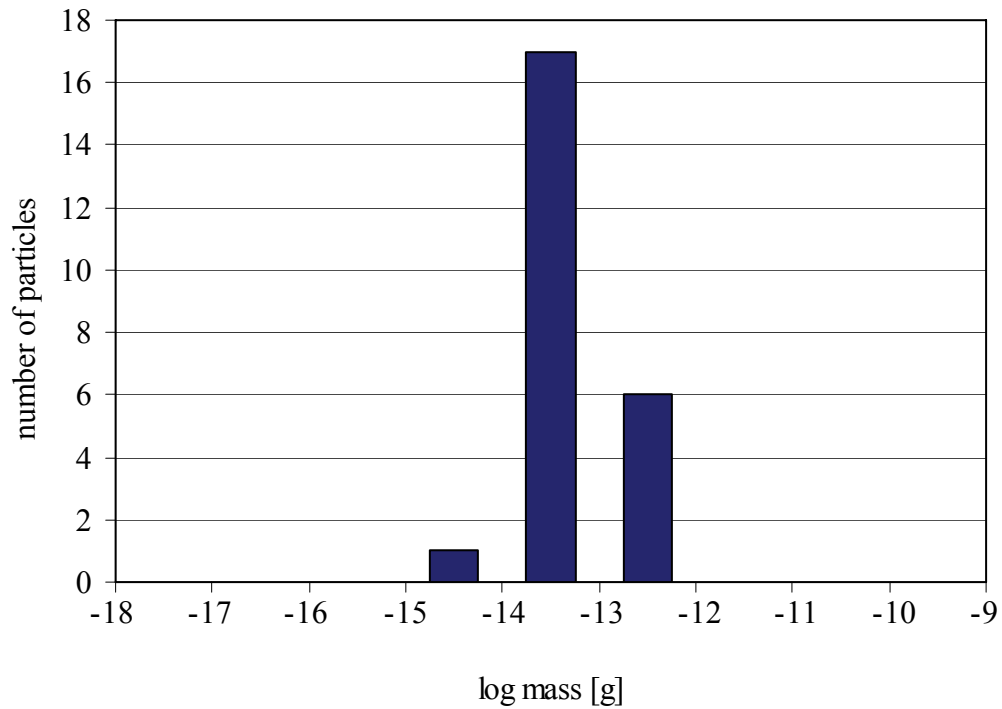


Figure 6-62: Mass distribution of population E2 particles

Population E2 particles have low mass from 10^{-12} g to 10^{-15} g, with a peak at 10^{-13} to 10^{-14} g.

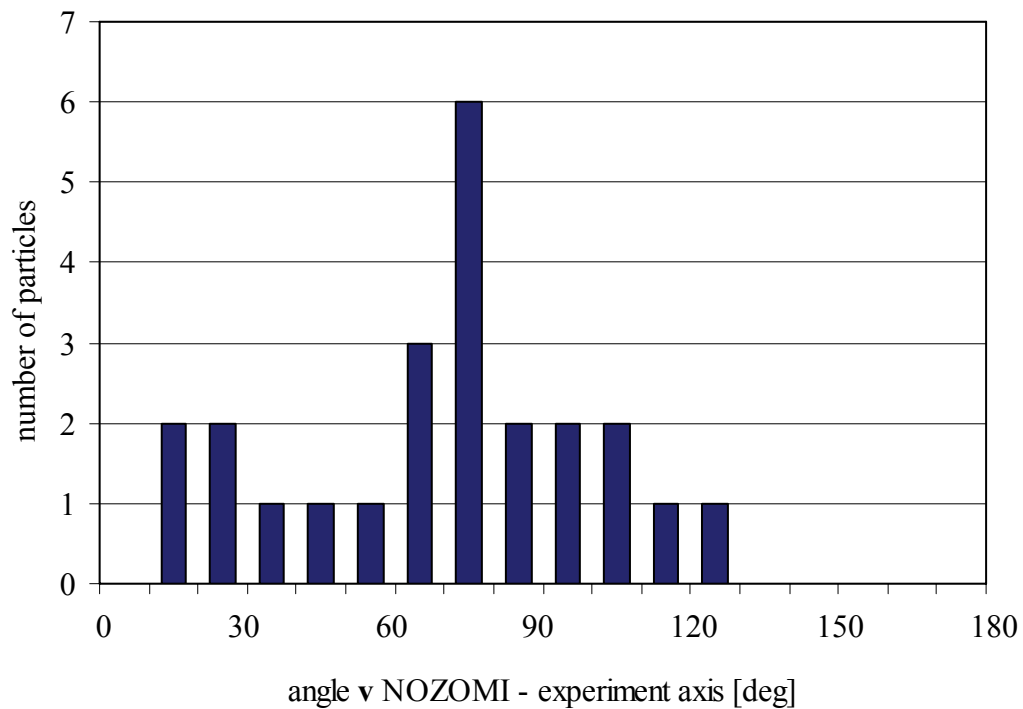


Figure 6-63: Impact direction distribution population E2 particles

Population E2 particles mainly arrive from the spacecrafts apex direction (angle experiment axis – flight direction $< 90^\circ$).

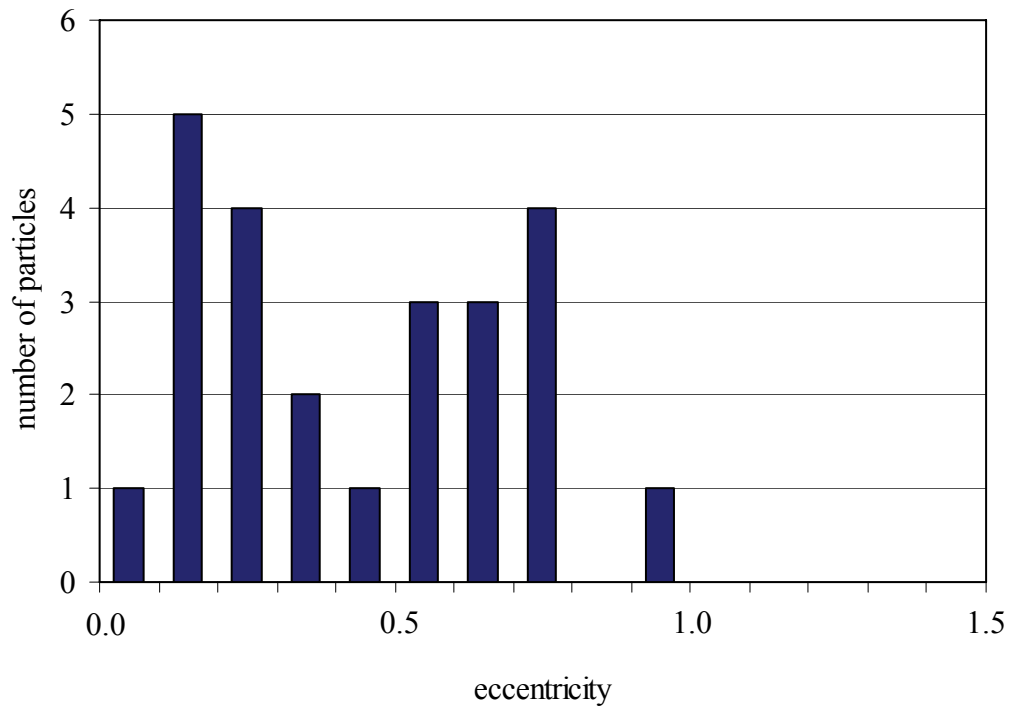


Figure 6-64: Eccentricity distribution population E2 particles
 Population E2 particles have a bimodal distribution in eccentricity with a peaks at 0.1 to 0.2 and at 0.7 to 0.8.

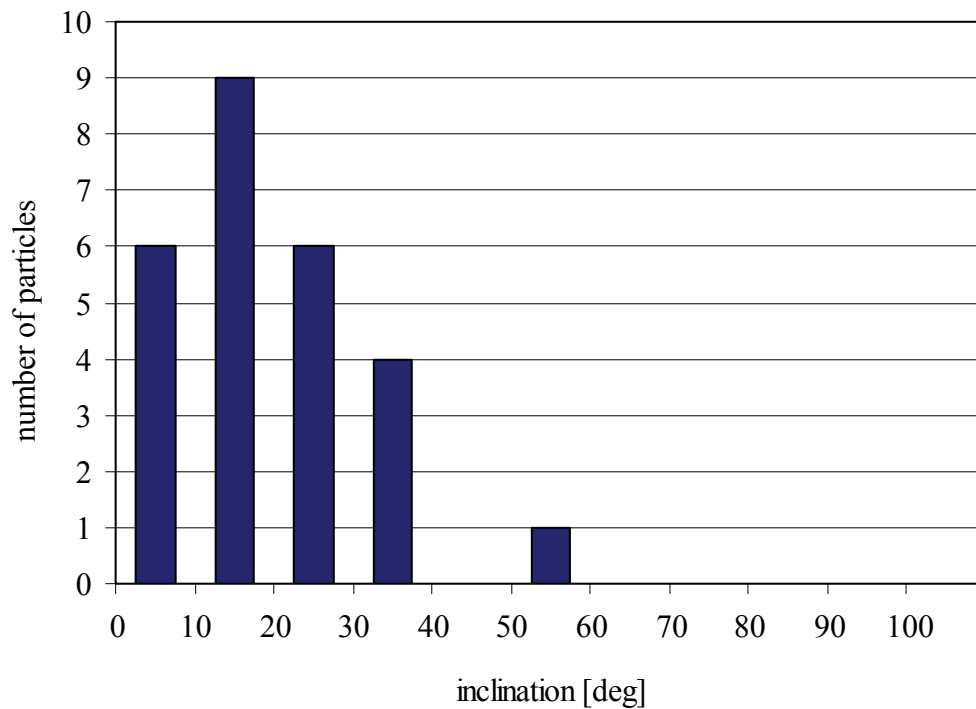


Figure 6-65: Inclination distribution population E2 particles
 Population E2 particles have medium inclination (up to 60°) with a peak at 10° to 20°.

Populations E3 and E4 contain only 6 and 3 particles, respectively. Because of this low number of particles, no distributions in orbital elements or further statistical analyses were made. Particles of both populations have high inclinations with mean values of 60° (E3) and 80° (E4), and medium eccentricity of 0.77 (E3) and 0.66 (E4). While population E4 particles are of medium mass with a mean value of $1.18 \cdot 10^{-12}$ g, population E3 particles are very light with a mean mass of $5.85 \cdot 10^{-15}$ g.

All particles of both populations were impacting from the apex direction of the spacecraft.

Table 6-16: Properties of the 6 population E3 particles

Pop. E3	Mass [g]	Eccentricity	Incl. [deg]	Sm. ax. [AU]
Max	1.60E-14	1.02	93.10	2.89
Min	4.10E-16	0.49	38.56	0.58
Mean	5.85E-15	0.77	60.10	2.12

One hyperbolic value omitted in semimajor axis mean value

Table 6-17: Properties of the 3 population E4 particles

Pop. E4	Mass [g]	Eccentricity	Incl. [deg]	Sm. ax. [AU]
Max	2.20E-12	0.81	93.42	1.38
Min	6.00E-13	0.45	70.08	0.68
Mean	1.18E-12	0.66	80.11	0.96

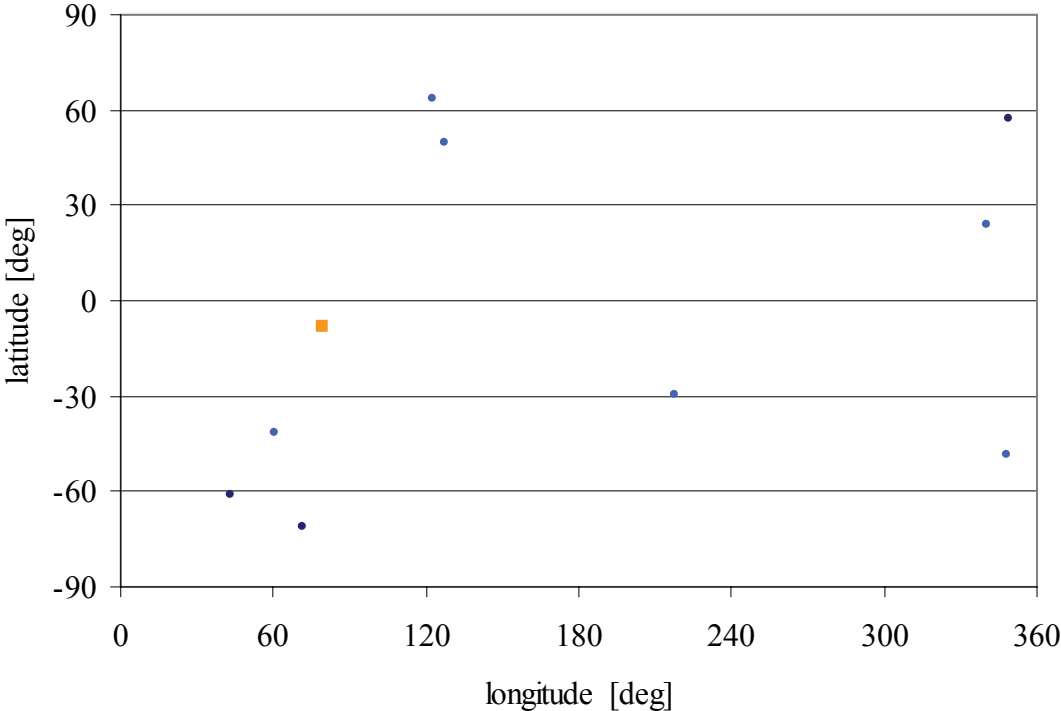


Figure 6-66: Latitude vs. longitude of population E3 and E4 particles
 Population E3 particles (light blue dots) and population E4 (dark blue dots) do not show a preferred flight direction.

Population H1 particles have medium mass with a mean value of $1.78 \cdot 10^{-13}$ g, hyperbolic eccentricity with a mean value of 1.62 and low inclinations with a mean value of 11.12° .

All but one of the 7 population H1 particles were impacting from the anti-apex direction of the spacecraft.

From the hyperbolic characteristics of the orbits, the strongly preferred anti-apex impact direction, and the low inclinations of population H1 particles, it can be supposed that population H1 may (at least partially) consist of β -meteoroids. It is indeed true that from the 7 population H1 particles, two were registered during mission times where the detector sensitivity for particles traveling on nearly radial trajectories was nearly maximal, and four were registered at a time where this detector sensitivity was in medium range (see Figure 6-30 for the detector sensitivities). In addition, population H1 particles do not show a preferred flight direction (see Figure 6-67) and thus do not belong to a particle stream of any origin. However, a more detailed analysis of this assumption cannot be done within the scope of this work.

Table 6-18: Properties of the 7 population H1 particles

Pop. H1	Mass [g]	Eccentricity	Incl. [deg]
Max	6.50E-13	1.97	21.41
Min	1.40E-15	1.02	2.38
Mean	1.78E-13	1.62	11.12

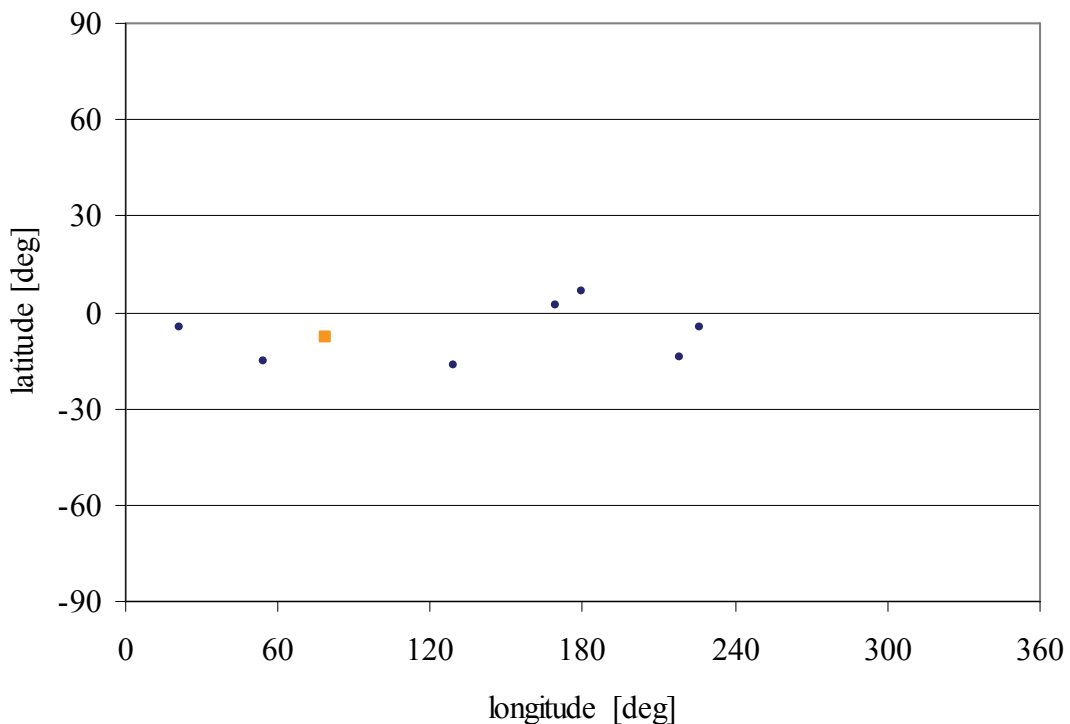


Figure 6-67: Latitude vs. longitude of population H1 particles

Population H1 particles do not show a preferred flight direction. The orange square marks the downstream direction of interstellar dust flux.

Population H2 particles have small mass with a mean value of $2.83 \cdot 10^{-14}$ g, hyperbolic eccentricity with a mean value of 2.99 and medium inclinations with a mean value of 28.70° .

All of the 5 population H1 particles were impacting from the anti-apex direction of the spacecraft.

Population H2 particles show a correlation in flight direction to the downstream direction of the interstellar gas and dust flux that is within the accuracy of the determination of particle flight direction, see Figure 6-68. The high speed of the particles and the correlation to the direction of the interstellar gas and dust flux suggests that population H2 particles may be of interstellar origin. This possibility must be discussed with respect to the known properties of ISD grains and their dynamics in the heliosphere.

Table 6-19: Properties of the 5 population H2 particles

Pop. H2	Mass [g]	Eccentricity	Incl. [deg]
Max	1.30E-13	3.27	43.93
Min	1.60E-15	2.80	16.67
Mean	2.83E-14	2.99	28.70

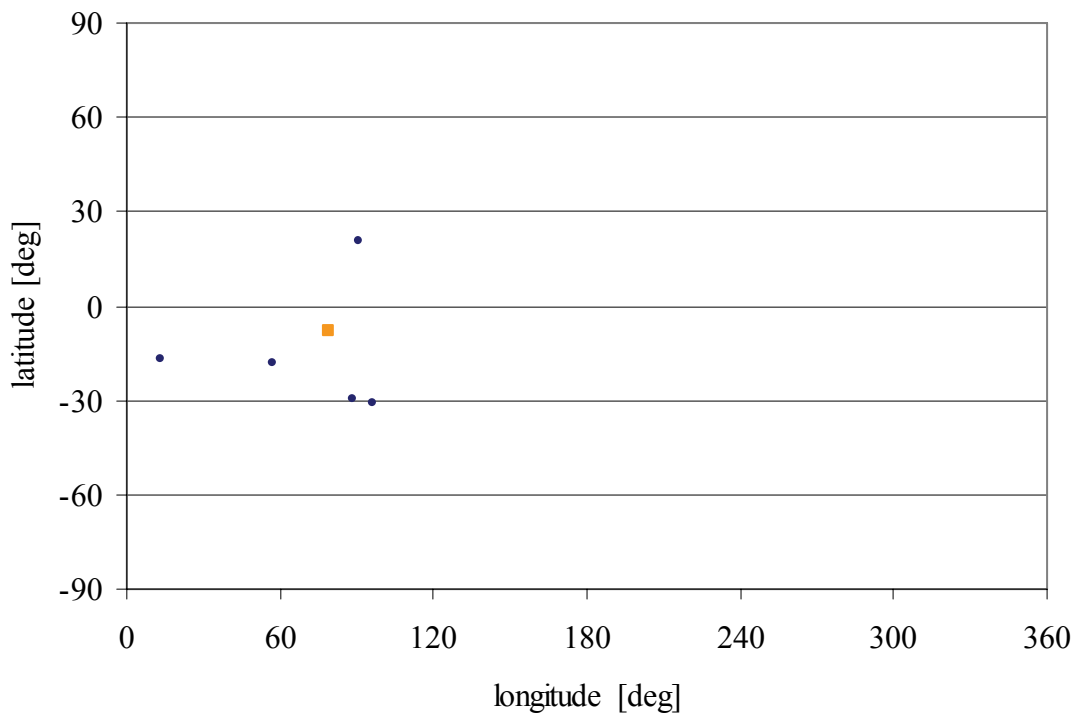


Figure 6-68: Latitude vs. longitude of population H2 particles

Population H2 particles show a preferred flight direction that is correlated with the downstream direction of the interstellar gas and dust flux.

6.5 Summary

In this chapter, the scientific results of the MDC on NOZOMI were presented and discussed. For the first time, the full dust data recorded by the MDC were analyzed in a consistent way and with respect to the instrument's and the spacecraft's properties. In advance, the characteristics of the NOZOMI flight data, the noise signals recorded by the MDC during the mission, the MDC detection capabilities and the instrument conditions throughout the mission were discussed.

At first, the huge amount of noise signals recorded by the MDC was examined. It was shown that about a third of all noise signals recorded is likely caused by solar radiation that influences the MDC sensor electronics indirectly. A number of clusters of noise signals of very similar shape were identified within the whole noise data. The origins of these signals, which are assumed the same within each single cluster, could not be assigned to any known source of noise (no information about the NOZOMI spacecraft's internal operations that may be a source of noise recorded by the MDC was available). Several periods of highly increased noise rates were identified during the whole mission time, each lasting hours to weeks, which are surrounded by periods with very low noise rates. A temporal correspondence of these high noise periods to solar eruptions detected by the SOHO satellite was not approved. In summary, the origin of most of the high amount of noise recorded by the MDC and the observed patterns within the noise data could not be clarified with the available information. However, the detector dead time caused by the processing of recorded noise signals was shown to be negligible, since only during some short periods a significant value of a few percent of time was reached.

The NOZOMI flight data and the MDC sensor pointing directions were examined in detail. The determination of the MDC view axis at a given impact time from the NOZOMI attitude and orbit data is required for the later analysis of impact data and was carried out thoroughly. For a later statistical interpretation of the impact data recorded by the MDC, knowledge about the pointing directions and detection capabilities of the MDC over the mission time is required, both strongly dependent on the NOZOMI attitude data and its orbit positions. The NOZOMI orbit and attitude data was analyzed and discussed. Detection capabilities of the MDC were determined and discussed with respect to the NOZOMI attitude and orbit data.

The MDC operating data as derived from the telemetry data was analyzed and discussed. The MDC was in good condition throughout the mission. Fluctuations of the power supply voltage and the high voltage inside the sensor box are correlated with the MDC instruments temperatures, which in turn are correlated to the NOZOMI distance from the Sun. Influences of the high voltage fluctuations on the results of the primary data analysis process (which are mass and impact speed of the detected particles) were not considered. From the MDC command log, a detector down time of a few percent of the total mission time can be determined that should be considered for later dust flux determinations, but was neglected due to missing command data, which prevented an exact down time determination for the time after September 1999.

From the results of the primary analysis of the detected particles (particle mass and impact speed), the MDC pointing direction at the moment of impact, and the NOZOMI flight data (attitude, orbital position and flight speed), a full set of data (orbital position \mathbf{r} and speed

vector \mathbf{v}) was derived that describes the particle's orbits. From this, the orbital elements inclination, eccentricity and semi major axis, which are more convenient for further interpretation, were calculated. The analysis of the impacts that were detected by the MDC was split into two parts with respect to the different environmental conditions during the first half year of the mission when NOZOMI was in an orbit around the Earth, and the rest of the mission time when NOZOMI was in the interplanetary space. Unlike it was expected, the MDC did neither detect dust particles on orbits bound to the Earth, nor space debris. All particles detected during the first half year were of interplanetary or interstellar origin and were discussed together with the particles detected in the interplanetary space. From the whole set of particles detected, a number of populations were identified that showed similarities in mass, inclination and eccentricity, four (plus one small) bound populations and two (plus two small) hyperbolic populations. From the four bound populations identified, two showed significant similarities in the distributions of mass, inclination and eccentricity to populations described in literature that are part of a model of the interplanetary dust cloud derived from dust data of optical observations and other in-situ experiments. Two of the four hyperbolic populations may consist of ISD grains or β -meteoroides, respectively. These assumptions need further discussion.

All data discussed in this chapter will be available in the MDC file database, see chapter 7 for more information.

7 MDC online application and file database

In this chapter, some problems that occurred during the project lifetime are described that were caused by proprietary data formats and software. A solution based on modern information technology methods was developed to prototype status and is discussed here.

7.1 Basics and motivation

The analysis of the MDC data was subject of intense discussion among the involved scientists and engineers. This, and the fact that scientists and engineers are distributed to several different institutes in Europe and Japan as well as the long running project (designed project life was 3 years initially) and thus several personnel changes at the LRT have lead to several problems regarding information flow and consistency of different existing copies of data files. In this chapter, a solution started in the year 2002 and based on a central project database and a standard user interface that is able to avoid these problems in future projects and additionally is a good platform for the publication and distribution of the MDC-NOZOMI data is presented.

An analog, but much more general approach is made by the DLR Neustrehlitz by developing the DLR-VirtualLab, “*a repository of online executable scientific software*”, see Ernst et al. [Ern2003] (also <http://vl.nz.dlr.de/VL>, hyperlink valid on October 27, 2005). The main idea of this project is to collect software solutions developed by scientists for usage in their individual projects, and connect these software packages to the internet via a web-browser based standardized user interface. This shall enable scientists all over the world to profit from their colleagues work in a much easier way than it is possible until today.

7.2 Description

The proprietary data formats, the data storage and the analysis process that is based on a proprietary single user application described in [Nau2000] lead to some serious trouble during the MDC project. One of the main problems was that inconsistencies occurred due to redundant copies of the data files that contain the final data analysis results, and there was no more chance to reproduce the validity of the different copies due to the ineluctably information loss during the handovers of the project from one scientist to the next. The disadvantages of the current data storage and data processing can be summarized as follows:

- No centralized data storage
- No consistent storage of additional information (comments etc.)
- Distribution of analysis results without intermediate results and information
- Data storage based on proprietary, platform dependent data formats

To avoid these disadvantages, a solution that satisfies the requirements of a distributed scientific community, especially concerning data access, data processing and consistent documentation of analysis tasks and discussions, was designed and developed with respect to the requirements of the MDC project's IT structure. The improvements can be summarized as follows:

- Raw data, intermediate analysis results, final results and additional information are stored in a central database
- Decentral data access for all users by platform independent standard software with adapted user rights
- Efficient data browsing, searching and comparing

The database system, the corresponding user interface and the server architecture are described in the following paragraphs.

7.2.1 Online application

The basic technologies used for the implementation of the MDC online database are HTML for the user interface, PostgreSQL as database engine and Java™ as programming language of the online application. Furthermore, all data that is imported into the database was converted from proprietary formats to the standardized XML document description language. As server applications, Apache as standard internet server and Jakarta-Tomcat for processing the Java™ applets that build the online application are being used. For the development of the Java™ applets, the developer software Eclipse was used which is also available as open source.

The use of these standard technologies ensures that not only access to the database but also the database and the online application themselves are platform independent. The open source character of all used technologies and server applications ensures that future use and upgrading of the online application can easily be done due to unlimited availability of the required developer software and documentation.

The online application is based on the MVC architecture (Model – View - Controller), see e.g. Buschmann et al. [Bus1996]. The separation of the tasks into three independent layers eases future improvements due to modular structure and central definition of variables. The different tasks are distributed as follows to the three layers:

- View layer: Creates HTML code for the user interface, based on JSP with CSS style-sheets.
- Model layer: Event dispatcher with subclasses for the different required tasks (e.g. LoginManager for Login processing etc.) and other supporting classes.
- Controller-layer: Management of user requests and access control.

Access control, managed by the controller-layer, supports and defines different user roles with corresponding user rights. This gives the opportunity to open the database for public and press as well as for scientists that are not involved in the project itself but may be interested in the mission results.

Central instance of the database is a single MDC memory segment that contains signal and basic housekeeping information. All other information, e.g. satellite flight data, further HSK data, intermediate analysis results, final analysis results, comments and links to calibration data are grouped around this central instance.

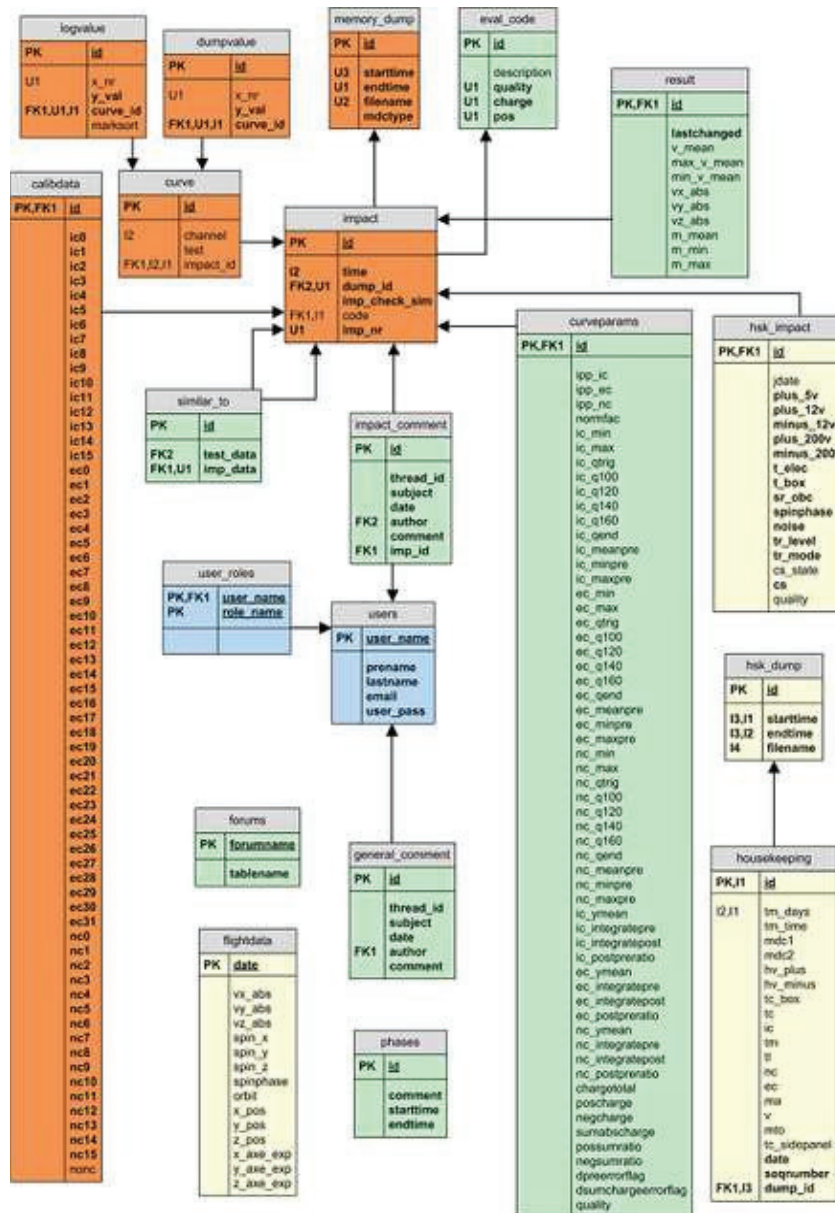


Figure 7-1: Table structure of the MDC online database

Central element is a single MDC signal (impact). All other tables are grouped around this element.

The user interface is based on pure HTML code and can be viewed and used with every standard internet browser.

Depending on the user role, the user interface offers the following functions:

1. Viewing, browsing and searching options on the full MDC signal data
2. Adding comments about single MDC signals/impacts
3. Adding classification parameters and analysis results to single MDC signals/impacts
4. Adding new raw data files

7.2.2 File database

At the end of the Mars Dust Counter project, all appropriate files were reorganized in a consistent directory structure. Here, the directory structure and the content of the final MDC data Volumes #1 to #8 are documented.

All essential data files of the MDC project were stored in platform independent data format where possible, either as formatted text or as XML data files (see also Appendix D for the structure of the MDC raw data XML files). *Microsoft*[®] *Office* files are stored in *Office 2002* or earlier data format. All thesis works on Volume #7 were developed by undergraduate students under supervision of the author of this work; parts of the results were used in this work. All files and the MDC Online Database will be published on the LRT WWW-Server after completion of the MDC-NOZOMI project.

Every directory and subdirectory contains a special file `0000_readme.txt`, that describes the content and structure of the files stored in the specific directory. For all files that are stored in proprietary data formats, the specific proprietary software and version number is given to ensure access to the files' content.

MDC_VOL#1: MDC_Scientific_Data_&_Results

- Directory Impact_Analysis
- Directory MDC_&_NOZOMI_Characteristics
- Directory Neural_Networks
- Directory Noise_Signals_Analysis
- Directory NOZOMI_Flight_Data_Analysis
- Directory Onboard_Qualification_Upgrade

MDC_VOL#2: MDC_Design_&_Technical_Documents

- Directory Design
- Directory Images

Directory Onboard_Software
Directory Technical_Documents

MDC_VOL#3: Raw_Data_&_Calibration_Data

Directory Calibration_Data_BIN
Directory Calibration_Data_XML
Directory Housekeeping_Data_BIN
Directory Housekeeping_Data_TXT
Directory Housekeeping_Data_XML
Directory Telemetry_Data_BIN
Directory Telemetry_Data_XML

MDC_VOL#4: MDC-HITEN_&_MDC-BremSat

Directory MDC_BremSat
Directory MDC_HITEN

MDC_VOL#5: Publications_&_Talks

Directory Publications
Directory Talks

MDC_VOL#6: Doctoral_Thesis_Works

Directory Dissertation_Robert_Senger

MDC_VOL#7: Collegiate_Thesis_Works

Directory DA_03_15_Dominic_Kyritsis
Directory IDP_Melanie_Dietz
Directory SA_03_06_Martin_Glas
Directory SA_03_07_Anna_Hübner
Directory SA_04_15_Ariane_Sauer
Directory SA_04_17_Christian_Rott
Directory SA_04_18_Johannes_Kellerer

MDC_VOL#8: MDC_Online_Database_&_WWW-Pages

Directory MDC_Online_Database
Directory MDC_WWW_Pages

Decentral access to the whole MDC file database via Internet can be realized in different ways. The simplest one, based on standard *Microsoft® Windows®* file sharing capabilities and server access via Virtual Private Network (VPN) from remote clients, was realized in the year 2001 and was used by the author of this work and contributing students throughout the project. However, since this requires proprietary clients with special system setups, it is planned to integrate the MDC file database into the MDC online application to enable platform independent access to the file database content via standard HTML browser software. Standard solutions like WebDAV (Web-based Distributed Authoring and Versioning) can be easily installed and configured on the LRT servers to enable browsing and downloading (and uploading if required) of project files from any standard remote client. More sophisticated solutions that enable enhanced file version control like CVS (Concurrent Versions System), a standard solution mainly used for Open Source software projects, can be used for a subset of files (e.g. software source code), but again require a special setup of the remote clients.

7.3 Summary and future prospects

The main intention of the decision to develop the MDC online database was to create a platform that provides central data storage and a corresponding user interface for data access to avoid the previously mentioned problems, namely the inconsistencies that occurred regarding the analysis results and their validity during the long running project time.

In its current version, the MDC online database provides useful features for data overview like searching, browsing, annotating and evaluating signals and add final analysis values to signals identified as impacts. In addition, a basic discussion forum was implemented that gives the scientific community the chance to discuss issues regarding MDC signal analysis in an easy and effective way.

Many future extensions of this basic functionality can be imagined. Until now, the whole data analysis process is still based on proprietary software that was developed at the LRT and runs as a single user application. As a first and most important step, the analysis software could be connected to the new MDC online database. Since the online database possesses standard database interfaces this can be made with little effort and would lead to a consistent and comprehensible data analysis process. The network based database structure would enable every user of the analysis software, independently of his or her location, to access the always up-to-date data and analysis results. As a perfection of this integration, the whole analysis process can be implemented as part of the online application using JSP or Java™ applets rather than proprietary single user software. Further extensions like the integration of all satellite flight data, technical documentation, and interpretation of the analyzed impact data displayed by dynamically created graphics or charts based on the actual analysis results can be implemented and integrated into the existing database and user interface. For future dust science projects that may be developed at the LRT, the author recommends the use of an adapted database system and online application as described in this chapter.

The consequent use of methods that enable simple and decentral access to project data, as they are described in this chapter, may open new possibilities for future science projects like the MDC project. Against the background of the great success of Open Source software projects, an “Open Science” project based on the technologies described above and supervised

by the project scientist may open up a new pool of brainpower that can contribute to the scientific success of small and concise projects like the MDC project.

One of the main activities of the European Planetology Network (EuroPlaNet, founded in January 2005, a network of research institutes from 17 European countries including the LRT and funded by the European Commission under the 6th Framework Programme), activity N7, is dedicated to the development of the so called Integrated and Distributed Information Service (IDIS) and its evolution into a European Virtual Planetary Observatory. The IDIS platform is described in the EuroPlaNet Green Paper for Activity N7 [Eur2006]:

“IDIS will provide a general platform for exchanging and accessing data and information, integrating and linking relevant data centres, data bases and information systems, providing a more unified access to the information, [...] and to the benefit of the dissemination of data produced in Europe.”

Currently, a demo version of the IDIS platform based on the same technologies used for the MDC online application (Java™, Jakarta-Tomcat) is in development. This demo version is intended to allow access to sample contents coming from the CASSINI-HUYGENS mission. The possibility of an integration of the final MDC dust data into a forthcoming state-of-the-art IDIS platform should be considered and clarified.

8 Summary and discussion

In this work, the scientific data of the Mars Dust Counter mission on NOZOMI were analyzed and interpreted. The signals recorded by the MDC were investigated carefully to separate noise data from impact data. Impact data was reviewed and particle mass and impact speed were derived. The MDC detected 98 particles of interplanetary and interstellar origin during its 4-year journey through the solar system. Neither space debris nor planetary dust bound to the Earth were detected. The characteristics of the MDC experiment and the MDC/NOZOMI system were investigated thoroughly to allow further analysis of the derived dust data. The NOZOMI flight data was investigated and visualized, dust data must be interpreted with respect to the flight data and the sensor pointing directions during the flight. The MDC dust data was interpreted with respect to the derived characteristics of the MDC experiment and the MDC/NOZOMI system, and the NOZOMI flight data. Interpretation of the MDC dust data showed good correlation to the known properties of interplanetary dust particles. The dust flux derived from the MDC dust data correlates well with dust flux models from literature that were developed from dust data of various other sources. From the whole amount of particles, separate populations of dust particles were identified. The characteristics of some of these populations found in the MDC dust data fit to particle populations published in literature that were introduced to match dust data derived from other in-situ dust detection instruments.

With respect to the technical troubles the spacecraft NOZOMI suffered from, a new data compression method for the onboard data was developed and evaluated. The data compression method is based on Wavelet transformation of the original signal and subsequent compression of the transformed data set. Compression factors of 16 to 50 were achieved with this method, without losing relevant information for the latter analysis of the signals. This was proved by studies carried out with the existing MDC-NOZOMI and MDC-HITEN data. The data compression method was therefore suitable for the MDC-NOZOMI if it had reached Mars orbit. It can be used in future instruments to reduce the amount of data that has to be transferred to Earth. The routine that performs the compression onboard the MDC was ready for upload, but this was not possible any more due to the system failure on NOZOMI that occurred on April 24, 2002.

Also, an optimized parameter set for signal qualification onboard was determined. The qualification routine onboard the MDC can be used for a primitive distinction of impact signals from noise signals. With the introduction of a threshold value that separates all data into good and bad signals, and a simple upgrade of the memory readout routine, a reduction of data by a factor of 100 could be achieved. Optimization of the parameter set that is used by the qualification routine was carried out by a genetic algorithm.

These two improvements of the onboard data processing would enable the MDC to transmit its data back to earth despite the restricted NOZOMI telemetry capacities. For future missions, an even better signal qualification method based on neural networks was developed and tested on the existing MDC-NOZOMI data. It was proven by Hofschuster [Hof2002] in laboratory experiments that instruments based on the MDC experiment architecture can be equipped with a time-of-flight mass spectrometer. This would give such future experiments new capabilities for the additional determination of the chemical composition of cosmic dust

particles. For such instruments, efficient methods for onboard processing of the data become even more important.

All MDC-NOZOMI data was stored in a new developed database system that is easily accessible for public and interested scientists. Further data that is not included in the database is stored in standard XML format, or proprietary data formats where no conversion was possible. This ensures that the project data will be accessible in the future for further investigations. All data that is presented in this work is available electronically from the LRT.

Appendix A: Bibliography

- [Alt2003] Altobelli, N., Kempf, S., Landgraf, M., Srama, R., Dikarev, V., Krüger, H., Moragas-Klostermeyer, G., Grün, E., “CASSINI between Venus and Earth: Detection of interstellar dust”, *J. Geophys. Res.*, Vol. 108, No. A10, 8032, 2003
- [Alt2005] Altobelli, N., Kempf, S., Krüger, H., Landgraf, M., Roy, M., Grün, E., “Interstellar dust flux measurements by the GALILEO dust instrument between the orbits of Venus and Mars“, *J. Geophys. Res.*, Vol. 110, A07102, 2005
- [Alt2006] Altobelli, N., Grün, E., Landgraf, M., “A new look into the HELIOS dust experiment data: presence of interstellar dust inside the Earth’s orbit“, *Astron. Astroph.*, Vol. 448, pp. 243-252, 2006
- [Aue2002] Auer, S., Grün, E., Srama, R., Kempf, S., Auer, R., “The charge and velocity detector of the cosmic dust analyzer on CASSINI”, *Planet. Space Sci.*, Vol. 50, pp. 773-779, 2002
- [Bag1995] Baguhl, M., Grün, E., Hamilton, D.P., Linkert, G., Riemann, R., Staubach, P., Zook, H.A., “The flux of interstellar dust observed by ULYSSES and GALILEO”, *Space Sci. Rev.*, Vol. 72, pp. 471-476, 1995
- [Bag1996] Baguhl, M., Grün, E., Landgraf, M., “In-situ measurements of interstellar dust with the ULYSSES and GALILEO spaceprobes“, *Space Sci. Rev.*, Vol. 78, pp. 165-172, 1996
- [Ban1991] Banaszekiewicz, M., Ip, W.H., “A statistical study of impact ejecta distribution around Phobos and Deimos”, *Icarus*, Vol. 90, pp. 237-253, 1991
- [Ban1994] Banaszekiewicz, M., Fahr, H.J., Scherer, K., “Evolution of dust particle orbits under the influence of solar wind outflow asymmetries and the formation of the zodiacal dust cloud“, *Icarus*, Vol. 107, pp. 358-374, 1994
- [Bau1996] Baumgärtel, K., Sauer, K., Bogdanov, A., Dubinin, E., Dougherty, M., “Phobos events?: signatures of solar wind dust interactions“, *Planet. Space Sci.*, Vol. 44, No. 6, pp. 589-601, 1996
- [Bro1996] Brownlee, D.E., Burnett, D., Clark, B., Hanner, M.S., Horz, F., Kissel, J., Newburn, R., Sandford, S., Sekanina, Z., Tsou, P., Zolensky, M., “STARDUST: Comet and interstellar dust sample return mission”, in *Phys. Chem. and Dyn. of Interplanetary Dust*, ASP Conf. Series 104 (eds. B.A.S. Gustafson and M.S. Hanner), pp. 223-226, 1996

- [Bur1979] Burns, J.A., Lamy, P.L., Soter, S., “Radiation forces on small particles in the solar system”, *Icarus*, Vol. 40, pp. 1-48, 1979
- [Bur2002] Burchell, M.J., Willis, M.J., Armes, S.P., Khan, M.A., Percy, M.J., Perruchot, C., “Impact ionization experiments with low density conducting polymer-based micro-particles as analogues of solar system dusts”, *Planet. Space Sci.*, Vol. 50, pp. 1025-1035, 2002
- [Bus1996] Buschmann, F., Meunier, R., Rohnert, H., Sommerlad, P., Stal, M., “Pattern-Oriented Software Architecture”, John Wiley and Sons, 1996
- [Cas1699] Cassini, G.D., “Découverte de la lumière celeste qui paroist dans le zodiaque”, *Mémoires de l'Académie Royale des Sciences depuis 1666 jusqu'a 1699*, Vol. VIII, pp. 119-209, 1699
- [Cer1995] Cermák, I., Grün, E., Švestka, J., “New results in studies of electric charging of dust particles“, *Adv. Space Res.*, Vol. 15, No. 10, pp. (10)59-(10)64, 1995
- [Che2003] Chesley, S.R., Ostro, S.J., Vokrouhlický, D., Čapek, D., Giorgini, J.D., Nolan, M.C., Margot, J.-L., Hine, A.A., Benner, L.A.M., Chamberlin, A.B., “Direct detection of the Yarkovsky effect via radar ranging to asteroid 6489 Golevka”, *Science*, Vol. 302, pp. 1739-1742, 2003
- [Con1980] Consolmagno, G.J., “Influence of the interplanetary magnetic field on cometary and primordial dust orbits: Applications of Lorentz scattering”, *Icarus*, Vol. 43, pp. 203-214, 1980
- [Dal1977] Dalmann, B.K., Grün, E., Kissel, J., Dietzel, H., “The ion composition of the plasma produced by impacts of fast dust particles”, *Planet. Space Sci.*, Vol. 25, pp. 135-147, 1977
- [Dav1981] Davis, D.R., Housen, K.R., Greenberg, R., “The unusual dynamical environment of Phobos and Deimos”, *Icarus*, Vol. 47, pp. 220-233, 1981
- [Deb2001] Debnath, L., “Wavelet Transforms and Time-Frequency Signal Analysis”, Birkhauser, 2001
- [Dei1985] Deichsel, G., Trampisch, H.J., “Clusteranalyse und Diskriminanzanalyse”, Gustav Fischer Verlag, Stuttgart, 1985
- [Die1972] Dietzel, H., Neukum, G., Rauser, P., “Micrometeoroid simulation studies on metal targets”, *J. Geophys. Res.*, Vol. 77, No. 8, p. 1375, 1972
- [Dik2002] Dikarev, V., Jehn, R., Grün, E., “Towards a new model of the interplanetary meteoroid environment“, *Adv. Space Res.*, Vol. 29, No. 8, pp. 1171-1175, 2002

- [Dik2005] Dikarev, V., Grün, E., Baggaley, J., Galligan, D., Landgraf, M., Jehn, R., “The new ESA meteoroid model”, *Adv. Space Res.*, Vol. 35, pp. 1282-1289, 2005
- [Div1993] Divine, N., “Five populations of interplanetary meteoroids”, *J. Geophys. Res.*, Vol. 98, No. E9, pp. 17029-17048, 1993
- [Dob1980] Dobrovolskis, A.R., Burns, J.A., “Life near the Roche limit: Behavior of ejecta from satellites close to planets”, *Icarus*, Vol. 42, No. 3, pp. 422-441, 1980
- [Dra1974] Drapatz, S., Michel, K.W., “Theory of shock-wave ionization upon high-velocity impact of micrometeorites”, *Zeitschrift für Naturforschung*, Vol. 29a, pp. 870-879, 1974
- [Dra1984] Draine, B.T., Lee, H.M., “Optical properties of interstellar graphite and silicate grains”, *Astrophys. J.*, Vol. 285, pp. 89-108, 1984
- [Dub1991] Dubinin, E.M., Pissarenko, N.F., Barabash, S.V., Zacharov, A.V., Lundin, R., Pellinen, R., Schwingenschuh, K., Yeroshenko, Ye.G., “Plasma and magnetic field effects associated with Phobos and Deimos tori”, *Planet. Space Sci.*, Vol. 39, No. 1/2, pp. 113-121, 1991
- [Eic1975] Eichhorn, G., “Measurements of the light flash produced by high velocity particle impact”, *Planet. Space Sci.*, Vol. 23, pp. 1519-1522, 1975
- [Eic1976] Eichhorn, G., “Analysis of the hypervelocity impact process from impact flash measurements”, *Planet. Space Sci.*, Vol. 24, pp. 771-781, 1976
- [Ern2003] Ernst, Th, et al., “DLR’s VirtualLab: Scientific software just a mouse click away”, *Computing in Science and Engineering*, January/February 2003
- [ESA1999] ESA, “ESA Space Debris Mitigation Handbook”, Release 1.0, April 7, 1999
- [Eur2006] European Planetology Network (EuroPlaNet), “Green Paper for Activity N7: Integrated and Distributed Information Service”, 3rd draft, February 15, 2006
- [Fis1998] Fischer, F.G., “Mars Dust Counter on Planet-B: On-Board Software Internals”, Laboratory for Process Control and Real-Time Systems, Technische Universität München, Germany, 1998
- [Fis1999] Fischer, F.G., “On-Board Software ‘Autotrigger’ Extension: Closed Loop MDC Sensitivity Control”, Laboratory for Process Control and Real-Time Systems, Technische Universität München, 1999
- [Fri1963] Friichtenicht, J.F., Slattery, J.C., “Ionisation associated with hypervelocity impact”, NASA TN D-2091, 1963

- [Gla2003] Glas, M., "Signalklassifikation mit Neuronalen Netzen", Semesterarbeit RT SA 03/06, Lehrstuhl für Raumfahrttechnik, Technische Universität München, 2003
- [Göl1988] Göller, J.R., "Kalibrationsmessungen an Mikrometeoritendetektoren für die Missionen ULYSSES, GALILEO und GIOTTO", Dissertation, Ruprecht-Karls-Universität Heidelberg, 1988
- [Göl1989] Göller, J.R., Grün, E., "Calibration of the GALILEO/ULYSSES dust detectors with different projectile materials and at varying impact angles", *Planet. Space Sci.*, Vol. 37, No. 10, pp. 1197-1206, 1989
- [Gol2002] Goldsworthy, B.J., Burchell, M.J., Cole, M.J., Green, S.F., Leese, M.R., McBride, N., McDonnell, J.A.M., Müller, M., Grün, E., Srama, R., Armes, S.P., Khan, M.A., "Laboratory calibration of the CASSINI cosmic dust analyser (CDA) using new, low density projectiles", *Adv. Space Res.*, Vol. 29, No. 8, pp. 1139-1144, 2002
- [Gri1997] Grinberg, E.I., Grigoryev, B.V., Nikolaev, V.S., Sokolov, N.A., "Interaction of space debris with liquid metal circuit of RORSAT satellites", *Proc. 2nd European Conf. Space Debris*, pp. 273-277, 1997
- [Grj1964] Grjebine, T., Lalou, C., Ros, J., Capitant, M., "Study of magnetic spherules in three cores of the occidental basin of the mediterranean sea", *Ann. N.Y. Acad. Sci.*, Vol. 119, Art. 1, pp. 143-165, 1964
- [Grü1985] Grün, E., Zook, H.A., Fechtig, H., Giese, R.H., "Collisional balance of the meteoritic complex", *Icarus*, Vol. 62, pp. 244-272, 1985
- [Grü1992a] E. Grün, H. Fechtig, R.H. Giese, J. Kissel, D. Linkert, D. Maas, J.A.M. McDonnell, G.E. Morfill, G. Schwehm, H.A. Zook, "The Ulysses dust experiment", *Astron. Astrophys. Supp. Ser.* 92, 411-423, 1992
- [Grü1992b] E. Grün, H. Fechtig, M.S. Hanner, J. Kissel, B.-A. Lindblad, D. Linkert, D. Maas, G.E. Morfill, H.A. Zook, "The Galileo dust detector", *Space Science Reviews* 60, 317-340, 1992
- [Grü1994] Grün, E., Gustafson, B., Mann, I., Baguhl, M., Morfill, G.E., Staubach, P., Taylor, A., Zook, H.A., "Interstellar dust in the heliosphere", *Astron. Astrophys.*, Vol. 286, pp. 915-924, 1994
- [Grü1995a] Grün, E., Baguhl, M., Hamilton, D.P., Kissel, J., Linkert, D., Linkert, G., Riemann, R., "Reduction of GALILEO and ULYSSES dust data", *Planet. Space Sci.*, Vol. 43, No. 8, pp. 941-951, 1995
- [Grü1995b] Grün, E., Baguhl, M., Divine, N., Fechtig, H., Hamilton, D.P., Hanner, M.S., Kissel, J., Lindblad, B.-A., Linkert, D., Linkert, G., Mann, I., McDonnell, J.A.M., Morfill, G.E., Polanskey, C., Riemann, R., Schwehm, G., Siddique, N., Staubach, P., Zook, H.A., "Three years of GALILEO dust data", *Planet. Space Sci.*, Vol. 43, No. 8, pp. 953-969, 1995

- [Grü1995c] Grün, E., Baguhl, M., Divine, N., Fechtig, H., Hamilton, D.P., Hanner, M.S., Kissel, J., Lindblad, B.-A., Linkert, D., Linkert, G., Mann, I., McDonnell, J.A.M., Morfill, G.E., Polanskey, C., Riemann, R., Schwehm, G., Siddique, N., Staubach, P., Zook, H.A., “Two years of ULYSSES dust data”, *Planet. Space Sci.*, Vol. 43, No. 8, pp. 971-999, 1995
- [Grü1997] Grün, E., Staubach, P., Baguhl, M., Hamilton, D.P., Zook, H.A., Dermott, S., Gustafson, B.A., Fechtig, H., Kissel, J., Linkert, D., Linkert, G., Srama, R., Hanner, M.S., Polanskey, C., Horányi, M., Lindblad, B.A., Mann, I., McDonnell, J.A.M., Morfill, G.E., Schwehm, G., “South-north and radial traverses through the interplanetary dust cloud”, *Icarus*, Vol. 129, pp. 270-288, 1997
- [Grü2001] Grün, E., Landgraf, M., “Fast dust in the heliosphere”, *Space Sci. Rev.*, Vol. 99, pp. 151-164, 2001
- [Grü2001b] Grün, E., Baguhl, M., Svedhem, H., Zook, H.A., “In situ measurements of cosmic dust”, in *Interplanetary Dust* (eds. E. Grün, B.A.S. Gustafson, S.F. Dermott, H. Fechtig), Springer-Verlag Berlin Heidelberg, 2001
- [Gus1986] Gustafson, B.A.S., Misconi, N.Y., “Interplanetary dust dynamics: I. Long-term gravitational effects of the inner planets on zodiacal dust”, *Icarus*, Vol. 66, pp. 280-287, 1986
- [Gus1987a] Gustafson, B.A.S., Misconi, N.Y., Rusk, E.T., “Interplanetary dust dynamics: II. Poynting-Robertson drag and planetary perturbations on cometary dust”, *Icarus*, Vol. 72, pp. 568-581, 1987
- [Gus1994] Gustafson, B.A.S., “Physics of zodiacal dust”, *Ann. Rev. Earth Planet. Sci.*, Vol. 22, pp. 553-595, 1994
- [Ham1994] Hamilton, D.P., “A comparison of Lorentz, planetary gravitational, and satellite gravitational resonances”, *Icarus*, Vol. 109, pp. 221-240, 1994
- [Ham1996] Hamilton, D.P., “The asymmetric time-variable rings of Mars”, *Icarus*, Vol. 119, pp. 153-172, 1996
- [Har1976] Hartung, J.B., “Lunar microcraters and interplanetary dust fluxes”, *Lecture Notes in Physics*, Vol. 48, *Interplanetary Dust and Zodiacal Light*, pp. 209-226, 1976
- [Hei1990] Heistermann, J., “Learning in neural nets by genetic algorithms”, *Parallel Processing in Neural Systems and Compilers*, Elsevier Science Publishers North-Holland, 1990
- [Hei1994] Heistermann, J., “Genetische Algorithmen”, B.G. Teubner Verlagsgesellschaft, Stuttgart, 1994

- [Hem1964] Hemenway, C.L., Linscott, I., Secretan, L., Dubin, M., "Preliminary study of possible cosmic dust impacts on project Mercury vehicle periscopic lenses", *Ann. N.Y. Acad. Sci.*, Vol. 119, Art. 1, pp. 106-115, 1964
- [Hof1971] Hoffmann, H.-J., "Entwicklung eines Detektors zur Massen- und Geschwindigkeitsanalyse von kosmischen Staubteilchen", Dissertation, Ruprecht-Karls-Universität, Heidelberg, 1971
- [Hof2002] Hofschuster, G., "Hochgeschwindigkeitseinschläge auf teildurchlässige Oberflächen", Dissertation, Fachgebiet Raumfahrttechnik, Technische Universität München, 2002
- [Hor1981] Hornung, K., Drapatz, S., "Residual ionization after impact of large dust particles", *ESA SP-155*, pp. 23-37, 1981
- [Hor1996a] Hornung, K., Malama, Yu. G., Thoma, K., "Modeling of the very high velocity impact process with respect to in-situ ionization measurements", *Adv. Space Res.*, Vol. 17, No. 12, pp. (12)77-(12)86, 1996
- [Hor1996b] Horányi, M., "Charged dust dynamics in the solar system", *Annu. Rev. Astron. Astrophys.*, Vol. 34, pp. 383-418, 1996
- [Hüb2003] Hübner, A. "Charakterisierung des Rauschverhaltens am Mars Dust Counter", Semesterarbeit RT-SA 03/07, Technische Universität München, Lehrstuhl für Raumfahrttechnik, 2003
- [Ige1998] Igenbergs, E., Sasaki, S., Münzenmayer, R., Ohasi, H., Färber, G., Fischer, F., Fujiwara, A., Glasmachers, A., Grün, E., Hamabe, Y., Iglseeder, H., Klinge, D., Miyamoto, H., Mukai, T., Naumann, W., Nogami, K.-I., Schwehm, G., Svedhem, H., Yamakoshi, K., "Mars Dust Counter", *Earth Planets Space*, Vol. 50, pp. 241-245, 1998
- [Igl1993a] Iglseeder, H., Münzenmayer, R., Svedhem, H., Grün, E., "Cosmic dust and space debris measurements with the Munich Dust Counter on board the satellites HITEN and BremSat", *Adv. Space Res.*, Vol. 13, No. 8, pp. (8)129-(8)132, 1993
- [Igl1993b] Iglseeder, H., Grün, E., Münzenmayer, R., Svedhem, H., "Analysis of the results of two-year operations of the Munich Dust Counter - A cosmic dust experiment on board the satellite HITEN", in "Meteoroids and their parent bodies", (eds. J. Štohl and I.P. Williams), *Astronomical Inst., Slovak. Acad. Sci.*, Bratislava, 1993
- [Igl1996] Iglseeder, H., Uesugi, K., Svedhem, H., "Cosmic dust measurements in lunar orbit", *Adv. Space Res.*, Vol. 17, No. 12, pp. (12)177-(12)182, 1996
- [Ina1999] Inada, A., Kawamata, M., Sumikawa, S., Mukai, T., "Planned observation of Phobos/Deimos by Mars Imaging Camera (MIC) on NOZOMI", *Adv. Space Res.*, Vol. 23, No. 11, pp. 1911-1914, 1999

- [ISA1998] ISAS, "Planet-B Prelaunch Report", ISAS SES Data Center, SES-TD-98-002, 1998
- [Ish1994] Ishimoto, H., Mukai, T., "Phobos dust rings", *Planet. Space Sci.*, Vol. 42, No. 8, pp. 691-697, 1994
- [Ish1996] Ishimoto, H., "Formation of Phobos/Deimos dust rings", *Icarus*, Vol. 122, pp. 153-165, 1996
- [Ish1997a] Ishimoto, H., Kimura, H., Nakagawa, N., Mukai, T., "Planned observation of Phobos/Deimos dust rings by PLANET-B", *Adv. Space Res.*, Vol. 19, No. 1, pp. (1)123-(1)126, 1997
- [Jac1997] Jackson, A., Eichler, P., Reynolds, R., Potter, A., Johnson, N., "The historical contribution of solid rocket motors to the one centimeter debris population", *Proc. 2nd European Conf. Space Debris*, pp. 279-284, 1997
- [Jac2001] Jackson, A.A., "The capture of interstellar dust: the pure Poynting-Robertson case", *Planet. Space Sci.*, Vol. 49, pp. 417-424, 2001
- [Kaw1995] Kawaguchi, J., Yamakawa, H., Uesugi, T., Matsuo, H., "On making use of lunar and solar gravity assists in LUNAR-A, PLANET-B missions", *Acta Astronautica*, Vol. 35, No. 9-11, pp. 633-642, 1995
- [Kaw2003] Kawaguchi, J., Nakatani, I., Uesugi, T., Tsuruda, K., "Synthesis of an alternative flight trajectory for Mars explorer NOZOMI", *Acta Astronautica*, Vol. 52, pp. 189-195, 2003
- [Kel2004] Kellerer, J., "MDC BremSat Datenanalyse", Semesterarbeit RT-SA 04/18, Technische Universität München, Lehrstuhl für Raumfahrttechnik, 2004
- [Kho1993] Kholshchevnikov, K.V., Krivov, A.V., Sokolov, L.L., Titov, V.B., "The dust torus around Phobos orbit", *Icarus*, Vol. 105, pp. 351-362, 1993
- [Kis1987] Kissel, J., Krüger, F.R., "Ion formation by impact of fast dust particles and comparison with related techniques", *Appl. Phys. A*, Vol. 42, pp. 69-85, 1987
- [Kli1997] Klinkrad, H., Bendisch, J., Sdunnus, H., Wegener, P., Westerkamp, R., "An introduction to the 1997 ESA-MASTER model", *Proc. 2nd European Conf. Space Debris*, pp. 217-224, 1997
- [Kna1980] Knabe, W., "Untersuchungen am Einschlags-Ionisationsdetektor für die Galileo- und ISP-Mission", Diplomarbeit, MPI für Kernphysik, Heidelberg, 1980
- [Koc2003] Kocifaj, M., Kláčka, J., "The capture of interstellar dust: the pure electromagnetic case", *Planet. Space Sci.*, Vol. 51, pp. 617-626, 2003

- [Koc2004] Kocifaj, M., Klačka, J., “The capture of interstellar dust: the Lorentz force case”, *Planet. Space Sci.*, Vol. 52, pp. 839-847, 2004
- [Kri1997] Krivov, A., Hamilton, D.P., “Martian dust belts: waiting for discovery”, *Icarus*, Vol. 128, pp. 335-353, 1997
- [Kri1999] Krivov, A., Jurewicz, A., “The ethereal dust envelopes of the Martian moons”, *Planet. Space Sci.*, Vol. 47, pp. 45-56, 1999
- [Krü1999b] Krüger, H., Grün, E., Hamilton, D.P., Baguhl, M., Dermott, S., Fechtig, H., Gustafson, B.A., Hanner, M.S., Horányi, M., Kissel, J., Lindblad, B.A., Linkert, D., Linkert, G., Mann, I., McDonnell, J.A.M., Morfill, G.E., Polanskey, C., Riemann, R., Schwehm, G., Srama, R., Zook, H.A., “Three years of GALILEO dust data II: 1993-1995”, *Planet. Space Sci.*, Vol. 47, pp. 85-106, 1999
- [Krü1999c] Krüger, H., Grün, E., Landgraf, M., Baguhl, M., Dermott, S., Fechtig, H., Gustafson, B.A., Hamilton, D.P., Hanner, M.S., Horányi, M., Kissel, J., Lindblad, B.A., Linkert, D., Linkert, G., Mann, I., McDonnell, J.A.M., Morfill, G.E., Polanskey, C., Schwehm, G., Srama, R., Zook, H.A., “Three years of ULYSSES data: 1993-1995”, *Planet. Space Sci.*, Vol. 47, pp. 363-383, 1999
- [Krü2001a] Krüger, H., Grün, E., Graps, A., Bindschadler, D., Dermott, S., Fechtig, H., Gustafson, B.A., Hamilton, D.P., Hanner, M.S., Horányi, M., Kissel, J., Lindblad, B.A., Linkert, D., Linkert, G., Mann, I., McDonnell, J.A.M., Morfill, G.E., Polanskey, C., Schwehm, G., Srama, R., Zook, H.A., “One year of Galileo dust data from the Jovian system: 1996”, *Planet. Space Sci.*, Vol. 49, pp. 1285-1301, 2001
- [Krü2001b] Krüger, H., Grün, E., Landgraf, M., Dermott, S., Fechtig, H., Gustafson, B.A., Hamilton, D.P., Hanner, M.S., Horányi, M., Kissel, J., Lindblad, B.A., Linkert, D., Linkert, G., Mann, I., McDonnell, J.A.M., Morfill, G.E., Polanskey, C., Schwehm, G., Srama, R., Zook, H.A., “Four years of ULYSSES data: 1996-1999”, *Planet. Space Sci.*, Vol. 49, pp. 1303-1324, 2001
- [Kry1992] Krymskii, A.M., Breus, T.K., Dougherty, M.K., Southwood, D.J., Axford, W.I., “The electromagnetic effects of the solar wind interaction with the Phobos neutral gas halo and dust torus”, *Planet. Space Sci.*, Vol. 40, No. 8, pp. 1033-1041, 1992
- [Kyr2003] Kyritsis, D., “On-Board Software Upgrade of the Space Experiment Mars Dust Counter”, Diplomarbeit RT SA 03/15, Lehrstuhl für Raumfahrttechnik, Technische Universität München, 2003
- [Lan2002] Landgraf, M., Liou, J.-C., Zook, H.A., Grün, E., “Origins of solar system dust beyond Jupiter”, *The Astron. J.*, Vol. 123, pp. 2857-2861, 2002

- [Lev1990] Levasseur-Regourd, A.C., Dumont, R., "IRAS observations and local properties of interplanetary dust", *Adv. Space Res.*, Vol. 10, No. 3-4, pp. (3)163-(3)170, 1990
- [Lin2000] Linde, T. J., Gombosi, T. I., "Interstellar dust filtration at the heliospheric interface", *J. Geophys. Res.*, Vol. 105, No. A5, p. 10411, 2000
- [Lio1995a] Liou, J.-C., Zook, H.A., "Radiation pressure, Poynting-Robertson drag, and solar wind drag in the restricted three-body problem", *Icarus*, Vol. 116, pp. 186-201, 1995
- [Lio1995b] Liou, J.C., Dermott, S.F., Xu, Y.L., "The contribution of cometary dust to the zodiacal cloud", *Planet. Space Sci.*, Vol. 43, No. 6, pp. 717-722, 1995
- [Lio1996a] Liou, J.-C., Zook, H.A., Dermott, S.F., "Kuiper Belt dust grains as a source of interplanetary dust particles", *Icarus*, Vol. 124, pp. 429-440, 1996
- [Lio1996b] Liou, J.-C., Zook, H.A., "Comets as a source of low eccentricity and low inclination interplanetary dust particles", *Icarus*, Vol. 123, pp. 491-502, 1996
- [Lio1997] Liou, J.-C., Zook, H.A., "Evolution of interplanetary dust particles in mean motion resonances with planets", *Icarus*, Vol. 128, pp. 354-367, 1997
- [Lio1999] Liou, J.-C., Zook, H.A., Jackson, A.A., "Orbital evolution of retrograde interplanetary dust particles and their distribution in the solar system", *Icarus*, Vol. 141, 13-28, 1999
- [Lou1998] Louis, A.K., Maaß, P., Rieder, A., "Wavelets. Theorie und Anwendungen", Teubner-Verlag, 1998
- [Lov1994] Love, S.G., Joswiak, D.J., Brownlee, D.E., "Densities of stratospheric micrometeorites", *Icarus*, Vol. 111, pp. 227-236, 1994
- [Man1991] Mann, I., Kneißel, B., "Out-of-ecliptic distribution of interplanetary dust derived from near earth flux", *Adv. Space Res.*, Vol. 11, No. 12, pp. (12)123-(12)126, 1991
- [Man1996a] Mann, I., Grün, E., Wilck, M., "The contribution of asteroid dust to the interplanetary dust cloud: The impact of ULYSSES results on the understanding of dust production in the asteroid belt and on the formation of the IRAS dust bands", *Icarus*, Vol. 120, pp. 399-407, 1996
- [Mar1994] Marzari, F., Vanzani, V., "Orbital evolution of dust particles near mean motion resonances with the Earth", *Planet. Space Sci.*, Vol. 42, No. 2, pp. 101-107, 1994

- [McD2000] McDonnell, J.A.M., Burchell, M.J., Green, S.F., McBride, N., Vaughan, A.M., Zarnecki, J.C., Tsou, P., Hanner, M.S., Tuzzolino, A.J., DiDonna, F., Brownlee, D.E., Clark, B., “The STARDUST dust flux monitor”, *Adv. Space Res.*, Vol. 25, No. 2, pp. 335-338, 2000
- [Mel1964] Melton, C.E., “Atmospheric aerosol collection near 40,000 feet with DC-8”, *Ann. N.Y. Acad. Sci.*, Vol. 119, Art. 1, pp. 116-125, 1964
- [Mit1998] Mitchell, M., “An Introduction to Genetic Algorithms (Complex Adaptive Systems)”, The MIT Press, 1998
- [Mou2005] Moussi, A., Drolshagen, G., McDonnell, J.A.M., Mandeville, J.-C., Kearsley, A.T., Ludwig, H., “Hypervelocity impacts on HST solar arrays and the debris and meteoroids population”, *Adv. Space Res.*, Vol. 35, pp. 1243-1253, 2005
- [Mün1995] Münzenmayer, R., “Beiträge zur experimentellen Erforschung des Staubes im Weltall”, Dissertation, Lehrstuhl für Raumfahrttechnik, Technische Universität München, 1995
- [Mün1997] Münzenmayer, R., Igenbergs, E., Iglseeder, H., Svedhem, H., “The Munich Dust Counter on board the MUSES-A mission: Calibration of impacts inside and in front of the detector”, *Adv. Space Res.*, Vol. 20, No. 8, pp. 1485-1488, 1997
- [Nak1995] Nakatani, I., Tsuruda, K., Yamamoto, T., “PLANET-B: Mars mission with small spacecraft but potentially with large scale science reward”, *Acta Astronautica*, Vol. 35, pp. 337-344, 1995
- [Nau2000] Naumann, W., “Rechnergestützte Automatisierung eines Experiments im interplanetaren Raum”, Dissertation, Lehrstuhl für Raumfahrttechnik, Technische Universität München, 2000
- [Naz1997] Nazzario, R.C., Hyde, T.W., “The dust bands of the planet Mars”, *Adv. Space Res.*, Vol. 20, No. 8, pp. 1535-1538, 1997
- [Neu1984] Neugebauer, G.H., Habing, H., van Diunen, R., Aumann, H., Baud, B., Beichmann, C., Beintema, D., Boggess, N., Clegg, P., de Jong, T., Emerson, J., Gautier, T.N., Gillett, F., Harris, S., Hauser, M., Houck, J., Jennings, R., Low, F., Marsden, P., Miley, G., Olton, F., Pottasch, S., Raimond, E., Rowan-Robinson, M., Soifer, B., Walker, R., Wesselius, P., Young, E., “The Infrared Astronomical Satellite (IRAS) mission”, *Astroph. J.*, Vol. 278, pp. L1-L6, 1984
- [Poy1903] Poynting, J. H., “Radiation in the solar system: its effect on temperature and its pressure on small bodies”, *Philosophical Transactions of the Royal Society of London, Series A.* 202, pp. 525-552, 1903

- [Rat1996] Ratcliff, P.R., Gogu, F., Grün, E., Srama, R., “Plasma production by secondary impacts: Implications for velocity measurements by in-situ dust detectors”, *Adv. Space Res.*, Vol. 17, No. 12, pp. (12)111-(12)115, 1996
- [Rat1997] Ratcliff, P.R., Reber, M., Cole, M.J., Murphy, T.W., Tsembelis, K., “Velocity thresholds for impact plasma production”, *Adv. Space Res.* Vol. 20, No. 8, pp. 1471-1476, 1997
- [Rob1937] Robertson, H. P., “Dynamical effects of radiation in the solar system”, *Monthly Notices of the Royal Astronomical Society*, Vol. 97, pp. 423-438, 1937
- [Rot2004] Rott, C., “Validation of the Software Update on MDC NOZOMI with the MDC HITEN Data”, Semesterarbeit RT SA 04/17, Technische Universität München, Lehrstuhl für Raumfahrttechnik, 2004
- [Sas1999] Sasaki, S., “Dust ring/torus around mars, waiting for detection by NOZOMI”, *Adv. Space Res.*, Vol. 23, No. 11, pp. 1907-1910, 1999
- [Sas2002] Sasaki, S., Igenbergs, E., Ohashi, H., Münzenmayer, R., Naumann, W., Hofschuster, G., Born, M., Färber, G., Fischer, F., Fujiwara, A., Glasmachers, A., Grün, E., Hamabe, Y., Iglseider, H., Kawamura, T., Miyamoto, H., Morishige, K., Mukai, T., Naoi, T., Nogami, K., Schwehm, G., Svedhem, H., “Observation of interplanetary and interstellar dust particles by Mars Dust Counter (MDC) on NOZOMI”, *Adv. Space Res.*, Vol. 29. No. 8, pp. 1145-1153, 2002
- [Sau2004] Sauer, A., “Analyse der Housekeepingdaten im Jahr 1998 des Weltraum-experiments MDC auf der japanischen Mission NOZOMI“, Semesterarbeit RT-SA 04/15, Technische Universität München, Lehrstuhl für Raumfahrttechnik, 2004
- [Sch1964] Schmidt, R.A., “Microscopic extraterrestrial particles from the antarctic peninsula”, *Ann. N.Y. Acad. Sci.*, Vol. 119, Art. 1, pp. 186-204, 1964
- [Sch1995] Scholz, M., “Topologiegenerierung für Neuronale Netze durch Genetische Algorithmen”, Dissertation, Fachbereich 13 Informatik, Technische Universität Berlin, 1995
- [Sch1996] Schobert, D., “Aluminiumoxid-Belastung niedriger Erdumlaufbahnen durch feststoffgestützte Platzierung geostationärer Satelliten”, Dissertation, Fachgebiet Raumfahrttechnik, Technische Universität München, 1996
- [Sch1997] Scherer, A., “Neuronale Netze. Grundlagen und Anwendungen”, Friedr. Vieweg & Sohn Verlagsgesellschaft mbH, Braunschweig/Wiesbaden, 1997

- [Smi1999] Smith, S.M., Wilson, J.K., Baumgardner, J., Mendillo, M., “Discovery of the Distant Lunar Sodium Tail and its Enhancement Following the Leonid Meteor Shower of 1998”, *Geophys. Res. Letters* Vol. 26, pp. 1649-1652, 1999
- [Sot1971] Soter, S., “The dust belts of Mars”, Report of Center for Radiophysics and Space Research, No. 462, Cornell University, Ithaca, NY, 1971
- [Sra1997] Srama, R., Grün, E., “The dust sensor for CASSINI”, *Adv. Space Res.*, Vol. 20, No. 8, pp. 1467-1470, 1997
- [Sra2004] Srama, R., Ahrens, T.J., Altobelli, N., Auer, S., Bradley, J.G., Burton, M., Dikarev, V.V., Economou, T., Fechtig, H., Görlich, M., Grande, M., Graps, A., Grün, E., Havnes, O., Helfert, S., Horányi, M., Igenbergs, E., Jessberger, E.K., Johnson, T.V., Kempf, S., Krivov, A.V., Krüger, H., Mocker-Ahlreep, A., Moragas-Klostermeyer, G., Lamy, P., Landgraf, M., Linkert, D., Linkert, G., Lura, F., McDonnell, J.A.M., Möhlmann, D., Morfill, G.E., Müller, M., Roy, M., Schäfer, G., Schlotzhauer, G., Schwehm, G.H., Spahn, F., Stübig, M., Svestka, J., Tschernjawski, V., Tuzzolino, A.J., Wäsch, R., Zook, H.A., “The CASSINI cosmic dust analyzer”, *Space Sci. Rev.*, Vol. 114, pp. 465-518, 2004
- [Sri1999] Srikanth, R., “Physical interpretation of the Poynting-Robertson effect”, *Icarus*, Vol. 140, pp. 231-234, 1999
- [Sta1993] Staubach, P., Divine, N., Grün, E., “Temperatures of zodiacal dust“, *Planet. Space Sci.*, Vol. 41, No. 11/12, pp. 1099-1108, 1993
- [Sta1995] Staubach, P., Grün, E., “Development of an upgraded meteoroid model”, *Adv. Space Res.*, Vol. 16, No. 11, pp. (11)103-(11)106, 1995
- [Sta1997] Stark, J., Nombro, A., Walker, R., Crowther, R., “A model for the generation of micro-debris resulting from atomic oxygen impact”, *Proc. 2nd European Conf. Space Debris*, pp. 285-288, 1997
- [Ste2004] Steiner, W., Schagerl, M., “Raumflugmechanik. Dynamik und Steuerung von Raumfahrzeugen”, Springer Verlag, Berlin, Heidelberg, New York, 2004
- [Str1986] Strazzulla, G., “‘Primitive’ galactic dust in the solar system?”, *Icarus*, Vol. 67, pp. 63-70, 1986
- [Stü2001] Stübig, M., Schäfer, G., Ho, T., Srama, R., Grün, E., “Laboratory simulation improvements for hypervelocity micrometeorite impacts with new dust particle source”, *Planet. Space Sci.*, Vol. 49, pp. 853-858, 2001
- [Sve1992] Svedhem, H., Pedersen, A., “Behaviour of ejecta particles and generated plasma at hypervelocity impacts”, in “Hypervelocity Impacts in Space”, (ed. J.A.M. McDonnell), University of Kent at Canterbury, 1992

- [Syk1992] Sykes, M.V., Walker, R.G., “Cometary dust trails I: Survey”, *Icarus*, Vol. 95, pp. 180-210, 1992
- [Tsu1996] Tsuruda, K., Nakatani, I., Yamamoto, T., “PLANET-B mission to Mars – 1998”, *Adv. Space Res.*, Vol. 17, No. 12, pp. (12)21-(12)29, 1996
- [Ues1991] Uesugi, K., Matsuo, H., Kawaguchi, J., Hayashi, T., “Japanese first double lunar swingby mission ‘HITEN’”, *Acta Astronautica*, Vol. 25, Issue 7, pp. 347-355, 1991
- [Ues1996] Uesugi, K., “Results of the MUSES-A ‘HITEN’ mission”, *Adv. Space Res.*, Vol. 18, No. 11, pp. (11)69-(11)72, 1996
- [Weh1999] Wehry, A., Mann, I., “Identification of β -meteoroids from measurements of the dust detector onboard the Ulysses spacecraft”, *Astron. Astrophys.*, Vol. 341, pp. 296-303, 1999
- [Wen1989] Wenzel, K.-P., Marsden, R.G., Page, D.E., Smith, E.J., “ULYSSES: The first high-latitude heliospheric mission”, *Adv. Space Res.*, Vol. 9, No. 4, pp. (4)25-(4)29, 1998
- [Wil1996] Wilck, M., Mann, I., “Radiation pressure forces on ‘typical’ interplanetary dust grains”, *Planet. Space Sci.*, Vol. 44, No. 5, pp. 493-499, 1996
- [Wil2004] Willis, M.J., Burchell, M.J., Cole, M.J., McDonnell, J.A.M., “Influence of impact ionisation methods on determination of dust particle flux in space”, *Planet. Space Sci.*, Vol. 52, pp. 711-725, 2004
- [Zel1994] Zell, A., “Simulation Neuronaler Netze”, Addison-Wesley, Stuttgart, 1994

Appendix B: Picture credits

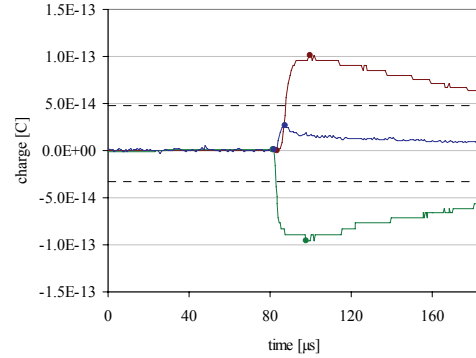
Figure 2-1	Dominic Cantin, Quebec, Canada, September 2, 2003
Figure 2-2	MPI-K, Heidelberg, Webpage http://www.mpi-hd.mpg.de/dustgroup/
Figure 2-4	[Ham1996]
Figure 2-5	NASA/JPL
Figure 2-6	NASA/JPL
Figure 2-7	NASA/JPL
Figure 2-8	NASA/JPL
Figure 2-9	MPI-K, Heidelberg
Figure 2-10	ISAS/JAXA
Figure 2-13	ISAS/JAXA
Figure 2-16	ISAS/JAXA
Figure 3-1	LRT
Figure 3-2	LRT
Figure 3-3	LRT
Figure 3-4	LRT
Figure 3-5	LRT
Figure 3-7	ISAS/JAXA
Figure 3-18	LRT
Figure 3-19	LRT
Figure 3-20	LRT
Figure 4-2	[Kyr2003]
Figure 4-3	[Kyr2003]
Figure 4-4	[Gla2003]
Figure 4-10	[Gla2003]
Figure 5-1	[Kyr2003]
Figure 5-2	[Kyr2003]
Figure 5-3	[Kyr2003]
Figure 5-4	[Kyr2003]
Figure 7-1	LRT

Appendix C: Tables

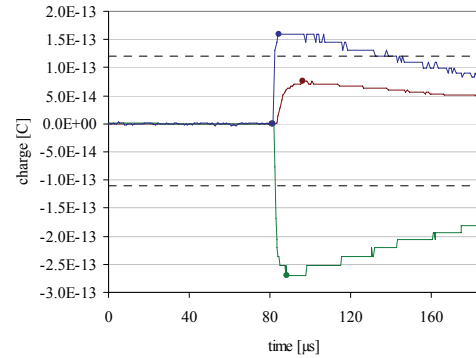
C.1 Signals, HK data and analysis results of the identified impacts

Imp. No.	98071101-26	Mass	3.0E-15 g		
Plus5V	4.94 V	ImpactSpeed	31.57 km/s		
Plus12V	12.12 V	ImpactPos	IC_COL		
Minus12V	12.77 V	CalibImpact	97102407-15		
Plus200V	225.76 V	PosX	47071711 km		
Minus200V	220.32 V	PosY	-144794138 km		
TElec	44.57 °C	PosZ	28784 km		
TBox	41.32 °C	Radius	1.02 AU		
Date	10-Jul-1998	AbsSpeedX	1.32 km/s		
Time	15:08:21	AbsSpeedY	5.19 km/s		
Spinphase	331.04	AbsSpeedZ	16.83 km/s		
Quality	189	AbsSpeed	17.66 km/s		
TRMode	135	Inclination	80.36°		
TRLLevel	127	Eccentricity	0.67		
Checksum	251				
Imp. No.	98071601-3	Mass	4.4E-12 g		
Plus5V	4.94 V	ImpactSpeed	15.24 km/s		
Plus12V	12.41 V	ImpactPos	EC		
Minus12V	12.84 V	CalibImpact	97102210-11		
Plus200V	233.92 V	PosX	60278018 km		
Minus200V	220.32 V	PosY	-139746168 km		
TElec	52.71 °C	PosZ	63454 km		
TBox	47.83 °C	Radius	1.02 AU		
Date	16-Jul-1998	AbsSpeedX	42.13 km/s		
Time	03:52:01	AbsSpeedY	9.46 km/s		
Spinphase	107.53	AbsSpeedZ	2.77 km/s		
Quality	165	AbsSpeed	43.27 km/s		
TRMode	152	Inclination	3.73°		
TRLLevel	143	Eccentricity	1.14		
Checksum	112				
Imp. No.	98073001-5	Mass	1.0E-10 g		
Plus5V	4.94 V	ImpactSpeed	7.69 km/s		
Plus12V	12.70 V	ImpactPos	EC_COL		
Minus12V	13.00 V	CalibImpact	97080801-39		
Plus200V	238.00 V	PosX	88381925 km		
Minus200V	221.68 V	PosY	-123617666 km		
TElec	49.46 °C	PosZ	59061 km		
TBox	46.20 °C	Radius	1.02 AU		
Date	28-Jul-1998	AbsSpeedX	26.34 km/s		
Time	23:23:54	AbsSpeedY	10.01 km/s		
Spinphase	211.03	AbsSpeedZ	0.60 km/s		
Quality	174	AbsSpeed	28.18 km/s		
TRMode	152	Inclination	1.26°		
TRLLevel	143	Eccentricity	0.27		
Checksum	131				
Imp. No.	98073101-29	Mass	1.3E-13 g		
Plus5V	4.94 V	ImpactSpeed	34.14 km/s		
Plus12V	12.56 V	ImpactPos	IC		
Minus12V	12.92 V	CalibImpact	97102108-18		
Plus200V	238.00 V	PosX	93191670 km		
Minus200V	221.68 V	PosY	-119958656 km		
TElec	52.71 °C	PosZ	49421 km		
TBox	49.46 °C	Radius	1.02 AU		
Date	31-Jul-1998	AbsSpeedX	17.86 km/s		
Time	06:37:46	AbsSpeedY	-8.56 km/s		
Spinphase	270.13	AbsSpeedZ	18.23 km/s		
Quality	180	AbsSpeed	26.92 km/s		
TRMode	152	Inclination	64.09°		
TRLLevel	143	Eccentricity	0.67		
Checksum	122				

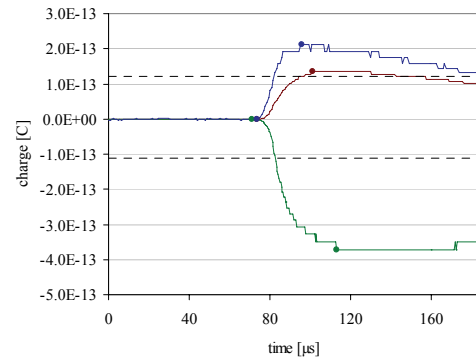
Imp. No.	98080701-3	Mass	1.7E-14 g
Plus5V	4.94 V	ImpactSpeed	20.04 km/s
Plus12V	12.99 V	ImpactPos	IC_COL
Minus12V	13.07 V	CalibImpact	97102403-49
Plus200V	244.80 V	PosX	102884667 km
Minus200V	227.12 V	PosY	-111488040 km
TElec	28.29 °C	PosZ	27355 km
TBox	25.04 °C	Radius	1.01 AU
Date	5-Aug-1998	AbsSpeedX	23.22 km/s
Time	11:14:40	AbsSpeedY	25.17 km/s
Spinphase	335.83	AbsSpeedZ	-19.06 km/s
Quality	188	AbsSpeed	39.19 km/s
TRMode	151	Inclination	29.18°
TRLevel	127	Eccentricity	0.76
Checksum	16		



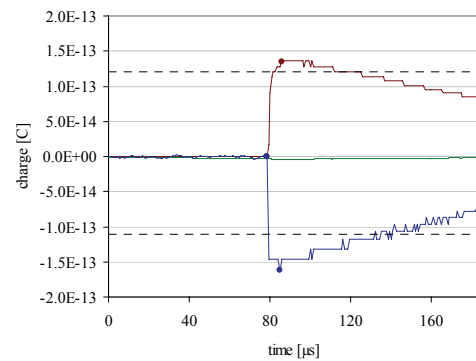
Imp. No.	98082201-8	Mass	1.6E-14 g
Plus5V	4.94 V	ImpactSpeed	25.34 km/s
Plus12V	12.70 V	ImpactPos	EC
Minus12V	13.07 V	CalibImpact	97102114-32
Plus200V	242.08 V	PosX	129049547 km
Minus200V	221.68 V	PosY	-78765918 km
TElec	51.08 °C	PosZ	55978 km
TBox	46.20 °C	Radius	1.01 AU
Date	22-Aug-1998	AbsSpeedX	16.05 km/s
Time	00:48:36	AbsSpeedY	25.81 km/s
Spinphase	23.55	AbsSpeedZ	25.42 km/s
Quality	154	AbsSpeed	39.62 km/s
TRMode	152	Inclination	39.91°
TRLevel	143	Eccentricity	0.79
Checksum	151		



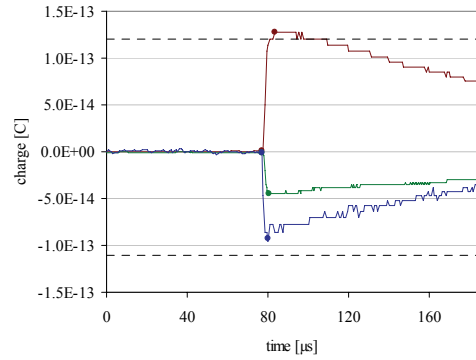
Imp. No.	98090501-14	Mass	6.7E-13 g
Plus5V	4.94 V	ImpactSpeed	9.89 km/s
Plus12V	12.78 V	ImpactPos	EC_COL
Minus12V	13.22 V	CalibImpact	97102402-5
Plus200V	243.44 V	PosX	141712211 km
Minus200V	223.04 V	PosY	-51326819 km
TElec	51.08 °C	PosZ	44935 km
TBox	46.20 °C	Radius	1.01 AU
Date	2-Sep-1998	AbsSpeedX	12.42 km/s
Time	21:28:35	AbsSpeedY	30.13 km/s
Spinphase	56.12	AbsSpeedZ	9.35 km/s
Quality	196	AbsSpeed	33.91 km/s
TRMode	152	Inclination	16.03°
TRLevel	143	Eccentricity	0.31
Checksum	123		



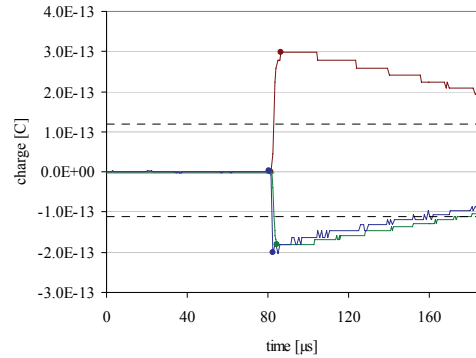
Imp. No.	98092201-9	Mass	1.4E-15 g
Plus5V	4.94 V	ImpactSpeed	37.41 km/s
Plus12V	12.78 V	ImpactPos	IC
Minus12V	13.15 V	CalibImpact	97102315-28
Plus200V	243.44 V	PosX	149955432 km
Minus200V	221.68 V	PosY	-4648768 km
TElec	55.97 °C	PosZ	-13433 km
TBox	52.71 °C	Radius	1.00 AU
Date	21-Sep-1998	AbsSpeedX	31.36 km/s
Time	10:30:04	AbsSpeedY	17.20 km/s
Spinphase	139.35	AbsSpeedZ	15.68 km/s
Quality	125	AbsSpeed	39.05 km/s
TRMode	152	Inclination	40.81°
TRLevel	143	Eccentricity	0.91
Checksum	28		



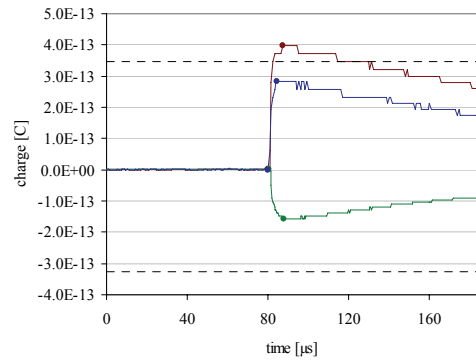
Imp. No.	98092201-23	Mass	1.6E-15 g
Plus5V	4.94 V	ImpactSpeed	35.85 km/s
Plus12V	12.70 V	ImpactPos	IC
Minus12V	13.22 V	CalibImpact	97080604-21
Plus200V	243.44 V	PosX	149929104 km
Minus200V	221.68 V	PosY	-3207880 km
TElec	57.60 °C	PosZ	-4758 km
TBox	52.71 °C	Radius	1.00 AU
Date	22-Sep-1998	AbsSpeedX	-0.64 km/s
Time	00:23:40	AbsSpeedY	0.30 km/s
Spinphase	321.15	AbsSpeedZ	-21.42 km/s
Quality	149	AbsSpeed	21.43 km/s
TRMode	152	Inclination	89.22°
TRLevel	143	Eccentricity	0.48
Checksum	193		



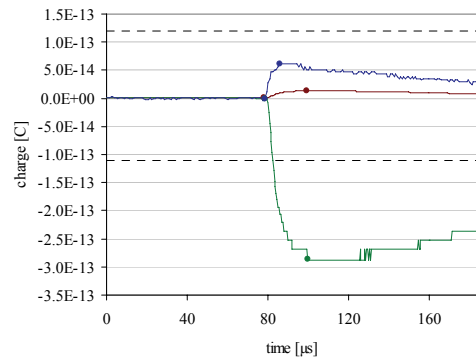
Imp. No.	98101401-21	Mass	2.1E-15 g
Plus5V	4.94 V	ImpactSpeed	36.46 km/s
Plus12V	12.78 V	ImpactPos	IC_C
Minus12V	13.22 V	CalibImpact	97102103-45
Plus200V	246.16 V	PosX	140661832 km
Minus200V	223.04 V	PosY	48872548 km
TElec	52.71 °C	PosZ	470810 km
TBox	49.46 °C	Radius	1.00 AU
Date	13-Oct-1998	AbsSpeedX	-11.78 km/s
Time	03:45:06	AbsSpeedY	41.10 km/s
Spinphase	304.89	AbsSpeedZ	-33.67 km/s
Quality	189	AbsSpeed	54.42 km/s
TRMode	152	Inclination	38.27°
TRLevel	143	Eccentricity	2.32
Checksum	128		



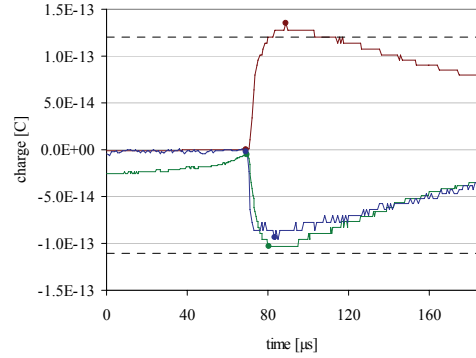
Imp. No.	98102701-37	Mass	8.5E-15 g
Plus5V	4.94 V	ImpactSpeed	28.64 km/s
Plus12V	12.78 V	ImpactPos	IC_COL
Minus12V	13.22 V	CalibImpact	97093010-19
Plus200V	246.16 V	PosX	125317767 km
Minus200V	221.68 V	PosY	79079706 km
TElec	52.71 °C	PosZ	597923 km
TBox	49.46 °C	Radius	0.99 AU
Date	26-Oct-1998	AbsSpeedX	-18.69 km/s
Time	10:07:48	AbsSpeedY	30.97 km/s
Spinphase	302.12	AbsSpeedZ	-27.82 km/s
Quality	161	AbsSpeed	45.63 km/s
TRMode	153	Inclination	37.57°
TRLevel	159	Eccentricity	1.32
Checksum	211		



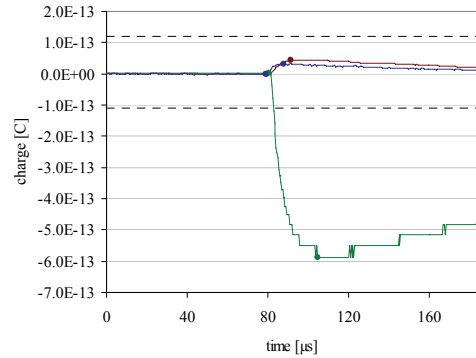
Imp. No.	98110901-17	Mass	1.9E-13 g
Plus5V	4.94 V	ImpactSpeed	17.15 km/s
Plus12V	12.99 V	ImpactPos	MLI_A
Minus12V	13.22 V	CalibImpact	97102413-5
Plus200V	247.52 V	PosX	102744228 km
Minus200V	221.68 V	PosY	105734878 km
TElec	54.34 °C	PosZ	623866 km
TBox	49.46 °C	Radius	0.99 AU
Date	8-Nov-1998	AbsSpeedX	-29.88 km/s
Time	23:02:03	AbsSpeedY	25.74 km/s
Spinphase	342.11	AbsSpeedZ	-14.29 km/s
Quality	148	AbsSpeed	41.95 km/s
TRMode	152	Inclination	19.94°
TRLevel	143	Eccentricity	0.96
Checksum	171		



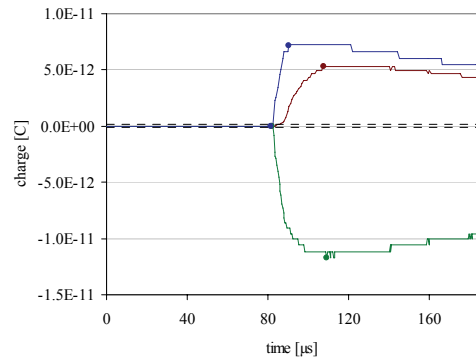
Imp. No.	98110901-29	Mass	1.3E-13 g
Plus5V	4.94 V	ImpactSpeed	16.82 km/s
Plus12V	13.43 V	ImpactPos	IC_C
Minus12V	13.30 V	CalibImpact	97102102-28
Plus200V	247.52 V	PosX	103639158 km
Minus200V	223.04 V	PosY	104886737 km
TElec	54.34 °C	PosZ	624512 km
TBox	49.46 °C	Radius	0.99 AU
Date	8-Nov-1998	AbsSpeedX	-27.04 km/s
Time	11:38:43	AbsSpeedY	22.46 km/s
Spinphase	4.92	AbsSpeedZ	-15.91 km/s
Quality	179	AbsSpeed	38.58 km/s
TRMode	152	Inclination	24.41°
TRLevel	143	Eccentricity	0.66
Checksum	120		



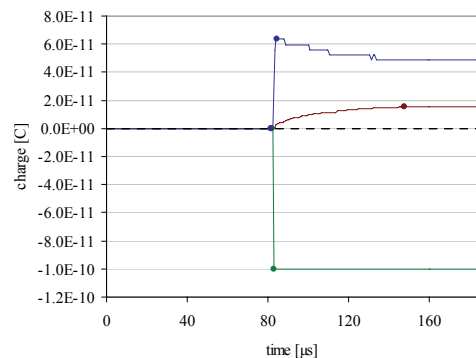
Imp. No.	98111001-1	Mass	N/A
Plus5V	4.94 V	ImpactSpeed	N/A
Plus12V	12.85 V	ImpactPos	GRID_EC
Minus12V	13.22 V	CalibImpact	97093003-35
Plus200V	247.52 V	PosX	101823105 km
Minus200V	223.04 V	PosY	106580827 km
TElec	54.34 °C	PosZ	623077 km
TBox	49.46 °C	Radius	0.99 AU
Date	9-Nov-1998	AbsSpeedX	N/A
Time	10:35:00	AbsSpeedY	N/A
Spinphase	331.88	AbsSpeedZ	N/A
Quality	153	AbsSpeed	N/A
TRMode	152	Inclination	N/A
TRLevel	143	Eccentricity	N/A
Checksum	96		



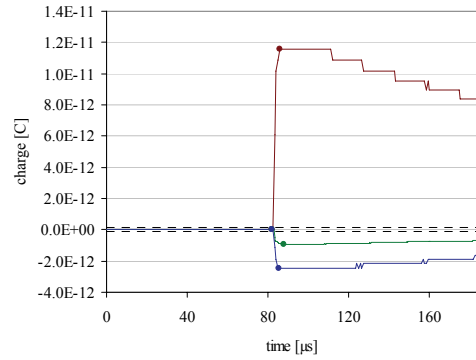
Imp. No.	98111701-8	Mass	1.5E-11 g
Plus5V	4.94 V	ImpactSpeed	11.86 km/s
Plus12V	12.85 V	ImpactPos	EC_C
Minus12V	13.22 V	CalibImpact	97102002-50
Plus200V	246.16 V	PosX	86086726 km
Minus200V	223.04 V	PosY	119183754 km
TElec	54.34 °C	PosZ	591866 km
TBox	49.46 °C	Radius	0.98 AU
Date	17-Nov-1998	AbsSpeedX	-16.68 km/s
Time	04:23:19	AbsSpeedY	25.48 km/s
Spinphase	164.93	AbsSpeedZ	-1.92 km/s
Quality	176	AbsSpeed	30.51 km/s
TRMode	152	Inclination	3.95°
TRLevel	143	Eccentricity	0.36
Checksum	202		



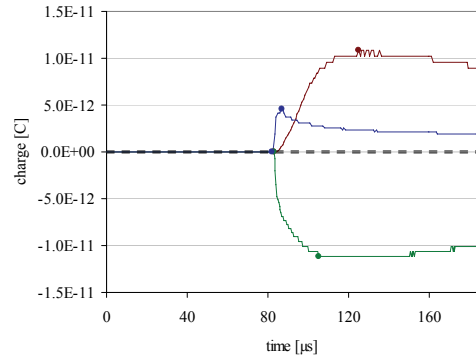
Imp. No.	98111801-1	Mass	6.0E-11 g
Plus5V	4.94 V	ImpactSpeed	13.92 km/s
Plus12V	12.85 V	ImpactPos	IC_COL
Minus12V	13.22 V	CalibImpact	96112004-15
Plus200V	247.52 V	PosX	84951085 km
Minus200V	224.40 V	PosY	119965169 km
TElec	54.34 °C	PosZ	588452 km
TBox	49.46 °C	Radius	0.98 AU
Date	17-Nov-1998	AbsSpeedX	-16.51 km/s
Time	17:02:59	AbsSpeedY	16.49 km/s
Spinphase	75.37	AbsSpeedZ	-11.15 km/s
Quality	184	AbsSpeed	25.86 km/s
TRMode	152	Inclination	25.90°
TRLevel	143	Eccentricity	0.30
Checksum	32		



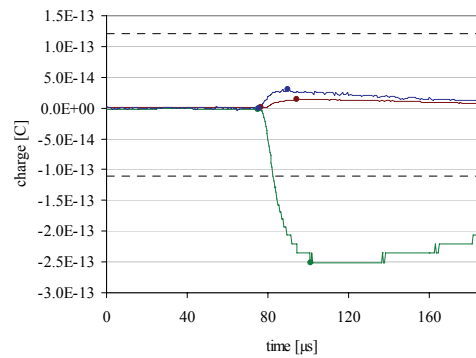
Imp. No.	98111801-6	Mass	3.3E-13 g
Plus5V	4.94 V	ImpactSpeed	26.09 km/s
Plus12V	12.85 V	ImpactPos	EC_C
Minus12V	13.38 V	CalibImpact	97093011-34
Plus200V	247.52 V	PosX	84273081 km
Minus200V	223.04 V	PosY	120428155 km
TElec	54.34 °C	PosZ	586334 km
TBox	49.46 °C	Radius	0.98 AU
Date	18-Nov-1998	AbsSpeedX	-5.42 km/s
Time	00:35:19	AbsSpeedY	33.13 km/s
Spinphase	154.95	AbsSpeedZ	-5.33 km/s
Quality	197	AbsSpeed	33.99 km/s
TRMode	152	Inclination	13.04°
TRLevel	143	Eccentricity	0.73
Checksum	116		



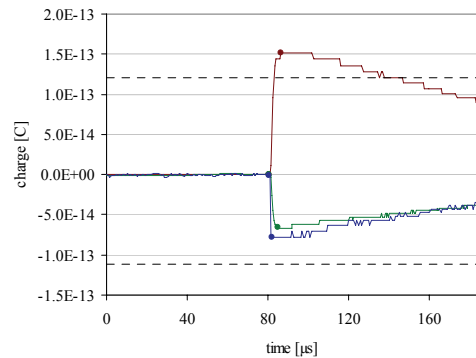
Imp. No.	98112101-6	Mass	1.9E-11 g
Plus5V	4.94 V	ImpactSpeed	10.80 km/s
Plus12V	12.92 V	ImpactPos	EC_C
Minus12V	13.30 V	CalibImpact	96112003-46
Plus200V	247.52 V	PosX	78952092 km
Minus200V	223.04 V	PosY	123855597 km
TElec	54.34 °C	PosZ	568035 km
TBox	49.46 °C	Radius	0.98 AU
Date	20-Nov-1998	AbsSpeedX	-31.47 km/s
Time	10:39:41	AbsSpeedY	21.21 km/s
Spinphase	305.90	AbsSpeedZ	-7.59 km/s
Quality	208	AbsSpeed	38.70 km/s
TRMode	152	Inclination	11.32°
TRLevel	143	Eccentricity	0.66
Checksum	181		



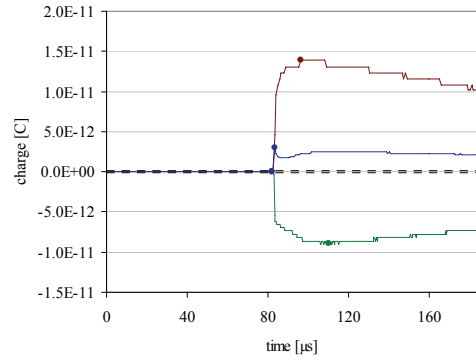
Imp. No.	98120201-17	Mass	1.5E-13 g
Plus5V	4.94 V	ImpactSpeed	17.46 km/s
Plus12V	12.99 V	ImpactPos	MLL_A
Minus12V	13.30 V	CalibImpact	97102413-5
Plus200V	248.88 V	PosX	52215696 km
Minus200V	223.04 V	PosY	136913926 km
TElec	54.34 °C	PosZ	431437 km
TBox	49.46 °C	Radius	0.98 AU
Date	1-Dec-1998	AbsSpeedX	-23.47 km/s
Time	18:58:50	AbsSpeedY	8.47 km/s
Spinphase	25.05	AbsSpeedZ	-16.74 km/s
Quality	144	AbsSpeed	30.04 km/s
TRMode	152	Inclination	33.86°
TRLevel	143	Eccentricity	0.02
Checksum	209		



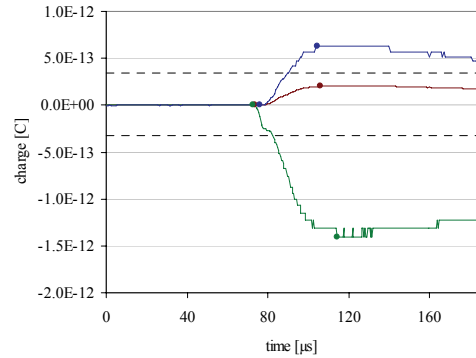
Imp. No.	98120301-9	Mass	1.6E-16 g
Plus5V	4.94 V	ImpactSpeed	50.90 km/s
Plus12V	12.85 V	ImpactPos	IC_C
Minus12V	13.22 V	CalibImpact	97102310-40
Plus200V	247.52 V	PosX	49768815 km
Minus200V	223.04 V	PosY	137804201 km
TElec	55.97 °C	PosZ	415244 km
TBox	51.08 °C	Radius	0.98 AU
Date	2-Dec-1998	AbsSpeedX	-44.21 km/s
Time	18:41:39	AbsSpeedY	15.97 km/s
Spinphase	329.59	AbsSpeedZ	-48.35 km/s
Quality	151	AbsSpeed	67.43 km/s
TRMode	152	Inclination	45.80°
TRLevel	143	Eccentricity	4.02
Checksum	209		



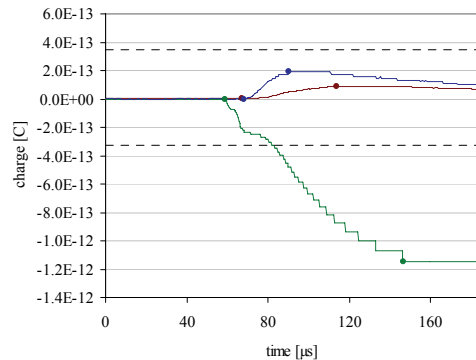
Imp. No.	98121801-35	Mass	2.0E-12 g
Plus5V	4.94 V	ImpactSpeed	19.65 km/s
Plus12V	12.85 V	ImpactPos	IC_COL
Minus12V	13.22 V	CalibImpact	97102408-4
Plus200V	247.52 V	PosX	12054841 km
Minus200V	223.04 V	PosY	146232969 km
TElec	57.60 °C	PosZ	65009 km
TBox	54.34 °C	Radius	0.98 AU
Date	17-Dec-1998	AbsSpeedX	-30.29 km/s
Time	10:17:34	AbsSpeedY	1.67 km/s
Spinphase	335.96	AbsSpeedZ	-19.97 km/s
Quality	214	AbsSpeed	36.32 km/s
TRMode	152	Inclination	33.37°
TRLevel	143	Eccentricity	0.46
Checksum	91		



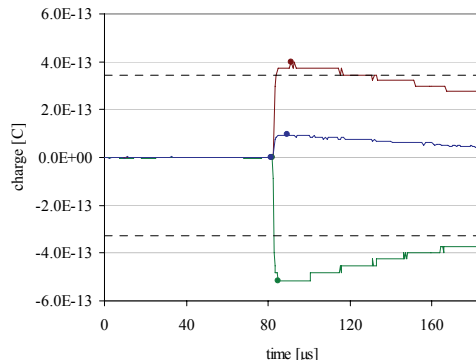
Imp. No.	99011201-43	Mass	4.6E-12 g
Plus5V	4.94 V	ImpactSpeed	8.89 km/s
Plus12V	12.85 V	ImpactPos	MLI_B
Minus12V	13.30 V	CalibImpact	97080811-2
Plus200V	248.88 V	PosX	-60090702 km
Minus200V	223.04 V	PosY	133262786 km
TElec	55.97 °C	PosZ	3301958 km
TBox	51.08 °C	Radius	0.98 AU
Date	11-Jan-1999	AbsSpeedX	-25.75 km/s
Time	17:36:43	AbsSpeedY	-19.00 km/s
Spinphase	213.79	AbsSpeedZ	5.91 km/s
Quality	153	AbsSpeed	32.54 km/s
TRMode	153	Inclination	11.03°
TRLevel	159	Eccentricity	0.26
Checksum	105		



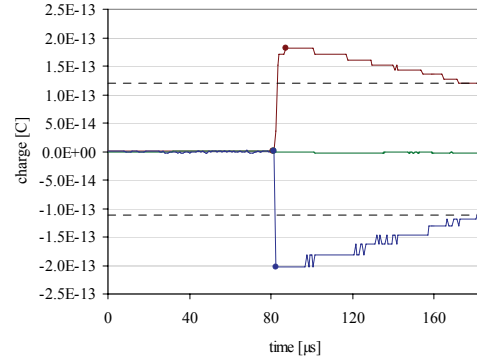
Imp. No.	99021401-20	Mass	4.4E-12 g
Plus5V	4.94 V	ImpactSpeed	15.24 km/s
Plus12V	12.99 V	ImpactPos	EC
Minus12V	13.38 V	CalibImpact	97102233-49
Plus200V	251.60 V	PosX	60278018 km
Minus200V	224.40 V	PosY	-139746168 km
TElec	51.08 °C	PosZ	63454 km
TBox	46.20 °C	Radius	1.02 AU
Date	12-Feb-1999	AbsSpeedX	12.70 km/s
Time	03:47:27	AbsSpeedY	15.17 km/s
Spinphase	210.81	AbsSpeedZ	-2.74 km/s
Quality	124	AbsSpeed	19.97 km/s
TRMode	153	Inclination	8.81°
TRLevel	159	Eccentricity	0.66
Checksum	240		



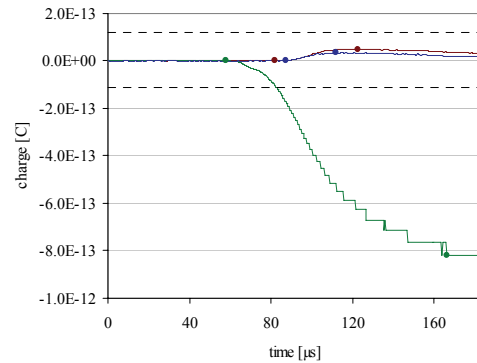
Imp. No.	99030104-29	Mass	1.6E-16 g
Plus5V	4.94 V	ImpactSpeed	69.58 km/s
Plus12V	12.99 V	ImpactPos	IC_C
Minus12V	13.45 V	CalibImpact	97102103-44
Plus200V	252.96 V	PosX	-152913439 km
Minus200V	225.76 V	PosY	40469814 km
TElec	47.83 °C	PosZ	7845675 km
TBox	42.94 °C	Radius	1.06 AU
Date	1-Mar-1999	AbsSpeedX	-68.94 km/s
Time	09:40:43	AbsSpeedY	4.25 km/s
Spinphase	343.43	AbsSpeedZ	24.34 km/s
Quality	193	AbsSpeed	73.23 km/s
TRMode	153	Inclination	57.20°
TRLevel	159	Eccentricity	2.07
Checksum	189		



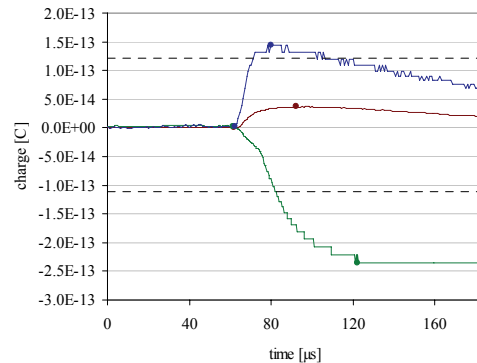
Imp. No.	99030901-3	Mass	4.1E-16 g
Plus5V	4.94 V	ImpactSpeed	47.41 km/s
Plus12V	12.99 V	ImpactPos	IC
Minus12V	13.45 V	CalibImpact	97102315-28
Plus200V	251.60 V	PosX	-157266956 km
Minus200V	224.40 V	PosY	29376881 km
TElec	47.83 °C	PosZ	8067958 km
TBox	42.94 °C	Radius	1.07 AU
Date	5-Mar-1999	AbsSpeedX	31.34 km/s
Time	22:01:49	AbsSpeedY	-11.02 km/s
Spinphase	122.56	AbsSpeedZ	14.82 km/s
Quality	159	AbsSpeed	36.37 km/s
TRMode	152	Inclination	72.88°
TRLevel	143	Eccentricity	0.93
Checksum	113		



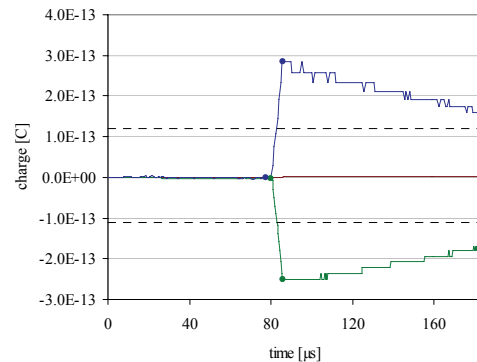
Imp. No.	99030901-31	Mass	6.8E-12 g
Plus5V	4.94 V	ImpactSpeed	7.95 km/s
Plus12V	12.99 V	ImpactPos	MLI_A
Minus12V	13.53 V	CalibImpact	97102411-39
Plus200V	252.96 V	PosX	-159641635 km
Minus200V	225.76 V	PosY	22221957 km
TElec	46.20 °C	PosZ	8188819 km
TBox	41.32 °C	Radius	1.08 AU
Date	8-Mar-1999	AbsSpeedX	-7.80 km/s
Time	19:07:38	AbsSpeedY	-24.77 km/s
Spinphase	335.04	AbsSpeedZ	-6.26 km/s
Quality	85	AbsSpeed	26.71 km/s
TRMode	152	Inclination	14.46°
TRLevel	143	Eccentricity	0.20
Checksum	213		



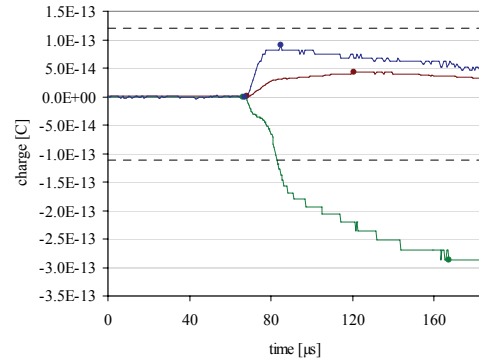
Imp. No.	99042001-29	Mass	3.3E-13 g
Plus5V	4.94 V	ImpactSpeed	10.18 km/s
Plus12V	13.07 V	ImpactPos	EC_COL
Minus12V	13.53 V	CalibImpact	96112204-34
Plus200V	257.04 V	PosX	-160847494 km
Minus200V	227.12 V	PosY	-81802403 km
TElec	34.80 °C	PosZ	8235959 km
TBox	28.29 °C	Radius	1.21 AU
Date	20-Apr-1999	AbsSpeedX	15.15 km/s
Time	09:14:18	AbsSpeedY	-20.76 km/s
Spinphase	197.18	AbsSpeedZ	3.25 km/s
Quality	151	AbsSpeed	25.91 km/s
TRMode	152	Inclination	8.13°
TRLevel	143	Eccentricity	0.17
Checksum	52		



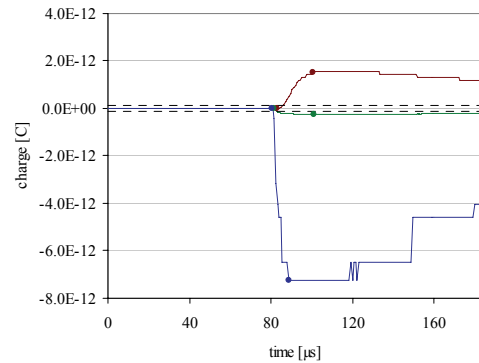
Imp. No.	99052701-39	Mass	1.5E-13 g
Plus5V	4.94 V	ImpactSpeed	16.78 km/s
Plus12V	13.14 V	ImpactPos	EC
Minus12V	13.53 V	CalibImpact	97102217-27
Plus200V	255.68 V	PosX	-121929404 km
Minus200V	227.12 V	PosY	-153506611 km
TElec	33.18 °C	PosZ	6228099 km
TBox	26.66 °C	Radius	1.31 AU
Date	27-May-1999	AbsSpeedX	27.58 km/s
Time	00:50:57	AbsSpeedY	-20.13 km/s
Spinphase	65.13	AbsSpeedZ	-13.39 km/s
Quality	135	AbsSpeed	36.68 km/s
TRMode	152	Inclination	21.43°
TRLevel	143	Eccentricity	0.99
Checksum	200		



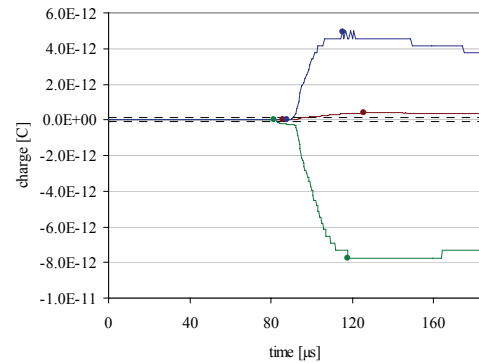
Imp. No.	99060201-15	Mass	2.1E-11 g
Plus5V	4.94 V	ImpactSpeed	4.23 km/s
Plus12V	13.14 V	ImpactPos	MLL_B
Minus12V	13.60 V	CalibImpact	97080810-42
Plus200V	257.04 V	PosX	-113496858 km
Minus200V	227.12 V	PosY	-162463142 km
TElec	31.55 °C	PosZ	5794150 km
TBox	25.04 °C	Radius	1.33 AU
Date	1-Jun-1999	AbsSpeedX	19.41 km/s
Time	18:55:49	AbsSpeedY	-14.17 km/s
Spinphase	143.57	AbsSpeedZ	-2.78 km/s
Quality	150	AbsSpeed	24.19 km/s
TRMode	152	Inclination	6.83°
TRLevel	143	Eccentricity	0.13
Checksum	26		



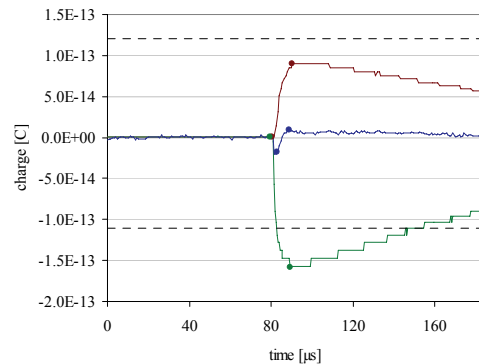
Imp. No.	99071201-29	Mass	1.3E-12 g
Plus5V	4.94 V	ImpactSpeed	12.45 km/s
Plus12V	13.14 V	ImpactPos	EC_C
Minus12V	13.60 V	CalibImpact	96112003-25
Plus200V	258.40 V	PosX	-45209701 km
Minus200V	227.12 V	PosY	-205043548 km
TElec	29.92 °C	PosZ	2284434 km
TBox	23.41 °C	Radius	1.40 AU
Date	11-Jul-1999	AbsSpeedX	26.48 km/s
Time	08:00:29	AbsSpeedY	1.79 km/s
Spinphase	233.57	AbsSpeedZ	5.83 km/s
Quality	152	AbsSpeed	27.18 km/s
TRMode	152	Inclination	13.09°
TRLevel	143	Eccentricity	0.32
Checksum	21		



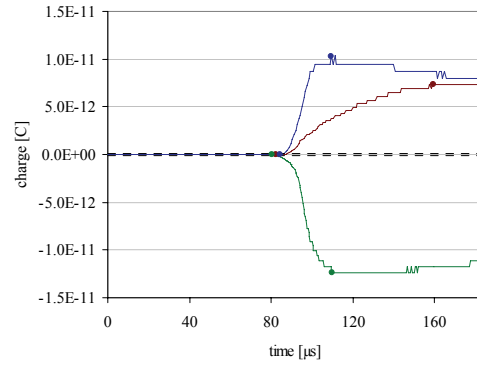
Imp. No.	99072401-34	Mass	4.2E-11 g
Plus5V	4.94 V	ImpactSpeed	6.38 km/s
Plus12V	13.21 V	ImpactPos	EC
Minus12V	13.60 V	CalibImpact	96112203-33
Plus200V	258.40 V	PosX	-25529578 km
Minus200V	227.12 V	PosY	-210559673 km
TElec	29.92 °C	PosZ	1273877 km
TBox	23.41 °C	Radius	1.42 AU
Date	21-Jul-1999	AbsSpeedX	26.26 km/s
Time	16:10:04	AbsSpeedY	-2.93 km/s
Spinphase	78.79	AbsSpeedZ	-5.64 km/s
Quality	151	AbsSpeed	27.02 km/s
TRMode	152	Inclination	12.05°
TRLevel	143	Eccentricity	0.17
Checksum	6		



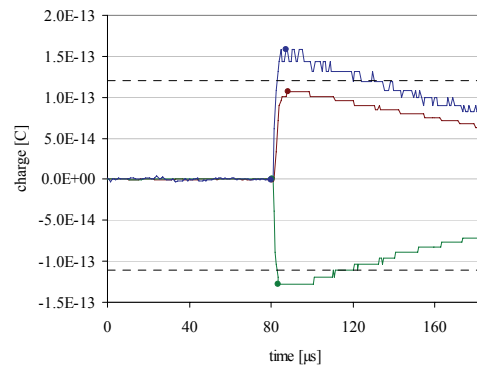
Imp. No.	99091201-12	Mass	2.1E-14 g
Plus5V	4.94 V	ImpactSpeed	18.55 km/s
Plus12V	13.14 V	ImpactPos	EC_COL
Minus12V	13.60 V	CalibImpact	97102402-36
Plus200V	257.04 V	PosX	73154780 km
Minus200V	228.48 V	PosY	-203522168 km
TElec	28.29 °C	PosZ	-3790628 km
TBox	23.41 °C	Radius	1.45 AU
Date	11-Sep-1999	AbsSpeedX	37.73 km/s
Time	13:53:33	AbsSpeedY	14.96 km/s
Spinphase	11.78	AbsSpeedZ	-3.48 km/s
Quality	122	AbsSpeed	40.74 km/s
TRMode	152	Inclination	5.03°
TRLevel	143	Eccentricity	1.70
Checksum	110		



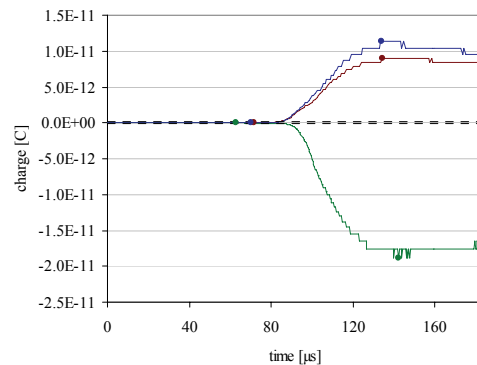
Imp. No.	99092401-7	Mass	1.4E-10 g
Plus5V	4.94 V	ImpactSpeed	6.76 km/s
Plus12V	13.14 V	ImpactPos	EC_C
Minus12V	13.68 V	CalibImpact	97102007-26
Plus200V	257.04 V	PosX	79662563 km
Minus200V	229.84 V	PosY	-200929557 km
TElec	28.29 °C	PosZ	-4124835 km
TBox	23.41 °C	Radius	1.45 AU
Date	15-Sep-1999	AbsSpeedX	20.13 km/s
Time	05:27:15	AbsSpeedY	13.83 km/s
Spinphase	242.93	AbsSpeedZ	3.32 km/s
Quality	172	AbsSpeed	24.65 km/s
TRMode	152	Inclination	7.77°
TRLevel	143	Eccentricity	0.22
Checksum	45		



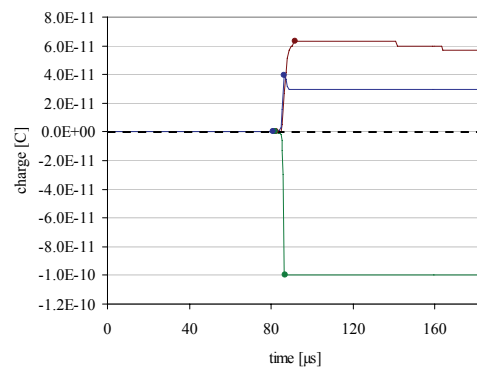
Imp. No.	99101901-45	Mass	3.8E-15 g
Plus5V	4.94 V	ImpactSpeed	44.83 km/s
Plus12V	13.14 V	ImpactPos	MLL_B
Minus12V	13.68 V	CalibImpact	97100206-49
Plus200V	258.40 V	PosX	132995420 km
Minus200V	228.48 V	PosY	-165734631 km
TElec	28.29 °C	PosZ	-6863033 km
TBox	23.41 °C	Radius	1.42 AU
Date	18-Oct-1999	AbsSpeedX	1.00 km/s
Time	09:37:27	AbsSpeedY	48.32 km/s
Spinphase	118.35	AbsSpeedZ	-27.55 km/s
Quality	194	AbsSpeed	55.63 km/s
TRMode	152	Inclination	42.84°
TRLevel	143	Eccentricity	3.08
Checksum	96		



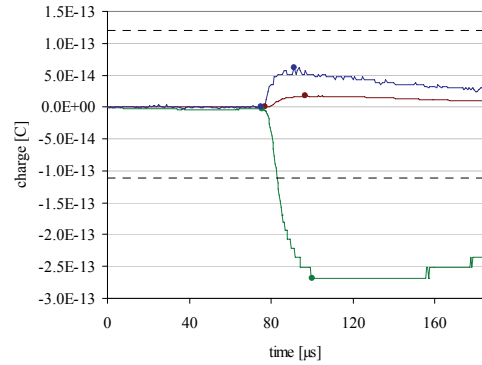
Imp. No.	99112001-13	Mass	2.3E-09 g
Plus5V	4.94 V	ImpactSpeed	3.04 km/s
Plus12V	13.21 V	ImpactPos	EC_C
Minus12V	13.60 V	CalibImpact	96112003-11
Plus200V	258.40 V	PosX	170868118 km
Minus200V	228.48 V	PosY	-112651281 km
TElec	29.92 °C	PosZ	-8803966 km
TBox	25.04 °C	Radius	1.37 AU
Date	20-Nov-1999	AbsSpeedX	9.71 km/s
Time	03:51:16	AbsSpeedY	23.82 km/s
Spinphase	72.77	AbsSpeedZ	-2.49 km/s
Quality	131	AbsSpeed	25.84 km/s
TRMode	152	Inclination	6.59°
TRLevel	143	Eccentricity	0.19
Checksum	237		



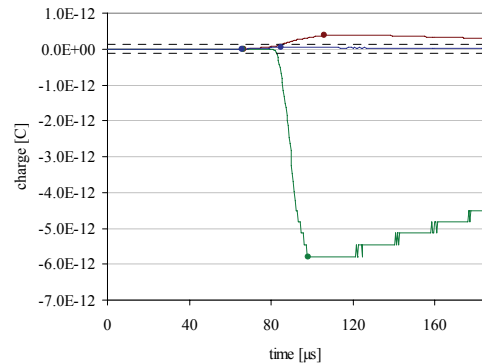
Imp. No.	99112501-3	Mass	3.6E-12 g
Plus5V	4.94 V	ImpactSpeed	26.72 km/s
Plus12V	13.14 V	ImpactPos	IC_COL
Minus12V	13.60 V	CalibImpact	97102409-25
Plus200V	258.40 V	PosX	174817334 km
Minus200V	228.48 V	PosY	-103541015 km
TElec	29.92 °C	PosZ	-9005852 km
TBox	25.04 °C	Radius	1.36 AU
Date	24-Nov-1999	AbsSpeedX	-15.37 km/s
Time	23:36:37	AbsSpeedY	31.53 km/s
Spinphase	193.32	AbsSpeedZ	5.02 km/s
Quality	222	AbsSpeed	35.43 km/s
TRMode	152	Inclination	11.19°
TRLevel	143	Eccentricity	0.98
Checksum	99		



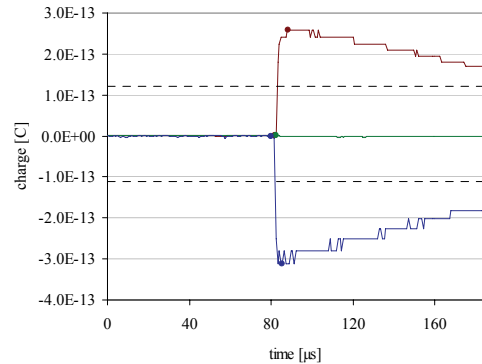
Imp. No.	00040501-19	Mass	1.9E-13 g
Plus5V	4.94 V	ImpactSpeed	17.18 km/s
Plus12V	12.99 V	ImpactPos	MLL_A
Minus12V	13.53 V	CalibImpact	96112208-18
Plus200V	251.60 V	PosX	50731385 km
Minus200V	224.40 V	PosY	142029583 km
TElec	52.71 °C	PosZ	-2592619 km
TBox	47.83 °C	Radius	1.01 AU
Date	2-Apr-2000	AbsSpeedX	-48.18 km/s
Time	15:23:17	AbsSpeedY	8.82 km/s
Spinphase	357.98	AbsSpeedZ	1.96 km/s
Quality	143	AbsSpeed	49.02 km/s
TRMode	152	Inclination	2.38°
TRLevel	143	Eccentricity	1.72
Checksum	27		



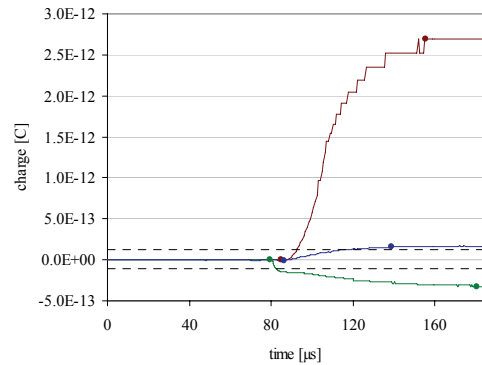
Imp. No.	00041101-7	Mass	N/A
Plus5V	4.94 V	ImpactSpeed	N/A
Plus12V	13.43 V	ImpactPos	GRID_EC
Minus12V	13.53 V	CalibImpact	97093003-35
Plus200V	251.60 V	PosX	42452439 km
Minus200V	223.04 V	PosY	143886305 km
TElec	52.71 °C	PosZ	-2166598 km
TBox	47.83 °C	Radius	1.00 AU
Date	5-Apr-2000	AbsSpeedX	N/A
Time	16:51:25	AbsSpeedY	N/A
Spinphase	206.63	AbsSpeedZ	N/A
Quality	107	AbsSpeed	N/A
TRMode	152	Inclination	N/A
TRLevel	143	Eccentricity	N/A
Checksum	244		



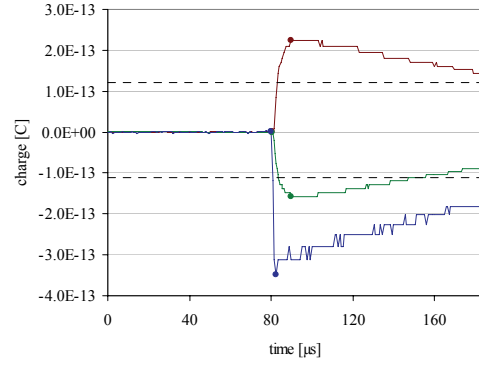
Imp. No.	00041601-8	Mass	4.5E-15 g
Plus5V	4.94 V	ImpactSpeed	34.44 km/s
Plus12V	13.07 V	ImpactPos	IC
Minus12V	13.45 V	CalibImpact	97102315-28
Plus200V	251.60 V	PosX	24907116 km
Minus200V	224.40 V	PosY	146475307 km
TElec	52.71 °C	PosZ	-1264008 km
TBox	49.46 °C	Radius	0.99 AU
Date	12-Apr-2000	AbsSpeedX	-29.54 km/s
Time	01:28:10	AbsSpeedY	-31.05 km/s
Spinphase	167.12	AbsSpeedZ	-3.49 km/s
Quality	160	AbsSpeed	42.99 km/s
TRMode	152	Inclination	9.02°
TRLevel	143	Eccentricity	1.02
Checksum	142		



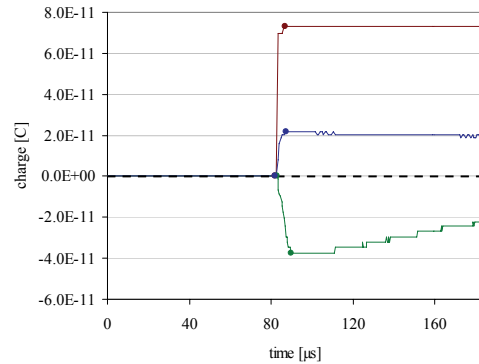
Imp. No.	00052301-29	Mass	1.6E-11 g
Plus5V	4.94 V	ImpactSpeed	5.55 km/s
Plus12V	12.99 V	ImpactPos	IC_COL
Minus12V	13.68 V	CalibImpact	97093011-34
Plus200V	251.60 V	PosX	-78913331 km
Minus200V	223.04 V	PosY	123954539 km
TElec	54.34 °C	PosZ	4072224 km
TBox	51.08 °C	Radius	0.98 AU
Date	20-May-2000	AbsSpeedX	-24.52 km/s
Time	04:29:12	AbsSpeedY	-20.40 km/s
Spinphase	198.85	AbsSpeedZ	2.54 km/s
Quality	169	AbsSpeed	32.00 km/s
TRMode	152	Inclination	5.04°
TRLevel	143	Eccentricity	0.18
Checksum	162		



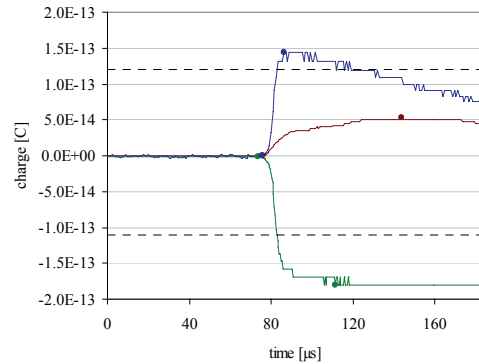
Imp. No.	00052301-36	Mass	5.1E-14 g
Plus5V	4.94 V	ImpactSpeed	23.97 km/s
Plus12V	12.99 V	ImpactPos	IC
Minus12V	13.45 V	CalibImpact	97080604-35
Plus200V	251.60 V	PosX	-71787710 km
Minus200V	223.04 V	PosY	127846302 km
TElec	54.34 °C	PosZ	3706283 km
TBox	51.08 °C	Radius	0.98 AU
Date	17-May-2000	AbsSpeedX	-39.43 km/s
Time	07:38:15	AbsSpeedY	-31.41 km/s
Spinphase	58.23	AbsSpeedZ	-12.65 km/s
Quality	155	AbsSpeed	51.97 km/s
TRMode	152	Inclination	14.11°
TRLevel	143	Eccentricity	1.97
Checksum	159		



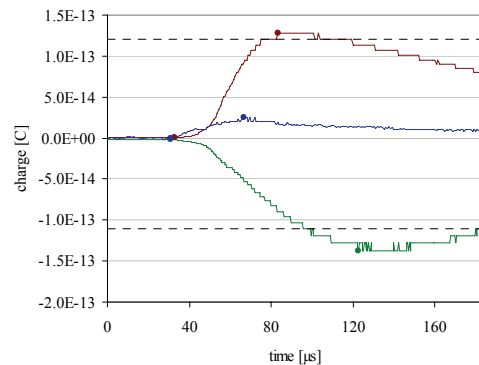
Imp. No.	00061301-19	Mass	N/A
Plus5V	4.94 V	ImpactSpeed	N/A
Plus12V	12.99 V	ImpactPos	EC_COL
Minus12V	13.68 V	CalibImpact	97080804-12
Plus200V	252.96 V	PosX	-123385600 km
Minus200V	223.04 V	PosY	87376625 km
TElec	54.34 °C	PosZ	6354660 km
TBox	49.46 °C	Radius	1.01 AU
Date	9-Jun-2000	AbsSpeedX	N/A
Time	20:39:49	AbsSpeedY	N/A
Spinphase	176.00	AbsSpeedZ	N/A
Quality	183	AbsSpeed	N/A
TRMode	152	Inclination	N/A
TRLevel	143	Eccentricity	N/A
Checksum	243		



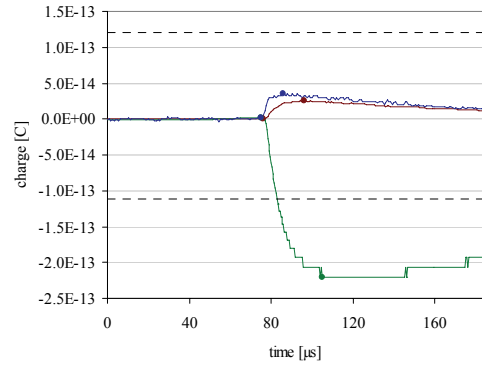
Imp. No.	00062101-4	Mass	3.1E-13 g
Plus5V	4.94 V	ImpactSpeed	10.88 km/s
Plus12V	13.07 V	ImpactPos	EC_C
Minus12V	13.53 V	CalibImpact	97102240-9
Plus200V	252.96 V	PosX	-139206255 km
Minus200V	223.04 V	PosY	66309094 km
TElec	52.71 °C	PosZ	7165354 km
TBox	47.83 °C	Radius	1.03 AU
Date	19-Jun-2000	AbsSpeedX	-7.96 km/s
Time	11:51:26	AbsSpeedY	-30.02 km/s
Spinphase	223.90	AbsSpeedZ	5.73 km/s
Quality	151	AbsSpeed	31.58 km/s
TRMode	152	Inclination	11.41°
TRLevel	143	Eccentricity	0.23
Checksum	22		



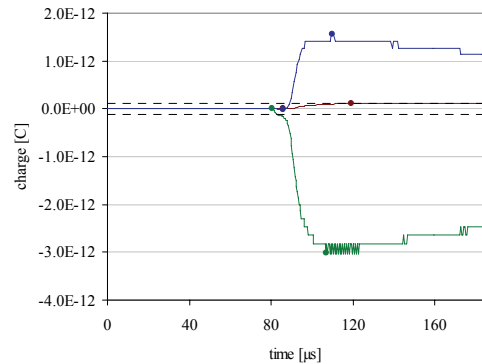
Imp. No.	00062101-37	Mass	4.0E-12 g
Plus5V	4.94 V	ImpactSpeed	5.07 km/s
Plus12V	13.07 V	ImpactPos	IC_C
Minus12V	13.68 V	CalibImpact	97102104-9
Plus200V	252.96 V	PosX	-139013539 km
Minus200V	224.40 V	PosY	66608656 km
TElec	52.71 °C	PosZ	7155521 km
TBox	47.83 °C	Radius	1.03 AU
Date	19-Jun-2000	AbsSpeedX	-12.12 km/s
Time	08:42:39	AbsSpeedY	-27.67 km/s
Spinphase	192.79	AbsSpeedZ	1.39 km/s
Quality	108	AbsSpeed	30.24 km/s
TRMode	152	Inclination	3.80°
TRLevel	143	Eccentricity	0.07
Checksum	30		



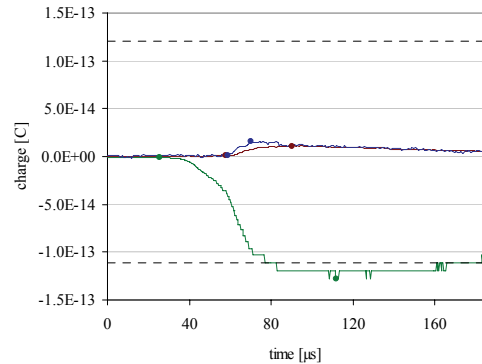
Imp. No.	00062101-42	Mass	N/A
		ImpactSpeed	N/A
Plus5V	4.94 V	ImpactPos	GRID_EC
Plus12V	12.99 V	CalibImpact	97102325-12
Minus12V	13.45 V		
Plus200V	251.60 V	PosX	-135938575 km
Minus200V	224.40 V	PosY	71223534 km
TElec	52.71 °C	PosZ	6998044 km
TBox	47.83 °C	Radius	1.03 AU
Date	17-Jun-2000	AbsSpeedX	N/A
Time	07:46:12	AbsSpeedY	N/A
Spinphase	41.84	AbsSpeedZ	N/A
Quality	148	AbsSpeed	N/A
TRMode	152		
TRLevel	143	Inclination	N/A
Checksum	164	Eccentricity	N/A



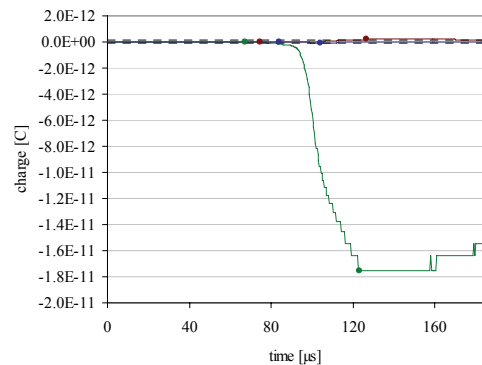
Imp. No.	00070701-22	Mass	5.1E-12 g
		ImpactSpeed	12.71 km/s
Plus5V	4.94 V	ImpactPos	MLI_A
Plus12V	13.07 V	CalibImpact	97102420-17
Minus12V	13.60 V		
Plus200V	254.32 V	PosX	-152766946 km
Minus200V	224.40 V	PosY	40869640 km
TElec	49.46 °C	PosZ	7859392 km
TBox	44.57 °C	Radius	1.06 AU
Date	30-Jun-2000	AbsSpeedX	-1.49 km/s
Time	05:52:23	AbsSpeedY	-30.94 km/s
Spinphase	230.14	AbsSpeedZ	6.98 km/s
Quality	147	AbsSpeed	31.75 km/s
TRMode	152		
TRLevel	143	Inclination	13.84°
Checksum	217	Eccentricity	0.28



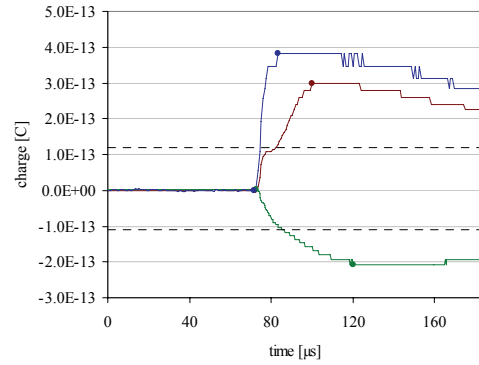
Imp. No.	00070701-26	Mass	2.6E-13 g
		ImpactSpeed	8.60 km/s
Plus5V	4.94 V	ImpactPos	EC
Plus12V	13.07 V	CalibImpact	97102123-37
Minus12V	13.53 V		
Plus200V	254.32 V	PosX	-153307441 km
Minus200V	223.04 V	PosY	39615177 km
TElec	51.08 °C	PosZ	7886932 km
TBox	46.20 °C	Radius	1.06 AU
Date	30-Jun-2000	AbsSpeedX	-3.62 km/s
Time	18:13:38	AbsSpeedY	-28.61 km/s
Spinphase	175.17	AbsSpeedZ	-0.34 km/s
Quality	102	AbsSpeed	28.84 km/s
TRMode	152		
TRLevel	143	Inclination	2.87°
Checksum	226	Eccentricity	0.13



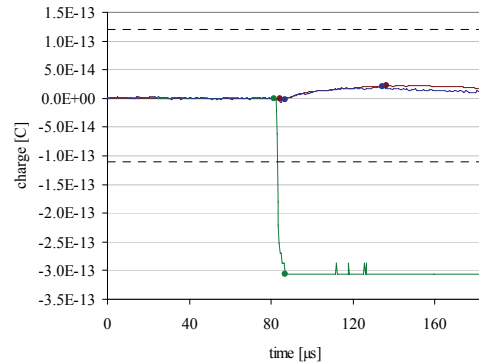
Imp. No.	00070701-29	Mass	4.3E-12 g
		ImpactSpeed	10.46 km/s
Plus5V	4.94 V	ImpactPos	EC_COL
Plus12V	13.07 V	CalibImpact	97080801-42
Minus12V	13.98 V		
Plus200V	254.32 V	PosX	-156281040 km
Minus200V	224.40 V	PosY	32162643 km
TElec	49.46 °C	PosZ	8038908 km
TBox	44.57 °C	Radius	1.07 AU
Date	3-Jul-2000	AbsSpeedX	-4.06 km/s
Time	19:07:25	AbsSpeedY	-31.92 km/s
Spinphase	110.52	AbsSpeedZ	-6.72 km/s
Quality	126	AbsSpeed	32.88 km/s
TRMode	152		
TRLevel	143	Inclination	11.96°
Checksum	113	Eccentricity	0.31



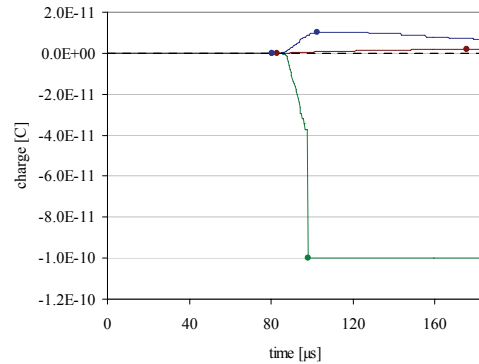
Imp. No.	00072601-17	Mass	2.8E-12 g
		ImpactSpeed	9.02 km/s
Plus5V	4.94 V	ImpactPos	MLL_B
Plus12V	13.07 V	CalibImpact	97100208-44
Minus12V	13.53 V		
Plus200V	255.68 V	PosX	-167002683 km
Minus200V	225.76 V	PosY	-14687530 km
TElec	44.57 °C	PosZ	8584081 km
TBox	41.32 °C	Radius	1.12 AU
Date	22-Jul-2000	AbsSpeedX	5.54 km/s
Time	12:16:06	AbsSpeedY	-26.32 km/s
Spinphase	164.36	AbsSpeedZ	-2.07 km/s
Quality	199	AbsSpeed	26.97 km/s
TRMode	152		
TRLevel	143	Inclination	5.02°
Checksum	50	Eccentricity	0.15



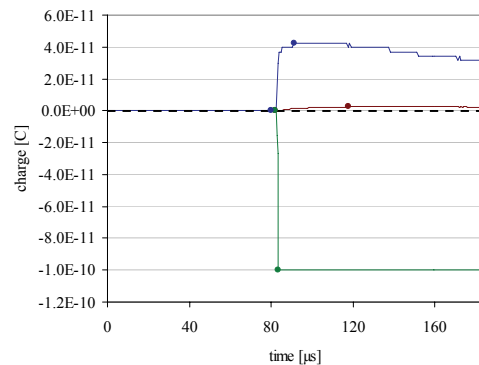
Imp. No.	00081301-3	Mass	2.0E-13 g
		ImpactSpeed	8.39 km/s
Plus5V	4.94 V	ImpactPos	EC_COL
Plus12V	13.14 V	CalibImpact	97080801-6
Minus12V	13.60 V		
Plus200V	257.04 V	PosX	-166716711 km
Minus200V	227.12 V	PosY	-51676975 km
TElec	41.32 °C	PosZ	8564725 km
TBox	36.43 °C	Radius	1.17 AU
Date	6-Aug-2000	AbsSpeedX	9.95 km/s
Time	12:18:13	AbsSpeedY	-23.56 km/s
Spinphase	165.72	AbsSpeedZ	-2.06 km/s
Quality	127	AbsSpeed	25.66 km/s
TRMode	152		
TRLevel	143	Inclination	5.18°
Checksum	122	Eccentricity	0.17



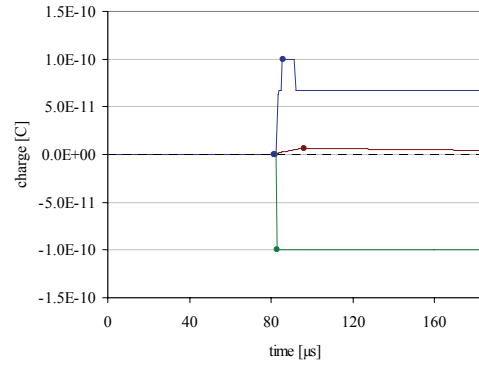
Imp. No.	00081801-37	Mass	1.7E-10 g
		ImpactSpeed	6.49 km/s
Plus5V	4.94 V	ImpactPos	EC
Plus12V	13.21 V	CalibImpact	96112105-34
Minus12V	13.60 V		
Plus200V	258.40 V	PosX	-163003944 km
Minus200V	227.12 V	PosY	-73553807 km
TElec	39.69 °C	PosZ	8370791 km
TBox	34.80 °C	Radius	1.20 AU
Date	15-Aug-2000	AbsSpeedX	11.00 km/s
Time	18:50:25	AbsSpeedY	-22.61 km/s
Spinphase	168.49	AbsSpeedZ	-1.57 km/s
Quality	174	AbsSpeed	25.19 km/s
TRMode	152		
TRLevel	143	Inclination	4.40°
Checksum	211	Eccentricity	0.15



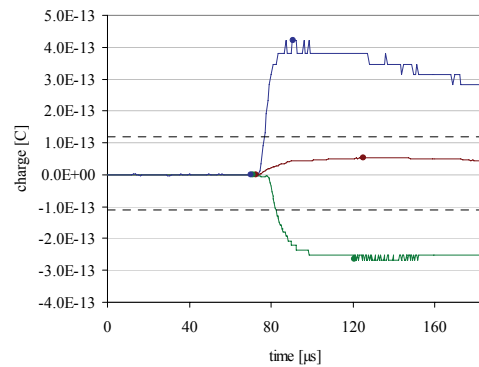
Imp. No.	00092901-3	Mass	3.5E-11 g
		ImpactSpeed	16.39 km/s
Plus5V	4.94 V	ImpactPos	EC_C
Plus12V	13.14 V	CalibImpact	97102245-14
Minus12V	13.68 V		
Plus200V	259.76 V	PosX	-121162129 km
Minus200V	227.12 V	PosY	-154420890 km
TElec	33.18 °C	PosZ	6208188 km
TBox	28.29 °C	Radius	1.31 AU
Date	25-Sep-2000	AbsSpeedX	20.83 km/s
Time	15:04:09	AbsSpeedY	-2.97 km/s
Spinphase	194.85	AbsSpeedZ	1.41 km/s
Quality	178	AbsSpeed	21.08 km/s
TRMode	152		
TRLevel	143	Inclination	5.75°
Checksum	28	Eccentricity	0.58



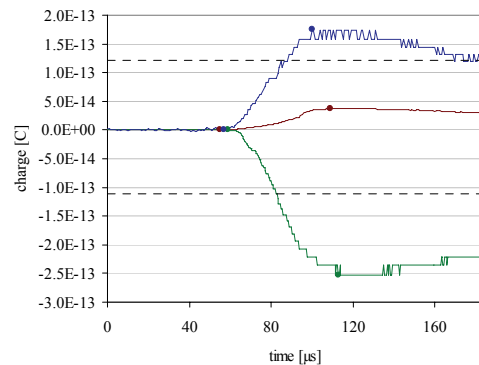
Imp. No.	00101201-16	Mass	7.3E-12 g
Plus5V	4.94 V	ImpactSpeed	21.79 km/s
Plus12V	13.21 V	ImpactPos	EC_C
Minus12V	13.76 V	CalibImpact	96112004-15
Plus200V	261.12 V	PosX	-102758167 km
Minus200V	227.12 V	PosY	-172353058 km
TElec	31.55 °C	PosZ	5259521 km
TBox	26.66 °C	Radius	1.34 AU
Date	7-Oct-2000	AbsSpeedX	21.82 km/s
Time	17:52:39	AbsSpeedY	4.72 km/s
Spinphase	209.09	AbsSpeedZ	5.76 km/s
Quality	182	AbsSpeed	23.05 km/s
TRMode	152	Inclination	20.73°
TRLevel	143	Eccentricity	0.67
Checksum	29		



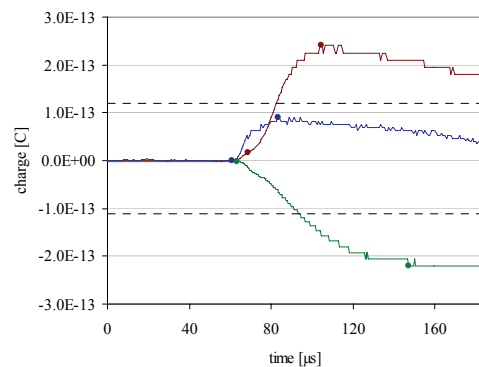
Imp. No.	00101501-37	Mass	2.3E-12 g
Plus5V	4.94 V	ImpactSpeed	8.62 km/s
Plus12V	13.21 V	ImpactPos	MLI_B
Minus12V	13.98 V	CalibImpact	97100205-5
Plus200V	259.76 V	PosX	-93199460 km
Minus200V	228.48 V	PosY	-179901458 km
TElec	31.55 °C	PosZ	4766798 km
TBox	25.04 °C	Radius	1.35 AU
Date	13-Oct-2000	AbsSpeedX	21.72 km/s
Time	14:04:38	AbsSpeedY	-7.86 km/s
Spinphase	243.85	AbsSpeedZ	4.29 km/s
Quality	155	AbsSpeed	23.49 km/s
TRMode	152	Inclination	10.87°
TRLevel	143	Eccentricity	0.20
Checksum	154		



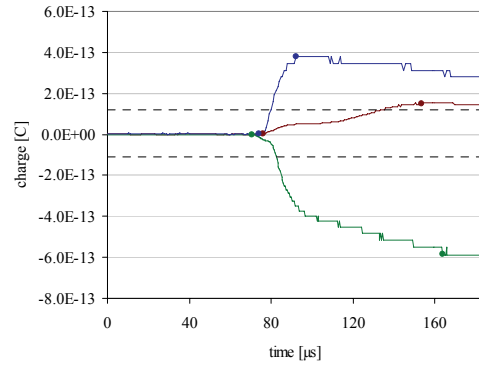
Imp. No.	00103001-13	Mass	3.2E-12 g
Plus5V	4.94 V	ImpactSpeed	5.55 km/s
Plus12V	13.29 V	ImpactPos	EC
Minus12V	13.83 V	CalibImpact	97080805-5
Plus200V	261.12 V	PosX	-69838166 km
Minus200V	229.84 V	PosY	-194489332 km
TElec	29.92 °C	PosZ	3563473 km
TBox	23.41 °C	Radius	1.38 AU
Date	27-Oct-2000	AbsSpeedX	19.99 km/s
Time	00:45:25	AbsSpeedY	-5.41 km/s
Spinphase	164.71	AbsSpeedZ	-2.27 km/s
Quality	140	AbsSpeed	20.84 km/s
TRMode	152	Inclination	6.28°
TRLevel	143	Eccentricity	0.33
Checksum	50		



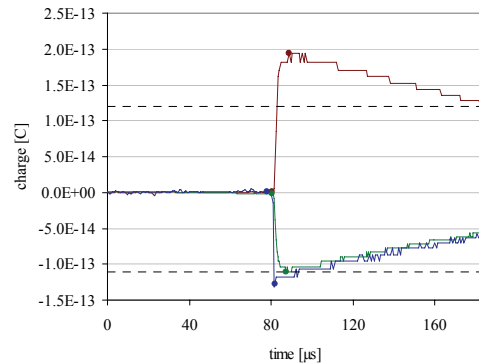
Imp. No.	00103001-22	Mass	3.7E-12 g
Plus5V	4.94 V	ImpactSpeed	6.81 km/s
Plus12V	13.29 V	ImpactPos	IC_C
Minus12V	13.68 V	CalibImpact	97092506-3
Plus200V	261.12 V	PosX	-74153607 km
Minus200V	229.84 V	PosY	-192156991 km
TElec	29.92 °C	PosZ	3785745 km
TBox	23.41 °C	Radius	1.38 AU
Date	24-Oct-2000	AbsSpeedX	20.10 km/s
Time	14:48:28	AbsSpeedY	-5.18 km/s
Spinphase	153.98	AbsSpeedZ	-3.36 km/s
Quality	146	AbsSpeed	21.03 km/s
TRMode	152	Inclination	9.19°
TRLevel	143	Eccentricity	0.33
Checksum	87		



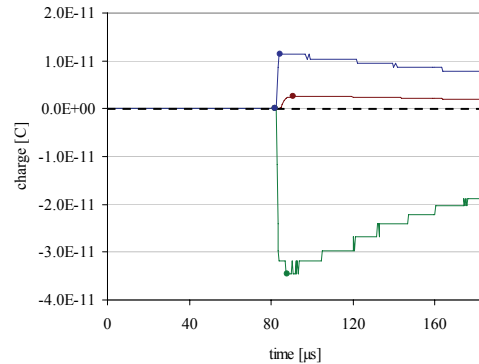
Imp. No.	01012501-8	Mass	2.7E-11 g
Plus5V	4.94 V	ImpactSpeed	3.99 km/s
Plus12V	13.29 V	ImpactPos	EC
Minus12V	13.76 V	CalibImpact	96112203-36
Plus200V	261.12 V	PosX	70699447 km
Minus200V	229.84 V	PosY	-204417263 km
TElec	23.41 °C	PosZ	-3665361 km
TBox	18.52 °C	Radius	1.45 AU
Date	9-Jan-2001	AbsSpeedX	21.30 km/s
Time	06:44:50	AbsSpeedY	10.61 km/s
Spinphase	220.25	AbsSpeedZ	1.42 km/s
Quality	155	AbsSpeed	23.84 km/s
TRMode	152	Inclination	3.45°
TRLevel	143	Eccentricity	0.15
Checksum	70		



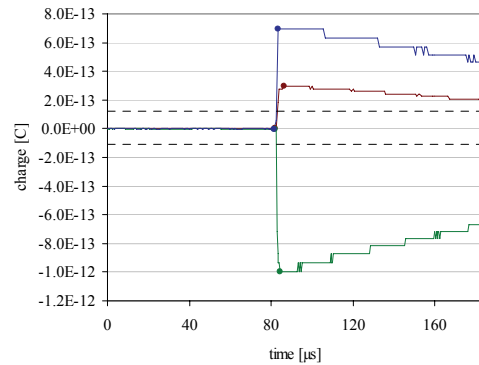
Imp. No.	01012501-19	Mass	7.4E-17 g
Plus5V	4.94 V	ImpactSpeed	62.40 km/s
Plus12V	13.29 V	ImpactPos	IC_C
Minus12V	13.76 V	CalibImpact	97102103-45
Plus200V	262.48 V	PosX	88861867 km
Minus200V	229.84 V	PosY	-196719539 km
TElec	21.78 °C	PosZ	-4598394 km
TBox	15.27 °C	Radius	1.44 AU
Date	19-Jan-2001	AbsSpeedX	-3.31 km/s
Time	13:17:01	AbsSpeedY	46.49 km/s
Spinphase	85.03	AbsSpeedZ	43.78 km/s
Quality	153	AbsSpeed	63.94 km/s
TRMode	152	Inclination	69.39°
TRLevel	143	Eccentricity	4.10
Checksum	232		



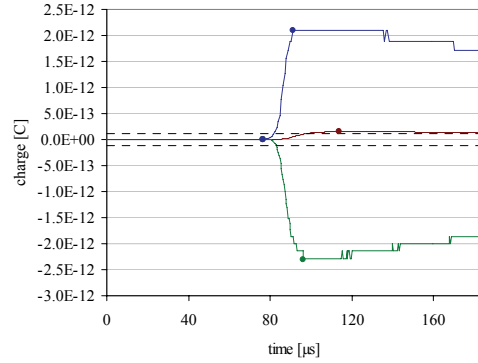
Imp. No.	01012501-29	Mass	6.5E-13 g
Plus5V	4.94 V	ImpactSpeed	26.36 km/s
Plus12V	13.21 V	ImpactPos	EC_COL
Minus12V	13.76 V	CalibImpact	97080801-34
Plus200V	262.48 V	PosX	92751876 km
Minus200V	231.20 V	PosY	-194750035 km
TElec	21.78 °C	PosZ	-4798212 km
TBox	15.27 °C	Radius	1.44 AU
Date	21-Jan-2001	AbsSpeedX	24.30 km/s
Time	19:41:04	AbsSpeedY	34.16 km/s
Spinphase	214.72	AbsSpeedZ	-11.27 km/s
Quality	175	AbsSpeed	43.41 km/s
TRMode	152	Inclination	17.79°
TRLevel	143	Eccentricity	1.89
Checksum	162		



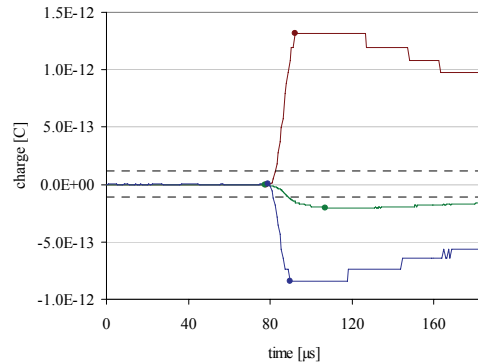
Imp. No.	01030701-32	Mass	3.1E-15 g
Plus5V	4.94 V	ImpactSpeed	42.48 km/s
Plus12V	13.21 V	ImpactPos	IC_C
Minus12V	13.68 V	CalibImpact	97102305-46
Plus200V	261.12 V	PosX	151659347 km
Minus200V	229.84 V	PosY	-144638115 km
TElec	26.66 °C	PosZ	-7821226 km
TBox	21.78 °C	Radius	1.40 AU
Date	2-Mar-2001	AbsSpeedX	-4.70 km/s
Time	17:23:13	AbsSpeedY	45.71 km/s
Spinphase	250.97	AbsSpeedZ	-27.42 km/s
Quality	163	AbsSpeed	53.51 km/s
TRMode	152	Inclination	43.93°
TRLevel	143	Eccentricity	2.80
Checksum	45		



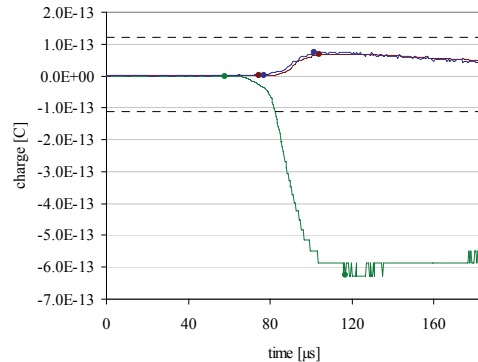
Imp. No.	01030701-42	Mass	2.8E-12 g
Plus5V	4.94 V	ImpactSpeed	11.86 km/s
Plus12V	13.21 V	ImpactPos	EC
Minus12V	13.68 V	CalibImpact	97102216-20
Plus200V	261.12 V	PosX	153407310 km
Minus200V	229.84 V	PosY	-142285263 km
TElec	26.66 °C	PosZ	-7910657 km
TBox	21.78 °C	Radius	1.40 AU
Date	4-Mar-2001	AbsSpeedX	2.37 km/s
Time	04:39:46	AbsSpeedY	16.94 km/s
Spinphase	338.64	AbsSpeedZ	-4.25 km/s
Quality	162	AbsSpeed	17.62 km/s
TRMode	152	Inclination	18.35°
TRLevel	143	Eccentricity	0.69
Checksum	36		



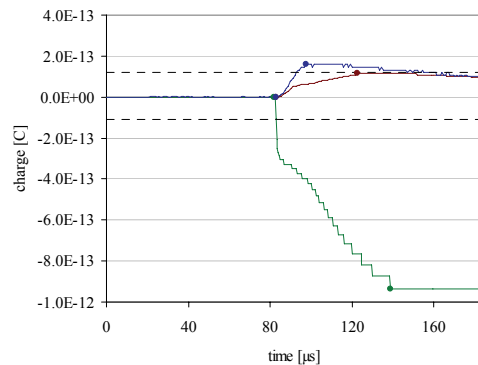
Imp. No.	01031401-28	Mass	1.6E-12 g
Plus5V	4.94 V	ImpactSpeed	12.86 km/s
Plus12V	13.21 V	ImpactPos	IC
Minus12V	13.83 V	CalibImpact	97093009-34
Plus200V	261.12 V	PosX	164272640 km
Minus200V	229.84 V	PosY	-125429220 km
TElec	28.29 °C	PosZ	-8467062 km
TBox	23.41 °C	Radius	1.38 AU
Date	14-Mar-2001	AbsSpeedX	5.26 km/s
Time	03:56:34	AbsSpeedY	29.21 km/s
Spinphase	238.27	AbsSpeedZ	-7.72 km/s
Quality	156	AbsSpeed	30.67 km/s
TRMode	152	Inclination	17.54°
TRLevel	143	Eccentricity	0.60
Checksum	237		



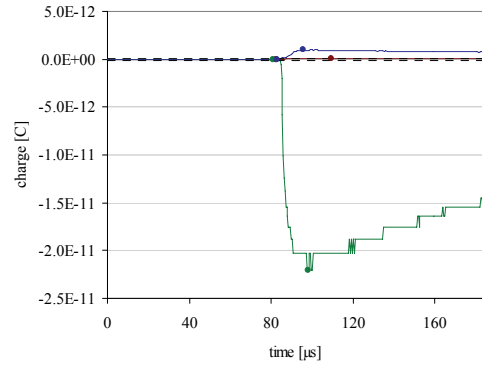
Imp. No.	01031401-30	Mass	N/A
Plus5V	4.94 V	ImpactSpeed	N/A
Plus12V	13.21 V	ImpactPos	GRID_EC
Minus12V	13.98 V	CalibImpact	97102325-12
Plus200V	259.76 V	PosX	164297309 km
Minus200V	229.84 V	PosY	-125385114 km
TElec	28.29 °C	PosZ	-8468330 km
TBox	23.41 °C	Radius	1.38 AU
Date	14-Mar-2001	AbsSpeedX	N/A
Time	04:32:27	AbsSpeedY	N/A
Spinphase	317.20	AbsSpeedZ	N/A
Quality	127	AbsSpeed	N/A
TRMode	152	Inclination	N/A
TRLevel	143	Eccentricity	N/A
Checksum	209		



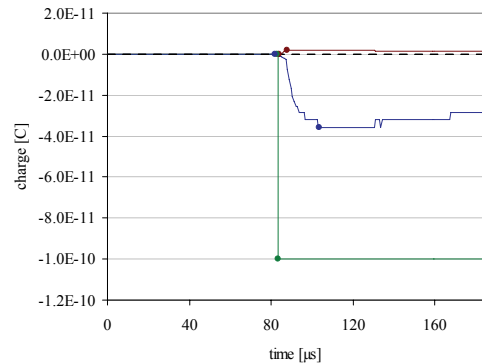
Imp. No.	01042801-43	Mass	N/A
Plus5V	4.94 V	ImpactSpeed	N/A
Plus12V	13.29 V	ImpactPos	GRID_EC
Minus12V	13.68 V	CalibImpact	97102325-12
Plus200V	261.12 V	PosX	187835874 km
Minus200V	227.12 V	PosY	-39757497 km
TElec	29.92 °C	PosZ	-9667764 km
TBox	25.04 °C	Radius	1.29 AU
Date	25-Apr-2001	AbsSpeedX	N/A
Time	18:20:58	AbsSpeedY	N/A
Spinphase	47.68	AbsSpeedZ	N/A
Quality	154	AbsSpeed	N/A
TRMode	152	Inclination	N/A
TRLevel	143	Eccentricity	N/A
Checksum	3		



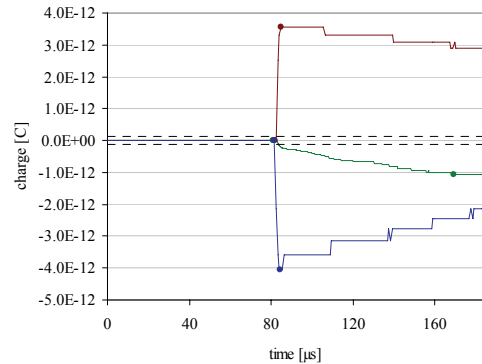
Imp. No.	01042801-49	Mass	N/A
		ImpactSpeed	N/A
Plus5V	4.94 V	ImpactPos	GRID_EC
Plus12V	13.21 V	CalibImpact	97080503-39
Minus12V	13.68 V		
Plus200V	261.12 V	PosX	185210475 km
Minus200V	228.48 V	PosY	-66819656 km
TElec	31.55 °C	PosZ	-9536246 km
TBox	26.66 °C	Radius	1.32 AU
Date	13-Apr-2001	AbsSpeedX	N/A
Time	05:21:54	AbsSpeedY	N/A
Spinphase	48.74	AbsSpeedZ	N/A
Quality	161	AbsSpeed	N/A
TRMode	152		
TRLevel	143	Inclination	N/A
Checksum	233	Eccentricity	N/A



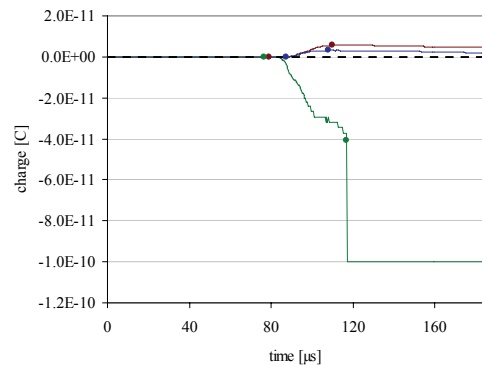
Imp. No.	01051701-6	Mass	2.3E-13 g
		ImpactSpeed	40.38 km/s
Plus5V	4.94 V	ImpactPos	EC
Plus12V	13.21 V	CalibImpact	97102203-31
Minus12V	13.68 V		
Plus200V	261.12 V	PosX	185013498 km
Minus200V	228.48 V	PosY	-3160239 km
TElec	33.18 °C	PosZ	-9517613 km
TBox	28.29 °C	Radius	1.24 AU
Date	12-May-2001	AbsSpeedX	-20.86 km/s
Time	03:53:34	AbsSpeedY	-8.85 km/s
Spinphase	24.35	AbsSpeedZ	12.60 km/s
Quality	131	AbsSpeed	25.93 km/s
TRMode	152		
TRLevel	143	Inclination	128.56°
Checksum	242	Eccentricity	0.82



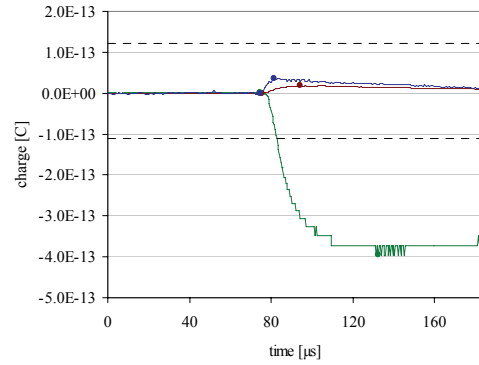
Imp. No.	01070201-1	Mass	7.0E-12 g
		ImpactSpeed	10.29 km/s
Plus5V	4.94 V	ImpactPos	EC_C
Plus12V	13.14 V	CalibImpact	97102315-3
Minus12V	13.60 V		
Plus200V	257.04 V	PosX	130348109 km
Minus200V	225.76 V	PosY	98285898 km
TElec	41.32 °C	PosZ	-6692786 km
TBox	36.43 °C	Radius	1.09 AU
Date	29-Jun-2001	AbsSpeedX	-22.57 km/s
Time	09:35:55	AbsSpeedY	13.19 km/s
Spinphase	72.20	AbsSpeedZ	8.33 km/s
Quality	200	AbsSpeed	27.44 km/s
TRMode	152		
TRLevel	143	Inclination	18.30°
Checksum	203	Eccentricity	0.39



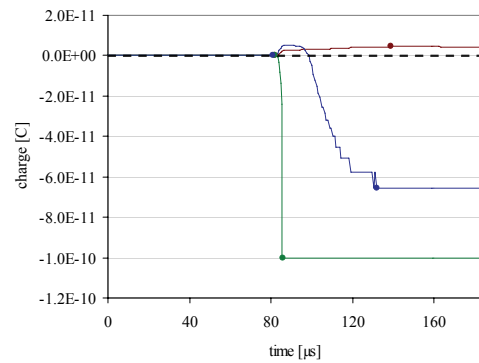
Imp. No.	01070201-6	Mass	6.0E-11 g
		ImpactSpeed	7.93 km/s
Plus5V	4.94 V	ImpactPos	EC_C
Plus12V	14.02 V	CalibImpact	96112003-25
Minus12V	13.68 V		
Plus200V	258.40 V	PosX	159342208 km
Minus200V	227.12 V	PosY	63034534 km
TElec	38.06 °C	PosZ	-8188596 km
TBox	33.18 °C	Radius	1.15 AU
Date	11-Jun-2001	AbsSpeedX	-16.68 km/s
Time	06:08:30	AbsSpeedY	17.61 km/s
Spinphase	307.05	AbsSpeedZ	-3.57 km/s
Quality	161	AbsSpeed	24.52 km/s
TRMode	152		
TRLevel	143	Inclination	10.43°
Checksum	147	Eccentricity	0.42



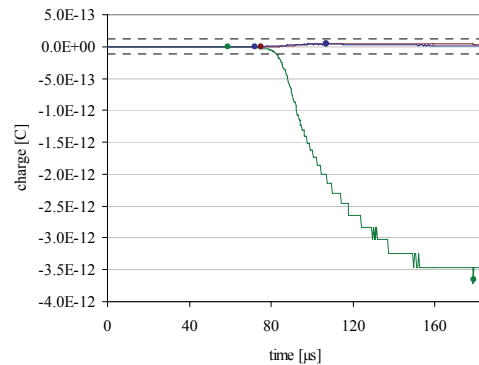
Imp. No.	01070201-40	Mass	N/A
		ImpactSpeed	N/A
Plus5V	4.94 V	ImpactPos	GRID_EC
Plus12V	13.21 V	CalibImpact	97093003-35
Minus12V	13.76 V		
Plus200V	258.40 V	PosX	142835370 km
Minus200V	227.12 V	PosY	85253451 km
TElec	41.32 °C	PosZ	-7336723 km
TBox	36.43 °C	Radius	1.11 AU
Date	22-Jun-2001	AbsSpeedX	N/A
Time	08:06:52	AbsSpeedY	N/A
Spinphase	350.95	AbsSpeedZ	N/A
Quality	148	AbsSpeed	N/A
TRMode	152		
TRLevel	143	Inclination	N/A
Checksum	132	Eccentricity	N/A



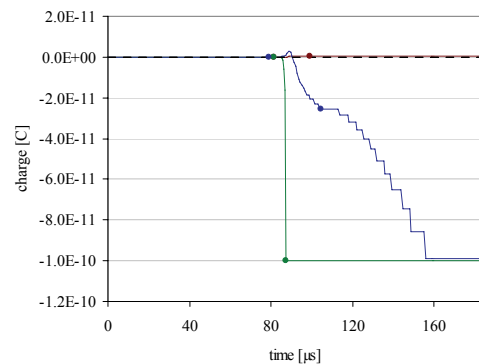
Imp. No.	01070201-50	Mass	N/A
		ImpactSpeed	N/A
Plus5V	4.94 V	ImpactPos	EC
Plus12V	13.58 V	CalibImpact	97102203-31
Minus12V	13.60 V		
Plus200V	257.04 V	PosX	144147630 km
Minus200V	225.76 V	PosY	83721769 km
TElec	41.32 °C	PosZ	-7404466 km
TBox	36.43 °C	Radius	1.12 AU
Date	21-Jun-2001	AbsSpeedX	N/A
Time	12:59:31	AbsSpeedY	N/A
Spinphase	348.35	AbsSpeedZ	N/A
Quality	107	AbsSpeed	N/A
TRMode	152		
TRLevel	143	Inclination	N/A
Checksum	200	Eccentricity	N/A



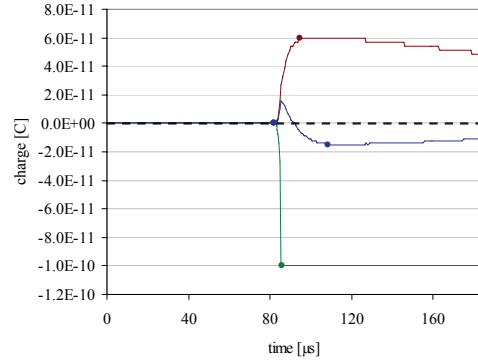
Imp. No.	01071101-3	Mass	6.2E-12 g
		ImpactSpeed	8.72 km/s
Plus5V	4.94 V	ImpactPos	MLI_A
Plus12V	13.29 V	CalibImpact	97102413-25
Minus12V	13.60 V		
Plus200V	257.04 V	PosX	124917369 km
Minus200V	225.76 V	PosY	103219225 km
TElec	42.94 °C	PosZ	-6412911 km
TBox	38.06 °C	Radius	1.08 AU
Date	2-Jul-2001	AbsSpeedX	-21.18 km/s
Time	05:38:10	AbsSpeedY	12.28 km/s
Spinphase	315.84	AbsSpeedZ	-3.16 km/s
Quality	140	AbsSpeed	24.69 km/s
TRMode	152		
TRLevel	143	Inclination	8.93°
Checksum	48	Eccentricity	0.42



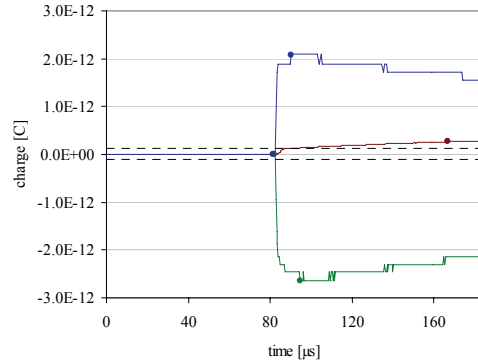
Imp. No.	01071101-14	Mass	N/A
		ImpactSpeed	N/A
Plus5V	4.94 V	ImpactPos	MLI_A
Plus12V	13.14 V	CalibImpact	97102422-43
Minus12V	13.60 V		
Plus200V	257.04 V	PosX	122701224 km
Minus200V	225.76 V	PosY	105114802 km
TElec	42.94 °C	PosZ	-6298786 km
TBox	38.06 °C	Radius	1.08 AU
Date	3-Jul-2001	AbsSpeedX	N/A
Time	08:32:53	AbsSpeedY	N/A
Spinphase	5.27	AbsSpeedZ	N/A
Quality	123	AbsSpeed	N/A
TRMode	152		
TRLevel	143	Inclination	N/A
Checksum	18	Eccentricity	N/A



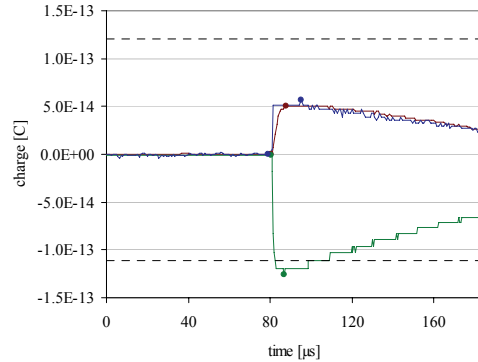
Imp. No.	01080701-35	Mass	N/A
		ImpactSpeed	N/A
Plus5V	4.94 V	ImpactPos	IC_C
Plus12V	13.07 V	CalibImpact	97080501-6
Minus12V	13.60 V		
Plus200V	254.32 V	PosX	40249764 km
Minus200V	223.04 V	PosY	144297129 km
TElec	52.71 °C	PosZ	-2053286 km
TBox	49.46 °C	Radius	1.00 AU
Date	6-Aug-2001	AbsSpeedX	N/A
Time	13:30:43	AbsSpeedY	N/A
Spinphase	338.07	AbsSpeedZ	N/A
Quality	162	AbsSpeed	N/A
TRMode	152		
TRLevel	143	Inclination	N/A
Checksum	209	Eccentricity	N/A



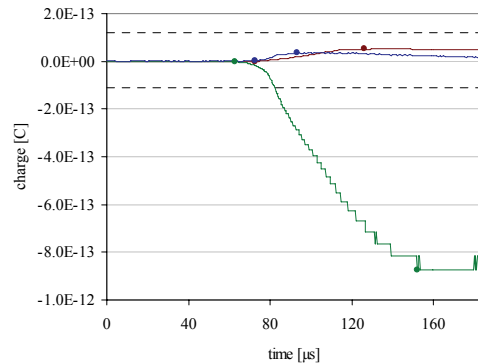
Imp. No.	01081601-8	Mass	7.1E-13 g
		ImpactSpeed	16.72 km/s
Plus5V	4.94 V	ImpactPos	EC_COL
Plus12V	13.14 V	CalibImpact	96112204-6
Minus12V	13.53 V		
Plus200V	254.32 V	PosX	17568823 km
Minus200V	223.04 V	PosY	147008013 km
TElec	52.71 °C	PosZ	-886524 km
TBox	47.83 °C	Radius	0.99 AU
Date	14-Aug-2001	AbsSpeedX	-31.95 km/s
Time	17:42:07	AbsSpeedY	-10.70 km/s
Spinphase	249.57	AbsSpeedZ	-9.37 km/s
Quality	165	AbsSpeed	34.97 km/s
TRMode	152		
TRLevel	143	Inclination	17.25°
Checksum	62	Eccentricity	0.53



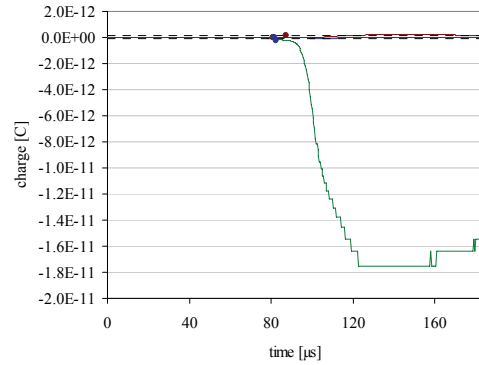
Imp. No.	01081601-14	Mass	1.6E-15 g
		ImpactSpeed	33.47 km/s
Plus5V	4.94 V	ImpactPos	EC_COL
Plus12V	13.07 V	CalibImpact	97080802-23
Minus12V	13.60 V		
Plus200V	254.32 V	PosX	16885348 km
Minus200V	223.04 V	PosY	147047013 km
TElec	52.71 °C	PosZ	-851363 km
TBox	47.83 °C	Radius	0.99 AU
Date	14-Aug-2001	AbsSpeedX	-29.44 km/s
Time	23:33:07	AbsSpeedY	-22.47 km/s
Spinphase	254.80	AbsSpeedZ	-21.12 km/s
Quality	187	AbsSpeed	42.63 km/s
TRMode	152		
TRLevel	143	Inclination	38.56°
Checksum	187	Eccentricity	1.02



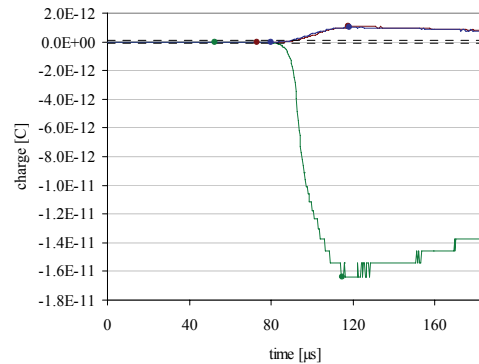
Imp. No.	01081601-39	Mass	4.7E-12 g
		ImpactSpeed	8.59 km/s
Plus5V	4.94 V	ImpactPos	MLL_A
Plus12V	13.07 V	CalibImpact	97102411-39
Minus12V	13.53 V		
Plus200V	254.32 V	PosX	27219203 km
Minus200V	221.68 V	PosY	146222479 km
TElec	52.71 °C	PosZ	-1382973 km
TBox	47.83 °C	Radius	0.99 AU
Date	11-Aug-2001	AbsSpeedX	-25.03 km/s
Time	06:49:33	AbsSpeedY	-0.60 km/s
Spinphase	335.70	AbsSpeedZ	-0.88 km/s
Quality	145	AbsSpeed	25.05 km/s
TRMode	152		
TRLevel	143	Inclination	2.22°
Checksum	194	Eccentricity	0.36



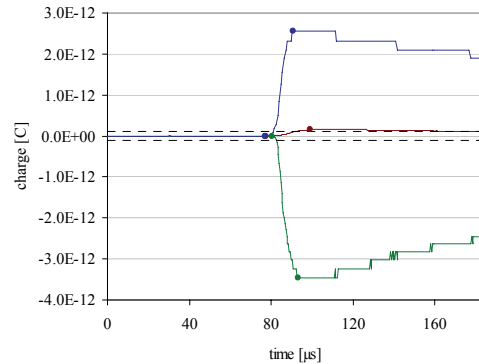
Imp. No.	01091201-4	Mass	1.6E-16 g
Plus5V	4.94 V	ImpactSpeed	69.58 km/s
Plus12V	13.07 V	ImpactPos	IC_C
Minus12V	13.98 V	CalibImpact	97102239-11
Plus200V	254.32 V	PosX	-152913439 km
Minus200V	224.40 V	PosY	40469814 km
TElec	49.46 °C	PosZ	7845675 km
TBox	44.57 °C	Radius	1.06 AU
Date	3-Jul-2000	AbsSpeedX	-68.94 km/s
Time	19:07:25	AbsSpeedY	4.25 km/s
Spinphase	110.52	AbsSpeedZ	24.34 km/s
Quality	126	AbsSpeed	73.23 km/s
TRMode	152	Inclination	57.20°
TRLevel	143	Eccentricity	2.07
Checksum	113		



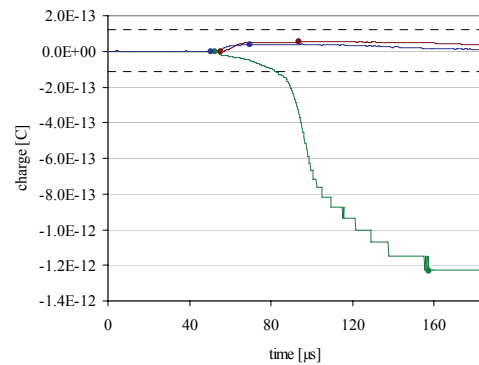
Imp. No.	01091201-24	Mass	6.4E-11 g
Plus5V	4.94 V	ImpactSpeed	5.40 km/s
Plus12V	13.07 V	ImpactPos	EC
Minus12V	13.68 V	CalibImpact	96112105-37
Plus200V	255.68 V	PosX	-52485293 km
Minus200V	225.76 V	PosY	136371100 km
TElec	51.08 °C	PosZ	2714743 km
TBox	46.20 °C	Radius	0.98 AU
Date	8-Sep-2001	AbsSpeedX	-25.69 km/s
Time	22:14:27	AbsSpeedY	-11.09 km/s
Spinphase	336.09	AbsSpeedZ	0.19 km/s
Quality	161	AbsSpeed	27.98 km/s
TRMode	152	Inclination	1.15°
TRLevel	143	Eccentricity	0.14
Checksum	91		



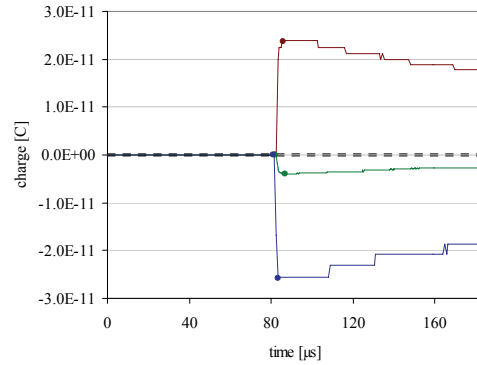
Imp. No.	01091201-33	Mass	2.2E-12 g
Plus5V	4.94 V	ImpactSpeed	13.66 km/s
Plus12V	13.07 V	ImpactPos	EC
Minus12V	13.68 V	CalibImpact	97102218-25
Plus200V	254.32 V	PosX	-28290410 km
Minus200V	224.40 V	PosY	143408893 km
TElec	49.46 °C	PosZ	1471372 km
TBox	46.20 °C	Radius	0.98 AU
Date	31-Aug-2001	AbsSpeedX	-25.41 km/s
Time	01:13:26	AbsSpeedY	-14.07 km/s
Spinphase	272.86	AbsSpeedZ	-7.99 km/s
Quality	163	AbsSpeed	30.13 km/s
TRMode	152	Inclination	15.94°
TRLevel	143	Eccentricity	0.30
Checksum	29		



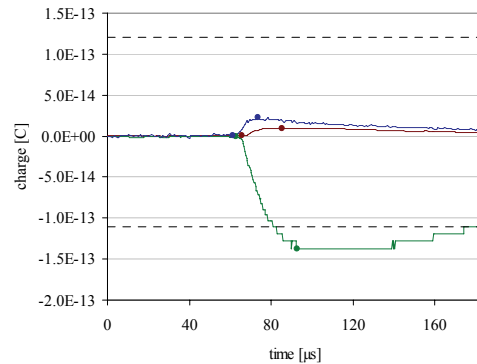
Imp. No.	01091201-35	Mass	N/A
Plus5V	4.94 V	ImpactSpeed	N/A
Plus12V	13.07 V	ImpactPos	GRID_EC
Minus12V	13.98 V	CalibImpact	97102239-11
Plus200V	255.68 V	PosX	-55854359 km
Minus200V	224.40 V	PosY	135073123 km
TElec	51.08 °C	PosZ	2887877 km
TBox	46.20 °C	Radius	0.98 AU
Date	10-Sep-2001	AbsSpeedX	N/A
Time	04:43:43	AbsSpeedY	N/A
Spinphase	251.15	AbsSpeedZ	N/A
Quality	113	AbsSpeed	N/A
TRMode	152	Inclination	N/A
TRLevel	143	Eccentricity	N/A
Checksum	69		



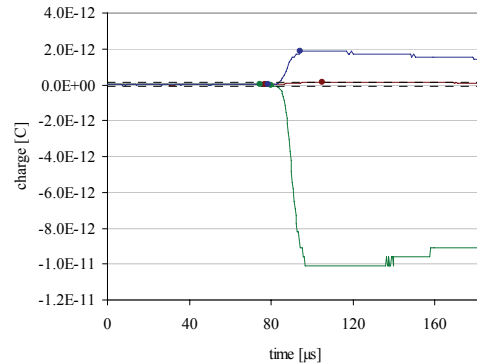
Imp. No.	01101501-15	Mass	1.1E-12 g
Plus5V	4.94 V	ImpactSpeed	28.96 km/s
Plus12V	13.07 V	ImpactPos	IC
Minus12V	13.60 V	CalibImpact	97080603-43
Plus200V	255.68 V	PosX	-118445072 km
Minus200V	225.76 V	PosY	92784313 km
TElec	47.83 °C	PosZ	6100892 km
TBox	42.94 °C	Radius	1.01 AU
Date	7-Oct-2001	AbsSpeedX	0.11 km/s
Time	06:07:38	AbsSpeedY	-17.25 km/s
Spinphase	297.95	AbsSpeedZ	-16.57 km/s
Quality	207	AbsSpeed	23.92 km/s
TRMode	152	Inclination	50.08°
TRLevel	143	Eccentricity	0.57
Checksum	151		



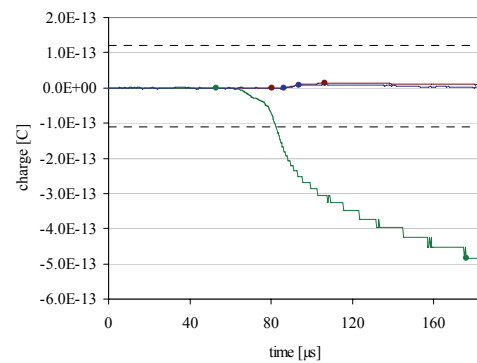
Imp. No.	01101501-37	Mass	1.7E-13 g
Plus5V	4.94 V	ImpactSpeed	13.84 km/s
Plus12V	13.07 V	ImpactPos	MLI_A
Minus12V	13.60 V	CalibImpact	97102413-13
Plus200V	255.68 V	PosX	-121445047 km
Minus200V	223.04 V	PosY	89542857 km
TElec	47.83 °C	PosZ	6254968 km
TBox	42.94 °C	Radius	1.01 AU
Date	8-Oct-2001	AbsSpeedX	-10.17 km/s
Time	20:27:08	AbsSpeedY	-16.33 km/s
Spinphase	338.82	AbsSpeedZ	-1.93 km/s
Quality	108	AbsSpeed	19.33 km/s
TRMode	152	Inclination	6.05°
TRLevel	143	Eccentricity	0.58
Checksum	150		



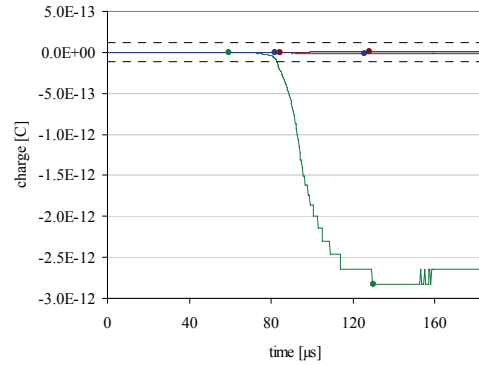
Imp. No.	01102601-47	Mass	1.2E-13 g
Plus5V	4.94 V	ImpactSpeed	14.26 km/s
Plus12V	13.29 V	ImpactPos	EC_COL
Minus12V	13.60 V	CalibImpact	97080801-43
Plus200V	257.04 V	PosX	-147692924 km
Minus200V	227.12 V	PosY	51559764 km
TElec	46.20 °C	PosZ	7599835 km
TBox	41.32 °C	Radius	1.05 AU
Date	25-Oct-2001	AbsSpeedX	-3.70 km/s
Time	20:22:45	AbsSpeedY	-29.54 km/s
Spinphase	105.12	AbsSpeedZ	9.99 km/s
Quality	165	AbsSpeed	31.40 km/s
TRMode	152	Inclination	19.65°
TRLevel	143	Eccentricity	0.24
Checksum	206		



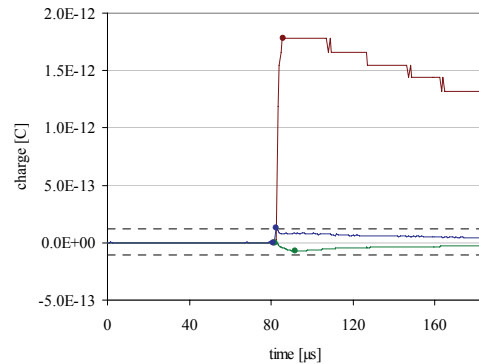
Imp. No.	01110301-8	Mass	N/A
Plus5V	4.94 V	ImpactSpeed	N/A
Plus12V	13.21 V	ImpactPos	GRID_EC
Minus12V	13.60 V	CalibImpact	97102325-12
Plus200V	257.04 V	PosX	-155260426 km
Minus200V	225.76 V	PosY	34800106 km
TElec	46.20 °C	PosZ	7986757 km
TBox	41.32 °C	Radius	1.06 AU
Date	1-Nov-2001	AbsSpeedX	N/A
Time	18:22:40	AbsSpeedY	N/A
Spinphase	335.30	AbsSpeedZ	N/A
Quality	112	AbsSpeed	N/A
TRMode	152	Inclination	N/A
TRLevel	143	Eccentricity	N/A
Checksum	209		



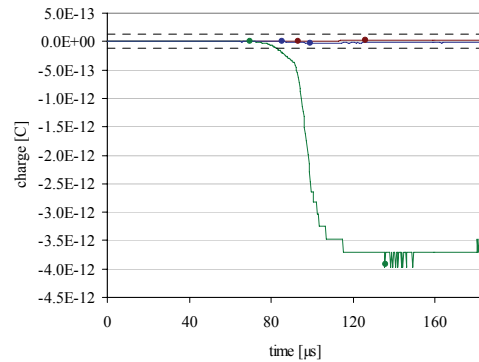
Imp. No.	01110301-43	Mass	9.2E-12 g
Plus5V	4.94 V	ImpactSpeed	8.45 km/s
Plus12V	13.29 V	ImpactPos	MLL_A
Minus12V	13.60 V	CalibImpact	97102413-25
Plus200V	257.04 V	PosX	-152106974 km
Minus200V	225.76 V	PosY	42349726 km
TElec	46.20 °C	PosZ	7825425 km
TBox	41.32 °C	Radius	1.06 AU
Date	29-Oct-2001	AbsSpeedX	-7.44 km/s
Time	16:13:37	AbsSpeedY	-23.83 km/s
Spinphase	302.39	AbsSpeedZ	-4.51 km/s
Quality	113	AbsSpeed	25.37 km/s
TRMode	152	Inclination	10.70°
TRLevel	143	Eccentricity	0.23
Checksum	174		



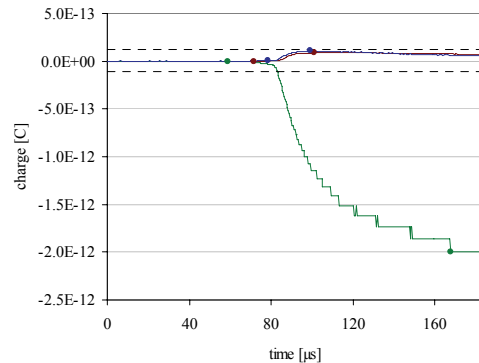
Imp. No.	01110301-50	Mass	6.5E-15 g
Plus5V	4.94 V	ImpactSpeed	34.64 km/s
Plus12V	13.14 V	ImpactPos	IC_C
Minus12V	13.60 V	CalibImpact	97102310-31
Plus200V	257.04 V	PosX	-152762671 km
Minus200V	224.40 V	PosY	40854760 km
TElec	46.20 °C	PosZ	7858999 km
TBox	41.32 °C	Radius	1.06 AU
Date	30-Oct-2001	AbsSpeedX	7.91 km/s
Time	06:59:05	AbsSpeedY	-1.62 km/s
Spinphase	336.93	AbsSpeedZ	-9.16 km/s
Quality	144	AbsSpeed	12.20 km/s
TRMode	152	Inclination	93.10°
TRLevel	143	Eccentricity	0.91
Checksum	68		



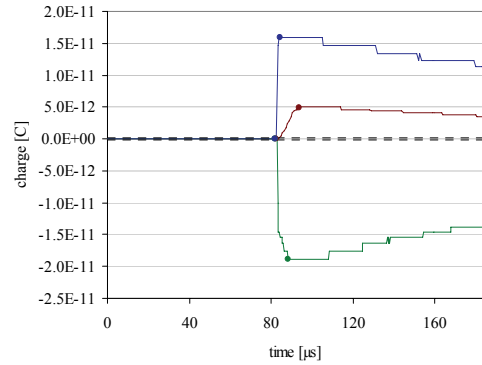
Imp. No.	01112101-3	Mass	N/A
Plus5V	4.94 V	ImpactSpeed	N/A
Plus12V	13.29 V	ImpactPos	GRID_EC
Minus12V	13.60 V	CalibImpact	97093003-35
Plus200V	258.40 V	PosX	-165364919 km
Minus200V	227.12 V	PosY	-2030892 km
TElec	44.57 °C	PosZ	8501495 km
TBox	39.69 °C	Radius	1.11 AU
Date	16-Nov-2001	AbsSpeedX	N/A
Time	12:16:52	AbsSpeedY	N/A
Spinphase	263.72	AbsSpeedZ	N/A
Quality	93	AbsSpeed	N/A
TRMode	152	Inclination	N/A
TRLevel	143	Eccentricity	N/A
Checksum	173		



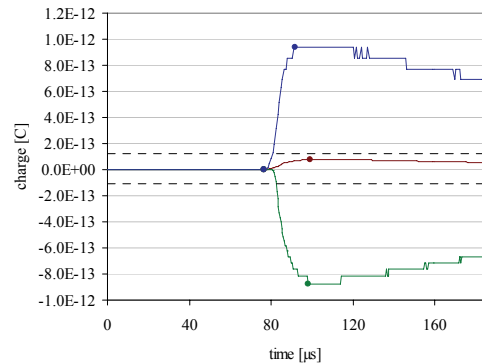
Imp. No.	01120901-40	Mass	N/A
Plus5V	4.94 V	ImpactSpeed	N/A
Plus12V	13.14 V	ImpactPos	GRID_EC
Minus12V	13.76 V	CalibImpact	97102239-11
Plus200V	258.40 V	PosX	-167460239 km
Minus200V	225.76 V	PosY	-42873428 km
TElec	41.32 °C	PosZ	8603767 km
TBox	36.43 °C	Radius	1.16 AU
Date	2-Dec-2001	AbsSpeedX	N/A
Time	22:06:35	AbsSpeedY	N/A
Spinphase	346.16	AbsSpeedZ	N/A
Quality	143	AbsSpeed	N/A
TRMode	152	Inclination	N/A
TRLevel	143	Eccentricity	N/A
Checksum	126		



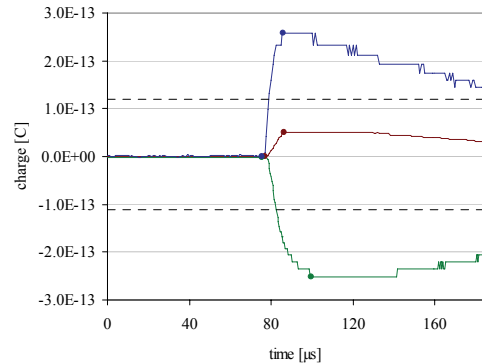
Imp. No.	01121801-31	Mass	6.0E-13 g
Plus5V	4.94 V	ImpactSpeed	27.87 km/s
Plus12V	13.14 V	ImpactPos	EC_C
Minus12V	13.83 V	CalibImpact	96112004-15
Plus200V	259.76 V	PosX	-163047897 km
Minus200V	227.12 V	PosY	-73317671 km
TElec	39.69 °C	PosZ	8373146 km
TBox	34.80 °C	Radius	1.20 AU
Date	15-Dec-2001	AbsSpeedX	7.11 km/s
Time	17:18:10	AbsSpeedY	-1.35 km/s
Spinphase	37.13	AbsSpeedZ	11.18 km/s
Quality	173	AbsSpeed	13.32 km/s
TRMode	152	Inclination	70.08°
TRLevel	143	Eccentricity	0.81
Checksum	97		



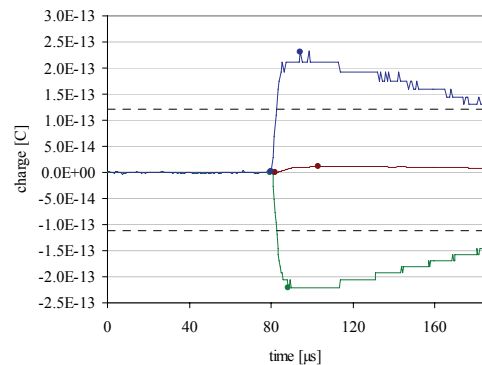
Imp. No.	02020501-2	Mass	6.4E-13 g
Plus5V	4.94 V	ImpactSpeed	14.15 km/s
Plus12V	13.29 V	ImpactPos	MLI_B
Minus12V	13.76 V	CalibImpact	97100207-42
Plus200V	261.12 V	PosX	-119420615 km
Minus200V	228.48 V	PosY	-156340981 km
TElec	34.80 °C	PosZ	6118480 km
TBox	28.29 °C	Radius	1.32 AU
Date	26-Jan-2002	AbsSpeedX	8.61 km/s
Time	20:50:42	AbsSpeedY	-7.41 km/s
Spinphase	339.83	AbsSpeedZ	-4.43 km/s
Quality	123	AbsSpeed	12.20 km/s
TRMode	152	Inclination	21.46°
TRLevel	143	Eccentricity	0.78
Checksum	208		



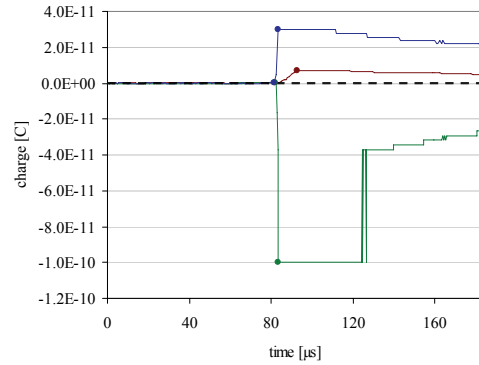
Imp. No.	02020501-30	Mass	1.9E-13 g
Plus5V	4.94 V	ImpactSpeed	14.51 km/s
Plus12V	13.21 V	ImpactPos	MLI_B
Minus12V	13.76 V	CalibImpact	97100205-9
Plus200V	261.12 V	PosX	-111524003 km
Minus200V	227.12 V	PosY	-164433827 km
TElec	33.18 °C	PosZ	5711383 km
TBox	28.29 °C	Radius	1.33 AU
Date	1-Feb-2002	AbsSpeedX	9.78 km/s
Time	04:10:21	AbsSpeedY	-6.04 km/s
Spinphase	33.71	AbsSpeedZ	4.54 km/s
Quality	152	AbsSpeed	12.35 km/s
TRMode	152	Inclination	21.68°
TRLevel	143	Eccentricity	0.77
Checksum	189		



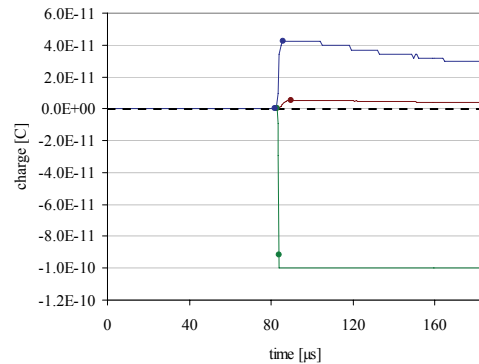
Imp. No.	02021501-14	Mass	1.6E-13 g
Plus5V	4.94 V	ImpactSpeed	15.72 km/s
Plus12V	13.21 V	ImpactPos	EC
Minus12V	14.59 V	CalibImpact	97102218-46
Plus200V	261.12 V	PosX	-94200049 km
Minus200V	228.48 V	PosY	-179153738 km
TElec	33.18 °C	PosZ	4818354 km
TBox	28.29 °C	Radius	1.35 AU
Date	12-Feb-2002	AbsSpeedX	22.52 km/s
Time	00:27:34	AbsSpeedY	-3.10 km/s
Spinphase	247.28	AbsSpeedZ	-11.50 km/s
Quality	147	AbsSpeed	25.47 km/s
TRMode	152	Inclination	27.92°
TRLevel	143	Eccentricity	0.31
Checksum	198		



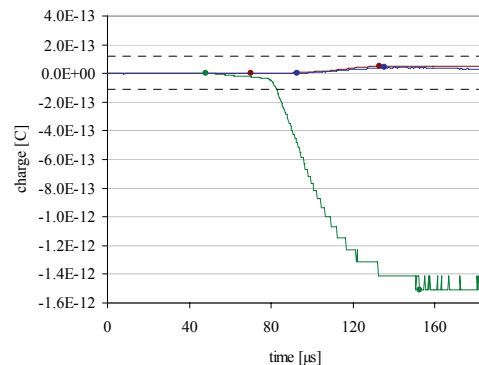
Imp. No.	02021501-31	Mass	2.2E-12 g
Plus5V	4.94 V	ImpactSpeed	29.10 km/s
Plus12V	13.29 V	ImpactPos	EC
Minus12V	13.76 V	CalibImpact	97102206-11
Plus200V	259.76 V	PosX	-96222343 km
Minus200V	227.12 V	PosY	-177623575 km
TElec	33.18 °C	PosZ	4922522 km
TBox	28.29 °C	Radius	1.35 AU
Date	10-Feb-2002	AbsSpeedX	1.55 km/s
Time	19:09:15	AbsSpeedY	4.60 km/s
Spinphase	320.80	AbsSpeedZ	-13.95 km/s
Quality	180	AbsSpeed	14.77 km/s
TRMode	152	Inclination	93.42°
TRLevel	143	Eccentricity	0.72
Checksum	26		



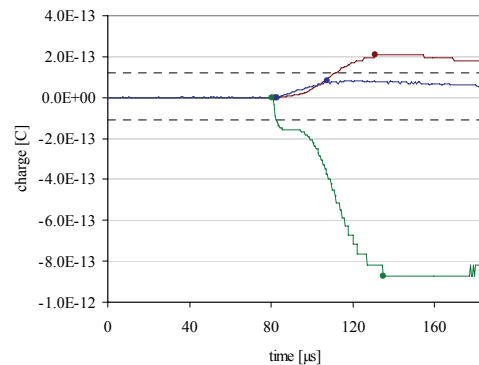
Imp. No.	02022501-25	Mass	7.4E-13 g
Plus5V	4.94 V	ImpactSpeed	31.35 km/s
Plus12V	13.21 V	ImpactPos	EC_C
Minus12V	13.68 V	CalibImpact	97080504-29
Plus200V	261.12 V	PosX	-74917678 km
Minus200V	228.48 V	PosY	-191727021 km
TElec	33.18 °C	PosZ	3825042 km
TBox	26.66 °C	Radius	1.38 AU
Date	23-Feb-2002	AbsSpeedX	8.84 km/s
Time	05:15:40	AbsSpeedY	8.41 km/s
Spinphase	288.19	AbsSpeedZ	-22.29 km/s
Quality	178	AbsSpeed	25.41 km/s
TRMode	152	Inclination	76.82°
TRLevel	143	Eccentricity	0.45
Checksum	197		



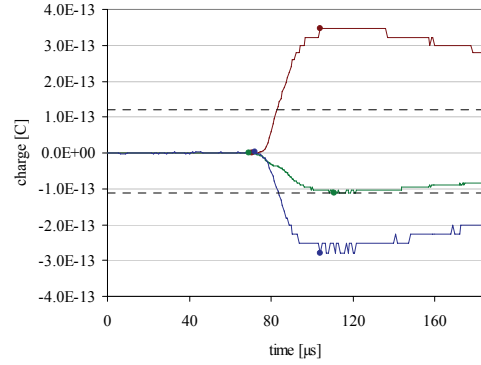
Imp. No.	02032301-8	Mass	N/A
Plus5V	4.94 V	ImpactSpeed	N/A
Plus12V	13.21 V	ImpactPos	EC_COL
Minus12V	13.76 V	CalibImpact	97080801-22
Plus200V	261.12 V	PosX	-29441565 km
Minus200V	229.84 V	PosY	-209681925 km
TElec	29.92 °C	PosZ	1483941 km
TBox	25.04 °C	Radius	1.42 AU
Date	19-Mar-2002	AbsSpeedX	N/A
Time	17:27:36	AbsSpeedY	N/A
Spinphase	337.50	AbsSpeedZ	N/A
Quality	104	AbsSpeed	N/A
TRMode	152	Inclination	N/A
TRLevel	143	Eccentricity	N/A
Checksum	163		



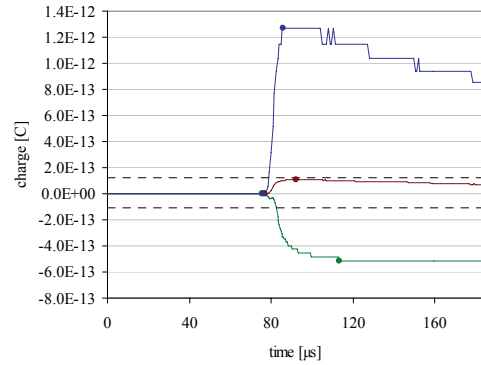
Imp. No.	02032301-12	Mass	N/A
Plus5V	4.94 V	ImpactSpeed	N/A
Plus12V	13.21 V	ImpactPos	GRID_EC
Minus12V	13.68 V	CalibImpact	97100115-41
Plus200V	262.48 V	PosX	-23430977 km
Minus200V	228.48 V	PosY	-211023843 km
TElec	29.92 °C	PosZ	1174685 km
TBox	25.04 °C	Radius	1.42 AU
Date	22-Mar-2002	AbsSpeedX	N/A
Time	20:37:50	AbsSpeedY	N/A
Spinphase	16.17	AbsSpeedZ	N/A
Quality	145	AbsSpeed	N/A
TRMode	152	Inclination	N/A
TRLevel	143	Eccentricity	N/A
Checksum	122		



Imp. No.	02033101-7	Mass	9.5E-13 g
Plus5V	4.94 V	ImpactSpeed	9.11 km/s
Plus12V	13.36 V	ImpactPos	IC_C
Minus12V	13.76 V	CalibImpact	97102314-10
Plus200V	261.12 V	PosX	-14980509 km
Minus200V	228.48 V	PosY	-212550436 km
TElec	29.92 °C	PosZ	739853 km
TBox	23.41 °C	Radius	1.42 AU
Date	27-Mar-2002	AbsSpeedX	14.11 km/s
Time	05:49:45	AbsSpeedY	-1.18 km/s
Spinphase	331.52	AbsSpeedZ	-4.31 km/s
Quality	153	AbsSpeed	14.80 km/s
TRMode	152	Inclination	16.92°
TRLevel	143	Eccentricity	0.65
Checksum	83		



Imp. No.	02041401-34	Mass	8.4E-13 g
Plus5V	4.94 V	ImpactSpeed	12.84 km/s
Plus12V	13.21 V	ImpactPos	EC
Minus12V	13.76 V	CalibImpact	97092510-10
Plus200V	261.12 V	PosX	-4703522 km
Minus200V	229.84 V	PosY	-213835193 km
TElec	28.29 °C	PosZ	211179 km
TBox	23.41 °C	Radius	1.43 AU
Date	1-Apr-2002	AbsSpeedX	12.48 km/s
Time	13:17:15	AbsSpeedY	1.60 km/s
Spinphase	308.41	AbsSpeedZ	-8.34 km/s
Quality	119	AbsSpeed	15.10 km/s
TRMode	152	Inclination	33.82°
TRLevel	143	Eccentricity	0.64
Checksum	89		



Appendix D: XML files Document Type Descriptions

File telemetry.dtd used for document type description of MDC telemetry files (downloaded data files from NOZOMI and calibration data files).

```
<!-- data type declaration for MDC telemetry files *.dat.xml -->
<!-- -->
<!-- Author:      Robert Senger -->
<!-- Date:       12/10/2002 -->

<!-- Main element segment, contains elements HSK data, segment info
and segment data -->
<!ELEMENT segment (hskdata, seginfo, segdata)>
<!ATTLIST segment
    filename    CDATA #REQUIRED
    segno       CDATA #REQUIRED
    impno       CDATA #REQUIRED>

<!-- Element HSK data, contains all HSK data -->
<!ELEMENT hskdata (plus5v, plus12v, minus12v, plus200v, minus200v,
telec, tbox)>
<!ELEMENT plus5v (#PCDATA)>
<!ELEMENT plus12v (#PCDATA)>
<!ELEMENT minus12v (#PCDATA)>
<!ELEMENT plus200v (#PCDATA)>
<!ELEMENT minus200v (#PCDATA)>
<!ELEMENT telec (#PCDATA)>
<!ELEMENT tbox (#PCDATA)>

<!-- Element segment info, contains information about the stored
signal and time/attitude, also calibration data -->
<!ELEMENT seginfo (jdate, date, time, spinphase, quality, trmode,
trlevel, checksum, (calibdata, calibdata, calibdata))>
<!ELEMENT jdate (#PCDATA)>
<!ELEMENT date (#PCDATA)>
<!ELEMENT time (#PCDATA)>
<!ELEMENT spinphase (#PCDATA)>
<!ELEMENT quality (#PCDATA)>
<!ELEMENT trmode (#PCDATA)>
<!ELEMENT trlevel (#PCDATA)>
<!ELEMENT checksum (#PCDATA)>
<!ATTLIST checksum
    state (true|false) #REQUIRED>
<!ELEMENT calibdata (#PCDATA)>
<!ATTLIST calibdata
    type (ic|ec|nc) #REQUIRED
    xmin CDATA "0"
```

```

    xmax CDATA      "0"
    ymin CDATA      "0"
    ymax CDATA      "0">

<!-- Element segment data, contains the data of the three channels
of the stored signal -->
<!ELEMENT segdata ((chdata, chdata, chdata)+)>
<!ELEMENT chdata (pdata)>
<!ATTLIST chdata
    type (ic|ec|nc) #REQUIRED
    format (dump|charge) #REQUIRED>
<!ELEMENT pdata (#PCDATA)>

```

File housekeeping.dtd used for document type description of MDC housekeeping files (downloaded files from NOZOMI).

```
<!-- data type declaration for MDC hsk files -->
<!-- -->
<!-- Author:    Robert Senger -->
<!-- Date:     08/01/2003 -->

<!-- Main element -->
<!ELEMENT hskfile (sequence)>

<!-- Element sequence, contains all HSK data -->
<!ELEMENT sequence (TMd, TMt, MDC1, MDC2, HVp, HVm, TB, TC, IC, TM,
TL, NC, EC, MA, V, MTO, TSP, D, T)>
<!ATTLIST sequence
    filename    CDATA #REQUIRED
    seqnumber   CDATA #REQUIRED>

<!ELEMENT TMd (#PCDATA)>
<!ELEMENT TMt (#PCDATA)>
<!ELEMENT MDC1 (#PCDATA)>
<!ELEMENT MDC2 (#PCDATA)>
<!ELEMENT HVp (#PCDATA)>
<!ELEMENT HVm (#PCDATA)>
<!ELEMENT TB (#PCDATA)>
<!ELEMENT TC (#PCDATA)>
<!ELEMENT IC (#PCDATA)>
<!ELEMENT TM (#PCDATA)>
<!ELEMENT TL (#PCDATA)>
<!ELEMENT NC (#PCDATA)>
<!ELEMENT EC (#PCDATA)>
<!ELEMENT MA (#PCDATA)>
<!ELEMENT V (#PCDATA)>
<!ELEMENT MTO (#PCDATA)>
<!ELEMENT TSP (#PCDATA)>
<!ELEMENT D (#PCDATA)>
<!ELEMENT T (#PCDATA)>
```


Appendix E: MDC-NOZOMI Publications

Igenbergs, E., Sasaki, S., Faber, G., Fischer, F., Münzenmayer, R., Fujiwara, A., Iglseeder, H., Glasmachers, A., Grün, E., Mukai, T., Ohashi, H., Schwehm, G., Svedhem, H., Yamakoshi, K., “Mars Dust Counter on Board ISAS PLANET-B”, in *Physics, Chemistry, and Dynamics of Interplanetary Dust* (ed. B.A.S. Gustafson and M.S. Hanner), ASP Conf. Series, Vol. 104, pp. 233-236, 1996

Igenbergs, E., Münzenmayer, R., Sasaki, S., Faber, G., Fischer, F., Fujiwara, A., Iglseeder, H., Glasmachers, A., Grün, E., Mukai, T., Ohashi, H., Schwehm, G., Svedhem, H., Yamakoshi, K., “Mars Dust Counter on Board ISAS PLANET-B”, in *Proceedings of 20th International Symposium on Space Technology and Space*, Gifu, Japan, pp. 1222-1229, 1996

Igenbergs, E., Sasaki, S., Muenzenmayer, R., Ohashi, H., Faber, G., Fischer, F., Fujiwara, A., Hamabe, Y., Iglseeder, H., Klinge, D., Miyamoto, H., Glasmachers, A., Gruen, E., Mukai, T., Naumann, W., Nogami, K., Schwehm, G., Svedhem, H., Yamakoshi, K., “Mars Dust Counter”, *Earth Planets Space*, Vol. 50, pp. 241-245, 1998

Sasaki, S., Igenbergs, E., Münzenmayer, R., Naumann, W., Ohashi, H., Born, M., Faber, G., Fischer, F., Fujiwara, A., Glasmachers, A., Grün, E., Hamabe, Y., Iglseeder, H., Miyamoto, H., Morishige, K., Mukai, T., Nogami, K.-I., Schwehm, G., Svedhem, H., Yamakoshi, K., “MDC (Mars Dust Counter) on Board NOZOMI: Launch and Initial Operations”, *Proc. 31st ISAS Lunar Planet. Symp.* (eds. H. Mizutani and M. Kato), pp.243-246, 1998

Sasaki, S., Igenbergs, E., Ohashi, H., Münzenmayer, R., Naumann, W., Born, M., Faber, G., Fischer, F., Fujiwara, A., Glasmachers, A., Grün, E., Hamabe, Y., Hofschuster, G., Iglseeder, H., Miyamoto, H., Morishige, K., Mukai, T., Nogami, K.-I., Schwehm, G., Svedhem, H., Yamakoshi, K., “Initial results of Mars Dust Counter (MDC) on board NOZOMI: Leonids encounter”, *Lunar Planet. Sci.*, XXX 1581, 1999

Sasaki, S., Igenbergs, E., Münzenmayer, R., Ohashi, H., Hofschuster, G., Naumann, W., Faber, G., Fischer, F., Fujiwara, A., Glasmachers, A., Grün, E., Hamabe, Y., Iglseeder, H., Miyamoto, H., Mukai, T., Nogami, K., Schwehm, G., Svedhem, H., Born, M., Kawamura, T., Klinge, D., Morishige, K., Naoi, T., Peeks, R., Yano, H., Yamakoshi, K., “Mars Dust Counter on board NOZOMI: First year results”, *Proceedings of 22nd International Symposium on Space Technology and Science*, Vol. 00-j-21, pp. 1664-1667, 2000

Sasaki, S., Igenbergs, E., Ohashi, H., Hofschuster, G., Münzenmayer, R., Naumann, W., Senger, R., Fischer, F., Fujiwara, A., Grün, E., Hamabe, Y., Kawamura, T., Mann, I., Miyamoto, H., Nogami, K., Svedhem, H., “Interplanetary dust observation in the Earth-Mars region by Mars Dust Counter (MDC) on board NOZOMI: Three-year results”, *Proceedings of the Meteoroids 2001 Conference*, ESA SP-495, pp. 595-599, 2001

Sasaki, S., Igenbergs, E., Ohashi, H., Münzenmayer, R., Naumann, W., Hofschuster, G., Born, M., Faber, G., Fischer, F., Fujiwara, A., Glasmachers, A., Grün, E., Hamabe, Y., Iglseider, H., Kawamura, T., Miyamoto, H., Morishige, K., Mukai, T., Naoi, T., Nogami, K., Schwehm, G., Svedhem, H., “Observation of interplanetary and interstellar dust particles by Mars Dust Counter (MDC) on board NOZOMI”, *Adv. Space Res.*, Vol. 29, pp. 1145-1153, 2002

Sasaki, S., Igenbergs, E., Münzenmayer, R., Ohashi, H., Hofschuster, G., Naumann, W., Faber, G., Fischer, F., Fujiwara, A., Glasmachers, A., Grün, E., Hamabe, Y., Iglseider, H., Miyamoto, H., Mukai, T., Nogami, K., Schwehm, G., Svedhem, H., Born, M., Kawamura, T., Klinge, D., Morishige, K., Naoi, T., Peeks, R., Yano, H., Yamakoshi, K., “Mars Dust Counter (MDC) on Board NOZOMI: Initial Results”, *Proceedings of IAU Colloquium 181, Dust in the solar System and Other Planetary Systems* (edited by S.F. Green, I. Williams, T. McDonnell & N. McBride), pp.176-180, 2002

Sasaki, S., Igenbergs, E., Ohashi, H., Senger, R., Hofschuster, G., Münzenmayer, R., Naumann, W., Grün, E., Hamabe, Y., Kawamura, T., Mann, I., Miyamoto, H., Nogami, K.-I., Shoji, S., Svedhem, H., “Mars Dust Counter (MDC) on board NOZOMI: Three-year results”, *Proceedings of 23rd International Symposium on Space Technology and Science, 2002-k-17*, 2002

Sasaki, S., Igenbergs, E., Ohashi, H., Senger, R., Hofschuster, G., Münzenmayer, R., Naumann, W., Grün, E., Fujiwara, A., Hamabe, Y., Mann, I., Miyamoto, H., Mukai, T., Nogami, K., Shoji, S., Svedhem, H., “Interplanetary and interstellar dust observation by Mars Dust Counter on board NOZOMI: Four-year operation” *Proceedings of Asteroids, Comets, Meteors (ACM2002)*, ESA-SP-500, pp. 79-82, 2002

Appendix F: Curriculum vitae

Feb. 9, 1970	born in Munich, Germany
1976-1980	Primary School, Munich
1980-1989	Luitpold Gymnasium, Munich
June 1989	High-school degree (Abitur)
Nov. 1989 - Feb. 1998	Physics studies at the Technische Universität München
Nov. 1994 - Oct. 1995	Diploma thesis at the Lehrstuhl für Biophysik at Technische Universität München, Prof. Dr. E. Sackmann
June 1995 - July 1995	Visiting undergraduate scientist at the University of Kent at Canterbury (UK), Research School of Biosciences, Prof. Dr. M. F. Tuite
Feb. 4, 1998	University degree (Diploma)
June 1999 - July 2004	Research assistant at LRT, Technische Universität München

Appendix G: Legal information

Microsoft, Excel, Visual Basic, Visual C and *Windows* are either registered trademarks or trademarks of Microsoft Corporation in the United States and/or other countries.

MATLAB is a registered trademark of The MathWorks, Inc.

Intel and *Pentium* are trademarks or registered trademarks of Intel Corporation or its subsidiaries in the United States and other countries.

Kapton and *Nomex* are registered trademarks of E.I. du Pont de Nemours and Company.

Java is a trademark or registered trademark of Sun Microsystems, Inc. in the U.S. or other countries.

